

**ELECTRON COUNTING
USING
PROPORTIONAL COUNTERS**

by

Jamil Akhtar Mir

A thesis submitted to the University of Leicester for the degree of
Doctor of Philosophy.

May 1992

UMI Number: U041434

All rights reserved

INFORMATION TO ALL USERS

The quality of this reproduction is dependent upon the quality of the copy submitted.

In the unlikely event that the author did not send a complete manuscript and there are missing pages, these will be noted. Also, if material had to be removed, a note will indicate the deletion.



UMI U041434

Published by ProQuest LLC 2015. Copyright in the Dissertation held by the Author.
Microform Edition © ProQuest LLC.

All rights reserved. This work is protected against
unauthorized copying under Title 17, United States Code.



ProQuest LLC
789 East Eisenhower Parkway
P.O. Box 1346
Ann Arbor, MI 48106-1346



X751978743

X751978743

Dedicated to my mother, father, sisters and in the loving memory of my brother Shakil Ahmed Mir who went into God's care during the course of the present research, at the tender age of 25. His pleasant and charismatic character will always be remembered.

Electron counting using proportional counters.

JAMIL AKHTAR MIR

ABSTRACT

The X-ray energy resolution achieved by conventional charge signal measurements using a gas proportional counter is determined by statistical fluctuations in the primary number of electrons and in the charge multiplication process. Conventional X-ray energy resolution thus increases as $(E)^{-1/2}$ where E is the X-ray energy. The proportional counter, therefore, gives a very unsatisfactory X-ray energy resolution for X-ray energies below 1 keV. By eliminating the statistical fluctuations due to the charge multiplication, it is possible to improve the X-ray energy resolution by a factor of 2 over that achieved by conventional charge signal measurements. The implementation of this concept requires an 100 % detection efficiency for the electrons present in the primary clusters.

The present work is based on electron counting method which uses the charge signals due to single electrons avalanching at the anode wire. The main aim of this work was to determine the maximum possible electron counting efficiency. This required a detailed examination of the parameters relevant to the operation of an electron counting system. An experimental chamber consisting of a uniform field drift tube and a coaxial proportional counter was constructed. Experimental work was carried out to determine electron loss mechanisms such as electron loss by capture, electron loss below the discriminator threshold of the electron counting electronics and electron loss due to the finite resolving time of the electron counting electronics. This involved the measurements of electron mobility and electron lifetime at very low drift fields ($E_d/p < 0.02$ V/cm Torr) for a number of different counter gas mixtures. Single electron response was also examined for these counter gas mixtures at a wide range of charge gains.

It was found possible to achieve 89.0 % electron counting efficiency at 1.49 keV using A-CH₄ (50%). The corresponding X-ray energy resolution was found to be 19.5 %FWHM, compared to 28.0 %FWHM achieved by the conventional charge signal measurements.

Acknowledgements

I would like to thank the Science and Engineering Research Council for providing financial support for the present research and to Professor K. Pounds for granting me permission to use the facilities of Leicester University's Physics Department.

I would also like to express my sincere thanks to my late supervisor Dr. E. Mathieson for his excellent supervision during the experimental phase of this research. Many thanks to my second supervisor, Dr. G.W. Fraser, who had "the eye for detail" and thus provided many valuable comments during the thesis write-up. Many thanks, also to my other colleagues who provided prompt technical assistance whenever it was required, particularly Dr. T. Harris, Dr. J.P. Hennessy, Mr. N. Dorsey, Mr. M. Harrison, Mr. K. Wallace and Mr. I. Samuel.

Finally, I would like to thank all the members of my family for their encouragement and support during all my education. Many thanks to all those friends who gave me the moral support during this work. In particular, Dr. T. Harris, Dr. R.E. Evans, Mrs. P. English, Mrs. D. Jerman, Mr. A. Hussain and Mr. A. Riaz.

Contents

Abstract.....	1
Acknowledgements.....	2

Chapter 1: Introduction.

1.1	X-ray spectroscopy.....	5
1.2	Proportional counters.....	6
1.3	The absorption process in counter gas.....	12
1.4	Quantum detection efficiency.....	14
1.5	Proportional counter operation.....	15
1.6	X-ray energy resolution.....	15
1.7	Imaging.....	20
1.8	Gas Scintillation Proportional Counters (GSPCs).....	23
1.9	Scintillation counters.....	28
1.10	Solid state detectors.....	29
1.11	Electron counting using charge.....	31
1.12	Scope of thesis.....	34

Chapter 2 : Conventional charge signal measurements to investigate pulse height spectra and charge gains.

2.1	Introduction.....	37
2.2	The statistics of avalanche growth.....	38
2.3	Experimental system.....	42
2.4	Experimental procedure.....	44
2.5	Conventional X-ray energy resolution measurements : results and discussion.....	57
2.6	Single electron pulse height spectra and charge gain measurements : results and discussion.....	59
2.7	Conclusions.....	95

Chapter 3 : Determination of electron losses due to capture.

3.1	Introduction.....	96
-----	-------------------	----

3.2	Basic theory for μ and D_1/μ measurement.....	96
3.3	Experimental system.....	101
3.4	Experimental procedure.....	105
3.5	Experimental μ and D_1/μ measurements : results and discussion.....	107
3.6	Mean electron lifetime measurements in counter gas mixtures.....	118
3.7	Theory of electron lifetime determination.....	119
3.8	Experimental procedure.....	122
3.9	Experimental electron lifetime measurements : results and discussion.....	123
3.10	Conclusions.....	131

Chapter 4 : Determination of electron counting losses due to the finite resolving time of the electron counting electronics.

4.1	Introduction.....	135
4.2	Experimental procedure.....	135
4.3	Experimental measurement of τ_r : results and discussion.....	137
4.4	Conclusions.....	144

Chapter 5 : Electron counting spectra.

5.1	Introduction.....	145
5.2	Experimental procedure.....	145
5.3	X-ray energy resolution measurements : results and discussion.....	147
5.4	Conclusions.....	163

Chapter 6 : Summary and discussion. 165

Appendix A.....	171
Appendix B.....	173
Appendix C.....	174
List of References.....	175
Publications	

Chapter 1

Introduction.

1.1 X-ray spectroscopy

The current investigations have been pursued to examine the possibility of improving proportional counter X-ray energy resolution in the 1.0-6.0 keV range by means of electron counting techniques. The X-ray energy range stated is governed by experimental limitations. The lower energy limit is determined by the counter's window material and its thickness. The upper energy limit is determined by the resolving time of the electron counting electronics.

The interaction of ionizing radiation with gases results in the formation of electron-ion pairs. For the energy range of interest, these primary ionisation clusters are formed in the vicinity of the initial photoionisation. Typical photoelectron ranges in the gas mixtures employed are only a few millimetres. The average number of electrons, N_0 , in the primary ionization cluster, formed by the photoelectric absorption of an X-ray photon in the gas is equal to E/W where E is the photon energy and W is the average energy dissipated during electron-ion pair production. In principal, W is determined by the gas species involved and by the nature and energy of the ionising radiation. Empirical observations, however, indicate that W is nearly independent of these parameters (Curran (1955)).

The concept of electron counting to improve proportional counter X-ray energy resolution was first suggested by Walenta (1979). This involves the decomposition of primary ionization clusters into individual signal peaks (see section 1.6) and differs from conventional proportional counter measurements due to its independence of the signal fluctuations inherent in electron multiplication.

If electron counting techniques are to be used practically for improving soft X-ray energy resolution then it is critical to examine parameters such as the mean electron lifetime against capture, usually by oxygen molecules, the maximum signal-to-noise of the electron counting electronics and the resolving time of the electron counting electronics. In this work, by the application of *experimental variables such as drift field and average counter charge gain*, an attempt was made to obtain the best possible electron counting efficiency. For example, oxygen concentration was reduced below 1 part per million (ppm) to minimize electron loss by capture. In order to minimize electron loss below the discriminator threshold level of the electron counting electronics large charge

gains were used. Large drift times were used to reduce electron loss due to the finite resolving time of the electron counting electronics.

1.2 Proportional counters

A schematic representation of a typical single wire proportional counter is shown in figure 1.1. It is known as a sealed type coaxial proportional counter due to the vacuum tight confinement of the counter gas. There also exist various forms of flow type proportional counters where the counter gas mixture is continuously circulated at a steady rate. In the former case, the radiation entrance window usually consists of thin beryllium, 25-500 μm thick. The anode consists of a fine stainless steel wire, typically 25 μm in diameter which is supported at both ends by much larger field tubes which are also made of steel. Good X-ray energy resolution depends upon the condition that each electron created during the original ionising event undergoes the same amount of charge multiplication. It is found, however, that field distortion occurs at the end points of the anode wire. By introducing field tubes, typically 0.25 mm in diameter, a dead region is created where no electron multiplication can take place.

Proportional counters are very versatile instruments with respect to their geometrical flexibility and constructional simplicity. Proportional counters have been employed in the fields of X-ray astronomy and applied nuclear physics since the early nineteen-sixties (Giacconi et al. (1962)). Campion (1968) and Bambynek (1973) give comprehensive reviews of proportional counter research applications. The proportional counter is a useful modification of the ionization chamber and was introduced by Rutherford and Geiger in 1908. However, the full potential of the proportional counter was only realised when pulse processing electronics became available, in the 1930s. Rossi and Staub pioneered many varieties of proportional counter during the second World War. Rossi and Staub (1949) give a comprehensive survey of constructional designs, performances and understanding of phenomena related to these devices, as then understood. They also introduced the multi-wire proportional counter (MWPC) which consisted of equally spaced anode wires. A MWPC provides a faster response and therefore a higher count rate capability. Significant contributions towards the understanding of MWPC were made by Charpak (1977) who used *planes of equally spaced conductive or resistive wires as the anode and cathode(s)*. Another category of proportional counters which has emerged is the parallel plate proportional counter (PPPC) which uses a conductive or resistive sheet as the anode and a fine mesh grid as a cathode (Hempel et al. (1975), Stelzer (1976), Sanford et al. (1979), Stumpel et al. (1973)). The PPPC

arrangement has been further modified by the introduction of multistep chambers where the overall charge gain is increased using more than one amplification stage (Breskin et al. (1979), Charpak et al. (1988)). The proportional counter has also been constructed using blade, needle and toroidal geometries. Figures 1.2a to 1.2g depict various proportional counter configurations.

In the present work, very weak drift fields were employed ($E_d/p < 0.02$ V/cm Torr) to determine different parameters which should assist towards the prediction of the performance of any single (charge pulse or light pulse) electron counting system. The parameters of interest were the mean electron lifetime in the counting gas mixtures employed, electron mobility and diffusion coefficients, signal-to-noise ratio of the electron counting electronics and the maximum possible usable charge gain before the onset of secondaries. The presence of secondaries causes avalanche breeding during which avalanche chains rather than individual avalanches are detected (Kluckow (1957)). There are three different categories of secondary processes : 1) Photoelectric effect 2) Positive ion drift and 3) Diffusion of metastable atoms. The first is far more effective than the others (Lauer (1952)) and involves the photoelectric emission of electrons from the cathode by UV photons originating from Townsend avalanches. UV photons in the 1200 Å to 1400 Å wavelength range are emitted by excited argon atoms (Suzuki et al. (1979)) and have sufficient energy (≈ 10 eV) to cause photoemission from the steel counter anterior with approximately 4 eV photoelectric work function. The photoelectric effect is also possible between the UV or visible photons emitted when excited gas molecules decay to their ground states and the less tightly bound electrons of the counter gas mixture. The secondary processes contribute another source of signal fluctuation to those already discussed and impose a further limitation on the ultimate X-ray energy resolution in a conventional proportional counter as well as in an electron counting system.

The choice of counter gas mixture influences the quantum detection efficiency, X-ray energy resolution (Agrawal et al. (1989)) and operational stability. Most counter gas predominately consist of large fraction of an inert gas with a smaller fraction of a polyatomic additive. The additive gas is referred to as a quenching gas and has several important roles which enhance the proportional counter operation. For example, polyatomic gas molecules help retain counter proportionality by suppressing avalanche breeding which would otherwise occur when the excited inert gas atoms emit UV photons. Preferential absorption of these photons takes place in presence of methane which shows a

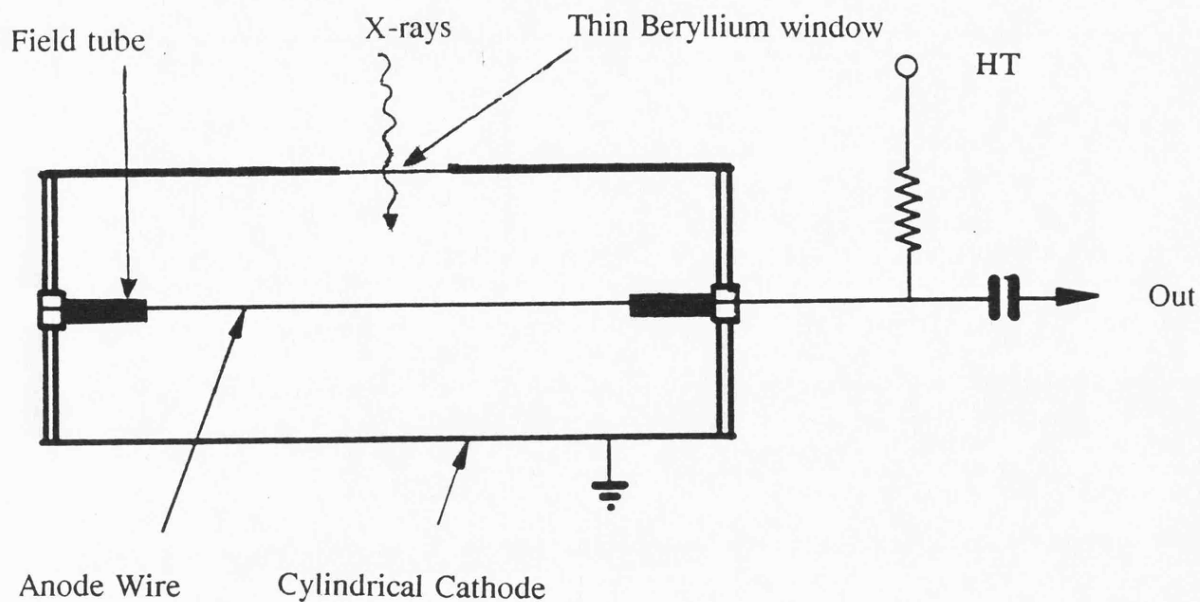


Figure 1.1 : A typical single-wire proportional counter.

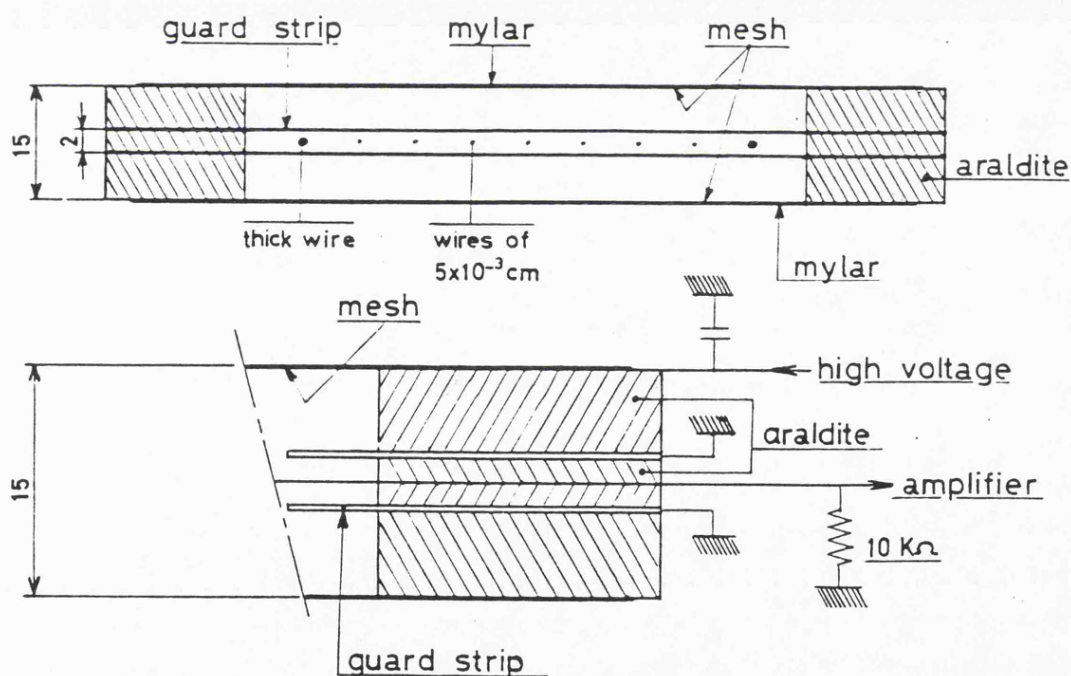


Figure 1.2a : The basic design of the prototype position-sensitive MWPC (Charpak et al. (1968)).

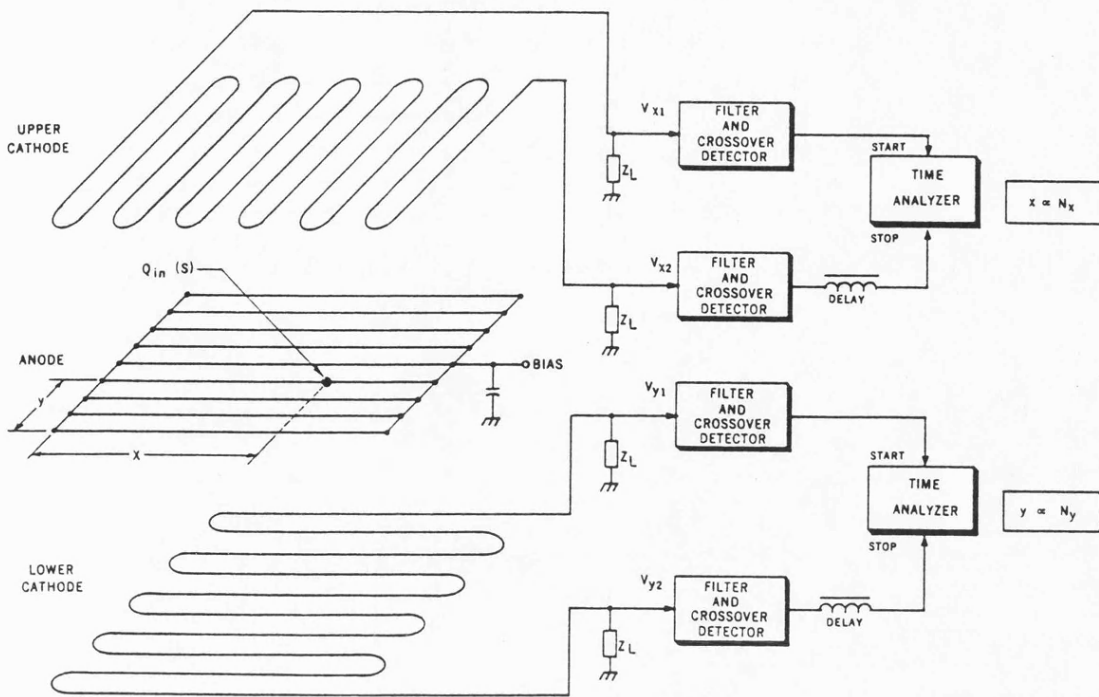


Figure 1.2b : A schematic diagram of a MWPC and the associated signal processing circuits (Borkowski and Kopp (1972)).

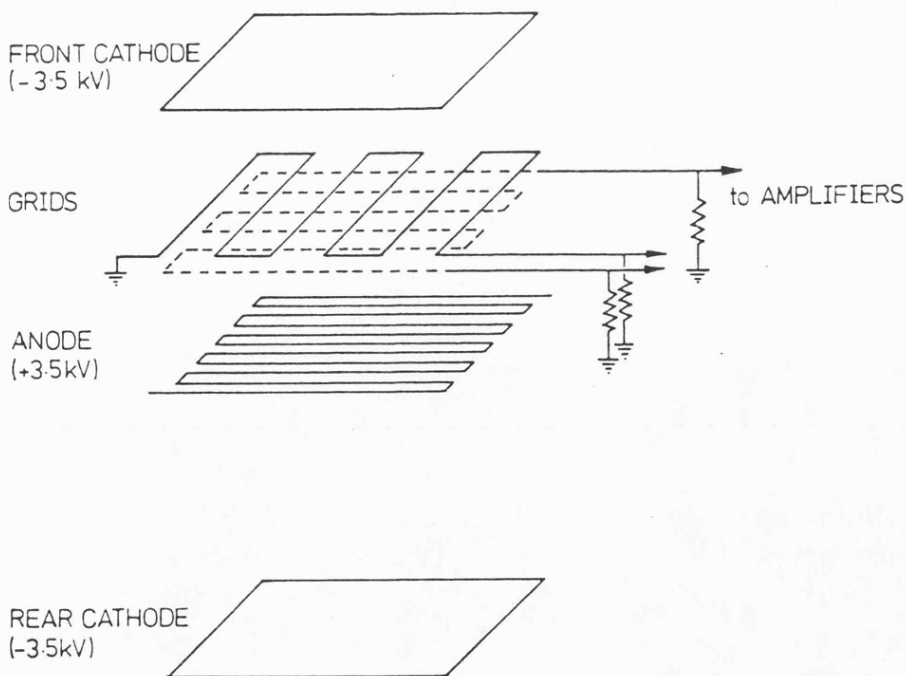


Figure 1.2c : A schematic diagram of MWPC (Hough and Drever (1972)).

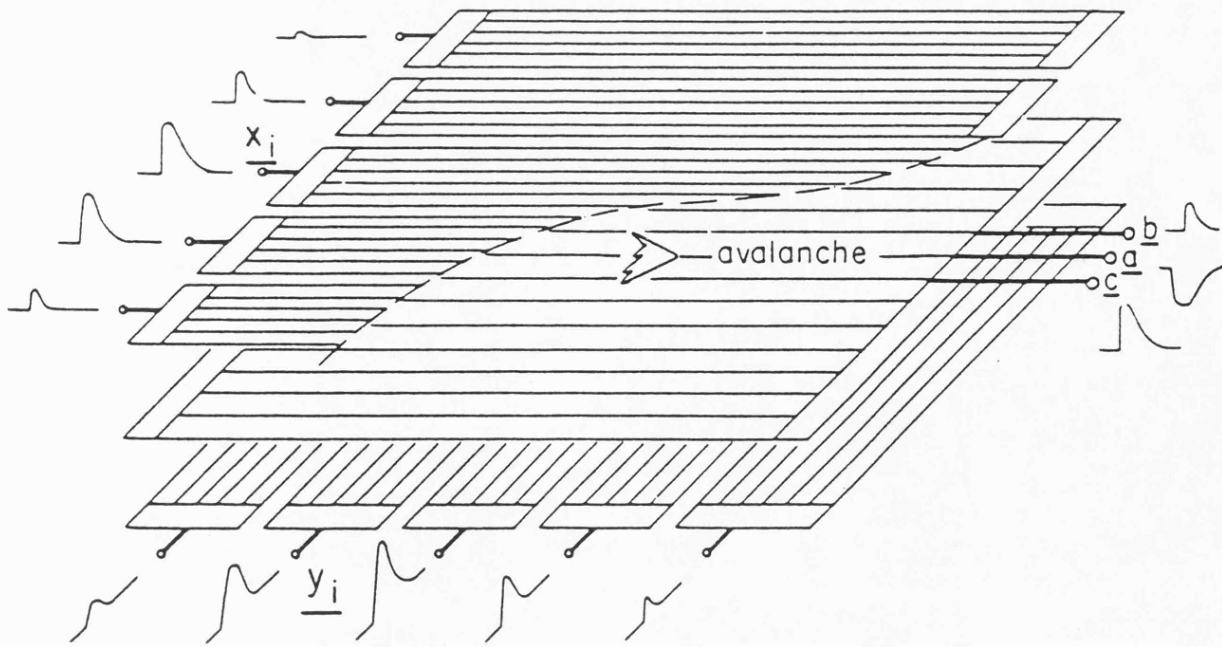


Figure 1.2d : A special form of MWPC with segmented electrode planes (Charpak et al. (1979)).

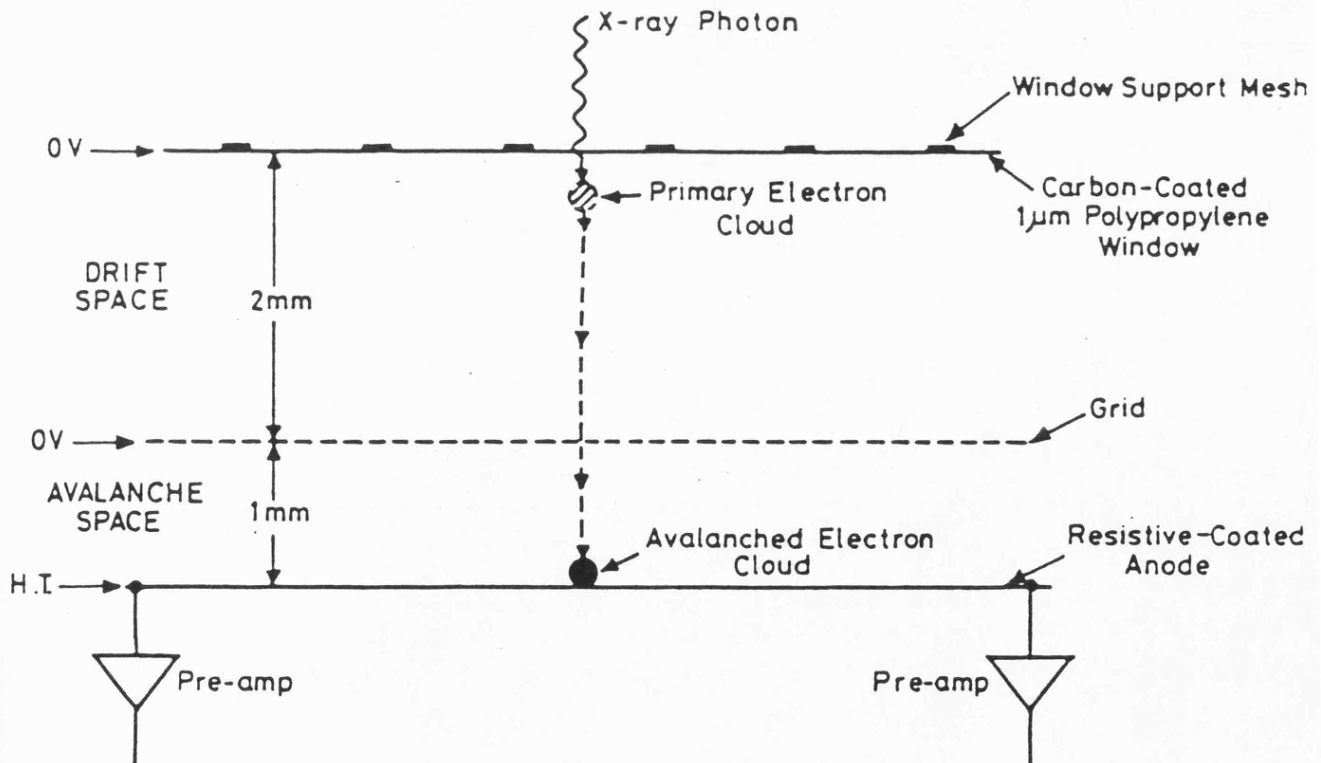


Figure 1.2e : A schematic diagram of a parallel plate proportional counter (Sanford et al. (1979)).

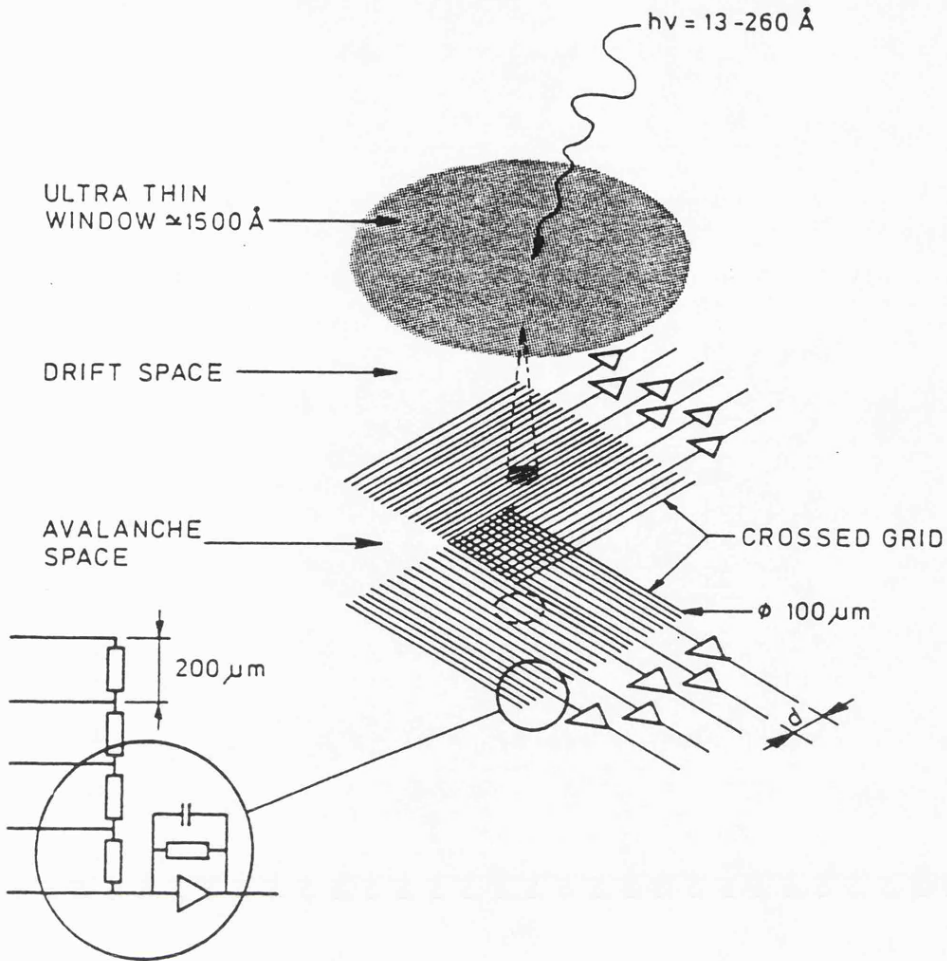


Figure 1.2f : A schematic diagram of a MWPC and the processing electronics (Bleeker et al. (1990)).

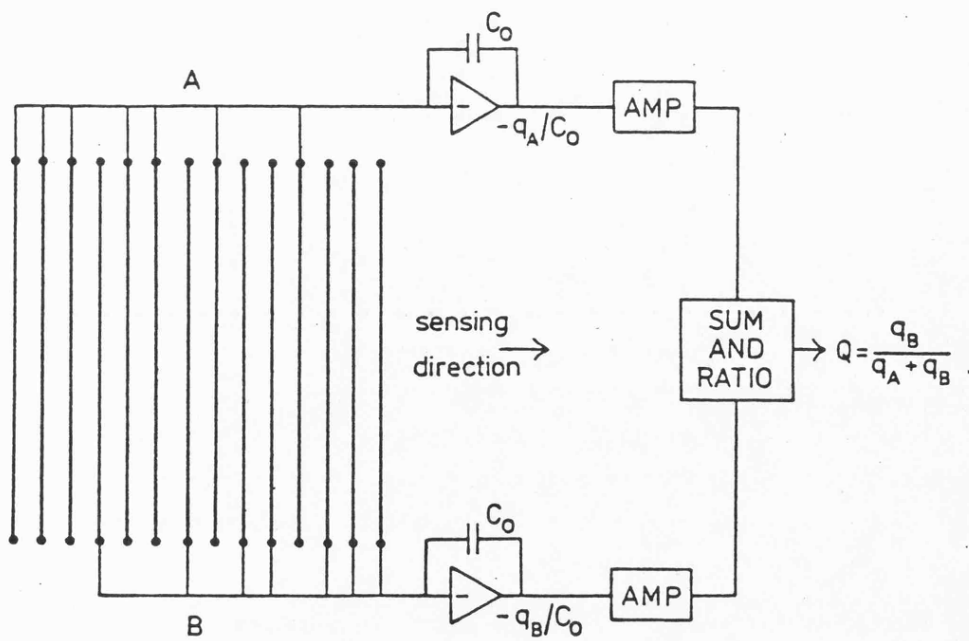


Figure 1.2g : A schematic diagram of a MWPC with a graded-density cathode (Gilvin et al. (1981)).

continuous absorption band in the 1300 Å region (Wilkinson et al. (1949)).

Long lived metastable states of inert gas atoms generated during Townsend avalanches also result in loss of proportionality. These cannot decay directly to the ground state since selection rules forbid this transition. Their surplus energy may be used to ionize polyatomic molecules provided the metastable state energy exceeds the ionization potential of the polyatomic molecules (Penning effect). Consequently, X-ray energy resolution improves because a greater fraction of incident radiation energy is converted into charge i.e. W decreases leading to an increase in N_0 , hence an improvement in X-ray energy resolution (see eqn. 1.6 below)

Argon-methane, argon-methane-nitrogen and argon-carbon dioxide mixtures were chosen for the present work. Nitrogen was used due to its ability to shift emission lines to convenient wavelengths for optical work and also for its ability to increase the light output (Policarpo et al. (1967)). Only limited work, however, was carried out using argon-methane-nitrogen gas mixtures which included their single electron response, electron mobility and mean electron lifetime. This should prove useful in any future investigations concerning light pulse detection.

Direct electron counting would be a useful technique for the sub-keV X-ray spectroscopy provided that high electron counting efficiencies are obtained. For instance, the X-ray energy resolution would not only be improved by a factor of two over that of conventional proportional counters but the data obtained should also allow a systematic study of the fundamental parameters such as the Fano factor F and the counter gas parameter W .

1.3 The absorption process in counter gas

The nature of the interaction between a photon and a gas atom or molecule is determined by the photon energy. The basic processes involved in photon-gas interactions are summarized in figure 1.3 (Fraser (1989)). The dominant mechanism by which photons transfer their energy to gas, for the energy range of our interest, is the photoelectric effect. The interaction cross sections for other competing mechanisms such as Compton scattering or incoherent scattering are about a thousand times lower. The photoelectric effect involves the interaction of a photon with a tightly bound electron, usually from K shell or L shell of the atom. Unlike the gradual rate of energy loss of charged particles, the photon loses energy very abruptly to the electron. A photoelectron is ejected from the atom with a kinetic energy, $E_{k.e}$ which is given by :

$$E_{k.e.} = E - E_b \quad 1.1$$

where E is the energy of the incident photon and E_b is the binding energy of the photoelectron in its original shell. Each photoelectric interaction leaves an atom in an ionized state with an inner shell vacancy. The de-excitation may take place by the capture of a free electron from the medium or by a series of internal electronic rearrangements. The internal transitions may cause the emission of one or more fluorescent X-rays. These could be reabsorbed in close proximity to the original photoelectric event by interacting with less tightly bound electrons. However, the counter gases usually have a relatively low absorption cross-section for such fluorescent radiation which leads to their escape from the active volume of the detector. In this case, the energy deposited is the difference between the incident photon energy and the escaping photon energy.

Atomic de-excitation may also take place by the Auger effect. The transitions involved here are radiationless. Energy is transferred to an outer electron leading to its ejection from the excited atom. The corresponding energy spectrum of Auger electrons is a continuous type which reflects the different initial and final states of the atom. The K-shell fluorescence yield, ω_k , is defined by the following expression :

$$\omega_k = X_k / (X_k + A_k) \quad 1.2$$

where X_k are the number of emitted X-ray photons of the K series, A_k is the number of K Auger electrons. Figure 1.4 shows the dependence of K-shell fluorescence yield upon atomic number (Broyles et al. (1953)).

In the present work, only argon based counter gas mixture were used. The electron binding energies for argon's K, L and M shells are 3.21, 0.247 and 0.030 keV, respectively. If the photon energy exceeds 3.2 keV then an interaction with argon K shell takes place leading to an emission of a photoelectron followed by emission of either a K shell fluorescence photons or Auger electrons. When 5.89 keV X-rays are used, for example, 2.69 keV photoelectrons are released. This is followed by either emission of 2.95 keV photons or 2.70 keV Auger electrons. The fluorescence yield of this process is approximately 13 % (Bambynek (1972)). An escape peak is observed due to the loss of 2.95 keV photons from the active volume of the detector, at approximately half the value of photopeak, in the 5.89 keV pulse height spectrum (see section 2.5).

When 1.49 keV X-ray are used, photons interact with the L shell of

argon atoms leading to emission of 1.24 keV photoelectrons. Hence, excited argon atoms release 0.19 keV Auger electrons.

1.4 Quantum detection efficiency

The quantum detection efficiency of any proportional counter may be expressed by the following equation (Fraser (1989)) :

$$Q = T_w \exp[-(t_w \mu_w)] [1 - \exp(-d \mu_g)] \quad 1.3$$

where T_w is the geometric transmission of the window support mesh. Typically, T_w equals between 0.7 to 0.8. The second term in equation 1.3 is the transmission of the window with t_w thickness and the third term in this equation represents the fraction of the incident beam absorbed in the gas. The quantum detection efficiency is, therefore, determined by the type of window material, window material thickness as well as the type and depth of gas being used. In order to maximise the quantum detection efficiency a thin window of low X-ray stopping power and a highly absorbent counter gas mixture are required. Hydrocarbon based plastic windows with a thin metallic coating are usually used below 1 keV since the photoelectric absorption edge varies according to $Z^4/E^{8/3}$ relationship (Zombeck (1982)) where Z is the atomic number and E is the X-ray energy. Metallic windows, typically 50 μm thick beryllium, are usually used above 2.0 keV. The choice of hydrocarbon-based plastic window material, however, becomes critical below about 500 eV. For example, the C-K absorption edge of at 0.28 keV causes a sharp reduction in quantum detection efficiency. Above 500 eV the nature of gas becomes critical since quantum detection efficiency in this energy region is determined by absorption edges of the counter gas used. For example, the K-shell absorption edge of argon occurs at 3.21 keV. Figure 1.5 shows the variation of detection efficiency with X-ray energy when using an argon-methane mixture for different window materials (Siegmund (1981)). Figure 1.6 shows the variation of detection efficiency with energy for different gases with constant depth (Siegmund (1981)).

A high quantum detection efficiency is required, for example, when the radiation source has a low intensity. In the present work, however, laboratory X-ray sources were used thus the intensity of the incident radiation was not a problem.

1.5 Proportional counter operation

Figure 1.7 shows a plot of pulse height versus anode voltage for a

single-wire proportional counter showing the different regions of detector operation. The electric field, E , at a distance, r , from the anode wire can be written as follows :

$$E(r) = \frac{V}{r} \ln\left(\frac{r_c}{r_a}\right) \quad 1.4$$

where V is the potential difference between the anode and the cathode, r_a is the anode radius and r_c is the internal radius of the cathode.

The electric field strength near the entrance window due to the high potential on the anode wire is relatively weak ($E < 200$ V/cm). Therefore, electrons drift very slowly towards the anode wire. The electron drift velocity in A-CH₄ (10%) at a drift field of 200 V/cm is, approximately 0.7 cm/ μ s. Electrons eventually encounter the high field region in the vicinity of the anode wire ($E > 1000$ kV/cm). The subsequent acceleration may provide sufficient kinetic energy to these electrons to cause ionization by collisions with counter gas molecules. Excited atomic and molecular species may also result. Electrons liberated by collisional processes produce more electrons by further collisions. This type of process is known as a Townsend avalanche (Townsend 1901). If the total charge produced after an electron avalanche is directly proportional to the photon energy then the detector is operating as a proportional counter. The charge multiplication factor, M , is defined as the average number of electrons formed as a result of a single original electron. The resulting charge signal at the anode is amplified by a charge sensitive preamplifier and shaping amplifier and a pulse height spectrum accumulated on a multichannel analyser.

1.6 X-ray energy resolution

The energy resolution in a conventional charge detection arrangement is limited by the fluctuations in the number of primary electrons as well as by fluctuations in the charge gain. If the formation of the number of primary electrons N_o is assumed to be a Poisson process (random) then one would expect a standard deviation of $(N_o)^{1/2}$ in that number. The formation of primary electrons, however, cannot be considered as a series of independent processes. The observed fluctuations in N_o are therefore smaller than would be expected from Poissonian statistics. The relative standard deviation in a pulse height spectrum due to the fluctuations in number of primary electrons at an X-ray energy E can therefore be written in the form (Fano (1947)) :

$$(\sigma_E/E) = (F/N_o)^{1/2} \quad 1.5$$

where F is the Fano factor which has been introduced to take into account the departure of the observed statistical fluctuations in N_0 from pure Poissonian statistics. The Fano factor ranges from 0.17 (argon, xenon) to 0.32 (carbon dioxide). The Fano factor for an inert gas containing a polyatomic gas, may be lower than for the corresponding value for the inert gas.

The gas gain fluctuation factor, B, has been found to be in the range 0.6-0.7 by Charles et al. (1968), Byrne (1969), Alkhazov (1970) and Genz (1973). Taking both factors together, the relative r.m.s. X-ray energy resolution of a conventional proportional counter may be expressed as :

$$(\sigma_E/E) = [(F+B)/N_0]^{1/2} \quad 1.6$$

Alkhazov (1970) has shown that if $N_0 \gg 1$ then the pulse height distribution asymptotically approaches a Gaussian distribution. For a Gaussian distribution, the full width at the half maximum equals 2.35σ . Therefore, the right hand side of equation 1.3 must be multiplied by 2.35 to give the relative FWHM energy resolution. It is evident from equation 1.6 that as N_0 decreases i.e. as the incident radiation energy decreases, the relative FWHM increases with $E^{-1/2}$. This behaviour is illustrated in figure 1.8. The current investigations were undertaken as an attempt to improve proportional counter X-ray energy resolution at sub-keV photon energies.

It is obvious that the elimination of B from the expression 1.6 would lead to a significant improvement in proportional counter X-ray energy resolution. Two successful techniques based on such a concept have been evolved. Both utilise the light emission properties of the counting gases (atomic or molecular excitation or ionization processes). The first technique employs a Gas Scintillation Proportional Counter (GSPC) to reduce the signal fluctuation processes (see figure 1.9) and will be discussed in section 1.7. The second technique counts the number of electrons in primary ionisation clusters to eliminate the gain fluctuation processes. One observes the light pulses emitted as electrons avalanche individually in a high electric field region (Siegmond et al. (1982, 1983)). The experimental arrangement to observe the light signals is shown in figures 1.10a and 1.10b.

The present project was, however, concerned with electron counting using charge (Harris et al. (1990)). This involved the determination of the maximum possible experimental electron counting efficiencies.

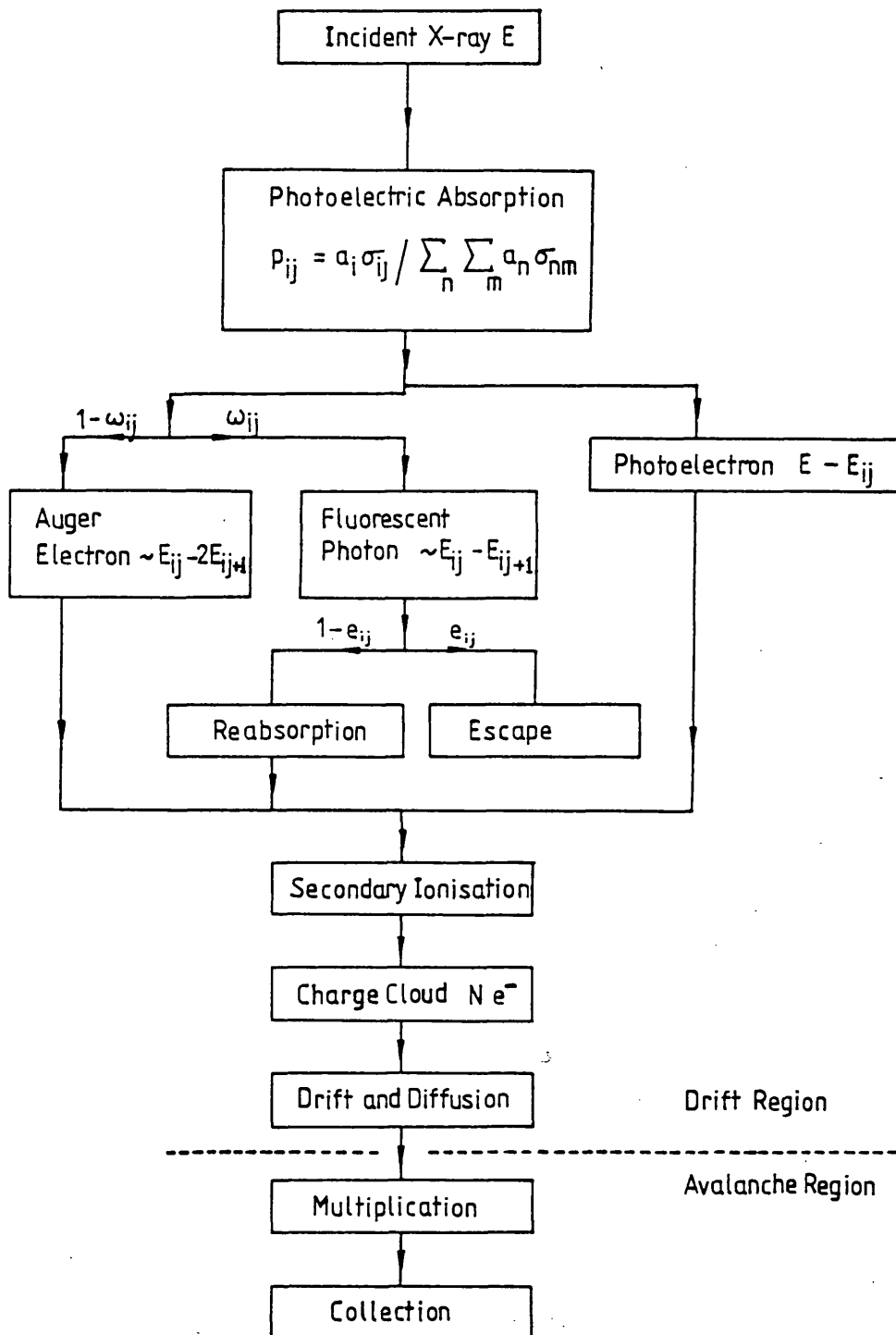


Figure 1.3 : Soft X-ray interactions with gas molecules (Fraser 1989)).

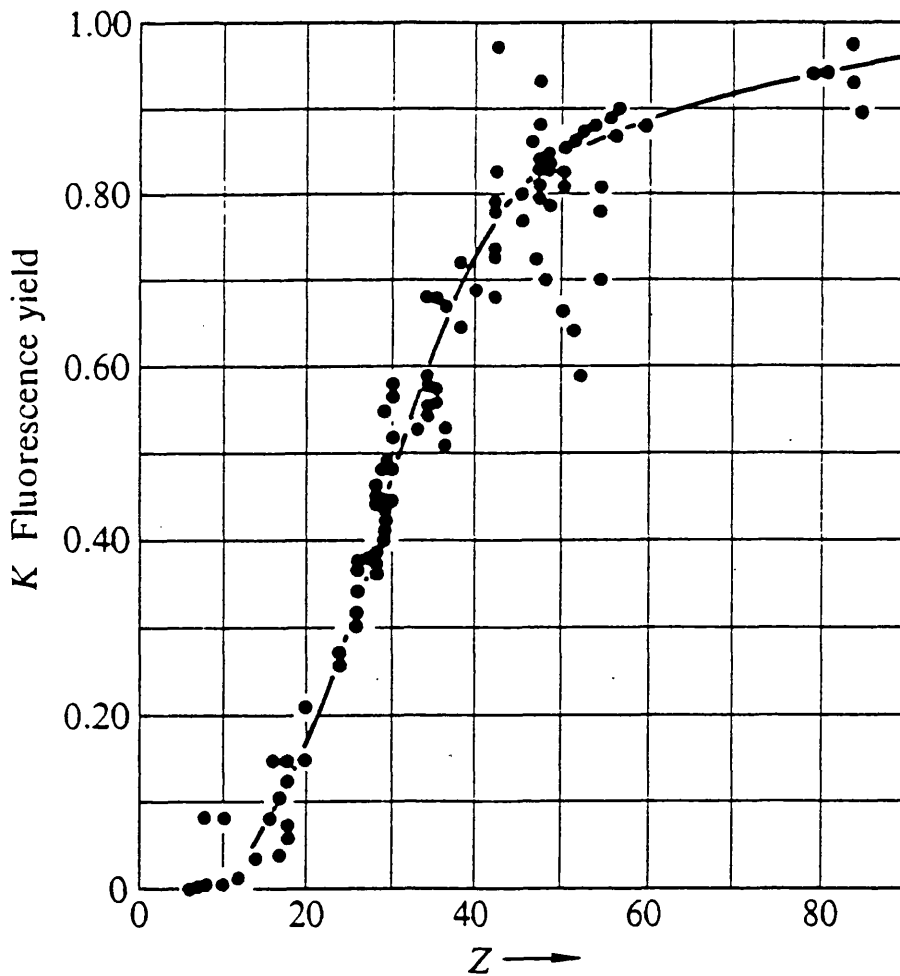


Figure 1.4 : The variation of K-shell fluorescence yield with the atomic number (Broyles et al. (1953)).

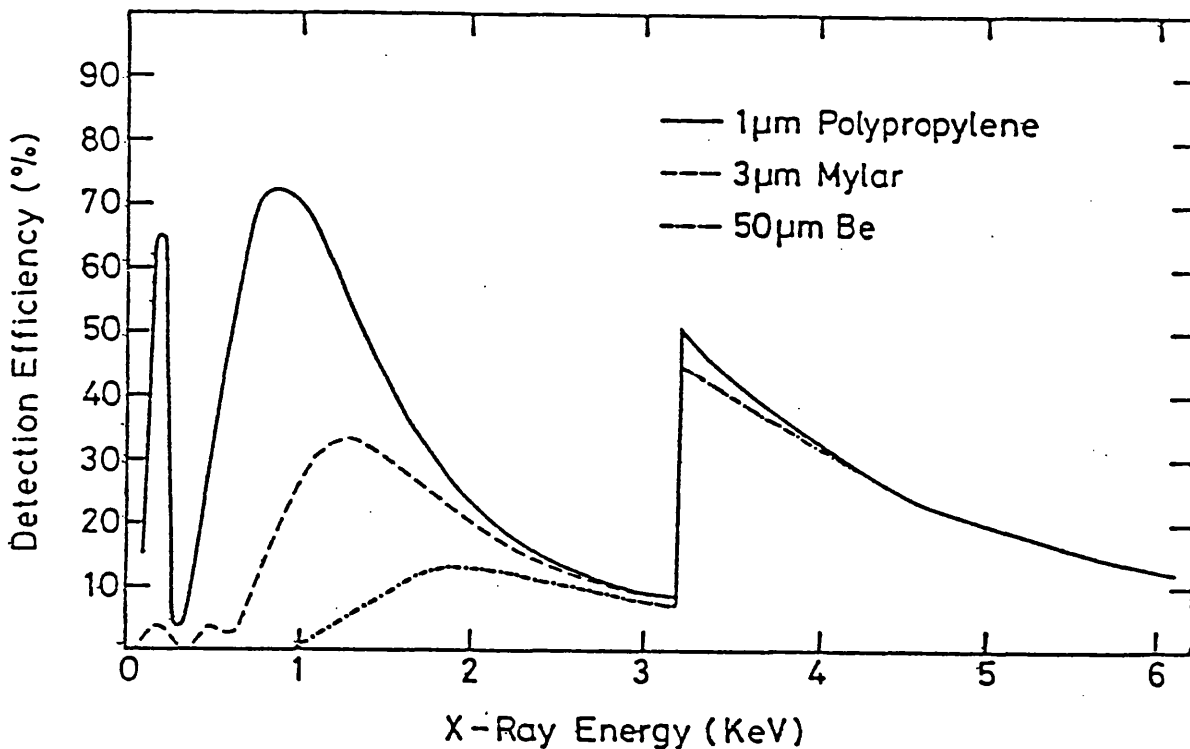


Figure 1.5 : The variation of the quantum detection efficiency with X-ray energy for a 3.5 mm depth of $A-CH_4(10\%)$ in a PPC with a number of different window materials (Siegmund (1981)).

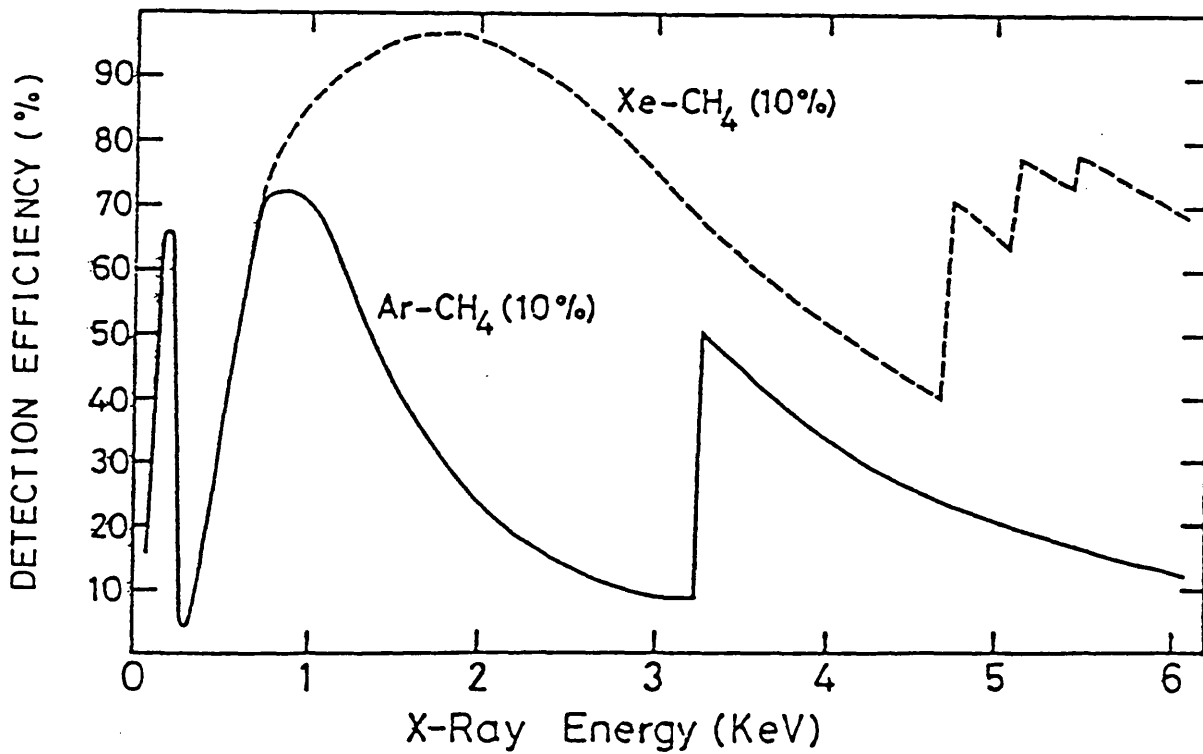


Figure 1.6 : The variation of quantum detection efficiency with X-ray energy for a 3.5 mm depth of A-CH₄(10%) and Xe-CH₄(10%) in a PPC with a 1 μ m polypropylene window (Siegmund (1981)).

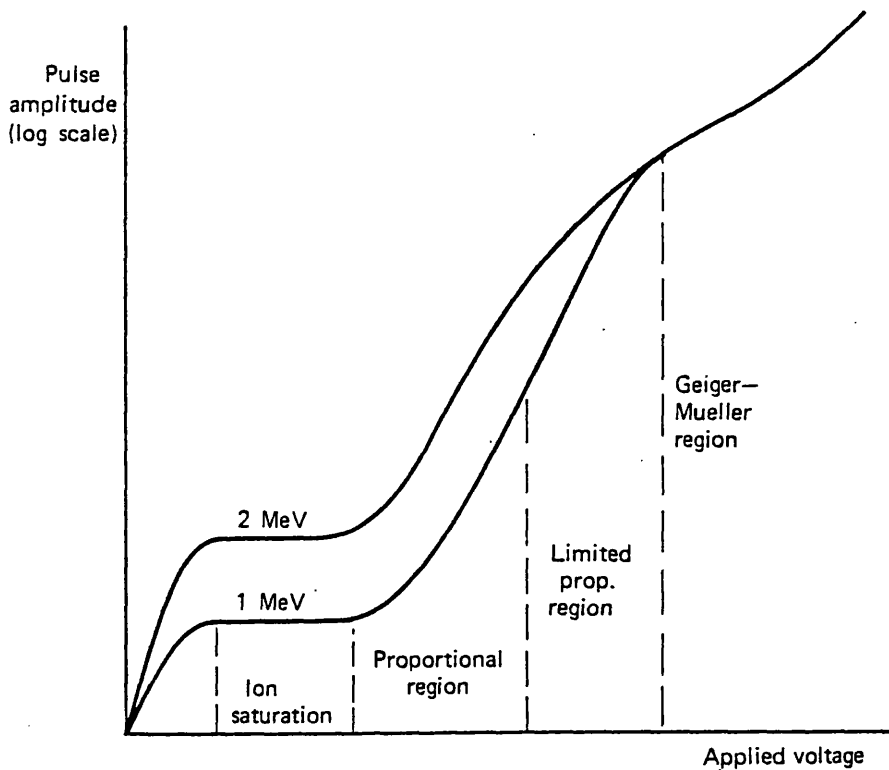


Figure 1.7 : The operation of a gas filled detector. The two different curves represent different radiation energies incident upon the detector (Knoll (1979)).

1.7 Imaging

The imaging properties of detectors used in X-ray astronomy have been discussed in detail by Fraser (1989). The FWHM spatial resolution, Δx , for any imaging proportional counter is determined by the sum of three contributions :

$$\Delta x = 2.35[(\Delta x_r)^2 + (\Delta x_d)^2 + (\Delta x_n)^2]^{1/2} \quad 1.7$$

where Δx_r and Δx_d are the fundamental components which represent the contributions of photoelectron range and lateral diffusion of primary electron clusters in the drift region, respectively. The third component, Δx_n , represents the contribution towards the overall spatial resolution due to a finite signal-to-noise of the position readout element.

The photoelectron range for argon at one atmosphere has been given by Stumpel (1973) as :

$$\Delta x_r = 2.2[\varepsilon(\text{keV})/10]^a \text{ mm} \quad 1.8$$

where ε is the photoelectron or Auger electron energy (in keV) and a is a constant ($a = 1.725$). For example, when 5.89 keV X-rays are used, ε equals 2.70 keV (see section 1.3). The photoelectron range in argon at 5.89 keV using equation 1.8, therefore, equals 230 μm . When 1.49 keV X-rays are used, ε equals 1.24 keV thus the photoelectron range equals 60 μm . Gilvin et al. (1981) and Smith et al. (1984) have also given the photoelectron range which can be expressed as follows :

$$\Delta x_r = 2(3)^{1/2} a(\varepsilon^n / \rho_g) \mu\text{m} \quad 1.9$$

where ε is the photoelectron energy (keV), ρ_g is the counter gas density (gram per litre) and a and n are constants ($a = 30$, $n = 1.3$ for $1 \text{ keV} < E < 5 \text{ keV}$). The photoelectron range for argon at STP using equation 1.9 for 1.49 and 5.89 keV X-rays is approximately 77 and 212 μm , respectively.

The contribution of lateral diffusion towards the overall spatial resolution is given by Bleeker et al. (1980) as :

$$\Delta x_d = (2\sigma_x)^{1/2} / (N_o)^{1/2} \quad 1.10$$

where σ_x is the transverse r.m.s. width of the primary ionisation clusters after diffusion and N_o is the average number of electrons in the primary ionisation

cluster. The transverse r.m.s. width of primary ionisation clusters after diffusion is given by :

$$\sigma_x = [2Dd/w]^{1/2} = [2(D/\mu)d/E_d]^{1/2} \quad 1.11$$

where w is the electron drift velocity ($w = \mu E_d$), μ is the electron mobility and E_d is the drift field, D/μ is the characteristic energy of the drifting electrons and d is the drift distance.

It must be emphasized that in any conventional charge signal detector a trade-off is made between spatial resolution and energy resolution. This is necessary due to a conflict between the experimental requirements for good spatial and energy resolution. For instance, to obtain good spatial resolution requires high charge levels to operate the position readout. The avalanche fluctuation factor B in equation 1.3, however, increases with an increasing charge gain (Alkhazov (1970), Sipila (1979)). This problem has been examined by Breskin et al. (1984). A low pressure multistep avalanche chamber was built which consisted of relatively low field regions separated by a high field region. The spatial information was derived from the high field region whereas the energy resolution information was derived from the low field region. The spatial resolution with a low pressure (5-20 Torr) multistep avalanche chamber using isobutane and a UV photons was found to be 200 μm FWHM (Breskin et al. (1984)). Smith et al. (1985) and Fischer et al. (1986) have reported the best spatial resolution to date at 5.89 keV using Xe-CO₂ counter gas mixtures. The spatial resolutions at 5 bar and 10 bar were 22 μm and 14 μm , respectively. High pressures were needed to increase gas density, causing a reduction in photoelectron range thus improving the spatial resolution (see eqn. 1.9).

It has been impossible to date to obtain good spatial resolution and X-ray energy resolution simultaneously by the electron counting technique using light originating from avalanches. Siegmund et al. (1983) have determined the spatial resolution at a drift field, $E_d = 300 \text{ V/cm}$ using 1.49 keV X-rays with an A-CH₄(5%)-CO₂(10%) gas mixture to be 350 μm FWHM (see figures 1.10a and 1.10b). A high drift field is required to minimize the contribution of lateral diffusion of the primary clusters towards the overall spatial resolution. This requirement, however, is in conflict with the low drift field, $E_d < 30 \text{ V/cm}$ needed to resolve the primary clusters into individual electrons and to improve the X-ray energy resolution. In other words, the electron counting efficiency deteriorates at higher drift fields due to the finite resolving time, typically a few nanoseconds, of the photomultiplier. The present investigations, however, were

not concerned with improving spatial resolution but were restricted to improving proportional counter X-ray energy resolution. Siegmund et al. (1983) also used the experimental arrangement shown in figure 1.10a and 1.10b to improve X-ray energy resolution. For example, using C-K X-rays (0.28 keV) 34 % FWHM was achieved compared to 85 % FWHM proportional counter X-ray energy resolution (see figure 1.8).

Breskin et al. (1991) have developed a similar technique to our technique (Harris et al. (1990)) to improve soft X-ray energy resolution by eliminating the parameter B in equation 1.6. Both research groups have used direct electrical signals from the anode wire during electron multiplication to count single electrons. A low pressure multistep proportional chamber known as the Primary Ionization Cluster Counter (PICC) was used by Breskin et al. (1991) to resolve primary ionization clusters into individual electrons. The experimental arrangement used by is shown in figure 1.11. A C-K X-ray source (0.28 keV) was used to produce primary ionization clusters in A-C₂H₆ (80:20) while the chamber pressure was maintained at 8 Torr. These drifted in a low and uniform drift field towards the first amplification stage. A fraction of the preamplified charge was transferred to the high field stage where fast counting electronics provided spatial as well as X-ray energy resolution information. Breskin et al. have obtained an X-ray energy resolution of 45% FWHM using C-K X-rays (0.28 keV) compared to 85% FWHM achieved by a conventional proportional counter. The spatial resolutions predicted at 0.28 keV and 1.0 keV are approximately 7 mm FWHM and 4 mm FWHM, respectively. The low pressure technique seems to very promising compared to other electron counting techniques because :

- (1) It uses thinner windows than those used in GSPCs or during the present investigations. As a result, higher quantum detection efficiencies are obtained. The use of thinner windows, therefore allows a more efficient detection of ultrasoft X-rays (0.1-1.0 keV). Since the chamber is maintained at a low pressure (8 Torr), leads to the requirement of enclosing the radiation source in a cell which is also maintained at the chamber pressure.
- 2) Low chamber pressure gives a larger photoelectron range since gas density decreases with decreasing pressure (see eqn. 1.9). The primary electron clusters are, therefore better separated which assists towards a more efficient electron counting. Furthermore, high count rate ability is achieved because a reduction in space charge effects occurs due to a

faster ion collection and lower charge density of electron avalanches (Hendricks (1969)).

3) This technique does not require the use of very low drift fields to diffuse and separate the primary electrons. Thus, this technique reduces electron losses which may otherwise occur, by electron capture to gas impurities.

4) Excellent signal-to-noise ratio is achieved due to the use of very high charge gains ($M > 10^7$).

1.8 Gas Scintillation Proportional Counters (GSPCs)

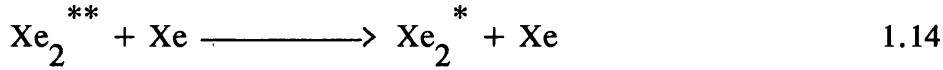
A GSPC can be regarded as an hybrid version of a proportional counter combined with a scintillation detector. The light emission from Townsend avalanches has long been known (Colli and Facchini (1952), Charpak and Renard (1956) and Grun and Schopper (1954). The realization of this light being used as a basis for radiation detection led to the development of gas scintillation proportional counters (GSPC). GSPCs were pioneered by Policarpo and Conde during the late 1960s (Policarpo and Conde (1967)) and by Alves in the 1970s (Alves (1973)). There are many different GSPC configurations (Policarpo (1977)) but the essential underlying principles are the same. The following discussion and analysis is based upon the parallel grid type construction shown in figure 1.9.

Radiation enters the detector through a thin mylar or beryllium window to produce primary electron clusters in the drift chamber. These drift under the influence of a weak field, typically 500 V/cm, towards the higher field scintillation region where the field is typically 5 kV/cm. The primary electron interactions in the scintillation region produce only atomic or molecular excitations. The field in the scintillation region is not high enough to initiate Townsend avalanches. UV or visible light is produced when the relaxation of the excited states occurs. GSPCs utilise the fast light signals originating from such excited states. A photomultiplier tube or an image intensifier is required to amplify the light signal and produce a signal output which is directly proportional to the number of UV photons incident on the tube.

Most GSPCs employ xenon due to the fact that it has high stopping power as well as the fact that its light emission is a maximum at approximately 1700 Å, a wavelength which is transmitted by quartz optics. The light emission processes in xenon have been studied by Manzo et al. (1980) at both one and two atmospheres pressure. Firstly, a vibrationally unrelaxed molecular xenon state is formed from the excited atomic xenon :



Xe_2^{**} then converts to the vibrationally relaxed molecular xenon state :



The decay of Xe_2^* leads to photon emission :



The light emission processes in other GSPCs have been studied at high pressures. The emission peaks for Kr and A occur at 1500 Å and 1300 Å, respectively (Strickler et al. (1964), Gedanken et al. (1972), Suzuki et al. (1979)). The fact that GSPCs operate at electric fields well below the onset of Townsend avalanches combined with relatively low fluctuations in the light yield lead to an improvement in energy resolution for soft X-rays as much as a factor of two better than that for conventional proportional counter arrangements. This advantage has enabled GSPCs to become well established as low energy X-ray detectors. The relative r.m.s. X-ray energy resolution equation equivalent to equation 1.6 for a GSPC can be written as :

$$(\sigma_E/E) = [F/N_o + G/m(G-1)]^{1/2} \quad 1.16$$

where F and N_o have their original meanings, m is the mean number of photons detected by the photomultiplier or image intensifier and G is the gain of the first dynode of the photomultiplier. If m is large then equation 1.16 simplifies to equation 1.5. Substituting for F and W ($W = 22$ eV for Xe) it can be seen that the theoretical relative energy resolution may be as low as 5.2% FWHM at 5.89 keV. Anderson (1978) and Alice et al. (1975) have reported energy resolutions of 8% FWHM at this energy. Inoue et al. (1978) have achieved energy resolutions of 70% FWHM and 50% FWHM for S-L (0.15 keV) and C-K X-rays (0.28 keV), respectively. Alice et al. (1975) have achieved an X-ray energy resolution of 36% FWHM using C-K X-rays (0.28 keV).

GSPCs are normally operated at atmospheric pressure because the light yield decreases linearly with pressure (Salette et al. (1982)). This imposes a limitation to the minimum window thickness that can be used. As a result, the

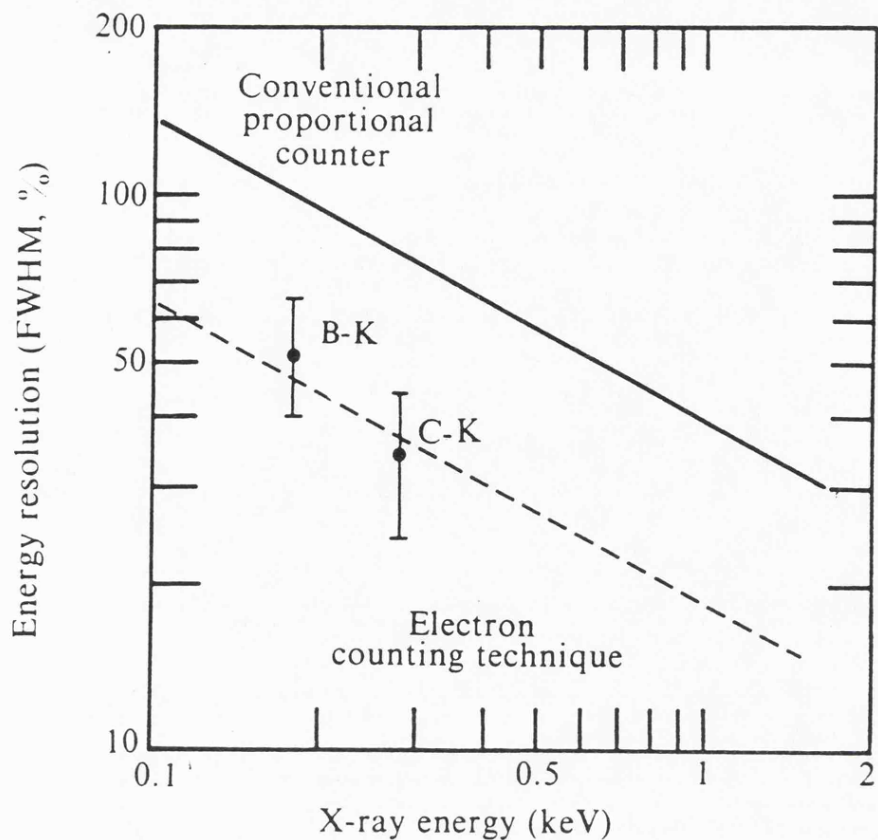


Figure 1.8 : A comparison between the %FWHM X-ray energy resolution obtained from a conventional proportional counter and the theoretical %FWHM X-ray energy resolution using any electron counting technique. The experimental %FWHM X-ray energy resolutions at C-K X-rays (0.28 keV) and B-K X-rays (0.18 keV) using light signals from avalanches to count single electrons are also shown (Siegmond et al. (1982)).

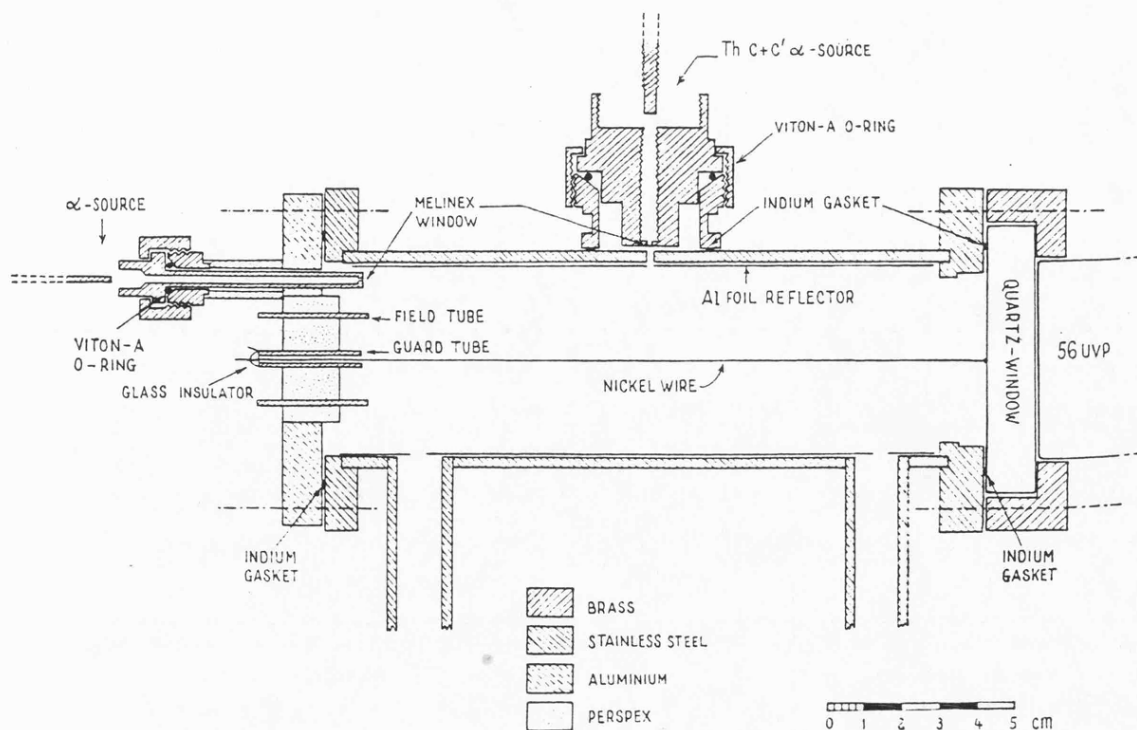


Figure 1.9 : A typical gas proportional scintillation counter (Policarpo et al. (1967)).

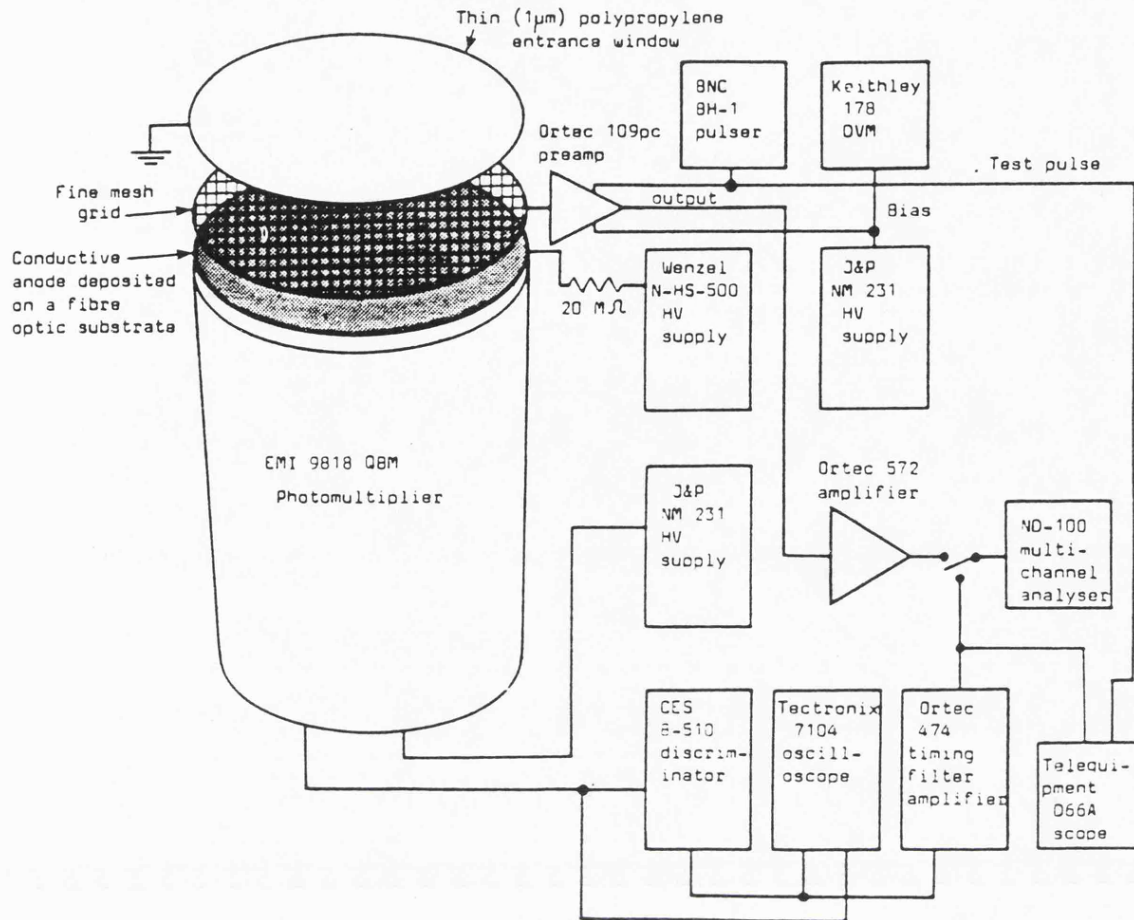


Figure 1.10a : Experimental arrangement used to count single electrons by observing light emitted during single electron avalanches (Siegmund et al. (1983)).

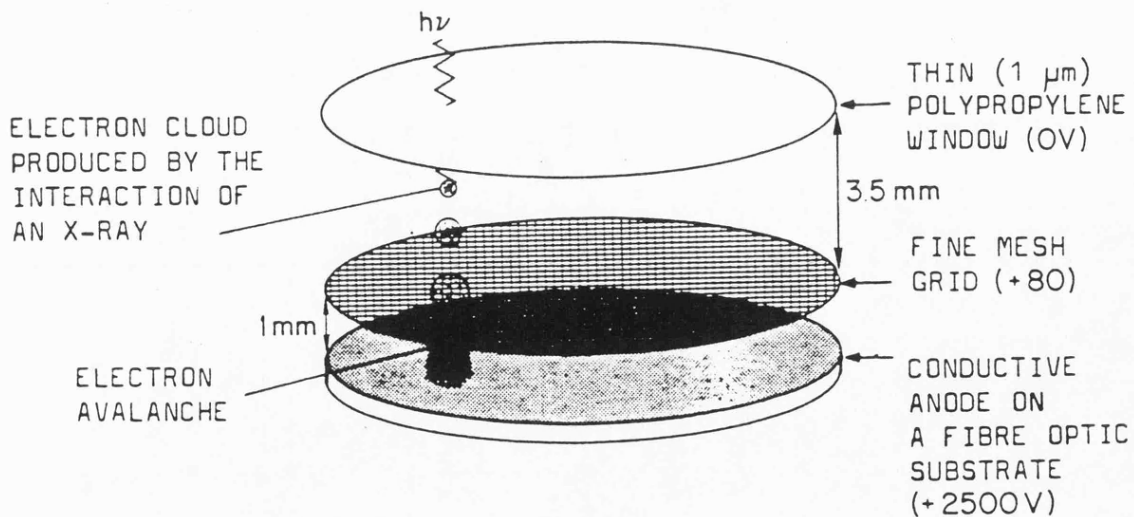


Figure 1.10b : A schematic diagram of the parallel plate proportional counter (Siegmund et al. (1983)).

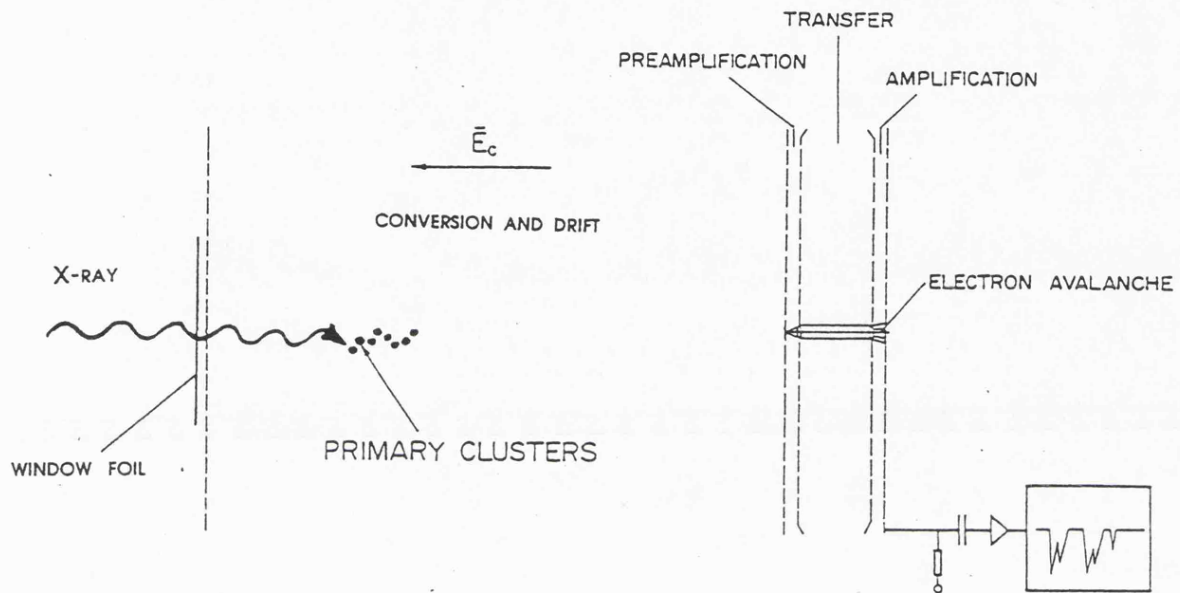


Figure 1.11 : A schematic diagram of the low-pressure PICC detector for ultrasoft X-ray spectroscopy (Breskin et al. 1990)).

quantum detection efficiencies of GSPCs tend to be low below 1.0 keV X-ray energy. GSPCs are also more sensitive to gas impurities than conventional gas proportional counters or PICC (Breskin et al. (1991)). GSPCs, therefore, require complex gas purification systems.

1.9 Scintillation counters

Scintillators utilise the fluorescence property of various organic and inorganic materials to detect radiation. A photomultiplier or an image intensifier is used to amplify the light signals (Birks (1964), Kaufmann et al. (1970)). A diverse range of crystal scintillators are used in applied nuclear physics and other related fields. The most common scintillation materials are Na(Tl), Cs(Tl) and some types of plastics. Scintillation materials usually contain Tl, Mn, Cu and various other elements as activators. These enhance light emission from the excited scintillator atoms as well as causing a wavelength shift towards the visible range. The penetration depth for incident X-rays on a scintillator material is very small due to the high crystal density leading to a very high stopping power. For example, at 10 keV, 90 % of the X-rays incident are absorbed within approximately 30 μm of CsI. The X-ray absorption in a scintillator occurs by the photoelectric effect producing many electron-hole pairs. It requires approximately three times the bandgap energy to produce an electron-hole pair. The electrons and holes diffuse through the crystal and cause excitations to the activator ions in the crystal. Light is emitted when relaxation of such ions takes place which is used as a basis of radiation detection. The energy required to produce an optical photon in sodium iodide is approximately 20 eV (Murray (1975)). In order to maximize the light output an optimum activator concentration needs to be determined.

Anderson (1978) has given the relative FWHM X-ray energy resolution for Na(Tl) as :

$$2.35(\sigma_E/E) = 1.22(E)^{-1/2} \quad 1.17$$

where E is the X-ray energy in keV. The light output, hence the relative X-ray energy resolution, is fairly linear above 10 keV but decreases rapidly below this value. This has been demonstrated by Gwin and Murray (1962), Kaizer et al. (1962), Aitken et al. (1967) and McCann and Smith (1968). Crystal scintillators are, therefore, not normally used below 10 keV. The criteria for selection of a crystal scintillator is governed not only by its inherent light conversion efficiency but also by the spectral response of the associated optics. For example, Na(Tl)

emits in the range 4200 Å - 4350 Å whereas Cs(Tl) emits in the range 5650 Å - 6000 Å (Scintillation Phosphor Catalogue, The Harshaw Chemical company). Na(Tl) is often preferred to Cs(Tl) since its emission is better matched to the photocathode response of photomultipliers. Detailed descriptions of crystal scintillators are given by Birks (1964), Stevels and Pingault (1975).

Single crystal sodium iodide scintillators approaching one cubic meter have been constructed (Heath et al. (1979)). A higher radiation stopping power and a larger attainable scintillation media yield much higher scintillator counter quantum detection efficiencies than for any other radiation detector. Solid state silicon and germanium detectors, for example, have much lower quantum detection efficiencies than scintillator counters. The main factor for a lower quantum detection efficiency of a solid state detector is the reduced photoelectric interaction probability for low atomic number elements such as silicon and germanium (see section 1.4). The other contributing factor is the limitation of active volume of solid state detectors. The use of larger p-n junctions leads to difficulties of proper depletion and charge collection.

Scintillation counter X-ray energy resolution at low X-ray energies is poor compared to that achieved by a conventional gas proportional counter. The X-ray energy resolution of a scintillation counter is limited by loss mechanisms which operate during ionisation, light emission, light collection and photocathode emission. Scintillation counters have also been used for low energy X-ray imaging. Some systems use an array of photomultipliers connected to position-decoding electronics. These systems are, however, very expensive and require complicated gain calibration procedure. Further disadvantages of these type of imaging systems include a limited stability during operation and a sensitivity to magnetic fields.

1.10 Solid state detectors

An extensive introduction to solid state detectors and their operating principles can be found in McKenzie (1979), Ferbel (1982), Stefanini (1983), Rancoita et al. (1982) and Fraser (1989). The term "solid state detector" usually implies a semiconductor detector which consists of silicon or germanium diode of the p-i-n type, operated in a reverse bias. Here, p and n represent the nature of dopants which have been diffused into the intrinsic substrate i. X-ray events in the detector create a large number of electron-hole pairs which drift under the influence of a large bias field ($\approx 10^4$ V/cm) and are eventually collected and amplified. Solid state detectors operate at liquid nitrogen temperatures to reduce electronic noise although special detectors have been constructed for room

temperature operations using Mercuric iodide. Mercuric iodide has a much larger bandgap than silicon or germanium and about 4.3 eV is required to create a single electron-hole pair (Swierkowski et al. (1974) and Slapa et al. (1976)) whereas 3.7 eV and 3.0 eV is required for the same purpose using silicon and germanium, respectively. The reason for the excellent X-ray energy resolution using solid state detectors is due to the formation of a large number of original electron-hole pairs for a given photon energy and due to the absence of variance due to electron multiplication. Approximately, 270 and 330 electron-hole pairs are created per 1 keV in silicon and germanium, respectively. The X-ray energy resolution when using solid state detectors is, therefore, much better when compared with proportional counters. This has led to widespread research and development interest in X-ray astronomy and particle physics. For example, large silicon detector arrays (1m^2) are being explored (Borer et al. (1987)) while low readout noise, low output capacitance devices such as charge coupled devices (CCDs) (Janesick and Blouke, 1987) and silicon drift chambers have been investigated (Gatti and Rehak (1984), Rawlings (1986), Ellison et al. (1987) and Sumner et al. (1988)). The relative r.m.s. X-ray energy resolution for a solid state detector is given by :

$$(\sigma_E/E) = [(\sigma_n)^2 + (\sigma_r)^2 + (\sigma_{sn})^2]^{1/2} \quad 1.18$$

where σ_n is the variance in the mean number, N_o , of electron-hole pairs created, σ_r is the variance due to charge loss during collection, drift or transfer and σ_{sn} is the variance in the detection system noise (preamplifier, amplifier and the processing electronics). The sources of signal fluctuation due to CCD readout, R, and amplifier noise, A, are commonly expressed in terms of noise charge and measured in signal equivalent electrons. Equation 1.18, therefore, may be rewritten as shown below :

$$(\sigma_E/E) = w[(FE_d/w) + (R)^2 + (A)^2]^{1/2} \quad 1.19$$

where F is the Fano factor, which is approximately 0.1 for Si. The theoretical relative X-ray energy resolution using a silicon detector at 1.49 keV and 5.89 keV are 3.7% FWHM and 1.7% FWHM, respectively. Typical practical values at 1.49 keV and 5.89 keV are 7.5% FWHM and 2.5% FWHM, respectively.

Solid state detectors also have their drawbacks. For example, the use of a cryogenic system requires more space and introduces an additional cost. Cryogenic Si-Li detectors are usually used in the X-ray energy range 0.1-1 keV

containing, for example, B-K (0.18 keV), C-K (0.28 keV), O-K (0.53 keV) and N-K characteristic X-rays (0.39 keV). The sample containing these elements is enclosed in a high vacuum and separated from the detector by a thin, usually 10 μm thick beryllium window. As a result, most of the radiation is absorbed by the window leading to a poor quantum detection efficiency (see eqn. 1.3).

1.11 Electron counting using charge

The present method to improve the soft X-ray energy resolution of proportional counters is based on an electron counting technique using charge. The project required the construction of an experimental chamber consisting of a coaxial proportional counter adjoined by a drift chamber. A schematic of the detector construction is shown in figure 1.12 while Figure 1.13 and 1.14 depict the experimental chamber from side and top elevation, respectively. Radiation could enter into the detector from three different locations depending upon the particular experimental requirements. The drift window, diameter 7 mm, consisted of 100 μm thick mylar upon which 100 nm thick aluminium had been deposited to provide a conducting surface. Soft X-rays entered the detector through the drift window to produce the primary electron clusters. It was also possible to eject single electrons from the inner surface of the drift window using UV light incident upon the quartz side window. These electrons have thermal energies ($D_1/\mu = kT/e$ where D_1 is the longitudinal diffusion coefficient, μ is the electron mobility, k is Boltzmann's constant and e is the electronic charge) and diffuse uniformly in the absence of any applied field with an agitation velocity, v . They encounter numerous elastic collisions with molecules until they become neutralised by capture, recombination or collision with drift tube walls. However, in the presence of an applied electric field, a net motion with a drift velocity w in the direction of the field superimposes on the random thermal motion. If d is the drift distance under the influence of electric field and x is the actual distance travelled by a drifting electron then usually $x \gg d$. Therefore, if $t_d (= d/w)$ is the time required for the electron to drift a distant d then the actual distance travelled equals $vt = (v/w)d$ where v/w is typically 100.

The present type of drift chamber was designed, used and analysed by Crompton et al. (1965). It consists of stainless steel cylinders, internal diameter 37.5 mm and height 5 mm or 10 mm, separated and insulated by thin neoprene O-rings. The internal diameter of the cylinder closest to the proportional chamber was 25.0 mm. The drift lengths used were 51 mm or 72 mm. A uniform electric field was maintained across the drift length by using graded potentials. This was achieved by using a potential divider across the drift length in which 47

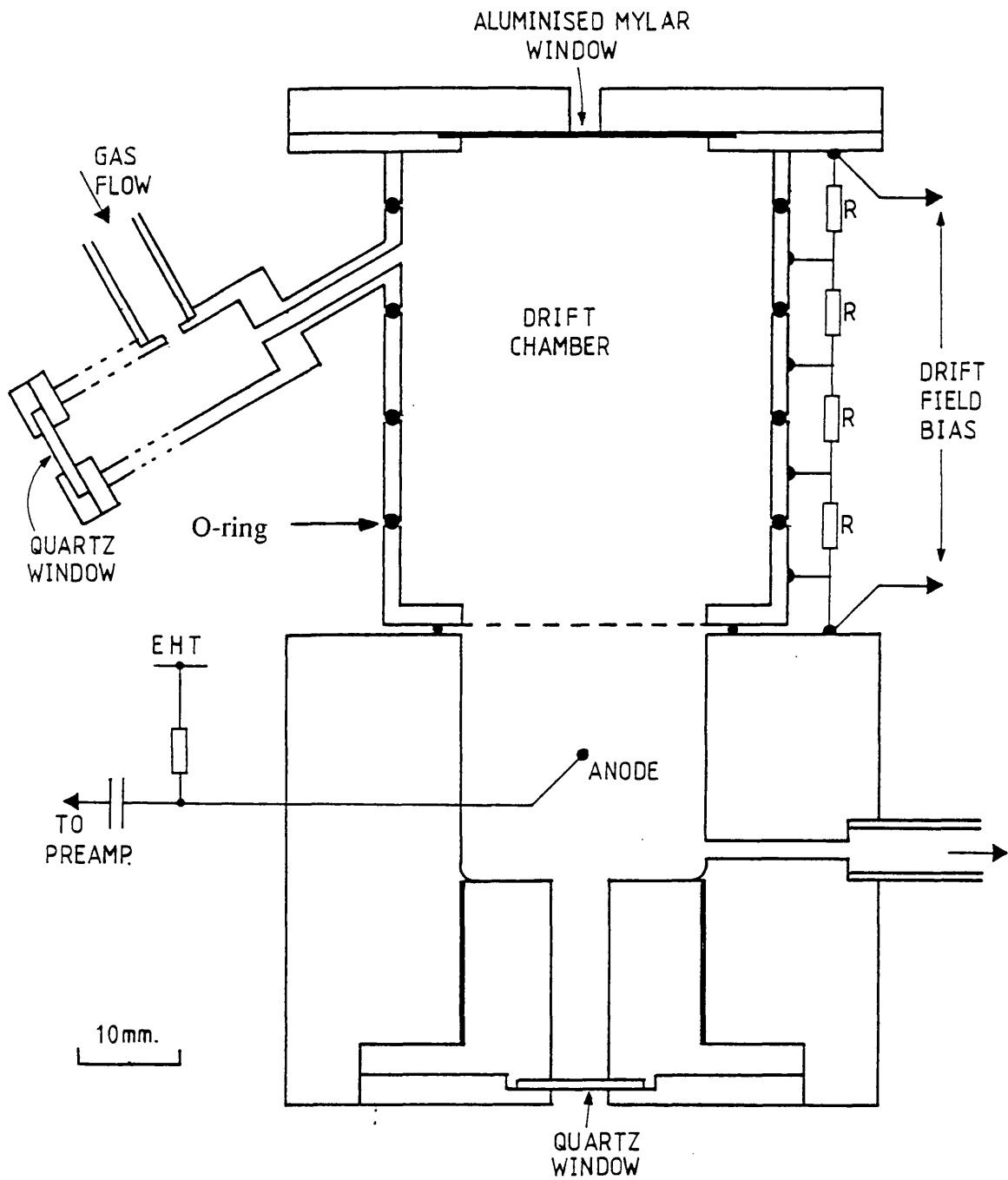


Figure 1.12 : A schematic diagram of the experimental chamber. The chamber material was stainless steel.

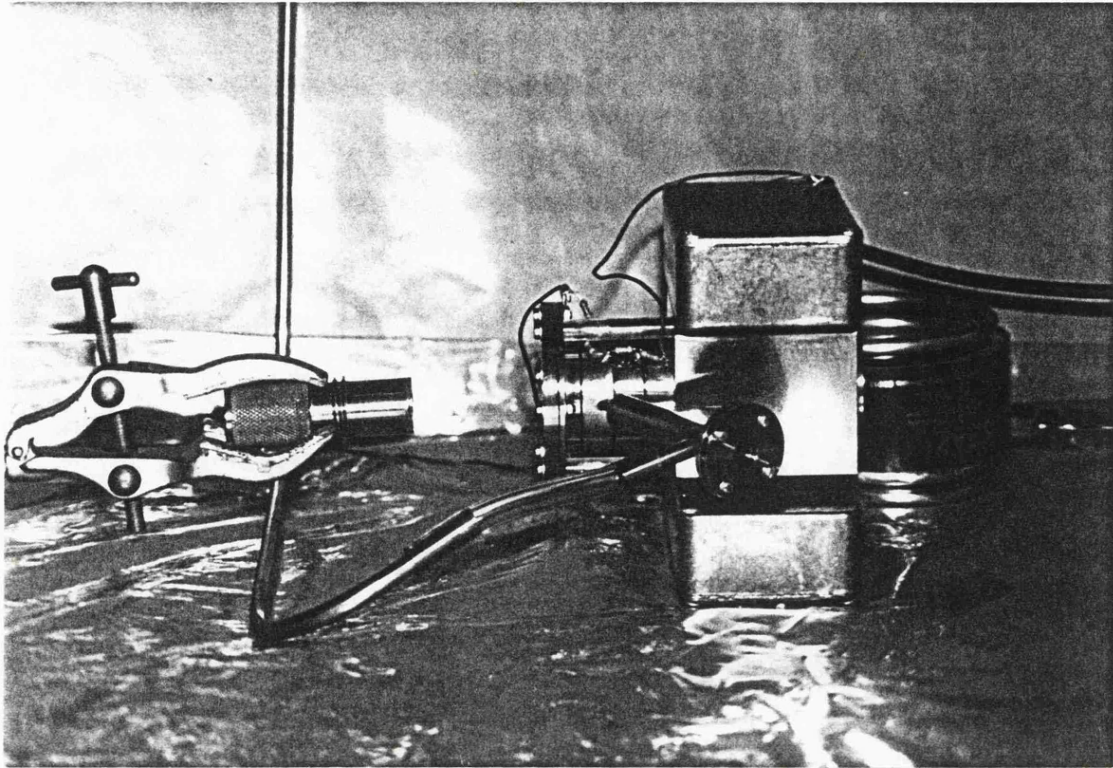


Figure 1.13 : Experimental chamber (side elevation).

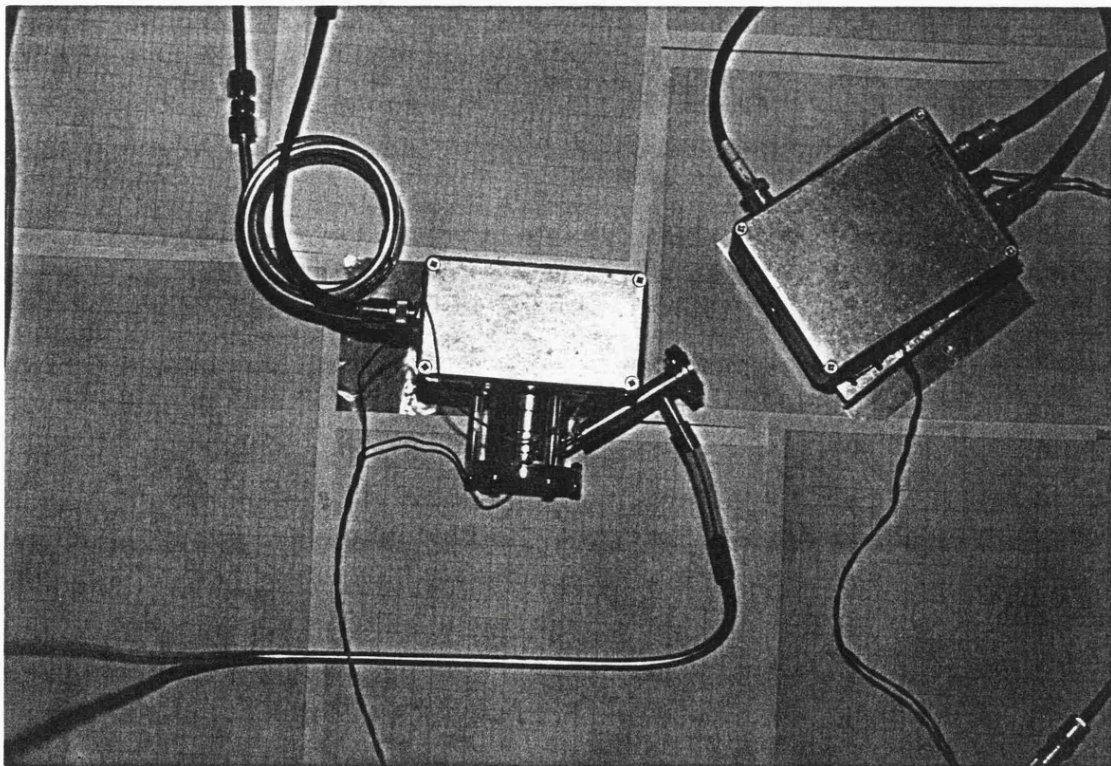


Figure 1.14 : Experimental chamber (top elevation).

k Ω high precision resistors were used. The drifting electrons pass into the conventional proportional counter region, mean radius 12.7 mm, through a coarse stainless steel mesh, aperture 2.5 mm. The anode consisted of tungsten wire, radius 12.5 μ m. Radiation could also enter the detector directly from a window in the counter base. The base window consisted of either mylar or quartz. The latter window was used when it was required to eject electrons from the stainless steel mesh by pulsed UV. The base piece could also be dismantled to allow the coupling of a photomultiplier tube to the detector for pursuing investigations concerning light pulse detection. The components of the experimental chamber were cleaned with IPA and distilled water and then baked overnight at 80 degrees centigrade. Then the experimental chamber was carefully assembled.

The drift chamber was an essential component for the present electron counting investigations as it allowed sufficient time separation between successive individual electron avalanches thereby increasing the individual electron counting efficiency. Drift chambers are sometime known as a time expansion chambers. They allow the measurements of microscopic ionisation processes and electron motion thereby providing a link with macroscopic observable transport parameters such as attachment coefficients (electron lifetime), ionisation coefficients, electron mobility and diffusion coefficients. The drift chambers achieve "time expansion" by employing very weak drift fields. Consequently, any signals from the drift chamber arrive at the grid after a much larger time delay than in a ordinary chambers. A relative time expansion is, therefore, said to have occurred since the anode signals have not been retarded. Early work using drift chambers has been carried out for a variety of experimental objectives by Crompton et al. (1965), Wagner et al. (1967), Saudinos (1970), Walenta et al. (1971).

1.12 Scope of thesis

The relative r.m.s. X-ray energy resolution using the direct electron counting technique is given by the following equation (Mathieson, private communication (1988)) :

$$(\sigma_E/E) = [(F + S_a + S_d/f_a + S_c/f_a f_d)/N_o]^{1/2} \quad 1.20$$

i) S_a represents the fluctuation factor due to electron loss by capture. S_a is determined by the purity level of the counting gas mixture. The concentration of gaseous impurities in a practical electron counting detector should be, at least,

less than 1 ppm.

$$S_a = (1-f_a)/f_a \quad 1.21$$

where f_a is the fraction of electrons remaining after capture which may be expressed as follows :

$$f_a = \exp[-(t_d/\tau_a)] \quad 1.22$$

where t_d is the average drift time of the primary electrons prior to Townsend avalanches and τ_a is the mean electron lifetime. Determination of the parameters f_a and S_a has been carried out in chapter 3. This required the measurements of electron mobility and the mean electron lifetime against capture using a number of different gas mixtures. A Time Of Flight (TOF) technique was used for this purpose. The mean electron lifetime was determined by observing the pulse height reductions due to electron loss by capture with increasing drift times. In order to estimate the mean electron lifetime the observed pulse height reductions were compared with theoretical pulse height reductions. The theoretical pulse height reductions were calculated assuming a different number of mean electron lifetimes.

ii) S_d represents the fluctuation factor due to electron loss below discriminator threshold. S_d is determined by the discriminator threshold level of the electron counting electronics and the mean charge gain of the counter gas.

$$S_d = (1-f_d)/f_d \quad 1.23$$

where f_d is the fraction of signals accepted above a discriminator threshold. If the pulse height spectrum is exponential then we may write :

$$f_d = \exp[-(q_d/n_{av})] \quad 1.24$$

where q_d is a discriminator threshold level which equals q_n (maximum electron noise level) when the discriminator threshold level is just above the noise level of the electron counting electronics and n_{av} is the mean charge gain for a given counter gas mixture. The determination of the parameters f_d and S_d has been carried out in chapter 2. This required the measurements of the maximum electron noise level for particular electron counting electronics and the maximum

charge gains for a number of different counter gas mixtures before the onset of secondary processes. The maximum electron noise for a particular electron counting system was measured by increasing its discriminator threshold level and then observing the decrease in count rate at the discriminator output. When the count rate at the discriminator reached zero Hz then the corresponding threshold level was at q_n . Four different sets of electron counting electronics were used. The maximum electron noise level for each set was determined.

iii) S_c represents the fluctuation factor due to electron counting loss by the burst counter. S_c is determined by the resolving time of the electron counting electronics and the r.m.s. spread in the arrival time distribution of electrons at the burst counter.

$$S_c = (1-f_c)/f_c \quad 1.25$$

where f_c is the fraction of signals from the discriminator which are actually counted by the burst counter and can be expressed as :

$$f_c \approx 1 - N\tau_r/2\tau(\pi)^{1/2} \quad 1.26$$

where N is the average number of counts per event after electron loss due to capture and due to loss below the discriminator threshold of the electron counting electronics (i.e. N is the product of f_a , f_d and N_o), τ_r is the resolving time of the electron counting electronics and τ is the r.m.s. spread in the arrival time distribution of electrons which can be expressed as :

$$\tau = (2D_1 t_d)^{1/2}/w^2 = (2(D_1/\mu)d)^{1/2}/\mu(E_d)^{3/2} \quad 1.27$$

where D_1 is the longitudinal diffusion coefficient, t_d is the electron drift time, w is the electron drift velocity, d is the drift distance, μ is electron mobility and E_d is drift field. The determination of the parameters f_c and S_c has been carried out in chapter 4. This required the measurements of the resolving time of the fast electron counting electronics and the r.m.s. width of the arrival time spectrum at a number of different drift fields.

Finally, chapter 5 will describe electron counting spectra at 1.49 keV and 5.89 keV obtained using the direct electron counting technique. The observed X-ray energy resolutions at these energies will be compared with the theoretical X-ray energy resolutions prediction by equation 1.20.

Chapter 2

Conventional charge signal measurements to investigate pulse height spectra and charge gains.

2.1 Introduction

Conventional charge signal measurements were first made to establish a "baseline" X-ray energy resolution with which the proposed "direct" electron counting technique could be compared. This investigation included a close examination of single electron pulse height spectra and their corresponding charge gains. These studies provided useful information about the nature of single electron avalanches and also assisted towards the estimation of the electron losses below the discriminator threshold level of the direct electron counting electronics. This type of loss is characterised by the parameters f_d and S_d (see eqns. 1.23 and 1.24). The magnitudes of f_d and S_d depend upon the signal-to-noise ratio of the fast electron counting electronics. This chapter will establish the values for f_d and S_d for a number of different electron counting electronics. It is important that single electron spectra are free from any secondary processes. These processes have been discussed in section 1.2. It was therefore essential to establish the proportional region for the various counter gas mixtures employed since any deviations from proportionality indicates the onset of secondary processes.

It can be seen from figure 1.7 that the onset of "limited proportionality" (the onset of secondary processes) does not occur abruptly. A sensitive experimental arrangement was therefore designed to determine departure from proportionality for different counter gas mixtures. This involved the determination of the parameter, γ , which is defined as the probability of producing a secondary electron per single electron avalanche from the cathode walls by means of photoelectric effect. Secondary electrons are produced by UV photons created during electron avalanching. The magnitude of γ depends upon the average charge gain and the quenching power of the counter gas mixture. The intensity of UV light emission from electron avalanching increases with charge gains (Romero et al. (1980); Siegmund (1981)). At higher charge gains, therefore, more secondary electrons are produced. Addition of a polyatomic gas such as methane to argon, for instance, leads to a reduction in γ due to the absorption of UV photons by methane molecules (see section 1.2). It was essential to measure γ to ensure that it remained much less than unity in later investigations.

A UV source was used to investigate the single electron response. This involved releasing individual electrons from the inner surface of the counter window or transmission grid (see figure 1.12), with insufficient kinetic energy to cause immediate collisional ionization. The subsequent Townsend avalanches could then be studied in the absence of the confusing effects which are inherent in the use of higher energy radiation sources due to the variation in the original number of primary electron-ion pairs. Differential and integral pulse height spectra were taken with a number of different counter gas mixtures and anode voltages. A differential pulse height spectrum shows the variation of dN/dH with H where dN is the number of pulses, observed in a differential amplitude increment dH and H is the pulse amplitude. Conversely, an integral pulse height spectrum shows the variation of the number of pulses N , whose amplitude exceeds a particular value of the pulse amplitude, with H . Differential and integral pulse height spectra for identical experimental conditions give the same information about the pulse height distribution. In the present work, however, it was necessary to obtain both types of spectra for the following reason : "Slow" conventional signal processing electronics (preamplifier, shaping amplifier and multichannel analyser) were used to obtain the differential pulse height spectra. The average charge gain was calculated from each pulse height spectra using a charge calibration procedure described in section 2.4. A number of different "fast" electron counting electronics were used to obtain the integral pulse height spectra. In contrast to the regular use of conventional electronics at Leicester University by the Nuclear Electronics Group, no prior work had been carried out using the electron counting electronics. Differential pulse height spectra, therefore, provided a comparison with the charge gain obtained by the integral pulse height spectra.

2.2 The statistics of avalanche growth

Avalanche multiplication processes can be described in terms of Townsend's first ionisation coefficient, α . An electron traversing a distance, x , towards the anode will produce an average number of $\exp(\alpha x)$ electrons. The average distance travelled by an electron between successive collisions with an atom or a molecule is $1/\alpha$. The dependence of the average charge multiplication factor, M , on proportional counter geometric parameters and gas composition is a very complex and challenging physical problem. There is no single satisfactory general theory which wholly describes the behaviour of a proportional counter under all operating conditions. Nevertheless, it is useful to derive empirical formulae which can assist in the prediction of proportional counter behaviour

under specified operational conditions.

Many theoretical investigations have been carried out into the shape of charge gain curves. Significant contributions to this topic have been made by Diethorn (1956), Zastawny (1966), Aoyama (1985) and Kowalski (1986). In the present work, the Diethorn formula will be used to compare theoretical and experimental values of M at a number of different anode voltages using A-CH₄(10%) and A-CH₄(50%). Kiser (1960) previously used the Diethorn formula and achieved good agreement between theoretical and experimental charge gains for a number of different argon-methane counter gas mixtures. The Diethorn formula (1956) assumes a linear dependence of the Townsend first ionisation coefficient on electric field due to the anode potential and can be expressed as follows :

$$\ln(n_p) = [V/\ln(r_c/r_a)] [(\ln 2)/(\Delta V)] [-\ln(K) + \ln\{V/p \ln(r_c/r_a)\}] \quad 2.1$$

where n_p is the average charge gain which excludes charge contributions from secondary processes, V is the anode voltage, p is the pressure, r_c and r_a are cathode and anode radii, respectively. ΔV represents the potential difference through which an electron moves between successive ionising collisions. K represents the minimum value of E/p below which electron avalanching cannot be sustained.

The total charge resulting from a Townsend avalanche will fluctuate. The statistics to describe these fluctuations were firstly derived by Furry (1937), Synder (1947), Wijsman (1949) and Legler (1955). These authors carried out theoretical work which showed that the probability of an avalanche producing n electrons declines exponentially with n (Furry's law) provided that the electron multiplication occurs by electron impact only and does not depend upon the previous history of the electron. The probability that an individual electron ionizes another atom to produce a single electron is given by αdx when the initial electron has travelled a distance dx. The pulse height probability distribution (differential pulse height distribution), P(n), for the final number of electrons at the anode can be expressed in the form :

$$P(n) = (n_{av})^{-1} [1 - (n/n_{av})]^{-1} n^{-1} \quad 2.2$$

where n_{av} is the mean value of n i.e. the average charge gain. For very large values of n_{av} equation 2.2 simplifies to :

$$P(n) = (n_{av})^{-1} \exp[-(n/n_{av})] \quad 2.3$$

Equation 2.3 has received experimental attention from many authors such as Curran et al. (1949), Frommhold (1958), Cookson et al. (1966), Schlumbohm (1965), Raether (1964), Alkhazov et al. (1967), Alkhazov (1970), Gold et al. (1966), Byrne et al. (1969), Genz (1973), Piuz (1983), Sephton et al. (1984) and Jahoda et al. (1988). All these authors found that the single electron differential pulse height distribution adhered to an exponential form only at lower charge gains ($M < 1.0 \times 10^4$ where M is the average charge multiplication factor (see section 1.2)). At higher charge gains a pronounced maximum was observed in the pulse height distribution where the number of avalanches with small numbers of electrons were much less than predicted. For example, Curran et al. (1949) found that the single electron differential pulse height distribution at charge gain of approximately 1.5×10^5 was of the form :

$$P(n) \approx (n/n_{av})^{1/2} \exp[-(3n/2n_{av})] \quad 2.4$$

with a maximum at $n_{av}/3$. The departure from the simple exponential pulse height distribution at higher charge gains has been examined theoretically (Byrne et al. (1969)). In contrast to α remaining constant at lower charge gains, it has been assumed that the probability for an electron to ionize depends upon the total number of electrons already present and the distance travelled from the original point of ionization. The mean ionization coefficient $\alpha(n,x)$ is assumed to vary with n and x according to the rule (Genz (1973)) :

$$\alpha(n,x) = \alpha(x)[1 + \theta/n], \quad \text{For } n > 0 \quad 2.5$$

where $\alpha(x)$ is dependent upon x and θ is an empirically defined parameter. A detailed treatment shows that differential pulse height distribution follows the Polya law which assumes an Erlang distribution for large values of $n(x)$ (Genz(1973)) :

$$P(n,x) \approx [n(1+\theta)/n_{av}(x)]^\theta \exp[-n(1+\theta)/n_{av}(x)] \quad 2.6$$

Equation 2.6 has been verified by Charles and Cooke (1968). It must be emphasized that all above equations are derived with the important assumption that electron multiplication occurs by impact only and the contributions from any secondary effects, such as cathode secondaries, which significantly alter the pulse height distribution, are ignored. A peaked pulse height distribution such as the Erlang distribution is preferred in the direct electron counting electronics as fewer counts would be lost below the discriminator threshold. Charge signals

from secondary processes, however, must not contribute towards this distribution.

Equation 2.3 can be integrated with respect to the pulse height, n , to give Furry's integral pulse height distribution :

$$N = N_0 \exp[-(n/n_{av})] \quad 2.7$$

where N is the number of counts above pulse height n , N_0 is the total number of counts and n_{av} is the average pulse height. The verification of Furry's law alone is insufficient to deduce the absence of secondary processes because it can be shown that the individual electron response retains an exponential pulse height distribution for "one electron" secondary events (Mathieson, private communication (1989)). A "one electron" secondary event involves the liberation of an electron from the counter walls by a UV photon released during a Townsend avalanche. UV emission occurs when excited inert gas atoms decay into ground states (see section 1.2). The secondary electron then drifts towards the anode wire and cause further electron avalanches on reaching the high field region. The integral pulse height distribution for this case can be expressed in the following form (Mathieson, private communication (1989)) :

$$N_1 = N_0 (1 + \gamma n_p) \exp[-(n/n_{av})] \quad 2.8$$

where γ is the probability of producing a secondary electron per one electron avalanche by photoelectric effect at the cathode walls. For "one electron" secondary events γ is much smaller than unity. The average charge gain n_{av} at high anode voltages consists of the sum of contributions due to secondary avalanching as well as ionisation by electron impact. The symbol n_p in equation 2.8 denotes the average charge gain which excludes charge contributions from secondary avalanching. In the present work, n_p will be calculated using the Diethorn formula (1956).

At very high charge gains an original Townsend avalanche may produce tertiary as well as secondary electrons. The tertiary electrons are produced at the cathode walls by UV photons originating from secondary avalanches. The tertiary electrons also drift towards the anode wire and cause further electron multiplication. A further, $0.4 \mu s$ drift time is required for the tertiary electrons to reach the high field region. Tertiary electrons were, therefore, observed at approximately $0.8 \mu s$ after the original electron avalanche. The single electron response for "two electron" secondary events shows a peaked integral pulse

height distribution which may be expressed in the following form (Mathieson, private communication (1989)) :

$$N_2 = N_o [1 + \gamma n_p + (\gamma n_p)^2 (1 + n/n_{av})] \exp[-(n/n_{av})] \quad 2.9$$

For "one electron" secondary events the pulse height distribution still follows an exponential distribution (see eqn. 2.8). It was therefore necessary to measure γ to confirm the presence of "one electron" secondary events. For "two electron" secondary events, the pulse height spectrum exhibits a peaked pulse height distribution (see eqn. 2.9). Position dependence of α at very high charge gains also gives a peaked pulse height distribution (see eqn. 2.6). In order to distinguish these two different effects, integral pulse height spectra at very high charge gains using A-CH₄ (10%) were examined with and without the presence of cathode secondaries. The experimental arrangement used to eliminate signals due to secondary events is described in the following section.

2.3 Experimental system

Figure 2.1 shows the experimental configuration used to obtain single electron differential pulse height spectra and conventional X-ray energy resolutions. A detailed description of the experimental chamber has already been given in section 1.11. The present chamber was designed for electron counting as well as conventional charge detection. Breskin et al. (1991) have used a low pressure chamber (8 Torr) during their electron counting investigations. It is advantageous to operate the chamber at a low pressure during single electron counting (see section 1.11). In the present work, the experimental chamber was operated at atmospheric pressure since it was not vacuum tight. The use of a low chamber pressure, therefore, would have introduced gas impurities into the chamber. The "outgassing" from neoprene O-rings would have also led to an accumulation of gas impurities. Therefore, research grade counter gas mixtures were fed continuously to remove gas impurities, at approximately 100 cc/minute, either directly into the chamber or via an Oxy-trap which had been installed in the gas line preceding the chamber itself. The Oxy-trap (Alltech Associates) contained powdered pyrophoric compounds in highly reduced states which were capable of reducing the oxygen level below 0.1 ppm. The gas line consisted of stainless steel piping. A gas mixing system was employed to obtain various mixtures of argon, methane and nitrogen. The outlet gases were passed through a throttle bottle containing diffusion pump oil, to ensure that no atmospheric gases diffused back into the chamber. A leak detector was used to

locate and eliminate any gas leaks in the system.

The anode wire was maintained at high potential by high voltage (0-5 kV) bias supply (Ortec 459). The accuracy of the anode voltage was ± 1 V. A mercury lamp (Philip Harris) with steady UV emission peaked at 254 nm was used to study the single electron response. Al-K X-rays (1.49 keV) and Mn-K X-rays (5.89 keV) were also used for this purpose. Al-K X-rays were produced by electron bombardment of an aluminium target in an evacuated tube and Mn-K X-rays by a Fe^{55} radioactive source which emits Mn-K X-rays by electron capture. The slow drift of positive ions towards the cathode after electron multiplication was the basis used to derive pulse signals from the anode. These signals were processed by either "slow" conventional electronics or "fast" electron counting electronics. The resolving time of the conventional electronics was approximately 2.5 μs compared to the approximately 26 ns of the fast electron counting electronics. In the present work, only one type of conventional electronics were used compared to four different fast electron counting electronics. The conventional electronics consisted of a charge sensitive preamplifier (Canberra Type 2001A) with a risetime and a falltime of 30 ns and 50 μs , respectively. This was followed by a shaping amplifier (Nuclear Enterprises Type 436) with either a single integration stage and a single differentiation stage (unipolar mode) or with a single integration stage and a double differentiation stage (bipolar mode). The filter time constants of each stage were equal and could be varied between 0.45 μs and 5.00 μs . A multichannel analyser (Northern Type TN 1705) was used to analyse the amplified signal pulses. A 50 MHz oscilloscope (Tektronix Type 2225) was also used to monitor signal pulses. The conventional electronic system (preamplifier, shaping amplifier and multichannel analyser) was calibrated for pulse height in terms of channel number using a precision pulser (Ortec Type 419). The charge level calibration procedure is described in detail in section 2.4 below. The charge level calibration allowed charge gains to be measured at various anode voltages. The precision pulser also enabled an assessment of the electronic linearity of the preamplifier, shaping amplifier and the multichannel analyser to be carried out. This was achieved by feeding different known step voltages into a known test capacitance at the preamplifier input. The channel number at the MCA due to each step voltage was recorded. A plot of channel number versus step voltage with a constant gradient implied that the electronic system had linear response with charge. The noise of the system was also measured by feeding a very small step voltage test input at the preamplifier stage while selecting large shaping amplifier and multichannel analyser gains to spread out

the pulser spectrum. The electronic noise of the "slow" system was found to be approximately 400 r.m.s. electrons.

The experimental system used to determine the γ parameter and also to examine the integral pulse height spectra using A-CH₄(10%) and A-CH₄(50%) consisted of fast electron counting electronics, a fast pulse generator (Philips PM 5785B) and an in-house built scaler. The fast electron counting electronics consisted of a preamplifier (approximately 2 ns risetime), a fast shaping amplifier (approximately 7 ns risetime) with a delay line clipping of 6 ns and a fast discriminator (approximately 7 ns risetime). The bias supplies to the fast preamplifier and shaping amplifier were maintained at +6V/-12V and +6V/-6V, respectively. A 125 mV step voltage was fed into the 1.0 pF test input capacitor at the fast preamplifier input stage. Figures 2.2 and 2.3 show the step impulse response of the fast preamplifier and shaping amplifier and discriminator, respectively. This system was designed at Brookhaven National Laboratories (Fischer et al. (1985)) for high count rate applications. It was initially applied in drift chamber proportional counters to resolve the primary clusters produced by Fe⁵⁵ X-rays (5.89 keV) into single electrons (Walenta (1979)). The negative output from the fast discriminator was fed into a fast pulse generator (Philips PM 5785B) which produced positive output pulses. An in-house built scaler which required positive input pulses was used to measure the count rates due to avalanches in the proportional counter. The resolving time of the scaler was found to be 120 ns. The charge signals due to secondary and tertiary processes arrive at the anode wire after 0.4 μ s and 0.8 μ s, respectively. It was therefore, possible to discriminate any signals from these processes by introducing a deadtime between 0.4 μ s to 0.8 μ s. This was achieved by increasing the pulse width of the Philips pulse generator (see section 2.4). The average charge gains used during the present work ranged from 1×10^4 to 3×10^7 . It was therefore essential to reduce the electronic gain of the fast electron counting electronics as the counter charge gains were raised. Four different electronic gains were used. The highest electronic gain system was referred as the electron counting electronics no. 1 and the lowest as the electron counting electronics no. 4. It was necessary to calibrate each electron counting electronics for the counter charge level and to determine the associated maximum electron noise, q_n .

2.4 Experimental procedure

A given counter gas mixture was allowed to circulate in the chamber for at least an hour prior to the start of an experiment. The radiation source (UV, Al-K X-rays (1.49 keV) or Fe⁵⁵ X-rays (5.89 keV)) was placed near the counter

window. The anode voltage was raised gradually to a suitable value and the shaping amplifier gain was also raised gradually until a signal appeared on the oscilloscope. The shaping amplifier was adjusted to bipolar mode and its time constant was adjusted to 0.45 μ s. The differential pulse height spectrum of these charge signals was displayed on a pulse height analyser and recorded (see eqns. 2.2-2.6). The count rate was maintained below 0.1 kHz. This procedure was repeated for a number of different anode voltages and different gas mixtures. When the counter charge signal reached very high levels then preamplifier and shaping amplifier saturation occurred leading to a distortion of the pulse height spectrum. The preamplifier and the shaping amplifier gains were, therefore, reduced to suitable lower levels. Differential pulse height spectra was taken at a number of different anode voltages using A-CH₄(10%), A-CH₄(50%), A-CH₄(50%)-N₂(2.5%), A-CH₄(50%)-N₂(5%), A-CH₄(50%)-N₂(10%) and A-CO₂(20%).

The conventional pulse processing electronic system (preamplifier, shaping amplifier and multichannel analyser) was calibrated for charge level using a precision pulser (Ortec Type 419) by introducing an accurately known step voltage input into an accurately known test input capacitance at the preamplifier stage and then recording the corresponding output channel number at the multichannel analyser. The pulser charge, Q_p , is given by the following equation :

$$Q_p = CV_t \quad 2.10$$

where C is the preamplifier test input capacitance and V_t is the test input voltage from the precision pulser. The average counter charge level, Q_c , is given by :

$$Q_c = CV_t (n_{av}/N_p) \quad 2.11$$

where N_p is the channel number on MCA due to pulser input, V_t .

The above charge level calibration procedure is, however, incomplete for charge signals from a proportional counter (Mathieson et al. (1969)). This arises due to a difference between the proportional counter pulse shape and that of test input voltage. The former has a large risetime, typically several microseconds, compared with the test input voltage which has a risetime of approximately 7 ns. The shaping filter, therefore, attenuates a counter pulse and a step function differently. In order to deduce the true proportional counter charge level, Mathieson et al. (1969) have calculated the attenuation of

proportional counter pulses in pulse shaping networks having equal, non-interacting single integrating and single or double differentiating time constants (unipolar and bipolar mode, respectively). For example, the corrected charge gain for an amplifying system in a unipolar mode with equal integrating and differentiating time constants T_i and T_d , respectively, can be expressed as follows (Mathieson et al. (1969)) :

$$Q_{cc} = CV_t(n_{av}/N_p)[(1/e)/f_{max}] \quad 2.12$$

where e equals 2.7183 and f_{max} can be written as follows :

$$f_{max} = 0.087C + 0.797\log_{10}[(T_d/t_o)] \quad 2.13$$

where C is a geometric constant and t_o is the characteristic time of a proportional chamber. The constant C can be expressed as follows :

$$C = 1/\ln(r_c/r_a)^2 \quad 2.14$$

where r_c is the mean cathode radius and r_a is the anode radius. The characteristic time for a proportional chamber can be written as follows :

$$t_o = (r_a)^2/(4\mu_1 VC) \quad 2.15$$

where μ_1 is the positive ion mobility for a particular counter gas mixture and V is the anode voltage.

The data required for the correction factor calculation are values for the filter time constant, anode radius, cathode radius, anode voltage and positive ion mobility in the given gas mixture. The anode and cathode radii were 12.5 μm and 12.7 mm, respectively. The anode voltage in the present experiments depended upon the type of counter gas mixture used since proportional response to charge depends upon the concentration of quenching gas. For example, the anode voltage range with A-CH₄(10%) was 1.70-2.00 kV, compared with the 2.20-2.80 kV used with A-CH₄(50%), A-CH₄(50%)-N₂(2.5%-10%) or A-CO₂(20%). The positive ion mobility assumed for these gases was 1.9 cm²/Vs (Schultz et al. (1977)). The calculated correction factors at 0.45 μs filter time constant (unipolar and bipolar) for the stated anode voltage ranges are shown in appendix A.

Counter charge gains were obtained using the single electron pulse

height spectra as follows : the natural logarithms of count rate against the channel number (or the corrected counter charge) were plotted for each spectrum. If the pulse height distribution followed a simple Furry law then the inverse slope of this plot represented the average channel number (or the average charge gain). If the pulse height distribution was non-exponential then the average channel number (or the average charge gain) was obtained numerically as follows :

$$n_{av} = \frac{\sum nk}{\sum k} \quad 2.16$$

where n_{av} is the average channel number and n is the channel number containing k counts.

The experimental arrangement to calibrate all four electron counting electronics for the counter charge and to determine the associated maximum electron noise is shown in figure 2.4. This charge calibration is analogous to that described above for the slower electronic system. The discriminator threshold level of a given electron counting system was increased to its highest value. A step voltage was introduced into the 1.0 pF test capacitor at the fast preamplifier input stage. The step voltage was adjusted until the pulse height at the shaping amplifier just began to exceed the discriminator threshold level. This occurred when the oscilloscope also began to show the shaping amplifier output. The step voltage corresponding to this point was noted and the pulser charge was calculated using equation 2.10. Then the discriminator threshold level was reduced slightly and the step voltage adjusted again until the fast shaping amplifier output was just visible on the oscilloscope. The new step voltage was noted and the corresponding pulser charge calculated. This procedure was repeated until the fast shaping amplifier output approached the maximum noise level.

The fast electron counting electronics also attenuate a step voltage and a counter pulse differently due to the differences in the associated pulse risetimes. In order to determine the counter charge from the pulser charge, a correction factor was calculated. Figures 2.5 and 2.6 show the theoretical response of the fast electron counting system to a step voltage input and a counter input (Mathieson, private communication (1989)). The correction factor was calculated by dividing the peak step pulse response with the peak counter response. The correction factor was found to be 10.73 which must be multiplied with the pulser charge to obtain the counter charge.

Figures 2.7-2.10 show the calibration of the fast electron counting

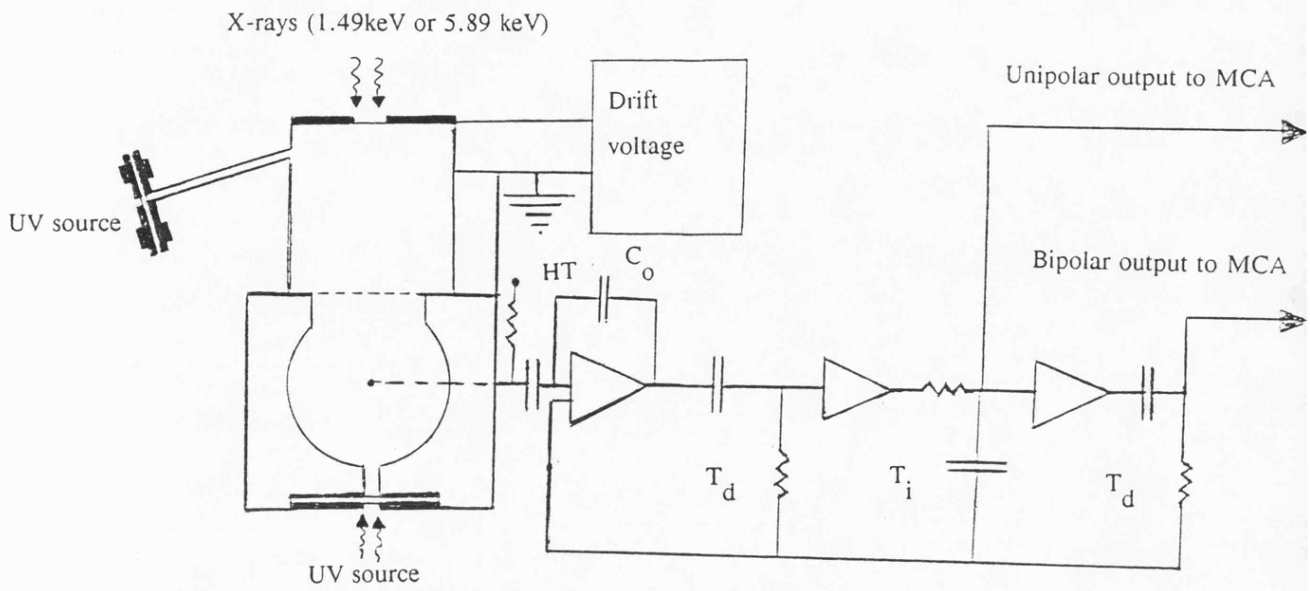
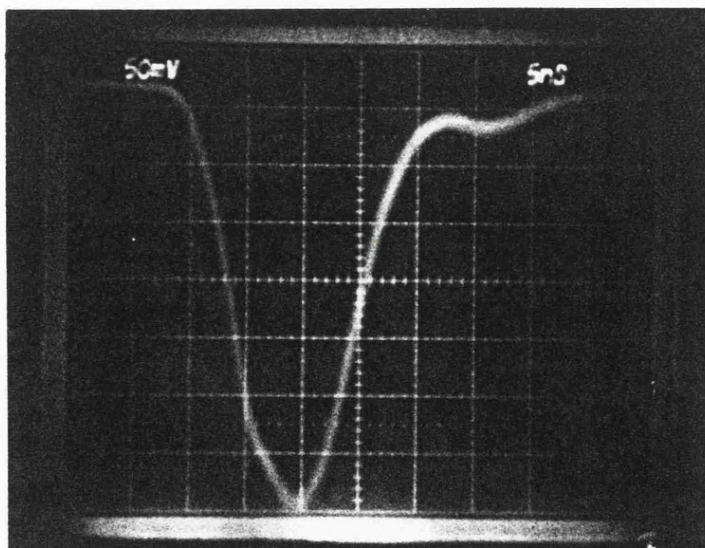


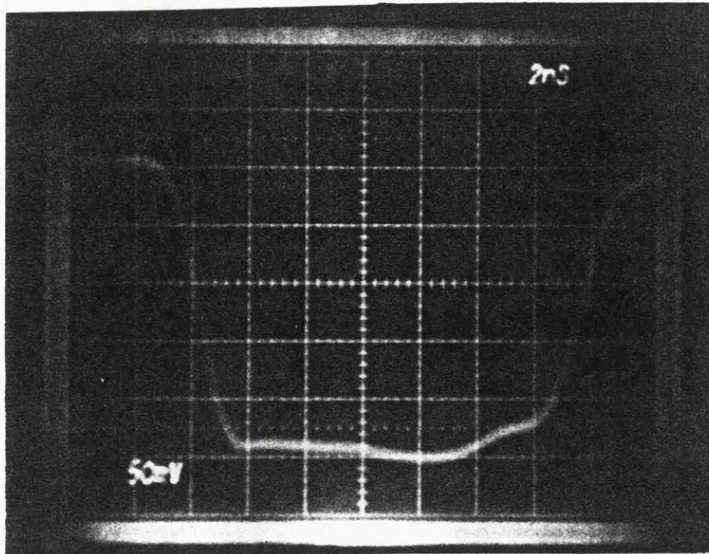
Figure 2.1 : Experimental arrangement to determine charge gains using differential pulse height spectra. Preamplifier feedback capacitance is denoted by C_o , differentiating and integrating filter time constants by T_d and T_i , respectively.



Vertical scale :
50 mV per division

Horizontal scale :
5 ns per division

Figure 2.2 : The step impulse response of the fast shaping amplifier (Photograph taken by the author).



Vertical scale :
50 mV per division

Horizontal scale :
2 ns per division

Figure 2.3 : The step impulse response of the fast discriminator (Photograph taken by the author).

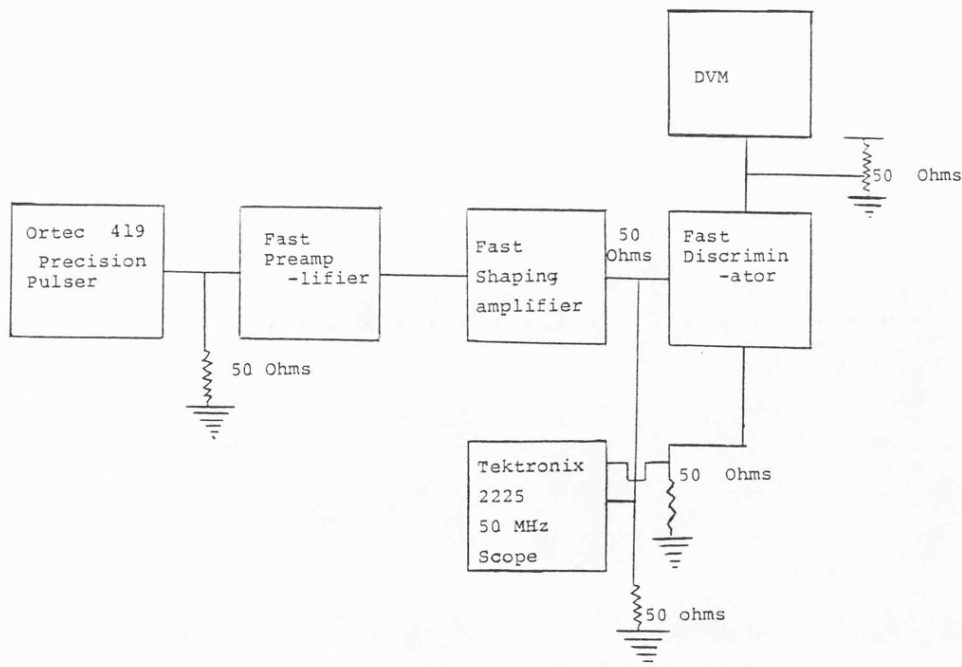


Figure 2.4 : Charge calibration of the fast electron counting electronics.

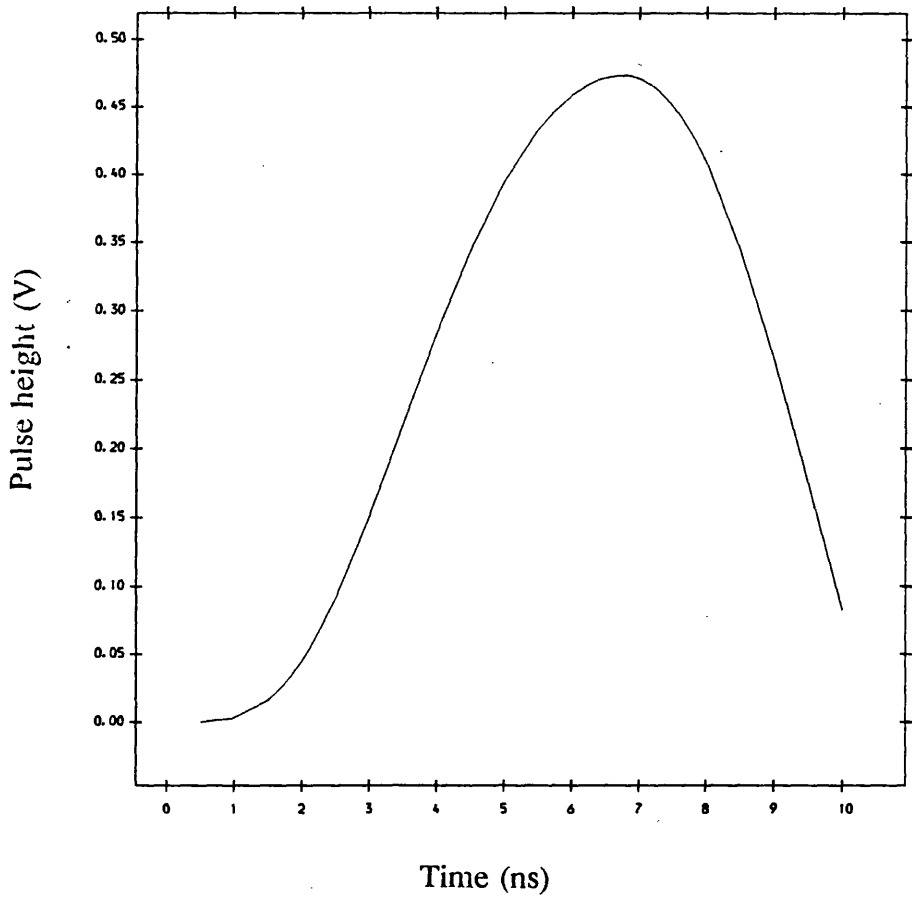


Figure 2.5 : The theoretical response of the fast shaping amplifier to a step voltage input (Mathieson, private communication (1989)).

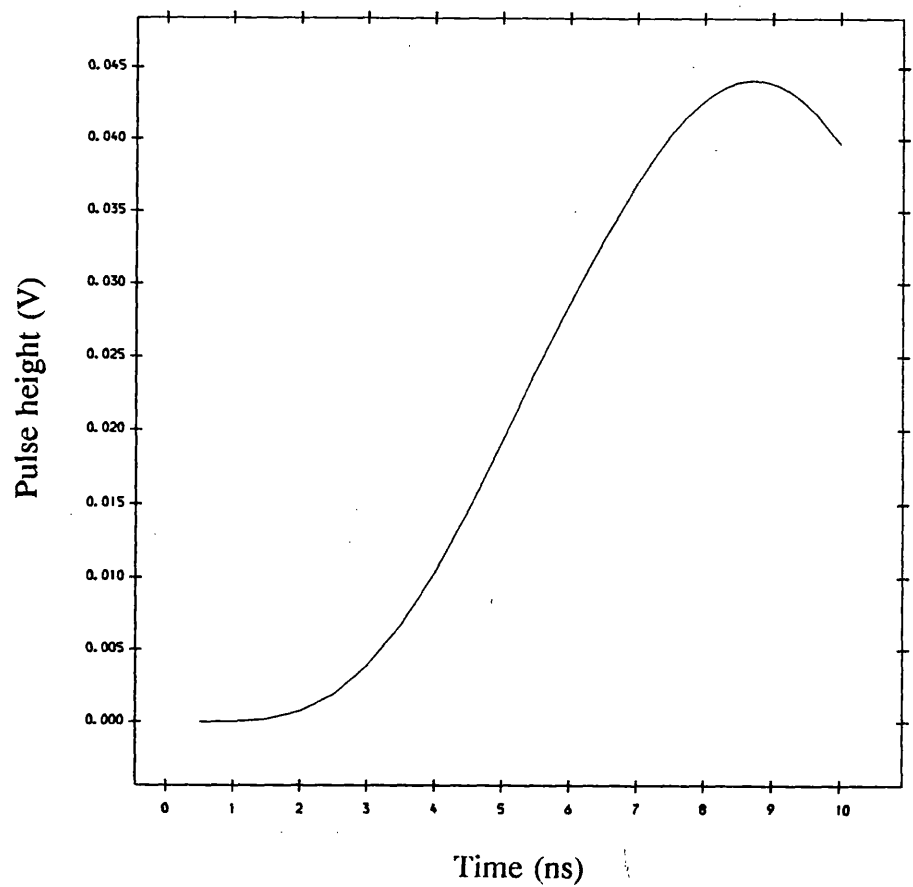


Figure 2.6 : The theoretical response of the fast shaping amplifier to a counter pulse input (Mathieson, private communication (1989)).

electronics for the counter charge level using the experimental arrangement shown in figure 2.4. The counter charge corresponding to a given discriminator threshold level of an electron counting electronics can be inferred using these figures. Table 2.1 shows the maximum step noise and the maximum counter noise for the four electron counting electronics used during the present studies.

The experimental arrangement to investigate the integral pulse height spectra is shown in figure 2.11. UV light was used to produce single electrons at the transmission grid. Integral pulse height spectra were recorded between 1.70-2.00 kV, using A-CH₄(10%). At a given anode voltage the number of counts per unit time at the fast discriminator output were recorded for a number of different discriminator thresholds. The anode voltage range 1.70-1.80 kV was examined using the fast electron counting electronics no. 1, from 1.80-1.90 kV using the fast electron counting electronics no. 2, at 1.95 kV using the fast electron counting electronics no. 3 and at 2.00 kV using the fast electron counting electronics no. 4. Integral pulse height spectra for A-CH₄(50%) were also recorded at 2.45 kV and 2.50 kV using the fast electron counting electronics no. 2 and at 2.55, 2.60 and 2.65 kV using the fast electron counting electronics no. 4.

The experimental configuration to measure γ and thus define the region of proportionality for A-CH₄(10%) and A-CH₄(50%) is shown in figure 2.12. The γ parameter was determined for a range of anode voltages for A-CH₄(10%) and A-CH₄(50%). For A-CH₄(10%) γ was determined at 1.75, 1.80, 1.85 and 1.90 kV using the fast electron counting electronics no. 1 and at 1.95 and 2.00 kV using the fast electron counting electronics no. 3. For A-CH₄(50%) γ was determined at 2.50, 2.55 and 2.60 kV using the fast electron counting electronics no. 1 and at 2.65 kV using the fast electron counting electronics no. 3.

The experimental procedure for a given counter gas mixture and anode voltage was as follows : The UV source was clamped firmly and its separation from the counter's window was kept constant. The threshold discriminator level of the fast discriminator was adjusted to lie slightly higher than the noise level. The UV source was checked for constant intensity by measuring count rate over several minutes at the fast discriminator output. The signals at the fast discriminator output may represent N , N_1 or N_2 depending upon the charge gain (see eqns. 2.7-2.9). Preliminary work on secondary and tertiary emission using an oscilloscope had shown that the secondary and tertiary electrons arrive at the anode wire approximately 0.4 μ s and 0.8 μ s, respectively, after the avalanche responsible for their emission. In order to veto the charge signals due

Electron counting electronics	Max. step noise (no. of electrons)	Max. counter noise, q_n (no. of electrons)
No. 1	5.03×10^3	5.40×10^4
No. 2	3.50×10^3	3.75×10^4
No. 3	6.99×10^3	7.50×10^4
No. 4	6.87×10^4	7.37×10^5

Table 2.1 : The maximum step noise and maximum counter noise for a number of different electron counting electronics.

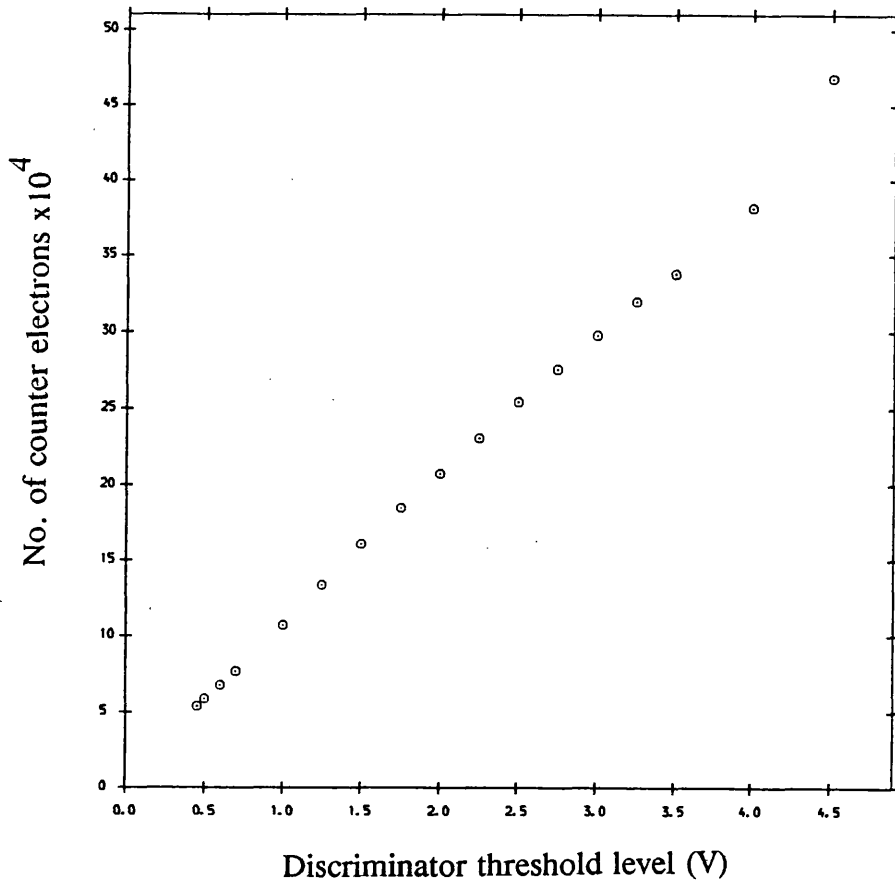


Figure 2.7 : Charge calibration for the electron counting electronics no. 1.

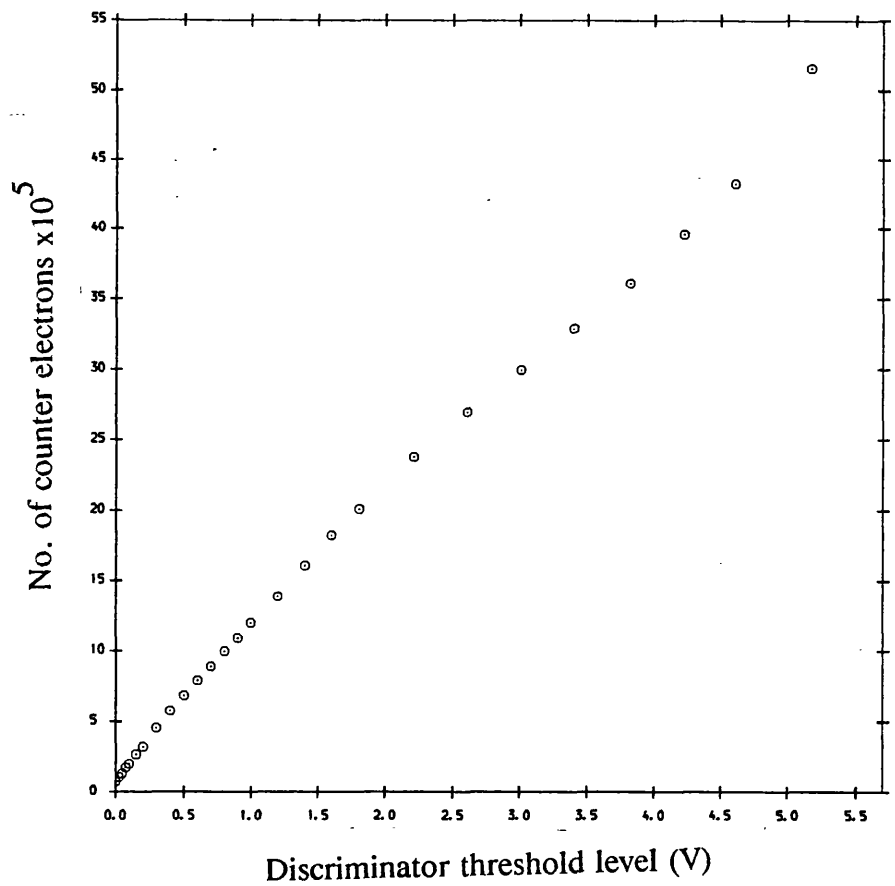


Figure 2.8 : Charge calibration for the electron counting electronics no. 2.

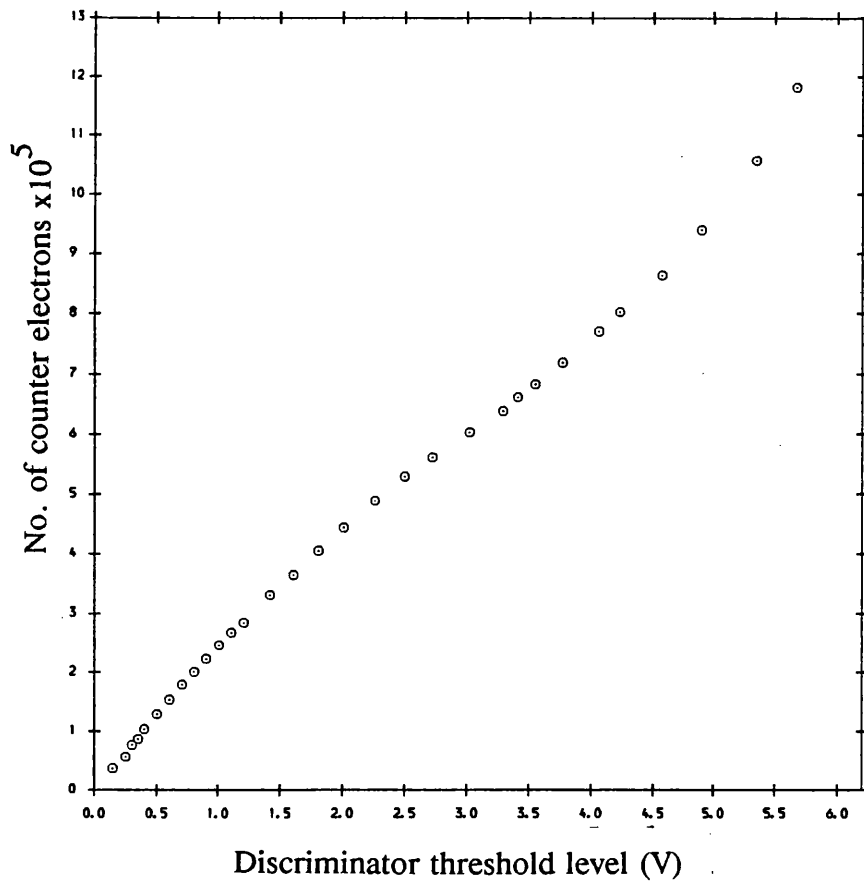


Figure 2.9 : Charge calibration for the electron counting electronics no. 3.

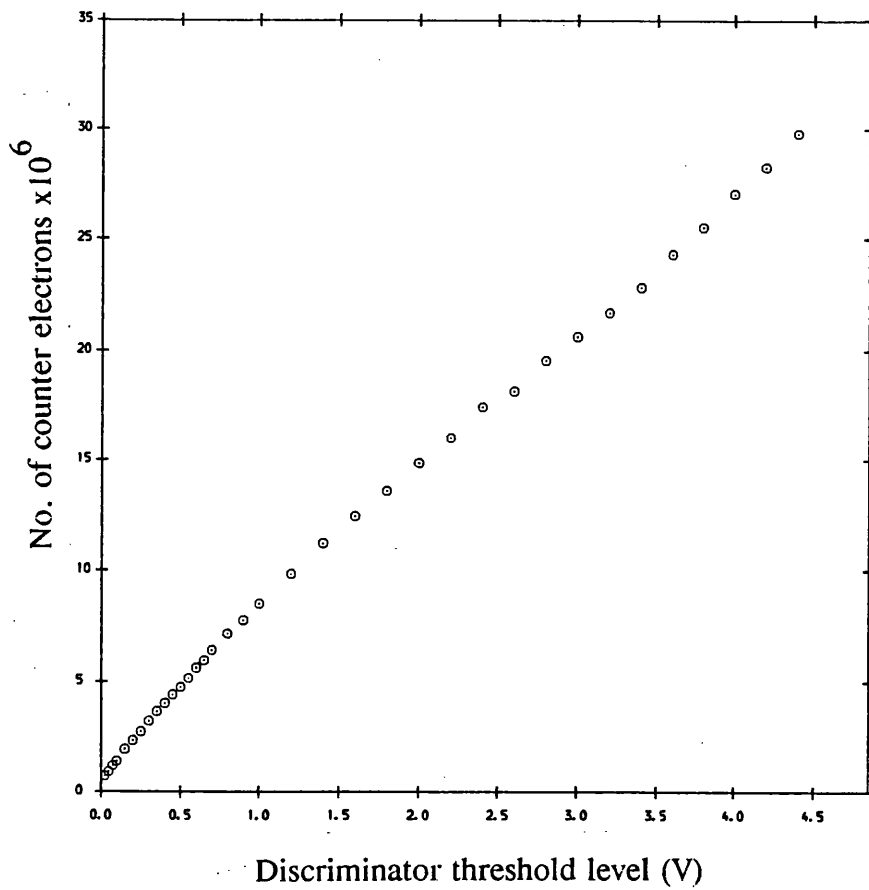


Figure 2.10 : Charge calibration for the electron counting electronics no. 4.

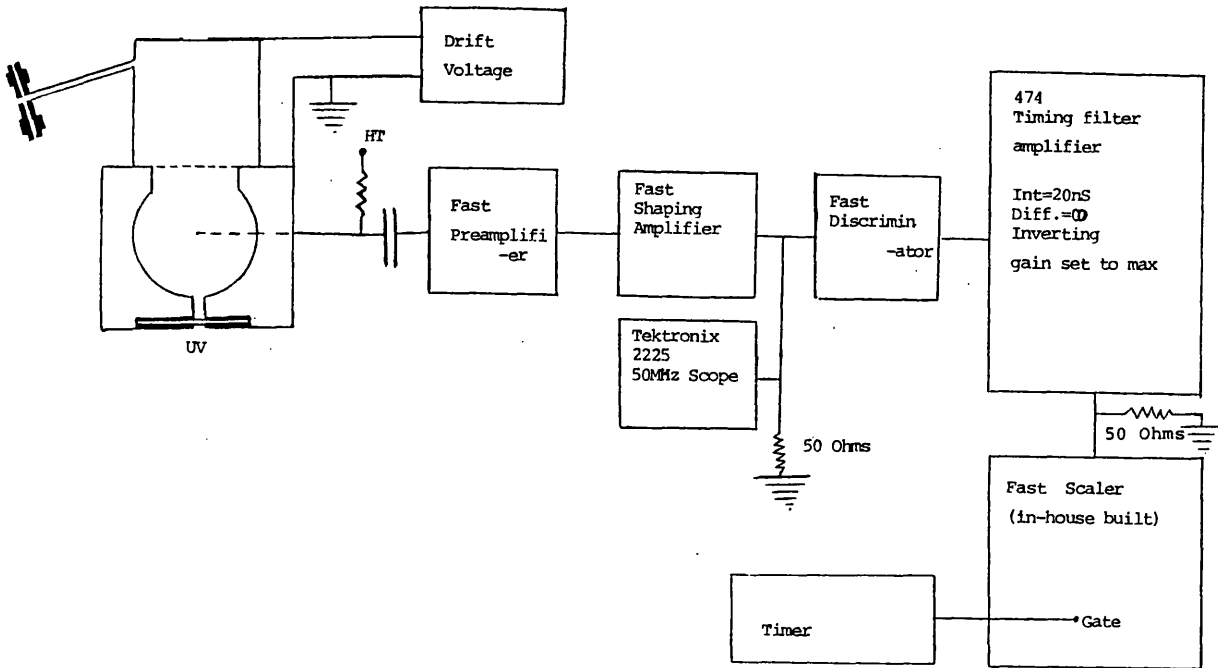


Figure 2.11 : Experimental arrangement to obtain the integral pulse height spectra.

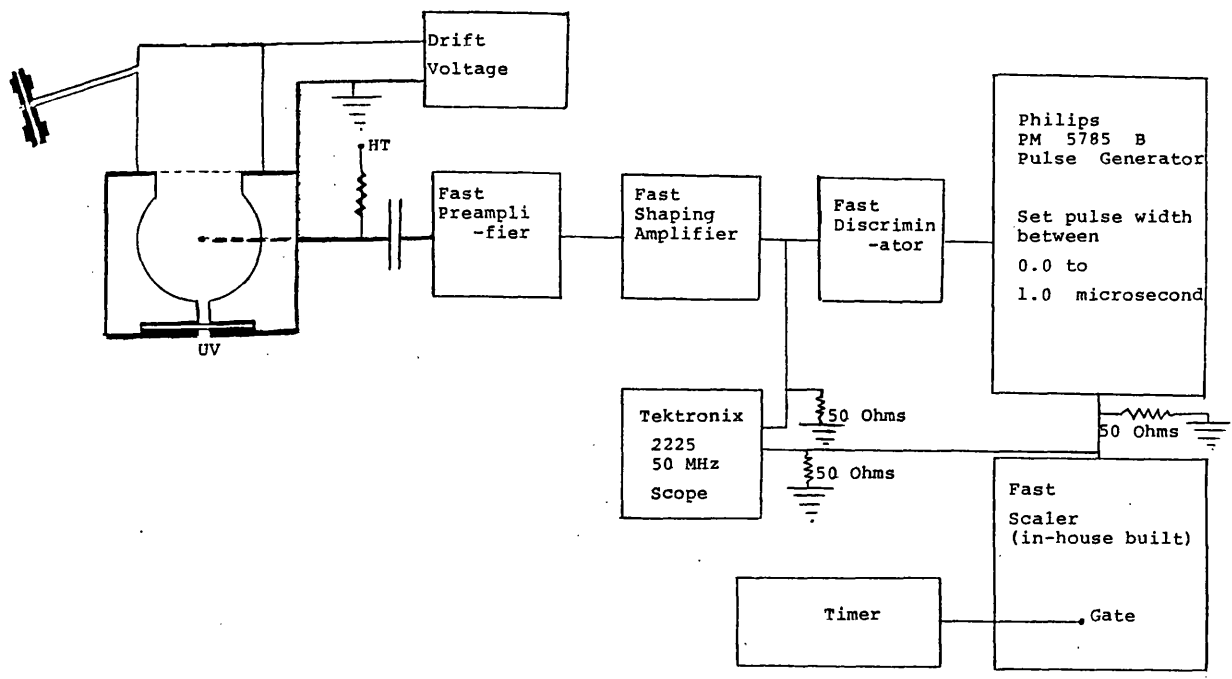


Figure 2.12 : Experimental arrangement to verify the onset of secondary emission.

to secondaries a deadtime was introduced by increasing the pulse width of Philips pulse generator up to 1.0 μ s. Each "genuine" avalanche, therefore triggered the pulse generator and single electrons were counted by in-house built scaler but charge signals due to secondary or tertiary processes were not counted since these were swamped by the large pulse width of pulse generator. Pulse generator deadtime was varied between 0.0 μ s and 1.0 μ s and the corresponding count rates were recorded. This procedure was repeated and the average count rate calculated for each value of deadtime. This ensured the error in the average count rate at the discriminator output due to the variation in UV intensity was minimized.

If $N_o \gamma n_p$ (i.e. total number of secondary events) is about 1 % of N_o then it is essential to measure each count rate at the fast discriminator output with at least 0.3 % accuracy i.e. 10^5 counts for every value of deadtime. Each count rate must be corrected for the resolving time (120 ns) of the in-house built scaler and for the deadtime introduced by the pulse generator. This correction is based on the following equation :

$$n_c = n_{ob} / (1 - n_{ob} \tau_d) \approx n_{ob} (1 + n_{ob} \tau_d) \quad 2.17$$

where n_c is the corrected count rate, n_{ob} is the observed count rate, τ_d is the total deadtime which is a sum of the resolving time of the scaler and the deadtime due to pulse generator width.

Figure 2.13 shows how γ is obtained from typical results using the experimental arrangement shown in figure 2.12. In order to determine γ , n_c is plotted versus τ_d . When the deadtime is smaller than 0.4 μ s, the number of counts at the fast discriminator equals $N_o (1 + \gamma n_p)$ (see eqn. 2.8). In the absence of secondary electrons, when deadtime is larger than 0.4 μ s, the number of counts equals N_o (see eqn. 2.7). Thus the difference between the corrected count rates obtained at 1.0 μ s deadtime and 0.1 μ s deadtime corresponds to the number of secondary electrons, $N_o \gamma n_p$. Thus, γ could be calculated by dividing number of secondary electrons with $N_o n_p$. It must be emphasised that the charge gains at high anode voltages calculated using equation 2.12 are apparent charge gains since secondary avalanches also contribute to the pulse height spectra. In order to determine γ , a knowledge of the average charge gains, n_p , due solely to ionisation by electron impact is required. In the present work, n_p was calculated using the Diethorn formula (1956).

It was necessary to distinguish the peaked pulse height distribution due

to the presence of secondary and tertiary events and due to a position dependence of Townsend's first ionisation coefficient. This was also accomplished using the experimental arrangement shown in figure 2.12. The counter gas mixture consisted of A-CH₄(10%) which was operated at 1.95 kV and 2.00 kV using the fast electron counting electronics no. 3 and the fast electron counting electronics no. 4, respectively. The number of counts per 30 seconds were recorded by a scalar for a large number of discriminator threshold levels while the pulse width of the pulse generator was maintained at 0.1 μ s. This allowed proportional signals as well as secondary and tertiary signals to be recorded by the scalar. The pulse generator width was adjusted to 10 μ s and the number of counts per 30 seconds were recorded again by the scalar for a large number of discriminator thresholds levels. In this case, the charge signals due to the secondary processes were blocked. The count rate for a given discriminator threshold level was corrected for the deadtime of the scalar and the deadtime introduced by pulse generator.

2.5 Experimental conventional X-ray energy resolution measurements : results and discussion

Figure 2.14 shows the variation of the relative FWHM X-ray energy resolution with anode voltage at 1.49 keV and 5.89 keV in A-CH₄(10%) using the present conventional proportional counter. Figure 2.14 also shows the variation of the relative FWHM X-ray energy resolution with anode voltage at 1.49 keV using A-CH₄(50%). There are several interesting features in this plot. It shows that the "best" X-ray energy resolution achieved in A-CH₄(10%) at 1.49 keV and 5.89 keV is approximately 28% FWHM and 17% FWHM, respectively. The "best" X-ray energy resolution at 1.49 keV using A-CH₄(50%) was also found to be approximately 28% FWHM. This compares to the theoretical prediction of approximately 27% FWHM and 13% FWHM at these X-ray energies (see eqn. 1.3). The X-ray energy resolution deteriorates both at low and moderately higher anode voltages (see figure 2.14). The degradation of X-ray energy resolution at lower anode voltages occurred due to smaller signal-to-noise ratio. The degradation of energy resolution at higher charge gains occurred due to the onset of cathode secondary emission and space charge effects. The onset of cathode secondary emission with respect the anode voltage is determined by the counter gas composition. It was found that the secondary onset, therefore the degradation of energy resolution, had been suppressed by increasing the methane concentration from 10% to 50%. This is apparent from the X-ray energy resolution degradation in A-CH₄(10%) above

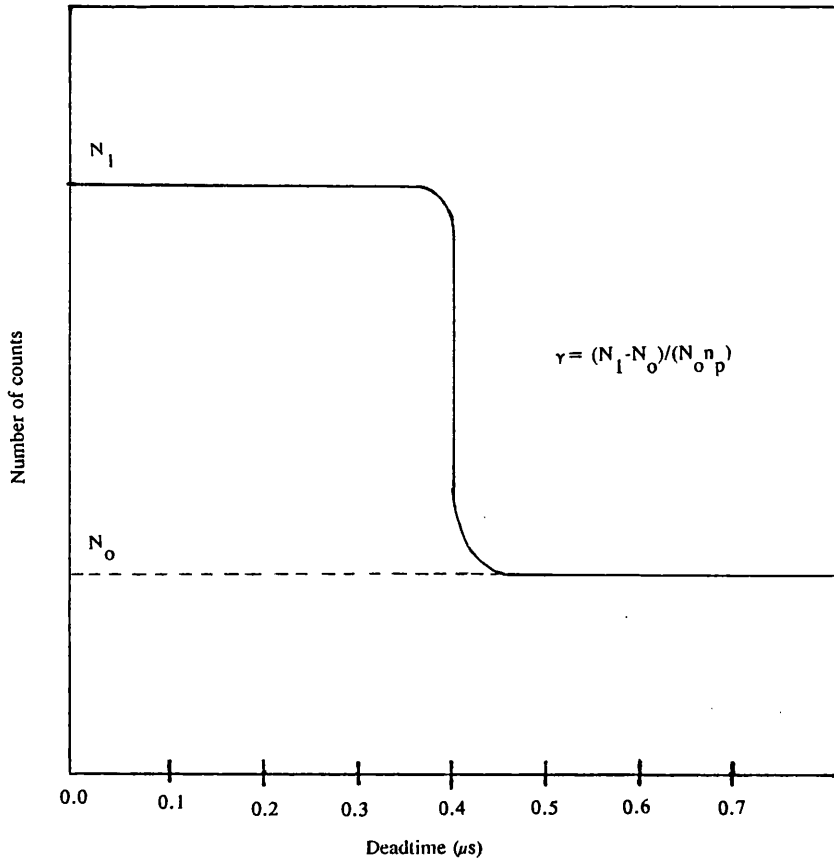


Figure 2.13 : A typical variation of the counts per unit time at the fast discriminator output with increasing deadtime. The parameter γ can be inferred from the knowledge of the reduction in number of counts at large deadtimes, N_0 and n_p .

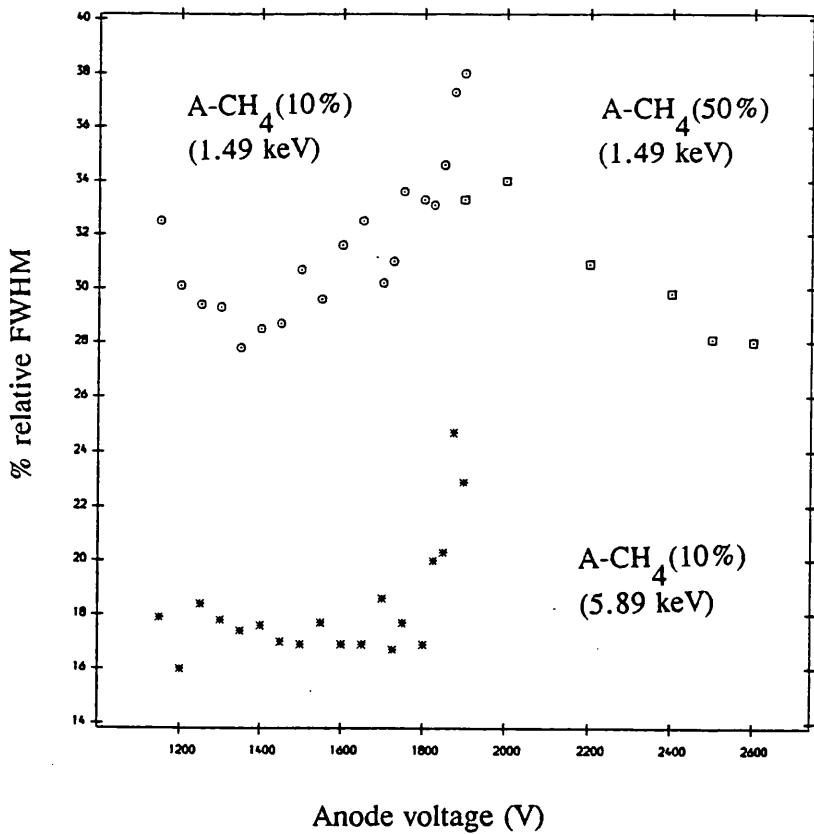


Figure 2.14 : The variation of %FWHM energy resolution with anode voltage at 1.49 keV and 5.89 keV X-ray energies using A-CH₄(10%) and A-CH₄(50%).

1.80 kV when compared to A-CH₄(50%) which retains a good X-ray energy resolution up to 2.60 kV. This observation is consistent with the discussions in section 1.2 regarding the UV quenching role of polyatomic molecules in inert gases. The space charge effects become significant at large anode voltages and count rates. The results shown in figure 2.14 correspond to a count rate of 0.1 kHz. The space charge effects arise due to the much lower mobilities of positive ions when compared with electrons. The slow moving positive ions reduce the electric field near the anode wire thus causing reduction and non-linearities to the output pulses (Hendricks (1969)). For example, the average charge gain using A-CH₄(10%) at 2.00 kV was found to be 3.20×10^7 when the count rate was maintained at 0.1 kHz. This compares to a charge gain of 4.10×10^6 when the count rate was increased to 2.0 kHz. Figure 2.15 shows the "best" pulse height spectrum at 1.49 keV using A-CH₄(50%).

The conventional X-ray energy resolution at 5.89 keV was well above theoretical limits when A-CO₂(20%) was used. For instance, the X-ray energy resolution at 5.89 keV was found to be about 27% FWHM. The pulse height spectrum showed the argon escape peak almost merged with the photopeak (see figure 2.16). The poor X-ray energy resolution in A-CO₂(20%) has been shown to be due to excessive gaseous impurities. These impurities cause a reduction in the mean electron lifetime. Figure 2.17 shows the theoretical pulse height spectra at 5.89 keV using A-CO₂(20%) assuming a number of different mean electron lifetimes (Mathieson, private communication (1988)). Comparing the theoretical pulse height spectra with the experimental spectrum (see figure 2.16) gives an estimation of the mean electron lifetime. This was found to be approximately 200 μ s. This result will be confirmed in chapter 3 (see section 3.7).

2.6 Experimental single electron pulse height spectra and charge gain measurements : results and discussion

Figures 2.18a to 2.18d illustrate the single electron differential pulse height spectra for A-CH₄(10%) for anode voltages ranging from 1.70 kV to 2.00 kV. The inverse slopes of these plots represent the average charge gains. At higher anode voltages, some large pulses could not be examined due to the saturation of the shaping amplifier. The charge level for a given spectrum was calculated using the charge calibration procedure described in section 2.4. The average charge multiplication factor, M, was calculated by dividing the average charge gain by the electronic charge. The average charge multiplication factors using A-CH₄(10%) differential pulse height spectra at a number of different

anode voltage voltages are shown in figure 2.19. Figure 2.19 also shows the variation of the average charge gain, M , with anode voltage when 1.49 keV and 5.89 keV X-rays were used.

The solid lines in figure 2.19 show the theoretical variations of charge gain with anode voltage for A-CH₄(10%) and A-CH₄(50%). The theoretical charge gains were calculated using equation 2.1 (Diethorn (1956)). This required a knowledge of the parameters ΔV and K for both counter gas mixtures. Figures 2.20 and 2.21 show, respectively, the variation of ΔV and K for a number of different argon-methane counter gas mixtures (Kiser (1960), Wolff (1974) and the present work). ΔV and K for A-CH₄(10%) were assumed to be 23.3 eV and 4.8×10^4 V/cm atmosphere, respectively (Wolff (1974)). The parameters for A-CH₄(50%) were determined using charge gain data shown in figure 2.19. This was necessary since no literature values were found for ΔV and K corresponding to A-CH₄(50%). This involved plotting of $\ln(M)\ln(r_c/r_a)/V$ versus $\ln\{V/pr_a \ln(r_c/r_a)\}$. The slope of this plot equals $\ln(2)/\Delta V$ and the intercept equals $-\ln(2)(\ln K)/\Delta V$. The parameters ΔV and K using A-CH₄(50%) were found to be 23.3 eV and 8.50×10^4 V/cm atmosphere, respectively.

A large discrepancy was observed between experimental and theoretical charge gains at higher anode voltages. For example, experimental charge gain at 2.00 KV using A-CH₄(10%) equals 3.20×10^7 compared to a theoretical charge gain 6.24×10^5 at the same anode voltage. Higher experimental charge gains are caused by the onset of secondary and tertiary processes.

As expected the single electron pulse height spectrum adhered to an exponential form at lower anode voltages. It can be seen from figure 2.18b that the differential pulse height spectrum retained an exponential form up to 1.90 kV (average charge gain 4.13×10^5). A departure from the exponential distribution was observed at 1.95 kV when the average charge gain was 2.87×10^6 (see figure 2.18c). The differential pulse height spectrum at 2.00 kV (average charge gain 3.20×10^7) showed a well defined peak (see figure 2.18d). In contrast to the Erlang pulse height distribution, a large number of smaller pulses were also observed (see the origin of figure 2.18d). The smaller pulses were thought to arise from the low field regions of the anode wire (ends) particularly due to source UV reflections by the counter interior.

Figures 2.22a-2.22d show the integral pulse height spectra measured using A-CH₄(10%) for the 1.70- 2.00 kV anode voltage range using the experimental arrangement shown in figure 2.11. The inverse slopes of these plots also represent the average charge gains. As expected, the change in the integral pulse height spectrum with increasing anode voltage was similar to the

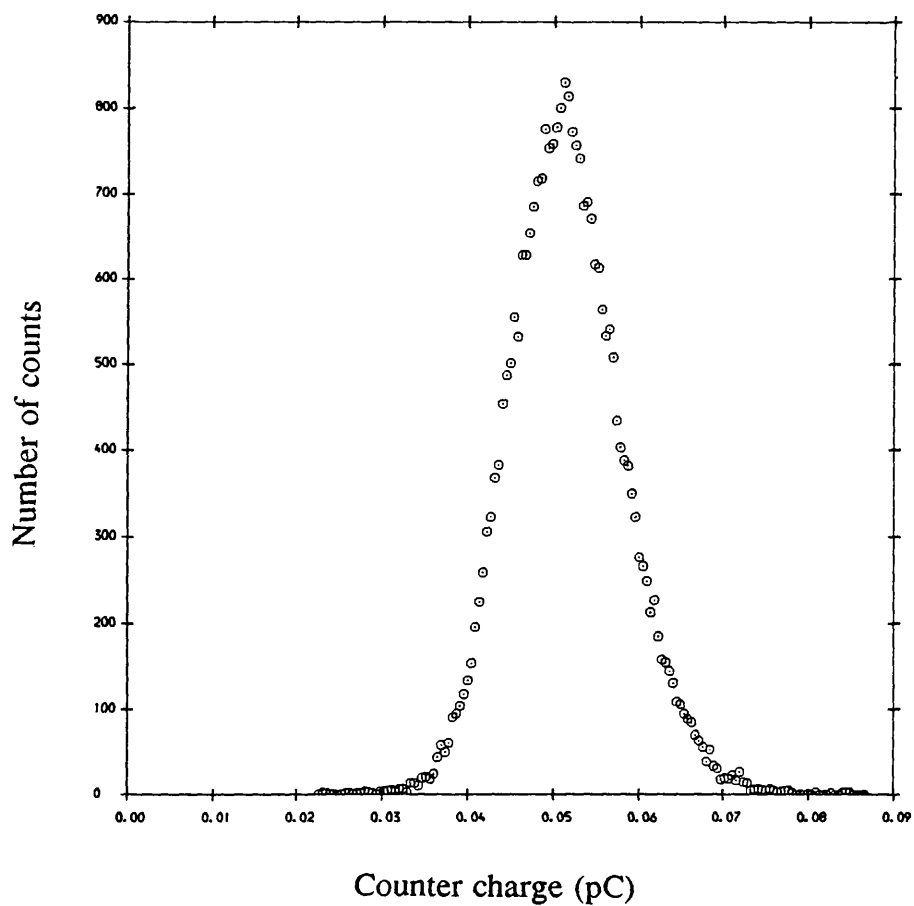


Figure 2.15 : Pulse height spectrum at 1.49 keV using A-CH₄ (10%).

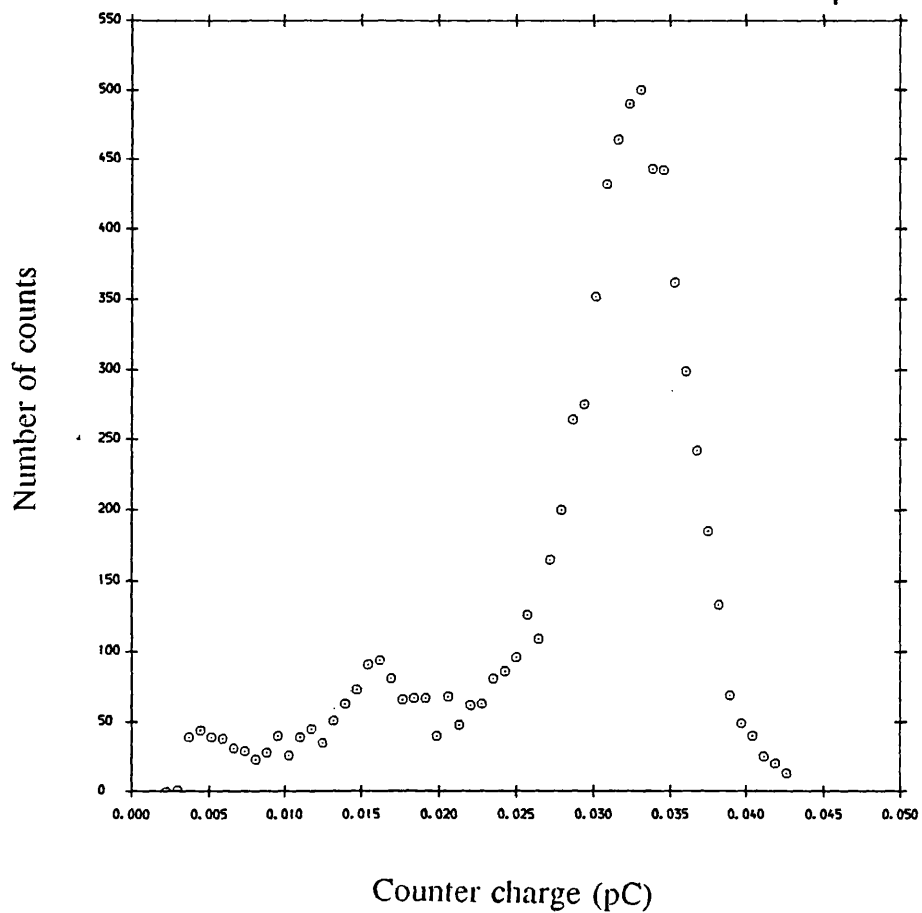


Figure 2.16 : Pulse height spectrum at 5.89 keV using A-CO₂ (20%).

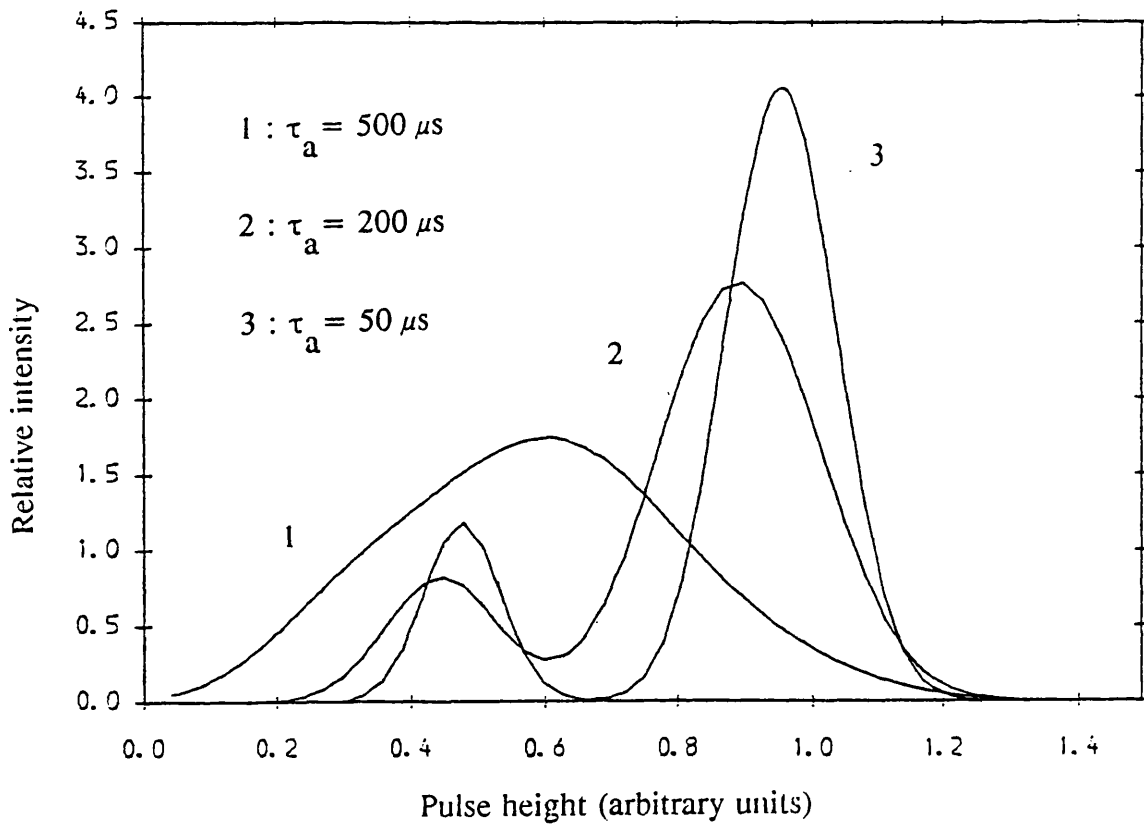


Figure 2.17 : The theoretical pulse height spectra at 5.89 keV using A-CO₂(20%) assuming a number of different mean electron lifetimes (Mathieson, private communication (1988)).

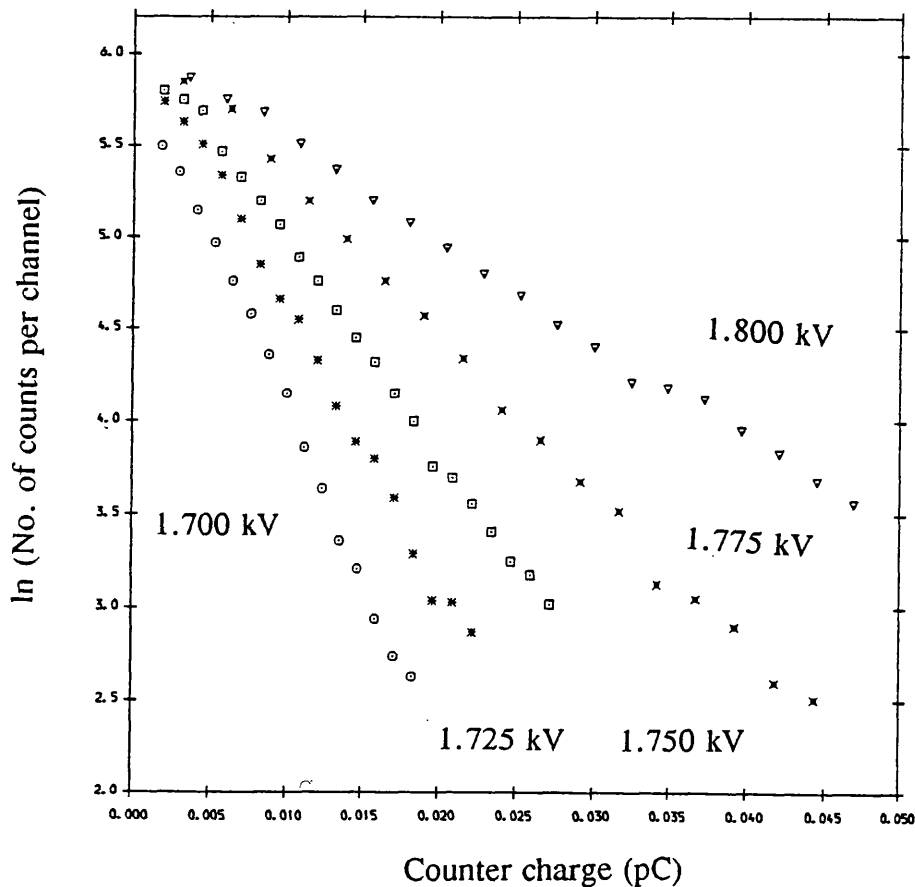


Figure 2.18a : Single electron differential pulse height spectra using A-CH₄(10%) at a number of different anode voltages.

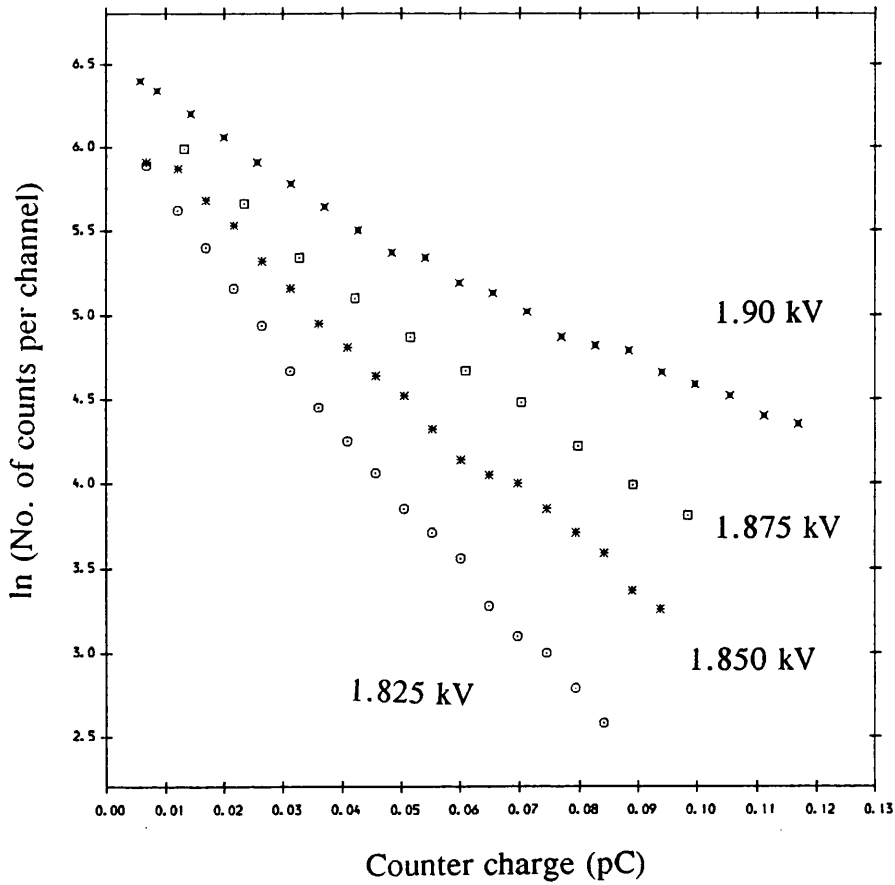


Figure 2.18b : Single electron differential pulse height spectra using A-CH₄ (10%) at a number of different anode voltages.

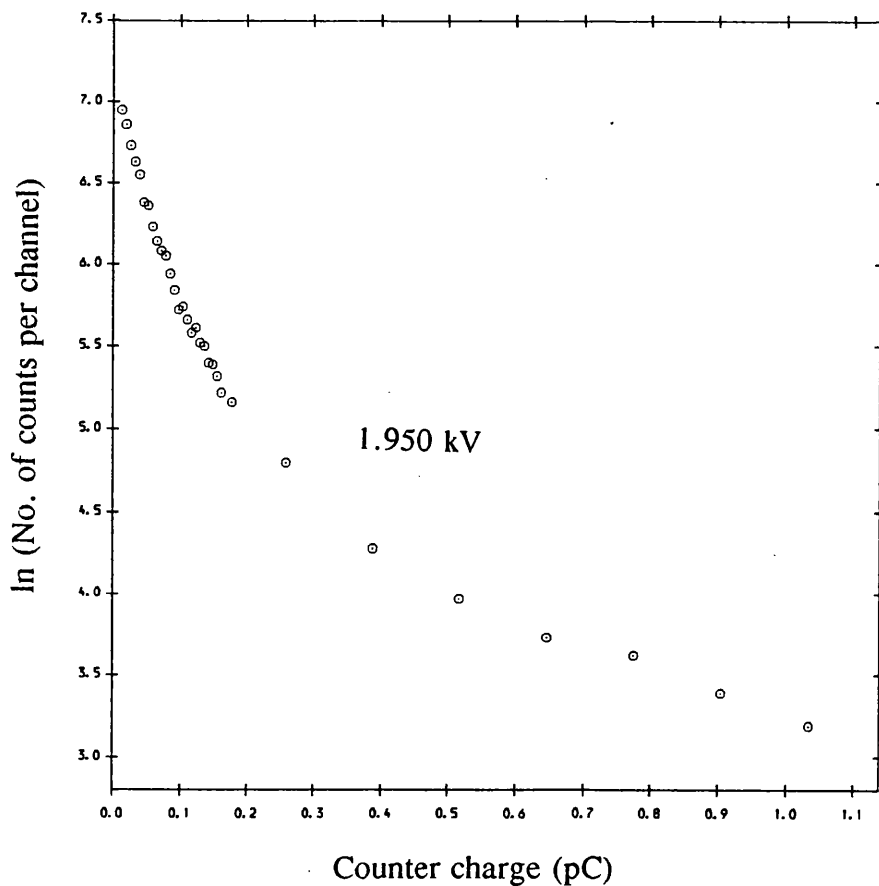


Figure 2.18c : Single electron differential pulse height spectra using A-CH₄ (10%) when the anode voltage was set at 1.950 kV.

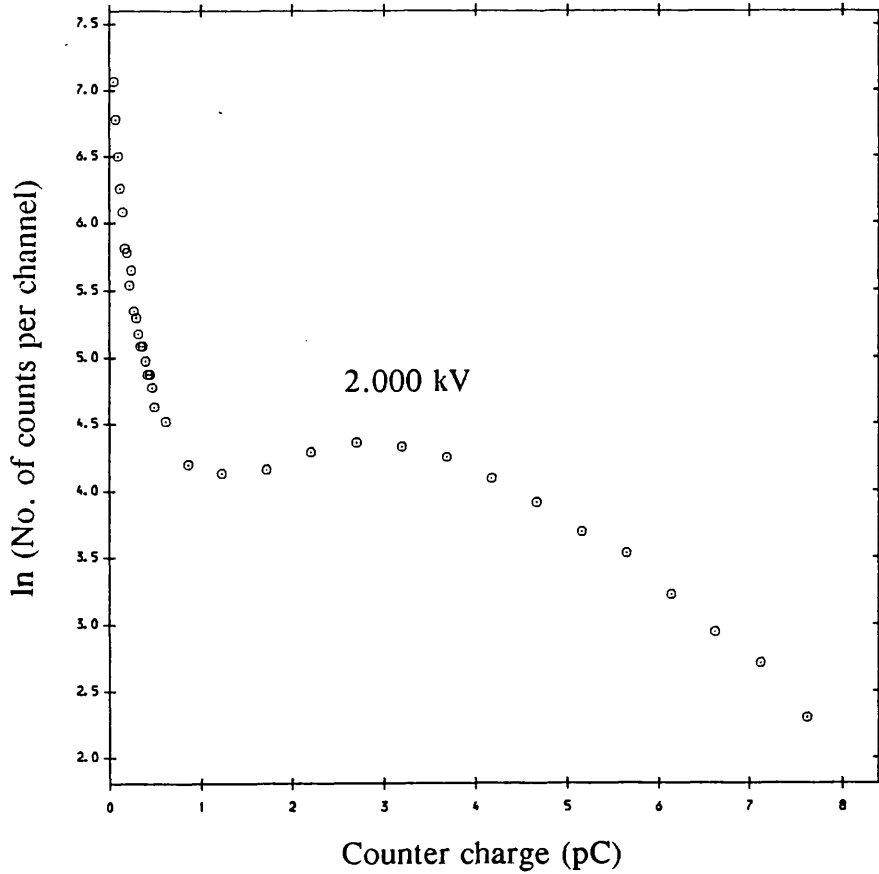


Figure 2.18d : Single electron differential pulse height spectra using A-CH₄(10%) when the anode voltage was set at 2.000 kV.

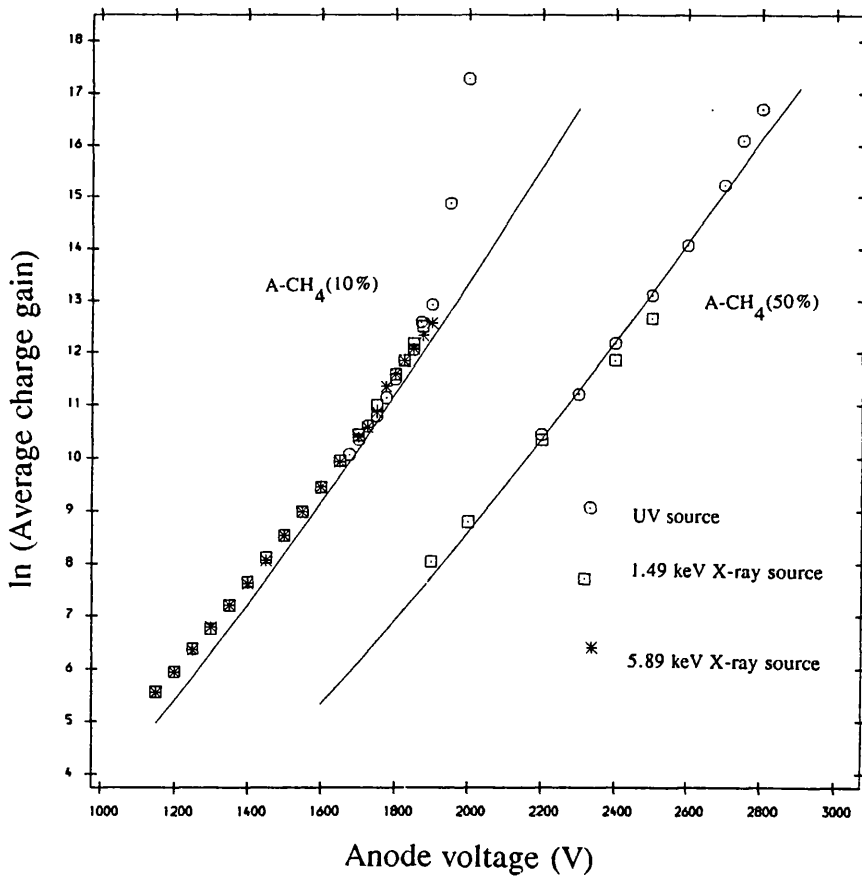


Figure 2.19 : The variation of the average charge gain with anode voltage for A-CH₄(10%) and A-CH₄(50%). The solid lines indicate theoretical charge gains calculated using Diethorn formula (1956).

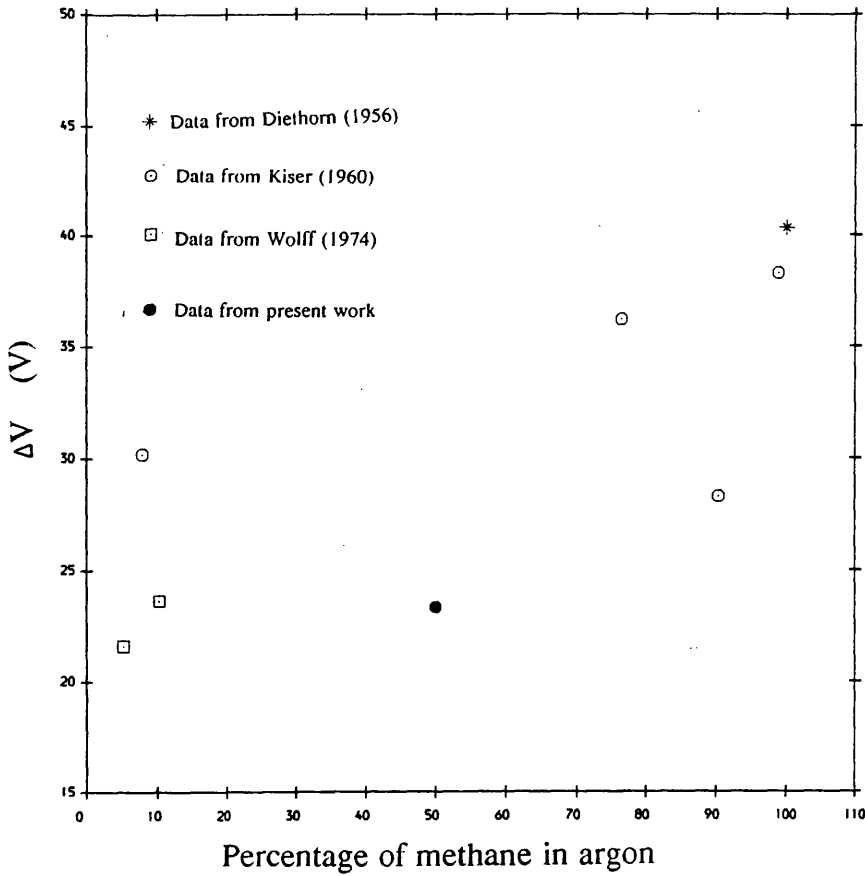


Figure 2.20 : Variation of the parameter ΔV for a number of different argon-methane counter gas mixtures.

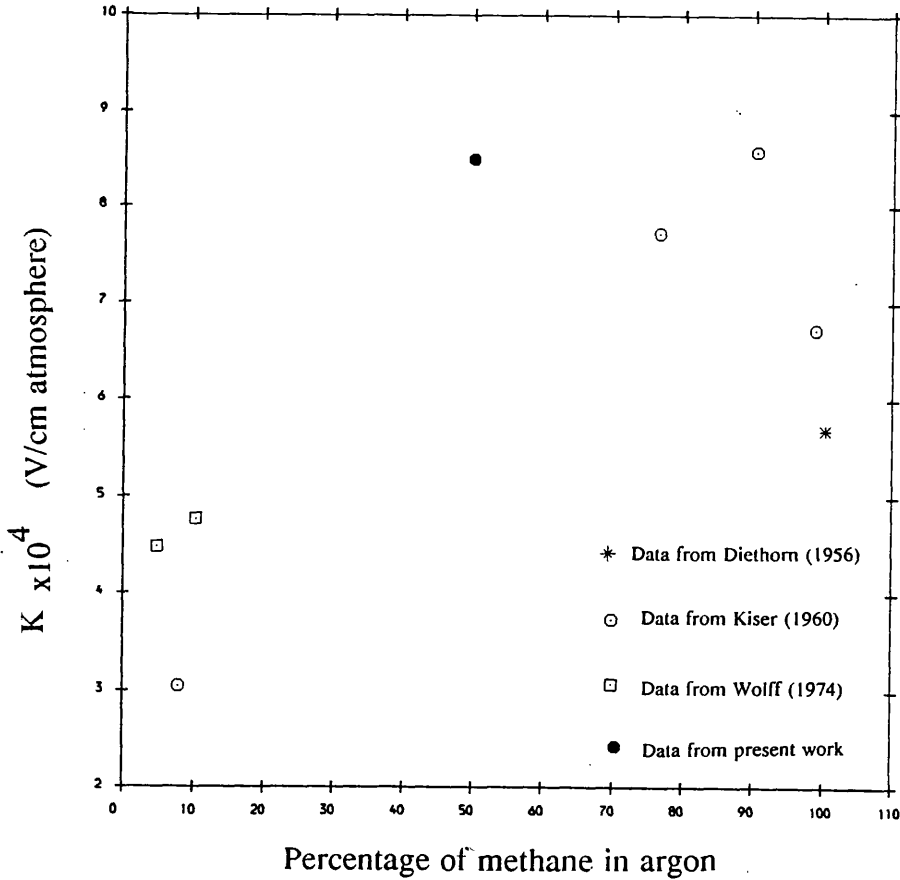


Figure 2.21 : Variation of the parameter K for a number of different argon-methane counter gas mixtures.

change already observed by examining the differential pulse height spectrum. Table 2.2 shows a comparison between the average charge gains for A-CH₄(10%) obtained by differential and integral pulse height analysis.

The single electron differential pulse height spectra for A-CH₄(50%) at a number of different anode voltages are shown in figures 2.23a and 2.23b. Figure 2.19 also shows the corresponding charge gains. It can be seen that an increase in methane concentration in argon from 10% to 50% has shifted the charge gain curve to higher anode voltages. The pulse height distribution departs from the exponential form at much higher anode voltages when compared with A-CH₄(10%). For instance, the single electron pulse height spectra assumes a non-exponential shape at 2.75 kV and a peaked pulse height distribution is obtained at 2.80 kV.

Figures 2.24a and 2.24b show the integral pulse height spectra for A-CH₄(50%) between 2.45 kV and 2.65 kV using the experimental arrangement shown in figure 2.11. The inverse slope of these plots represents the average charge gains. Table 2.3 shows a comparison between the average charge gain obtained from differential and integral single electron response using A-CH₄(50%).

It was pointed out in section 2.2 that an exponential single electron response does not necessarily imply the absence of secondary processes (see eqn. 2.7). Indeed, the shaping amplifier output examined by an oscilloscope showed faint after pulsing in A-CH₄(10%) at 1.85 kV at 0.4 μs corresponding to the arrival of secondary electrons from cathode walls. The preamplifier output examined at 2.00 kV showed after pulsing at 0.8 μs as well as 0.4 μs (see figure 2.25). Charge signal pulses at 0.4 μs and 0.8 μs were due to the secondary and tertiary electrons, respectively.

The γ parameter was determined for a number of different anode voltages using A-CH₄(10%) and A-CH₄(50%). Figures 2.26 and 2.27a-2.27f show the results of the examination of secondary processes in A-CH₄(10%) using the experimental arrangement shown in figure 2.12. Figure 2.26 shows the variation in UV source intensity with time while the deadtime introduced by pulse generator was kept constant. The average variation in UV intensity is approximately, 1%. This made possible the detection of small count rate changes at the discriminator output if secondary processes were present. Figures 2.27a-2.27f show the average number of counts in 30 seconds versus deadtime at the anode voltage 1.75, 1.80, 1.85, 1.90, 1.95 and 2.00 kV respectively. It can be seen from figure 2.27a that no fractional change in the count rate with an increasing deadtime occurred at 1.75 kV. The mean efficiency of the release of

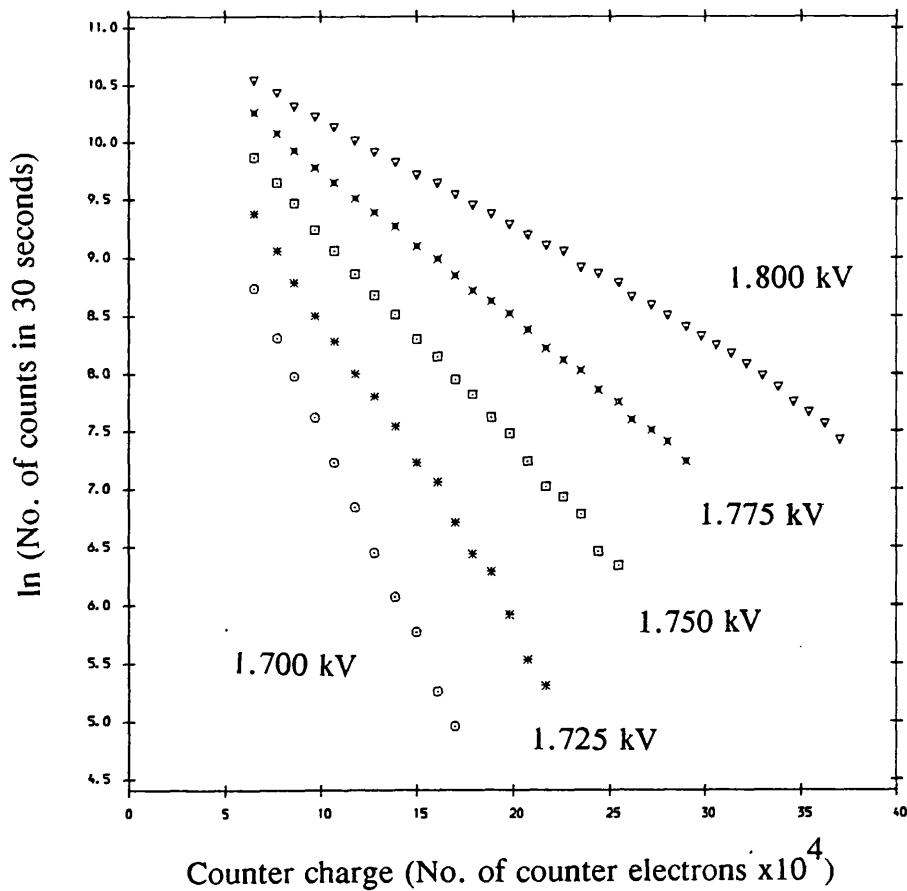


Figure 2.22a : Single electron integral pulse height spectra using A-CH₄(10%) at a number of different anode voltages.

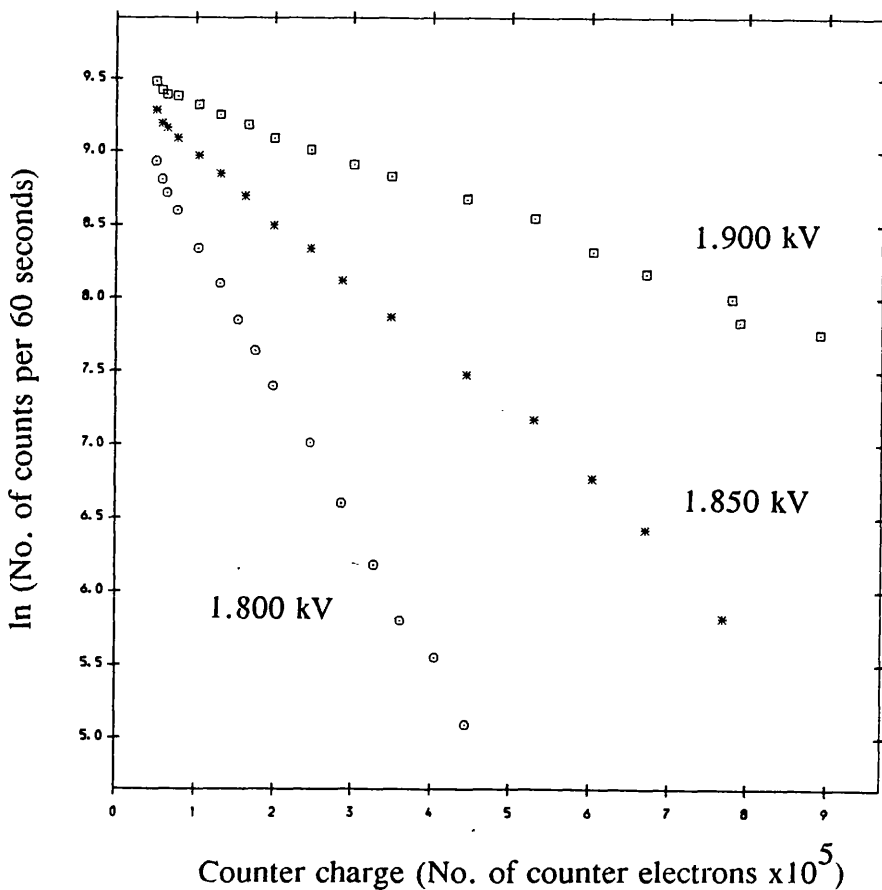


Figure 2.22b : Single electron integral pulse height spectra using A-CH₄(10%) at a number of different anode voltages.

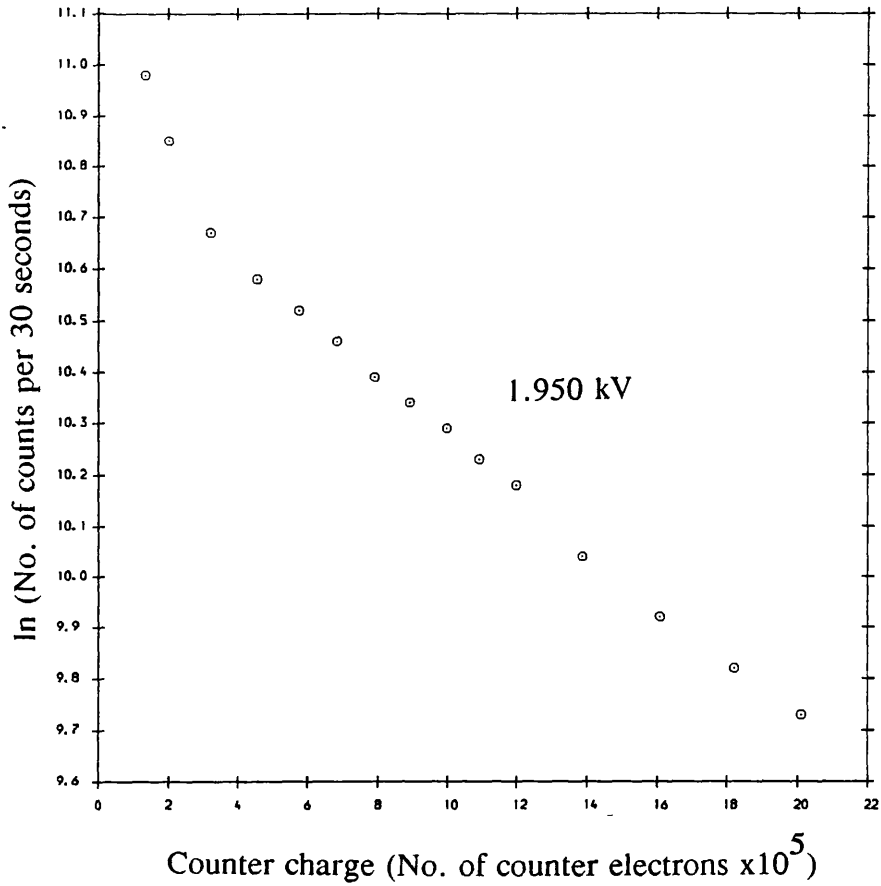


Figure 2.22c : Single electron integral pulse height spectra using A-CH₄(10%) when the anode voltage was set at 1.950 kV.

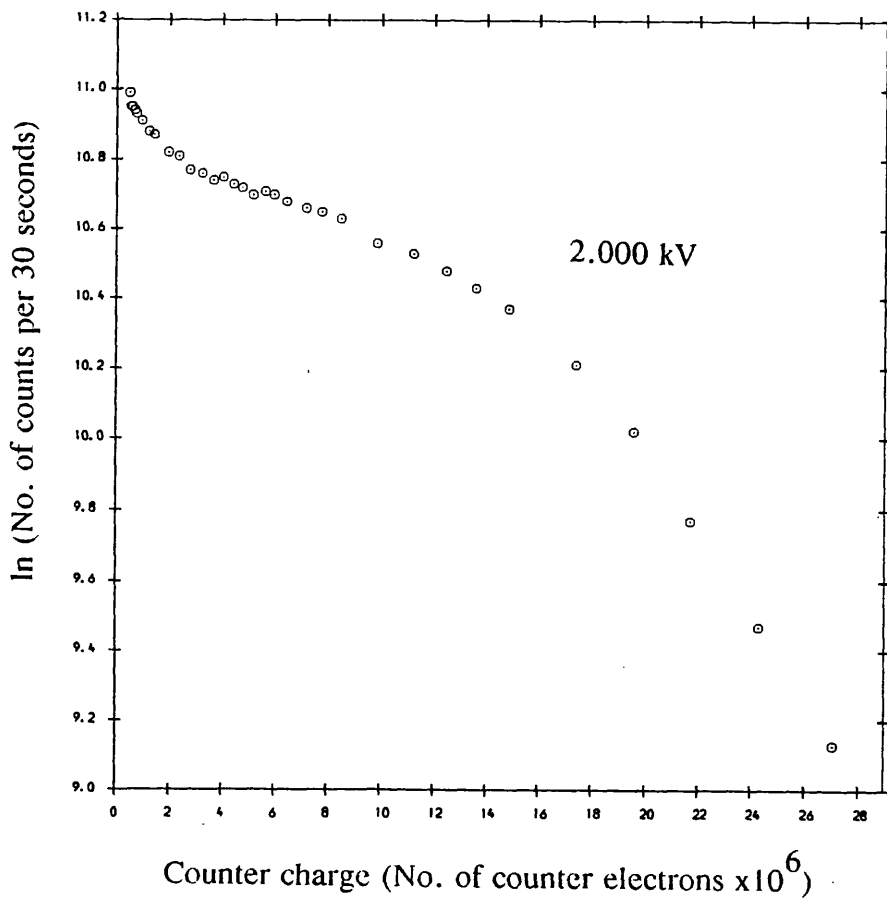


Figure 2.22d : Single electron integral pulse height spectra using A-CH₄(10%) when the anode voltage was set at 2.000 kV.

Anode Voltage (kV)	Average charge gain in A-CH ₄ (10%) by differential spectra	Average charge gain in A-CH ₄ (10%) by integral spectra
1.700	3.13 x10 ⁴	3.10 x10 ⁴
1.725	4.05 x10 ⁴	3.99 x10 ⁴
1.750	4.90 x10 ⁴	4.95 x10 ⁴
1.775	6.89 x10 ⁴	6.95 x10 ⁴
1.800	9.77 x10 ⁴	9.82 x10 ⁴
1.825	1.40 x10 ⁵	1.47 x10 ⁵
1.850	1.71 x10 ⁵	1.66 x10 ⁵
1.875	2.94 x10 ⁵	2.90 x10 ⁵
1.900	4.13 x10 ⁵	4.20 x10 ⁵
1.950	2.87 x10 ⁶	2.99 x10 ⁶
2.000	3.20 x10 ⁷	3.04 x10 ⁷

Table 2.2 : A comparison between the average charge gains for A-CH₄(10%) obtained by differential and integral pulse height analysis.

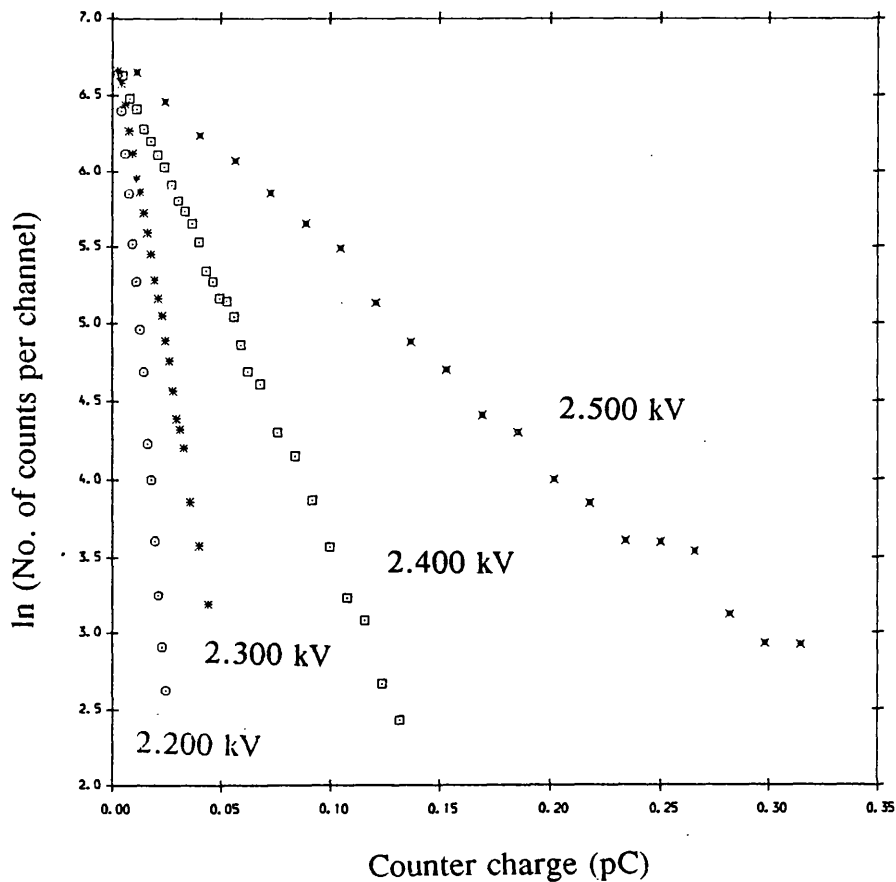


Figure 2.23a : Single electron differential pulse height spectra using A-CH₄ (50%) at a number of different anode voltages.

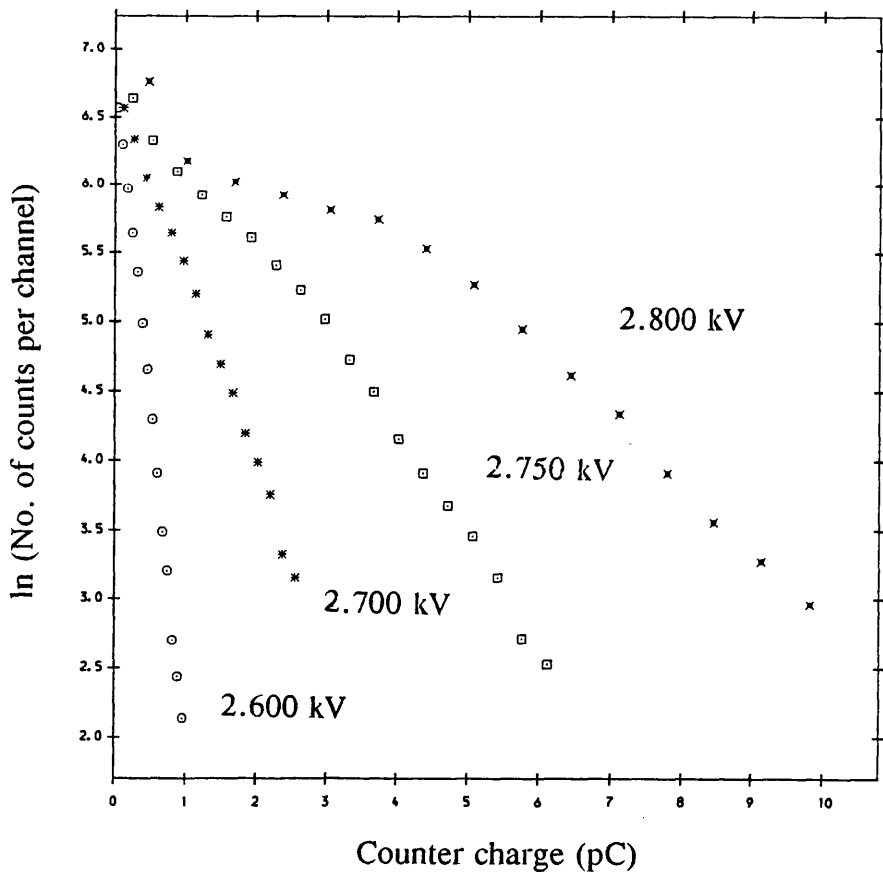


Figure 2.23b : Single electron differential pulse height spectra using A-CH₄ (50%) at a number of different anode voltages.

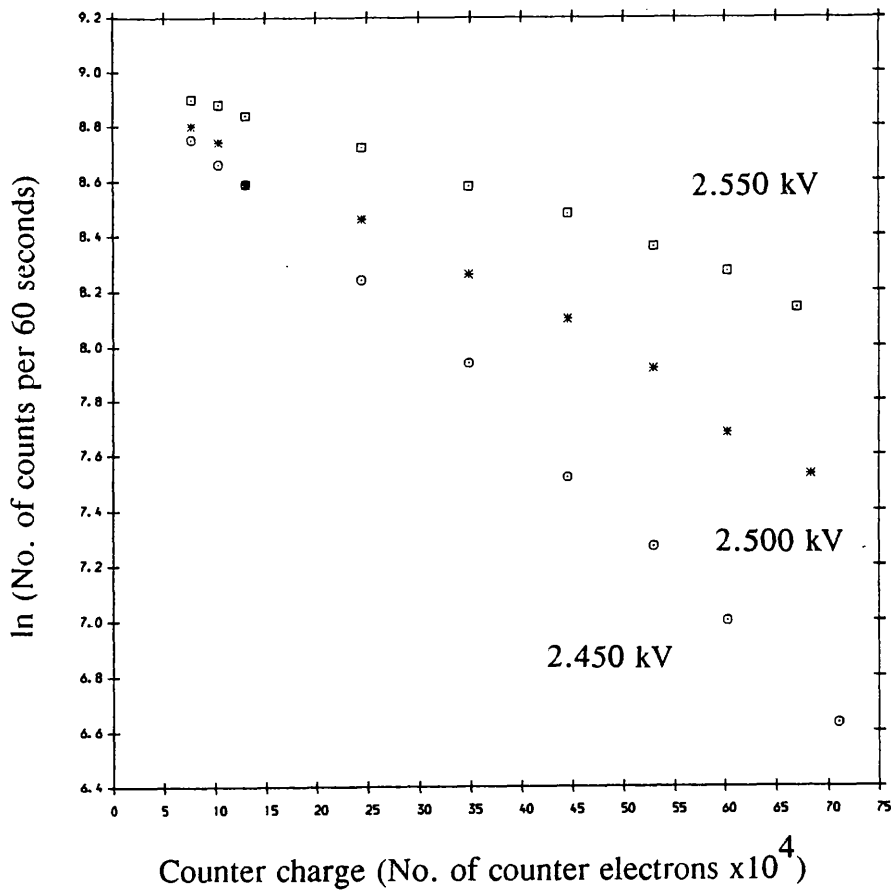


Figure 2.24a : Single electron integral pulse height spectra using A-CH₄(50%) at a number of different anode voltages.

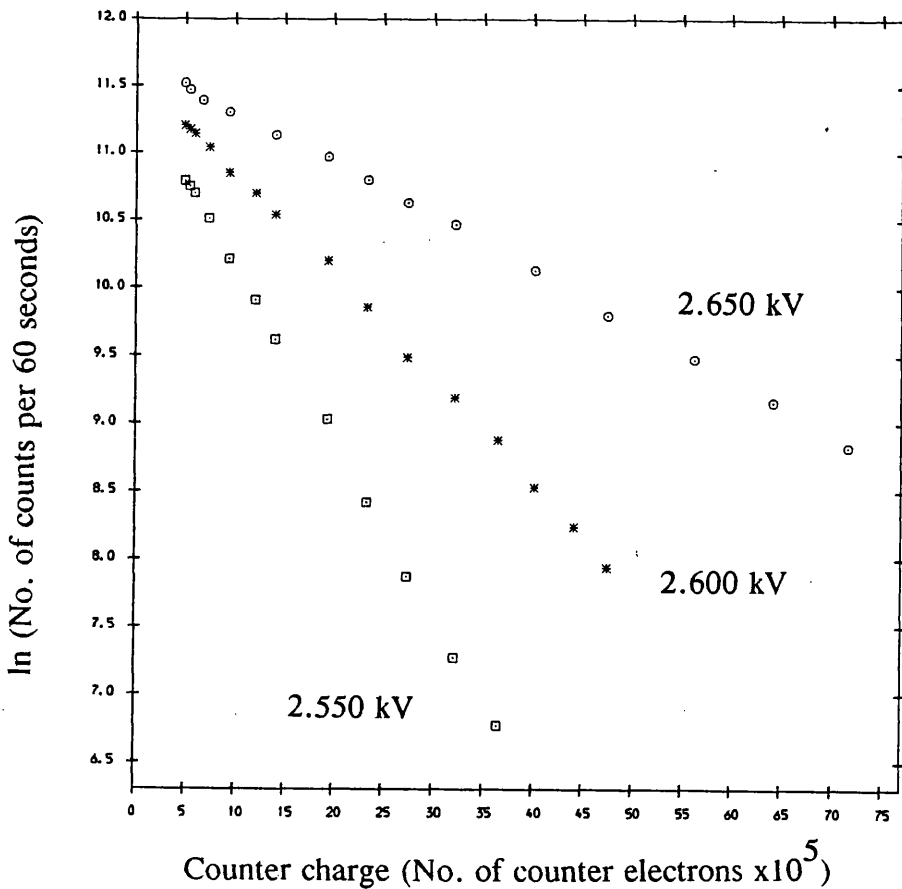
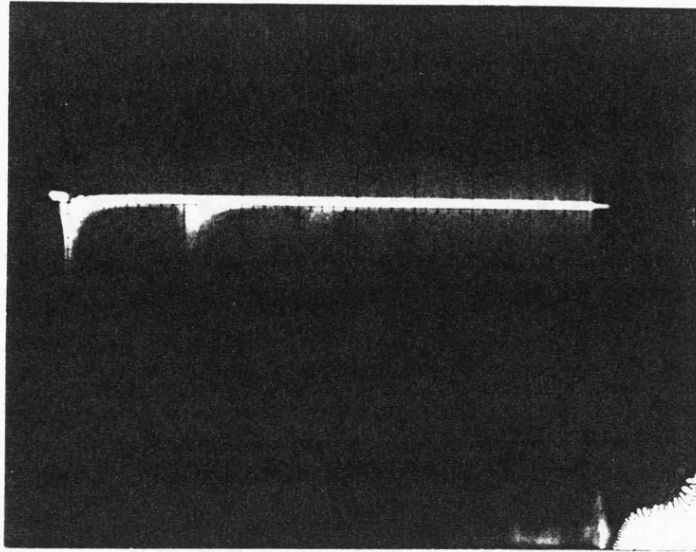


Figure 2.24b : Single electron integral pulse height spectra using A-CH₄(50%) at a number of different anode voltages.

Anode Voltage (kV)	Average charge gain in A-CH ₄ (50%) by differential spectra	Average charge gain in A-CH ₄ (50%) by integral spectra
2.20	3.45 x10 ⁴	-
2.30	7.39 x10 ⁴	-
2.40	1.95 x10 ⁵	-
2.45	-	2.98 x10 ⁵
2.50	4.94 x10 ⁵	4.98 x10 ⁵
2.55	-	8.02 x10 ⁵
2.60	1.29 x10 ⁶	1.28 x10 ⁶
2.65	-	2.53 x10 ⁶
2.70	4.11 x10 ⁶	-
2.75	9.82 x10 ⁶	-
2.80	1.79 x10 ⁷	-

Table 2.3 : A comparison between the average charge gains for A-CH₄(50%) obtained by differential and integral pulse height analysis.



Vertical scale :
 5 mV per division
 Horizontal scale :
 0.2 μ s per division

Figure 2.25 : An oscilloscope photograph showing the arrival of secondary signals at 0.4 μ s and tertiary signals at 0.8 μ s. The signal output was taken from the preamplifier (Canberra Type 2001A). A-CH₄(10%) gas mixture at 2.000 kV anode voltage (Photograph taken by the author).

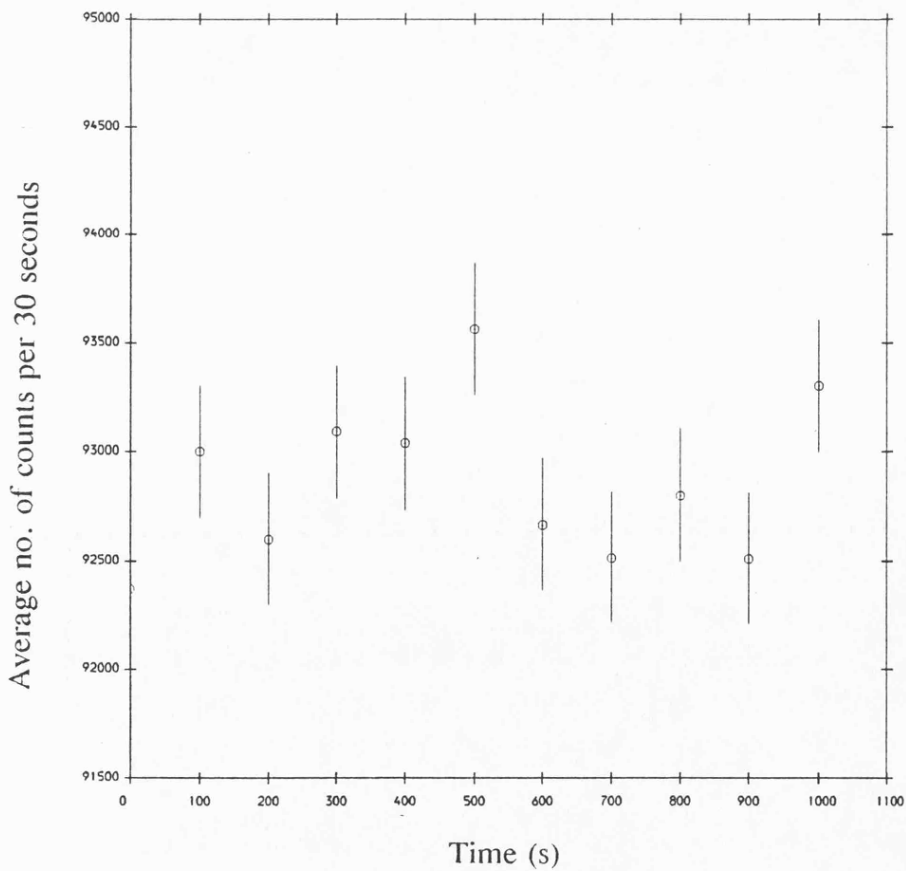


Figure 2.26 : The variation of the intensity of the UV source (Philip Harris) with time.

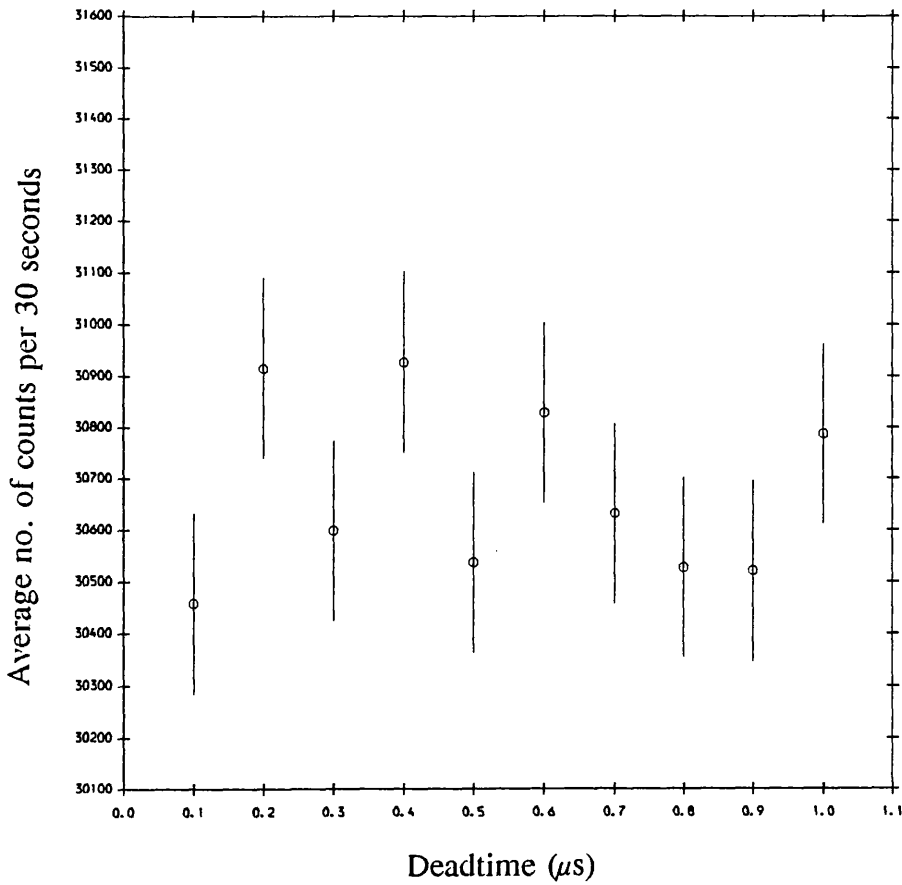


Figure 2.27a : Variation of the count rate at the discriminator output with deadtime using A-CH₄(10%) when the anode voltage was set at 1.750 kV.

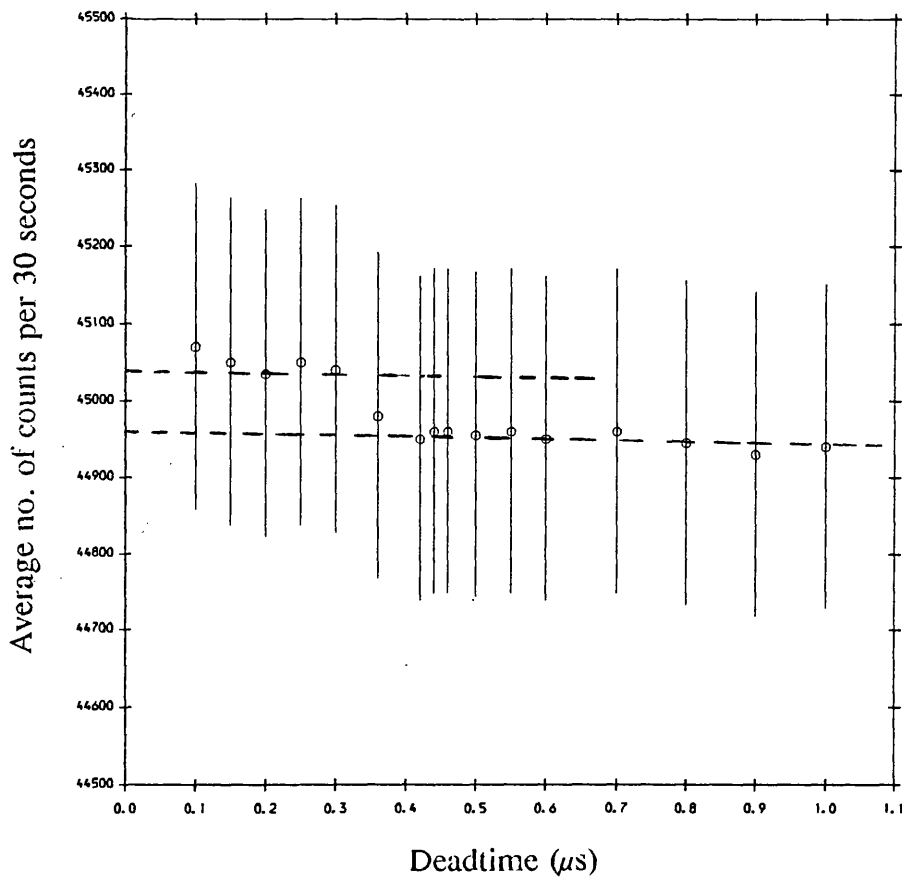


Figure 2.27b : Variation of the count rate at the discriminator output with deadtime using A-CH₄(10%) when the anode voltage was set at 1.800 kV.

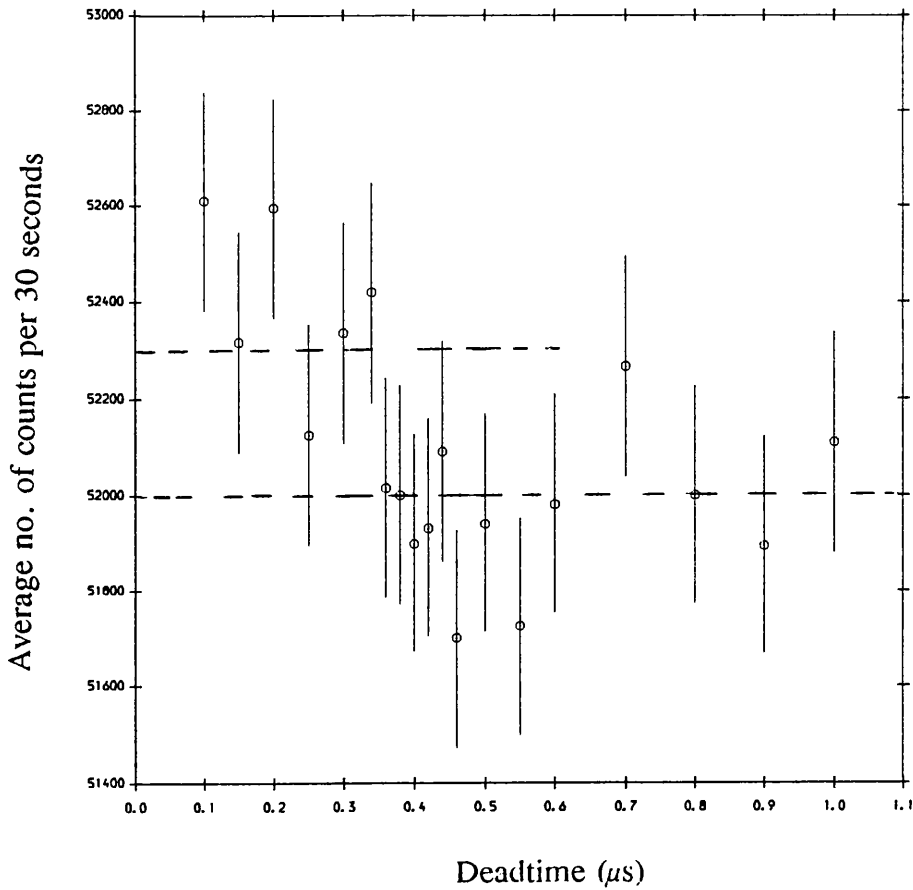


Figure 2.27c : Variation of the count rate at the discriminator output with deadtime using A-CH₄ (10%) when the anode voltage was set at 1.850 kV.

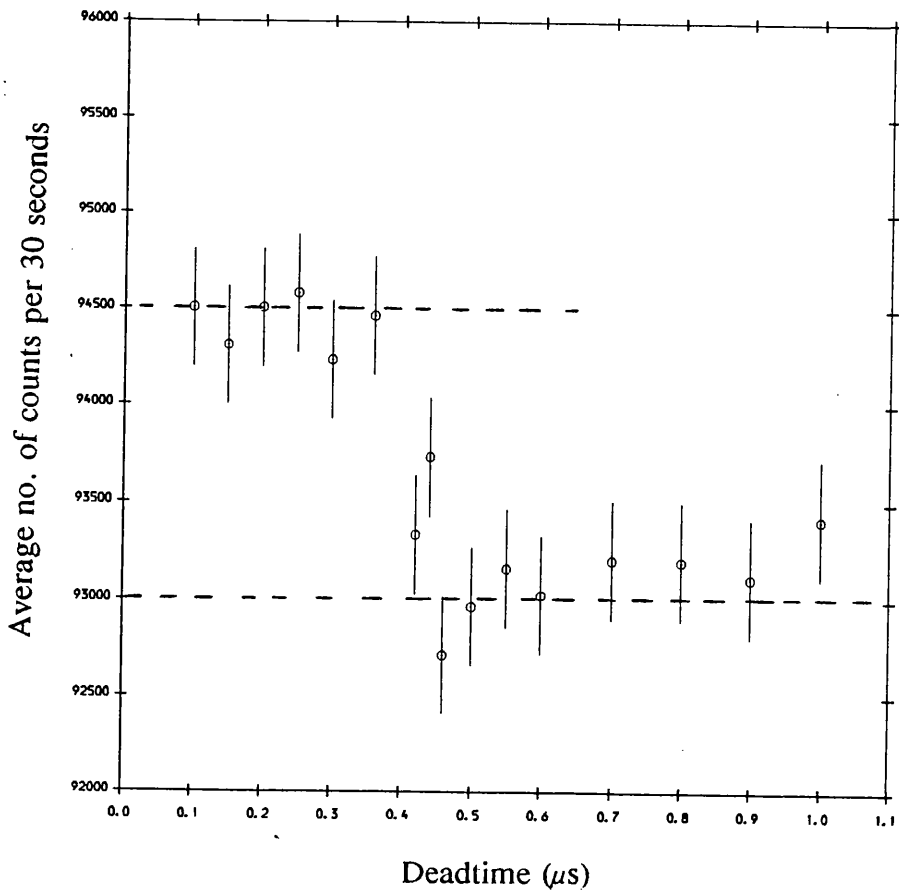


Figure 2.27d: Variation of the count rate at the discriminator output with deadtime using A-CH₄ (10%) when the anode voltage was set at 1.900 kV.

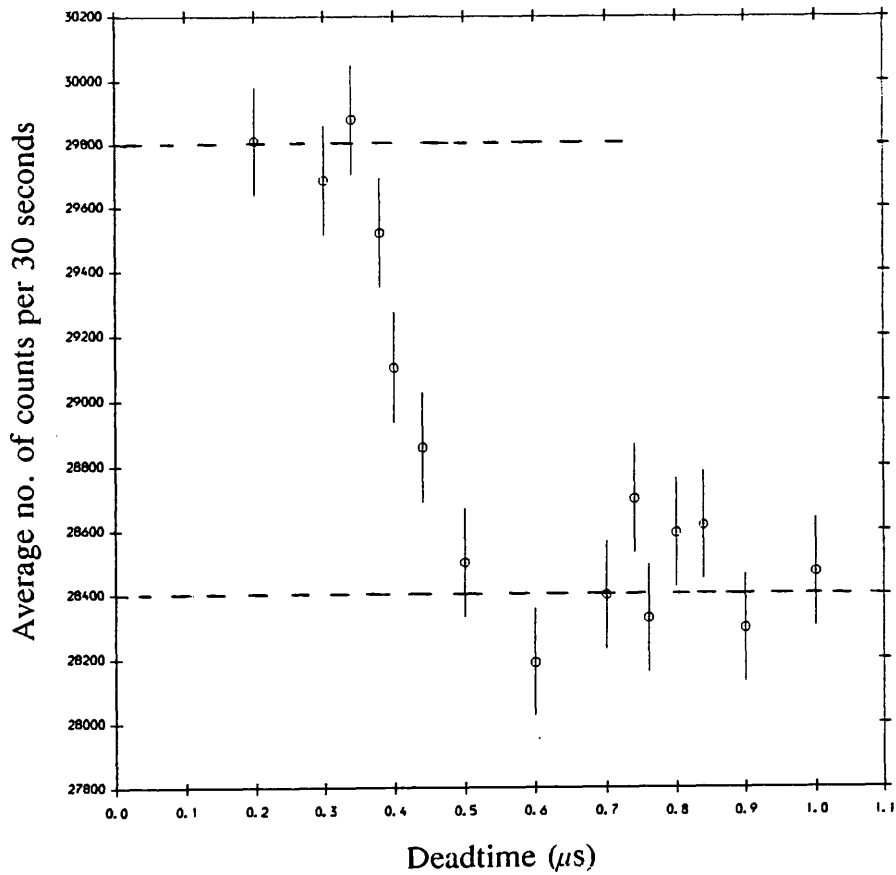


Figure 2.27e : Variation of the count rate at the discriminator output with deadtime using A-CH₄ (10%) when the anode voltage was set at 1.950 kV.

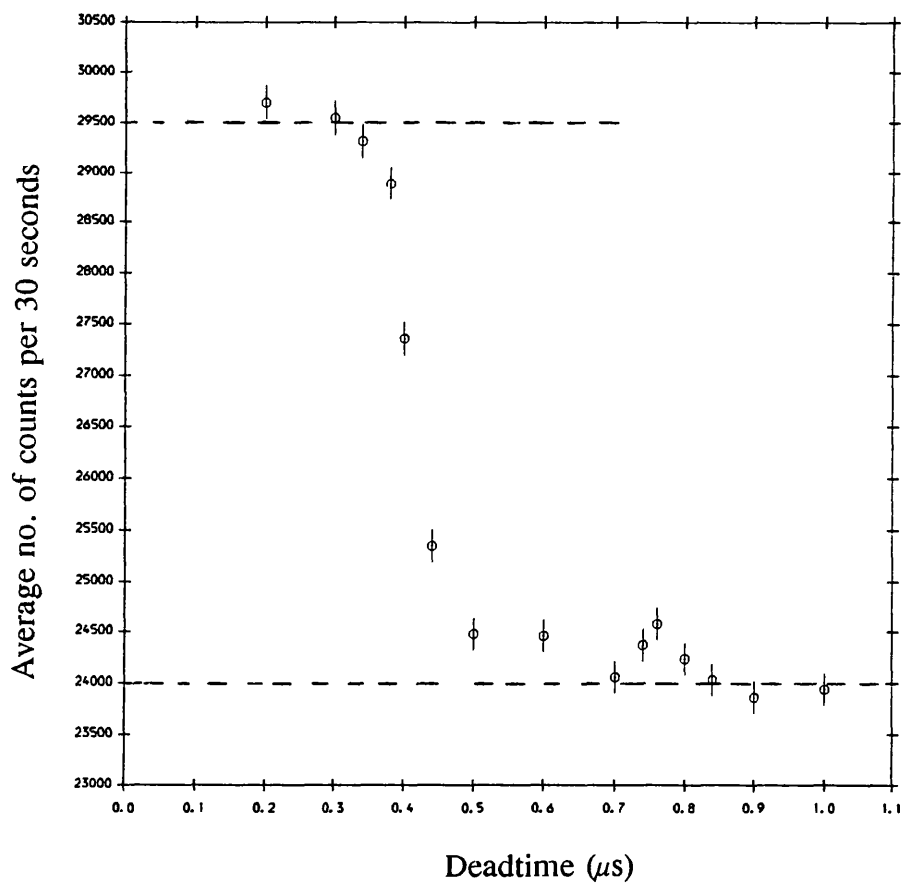


Figure 2.27f : Variation of the count rate at the discriminator output with deadtime using A-CH₄ (10%) when the anode voltage was set at 2.000 kV.

secondary electrons, γ , at this anode voltage is therefore zero i.e. no secondary processes exist in A-CH₄(10%) up to 1.75 kV. Fractional decreases in count rates with an increasing deadtime at 0.4 μ s were observed at 1.80, 1.85, 1.90, 1.95 and 2.00 kV (see figures 2.27b-2.27f). In all cases a sharp reduction in the number of counts at 0.4 μ s was observed due to discrimination of secondary signals. A small count rate reduction at 0.8 μ s was also observed at 2.00 kV due to the discrimination of tertiary signals. γ values were deduced from these fractional changes (see section 2.4). Table 2.4 shows the variation of $N_o \gamma n_p$, N_o and γ at a number of different anode voltages. For a given anode voltage N_o was obtained from the n_c -deadtime plot and n_p was obtained using the Diethorn formula (1956). Figure 2.28 shows the average charge gains obtained by single electron response using A-CH₄(10%) and A-CH₄(50%). The solid lines indicate the variation n_p with anode voltage for A-CH₄(10%) and A-CH₄(50%) using the Diethorn formula.

The γ parameter using A-CH₄(10%) increased as the anode voltage was raised above 1.75 kV (see table 2.4). This behaviour can be explained in terms of an increase in UV light intensity from electron avalanching as charge gains were increased (Romero et al. (1980); Siegmund (1981)). At higher charge gains, therefore, more secondary electrons were produced by the photoelectric effect at cathode walls. Raether (1964) has estimated γ values for argon-methane counter gas mixtures to be in the 10^{-7} to 10^{-9} range for charge gains between 10^7 to 10^4 . Byrne et al. (1970), however, have measured γ using A-CH₄(10%) at 600 mmHg as 6.7×10^{-7} and 55.3×10^{-7} at charge gains of 7.1×10^4 and 2.4×10^5 , respectively. The present values of γ at a charge gain range 10^4 - 10^5 , are an order of magnitude lower than those obtained by Byrne et al. (1970) (see table 2.4).

It would be intuitive to associate the peaked pulse height distribution at higher charge gains with the onset of secondary and tertiary processes. It was found, however, that even in the absence of secondary processes, a peaked pulse height distribution was retained. This was demonstrated with the experimental arrangement shown in figure 2.12. Figures 2.29 and 2.30 show the integral pulse height spectra from UV excitations at 1.95 kV and 2.00 kV, respectively, using A-CH₄(10%). The upper curves represent the cases where the secondary and tertiary as well as proportional signals were recorded. The lower curves represent the cases where the effects of secondary processes were suppressed by using a 10 μ s deadtime. The peaked pulse height distribution in the absence of secondary and tertiary processes is attributed solely to the position dependence of Townsend's first ionisation coefficient. Through the examination of the time

Anode voltage (kV)	n_{av}	n_p	$(N_o \gamma n_p)$	N_o	γ
1.75	$4.90 \cdot 10^4$	$4.38 \cdot 10^4$	0	30700	0.0
1.80	$9.77 \cdot 10^4$	$7.36 \cdot 10^4$	50	44975	$1.5 \cdot 10^{-8}$
1.85	$1.71 \cdot 10^5$	$1.24 \cdot 10^5$	300	52000	$4.7 \cdot 10^{-8}$
1.90	$4.13 \cdot 10^5$	$2.12 \cdot 10^5$	1500	93000	$7.6 \cdot 10^{-8}$
1.95	$2.87 \cdot 10^6$	$3.63 \cdot 10^5$	1400	28400	$1.4 \cdot 10^{-7}$
2.00	$3.20 \cdot 10^7$	$6.24 \cdot 10^5$	5500	24000	$3.7 \cdot 10^{-7}$

Table 2.4 : The γ parameter at a number of different anode voltages using A-CH₄(10%).

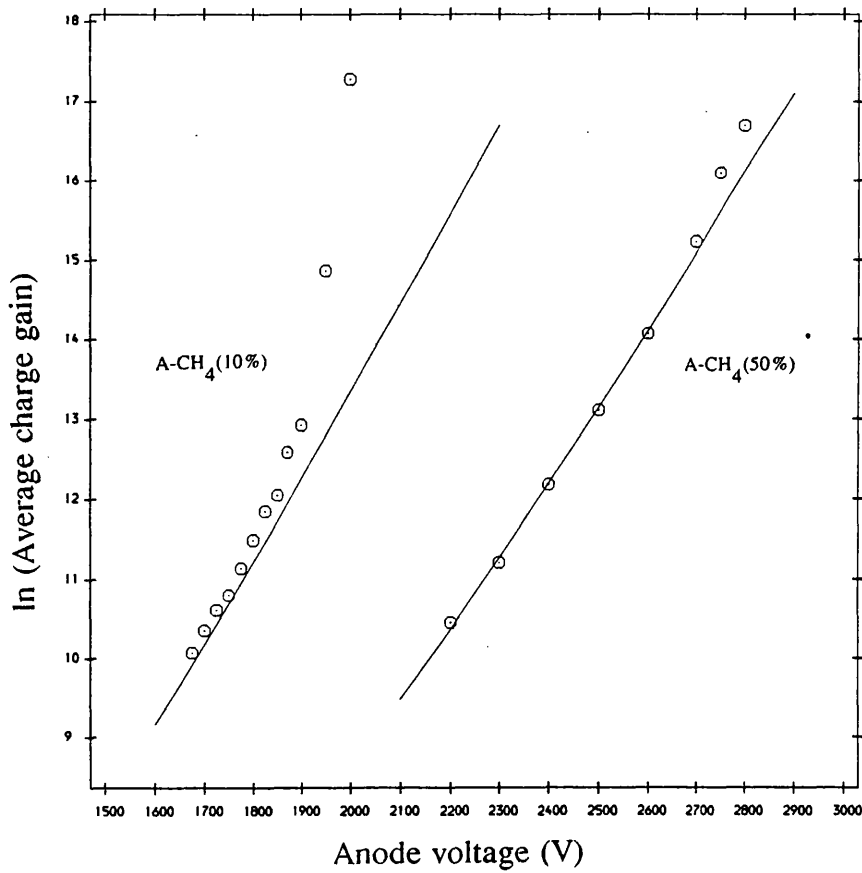


Figure 2.28 : The variation of the average charge gain, obtained by UV, with anode voltage using A-CH₄ (10%) and A-CH₄ (50%). The solid lines indicate theoretical charge gains calculated using Diethorn formula (1956).

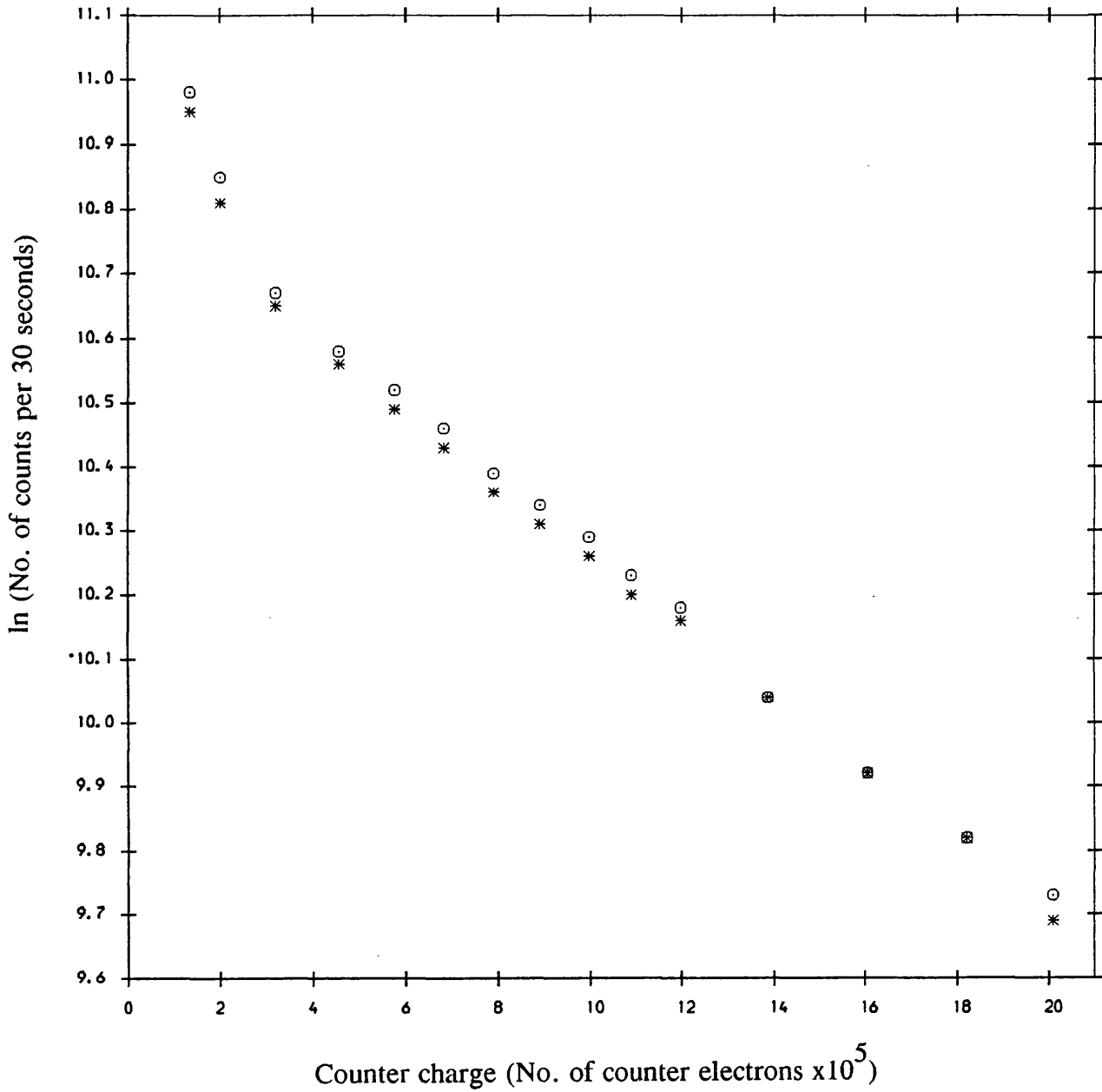


Figure 2.29 : Single electron integral pulse height spectra using A-CH₄(10%) when the anode voltage was set at 1.950 kV. The upper curve represents the pulse height distribution in presence of cathode secondaries (deadtime equals 0.1 μ s) and the lower curve in the absence of cathode secondaries (deadtime equals 10 μ s).

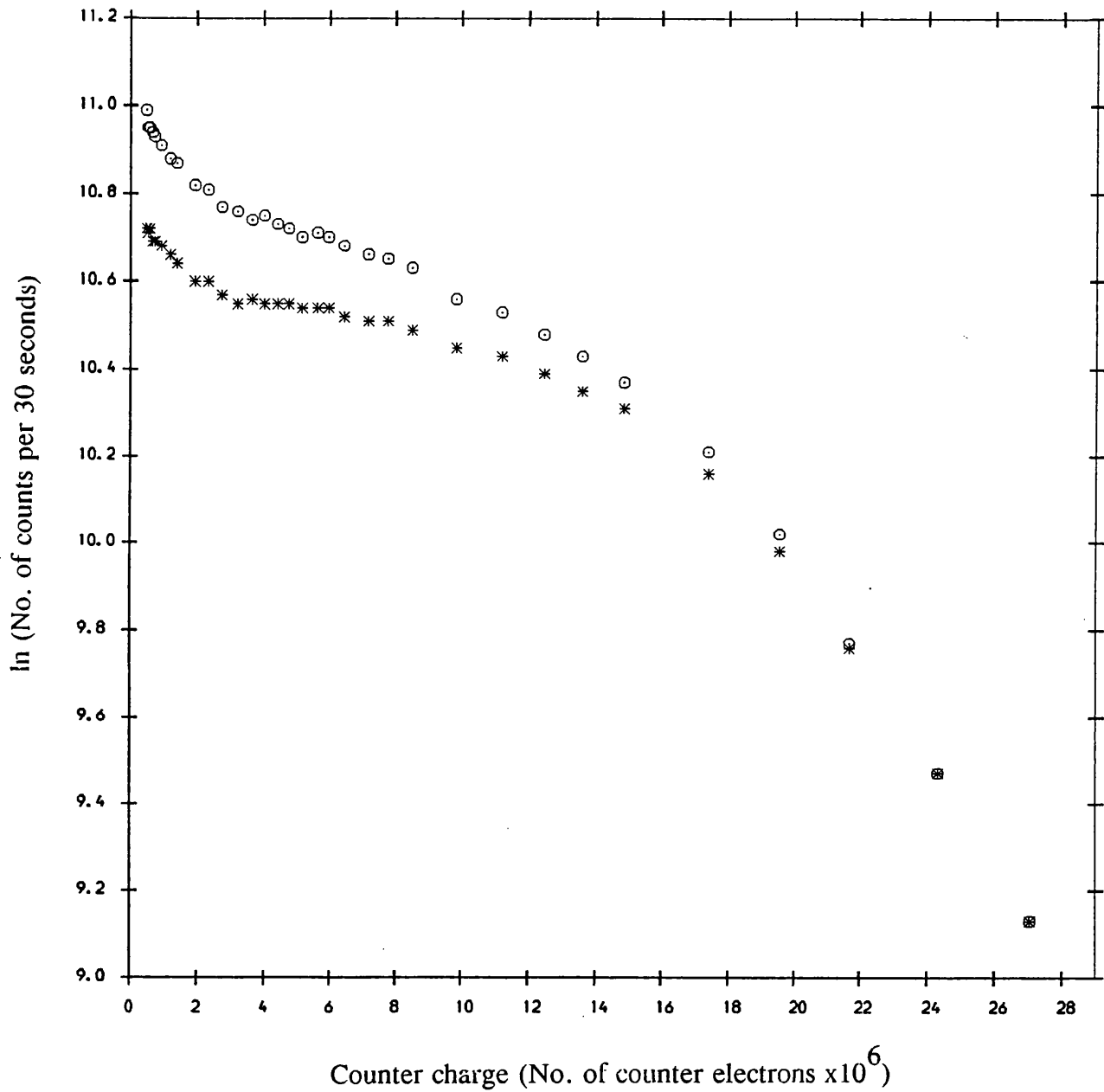


Figure 2.30 : Single electron integral pulse height spectra using A-CH₄(10%) when the anode voltage was set at 2.000 kV. The upper curve represents the pulse height distribution in presence of cathode secondaries (deadtime equals 0.1 μs) and the lower curve in the absence of cathode secondaries (deadtime equals 10 μs).

structure of signals from the proportional counter, therefore, it was possible to distinguish between the peaked pulse height distribution due to secondary and tertiary events and due to a position dependence of Townsend's first ionisation coefficient.

A peaked single electron response would be preferable to a simple exponential spectrum at higher charge gains in electron counting investigations provided secondary processes were absent. A peaked spectrum would lead to a smaller number of signals being lost below the discriminator threshold level of the electron counting electronics. Unfortunately, it has been demonstrated above that the peaked single electron pulse height spectra at higher charge gains is also accompanied by the onset of secondary processes. This is also in agreement with the results shown by figure 2.19 where the charge gain increases slightly faster than exponentially as anode voltage is raised above 1.75 kV in A-CH₄(10%). For the electron counting experiments, therefore, the maximum permissible charge gain using A-CH₄(10%) is 4.90×10^4 (anode voltage at 1.75 kV).

Figures 2.31a-2.31d show the average number of counts at the fast discriminator output in 30 seconds versus deadtimes at a number of different anode voltages using A-CH₄(50%). These results were obtained using the experimental arrangement shown in figure 2.12. It is clear that γ is zero up to an anode voltage of 2.60 kV since no count rate reduction occurred with the increasing deadtime. A fractional decrease in count rate was observed at 2.65 kV (see figure 2.31d). The γ parameter at 2.65 kV using A-CH₄(50%) was calculated in a similar manner to A-CH₄(10%) already discussed above. The fractional decrease in the number of counts at the fast discriminator output equals $N_o \gamma n_p$. This corresponds to approximately 650 secondary events. N_o equals 76500 counts (see figure 2.31d). Furthermore, n_p at 2.65 kV equals to 2.19×10^6 . The γ parameter at 2.65 kV in A-CH₄(50%), therefore equals 3.9×10^{-9} . The maximum permissible charge gain for electron counting experiments when using A-CH₄(50%) was found to be 1.29×10^6 (anode voltage at 2.60 kV).

The A-CH₄(50%) mixture behaved very differently from A-CH₄(10%) above 2.65 kV. Streamers (very fast and large pulses) were observed on the oscilloscope. These were too large to be recorded in the differential pulse height spectra shown by figure 2.23b. A streamer can be regarded as a low resistance conducting plasma. At high charge gains ($M > 10^6$), electron avalanching produces high concentrations of electrons and positive ions. As a result, an internal field is created in the opposite direction to the applied field due to these charges. At even higher charge gains ($M > 10^7$), the internal field becomes so great that it negates the applied field. Consequently, recombination of electrons

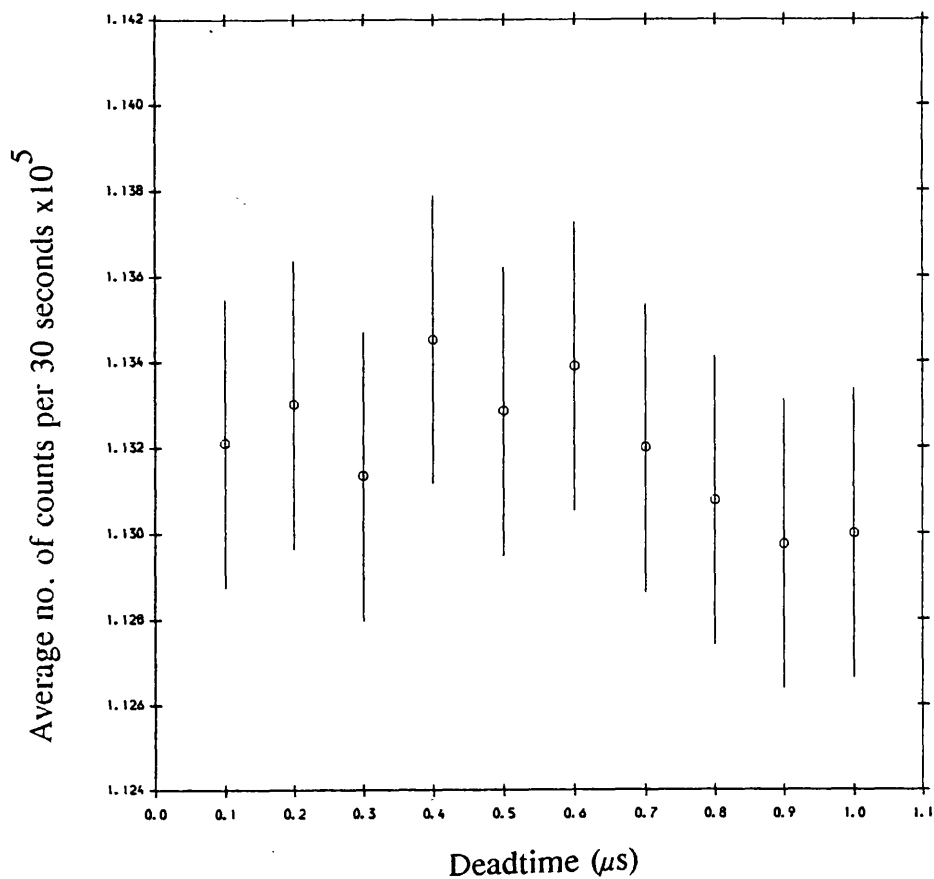


Figure 2.31a : Variation of the count rate at the discriminator output with deadtime using A-CH₄ (50%) when the anode voltage was set at 2.500 kV.

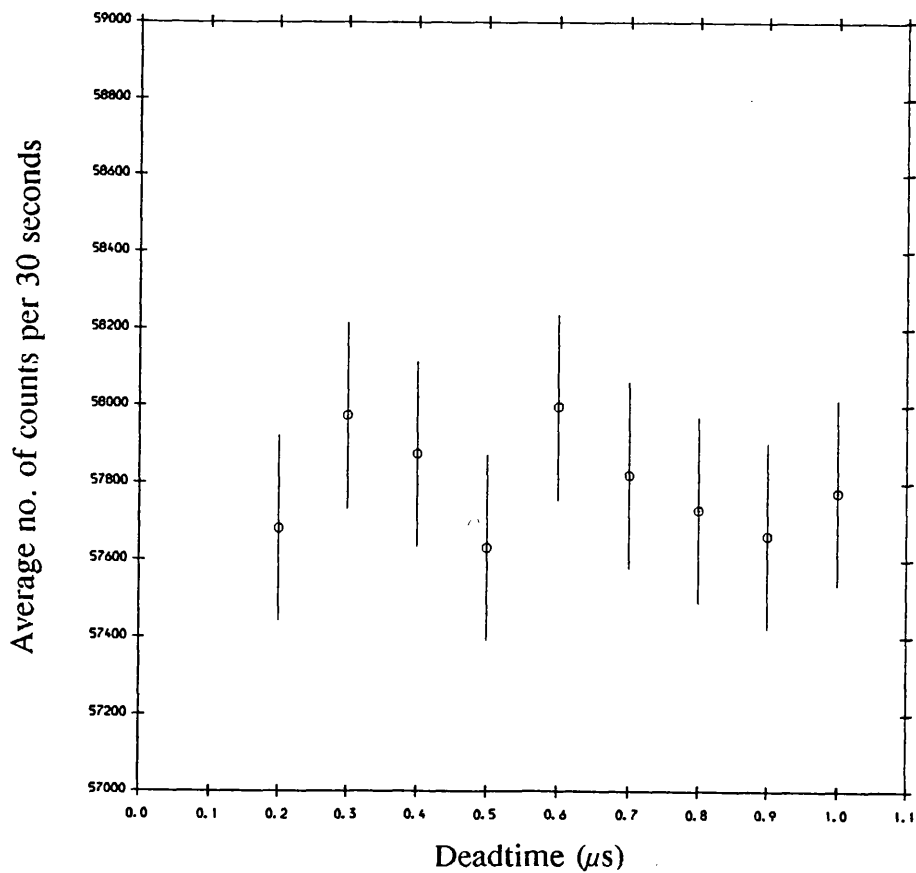


Figure 2.31b : Variation of the count rate at the discriminator output with deadtime using A-CH₄ (50%) when the anode voltage was set at 2.550 kV.

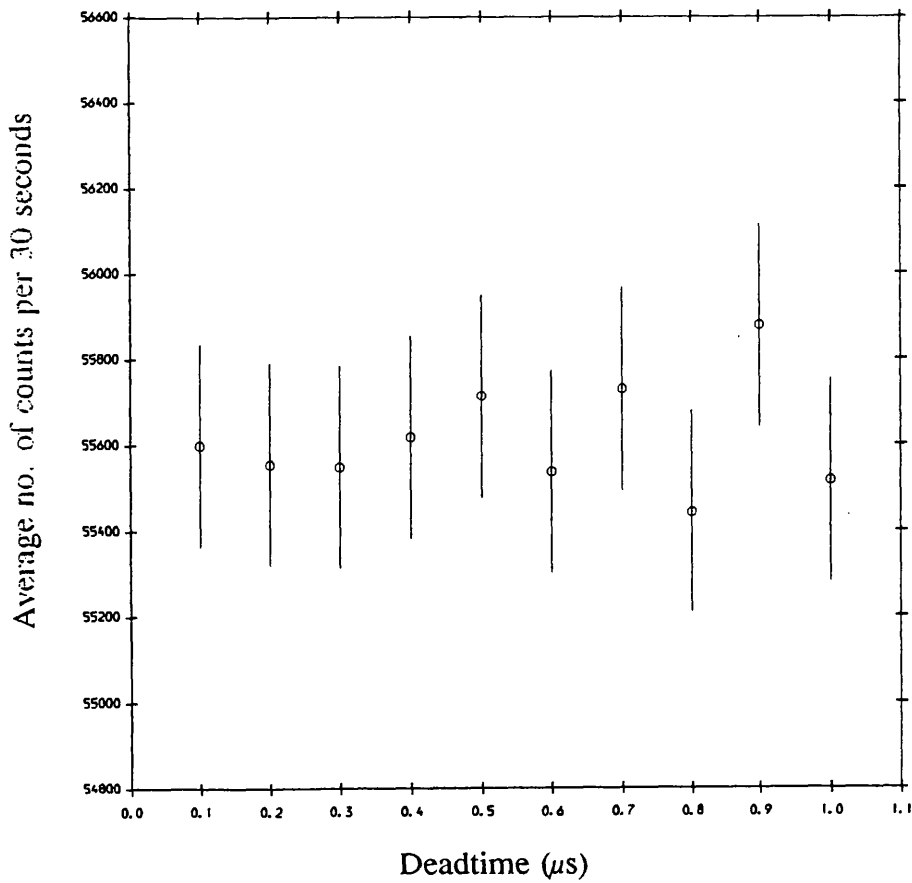


Figure 2.31c : Variation of the count rate at the discriminator output with deadtime using A-CH₄(50%) when the anode voltage was set at 2.600 kV.

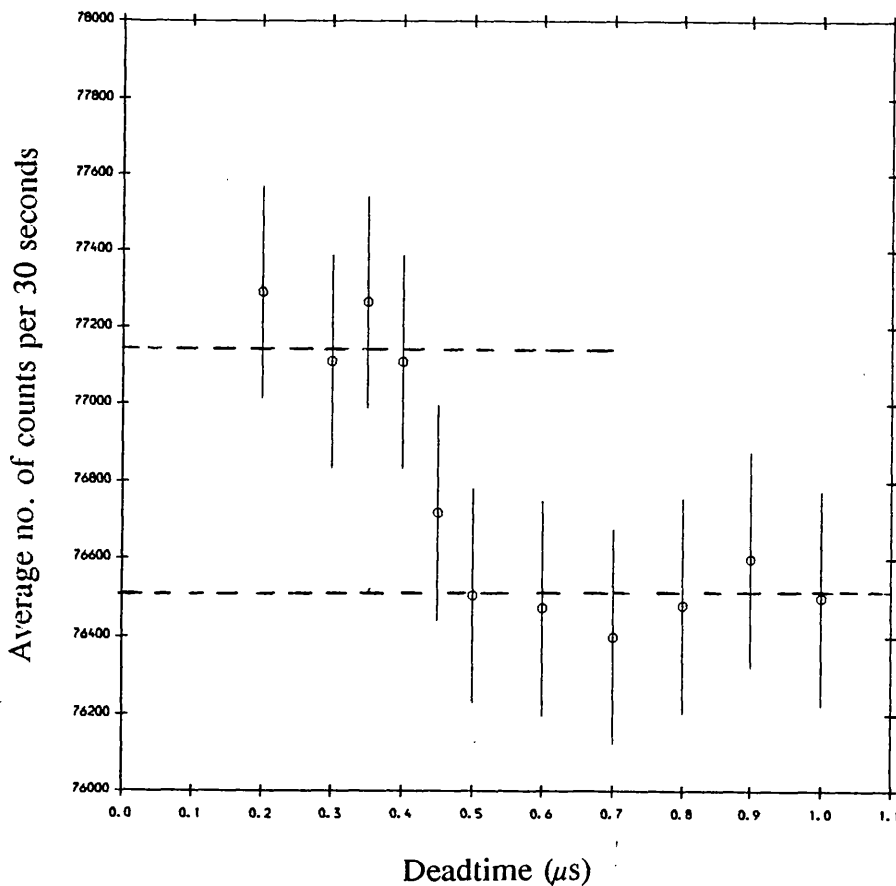


Figure 2.31d : Variation of the count rate at the discriminator output with deadtime using A-CH₄(50%) when the anode voltage was set at 2.650 kV.

and positive ions occurs leading to the emission of UV photons in all directions. The electron-ion pairs produced in front of the head and behind the tail of the initial avalanches, will experience an enhanced field. Further electron multiplication occurs until the above process repeats itself. These processes will continue until the old and the new avalanches merge to form a streamer whose extremities advance towards the anode and the cathode.

The single electron differential pulse height spectra for A-CH₄(50%)-N₂(2.5%-10%) mixtures at a number of different anode voltages are shown in figures 2.32a-2.32f. Figure 2.33 shows the variation of the average charge gain with anode voltage for A-CH₄(50%)-N₂(2.5%-10%). Table 2.5 compares the average charge gains for these counter gas mixtures for a number of different anode voltages. These mixtures behaved in a similar manner to A-CH₄(50%). This arises due to the fact that the collisional cross section for the interaction between N₂ and metastable argon atoms is approximately 20 times smaller than CH₄ or CO₂ (Bourene et al. (1973)). Furthermore, the absorption coefficient of N₂ in the wavelength region around 1300 Å is lower than of CH₄ or CO₂ (Nawrocki et al. (1962)).

Carbon dioxide has a similar interaction cross section with the metastable argon atoms to methane but a smaller UV absorption coefficient in the wavelength region around 1300 Å. The single electron response for A-CO₂(20%) at 1.90, 1.95 and 2.0 kV is shown in figure 2.34a. Figure 2.34b shows the single electron response at 2.05, 2.10 and 2.15 kV. Figure 2.35 shows the variation of charge gain with anode voltage for A-CO₂(20%). The average charge gains associated with each anode are also summarized in table 2.6. Surprisingly, the γ parameter in A-CO₂(20%) remained zero up to a charge gain of 2.61×10^6 (anode voltage at 2.05 kV). This is demonstrated by figure 2.36 which shows the average number of counts per 30 seconds at the fast discriminator output with an increasing deadtime. No fractional change in the count rate was observed at 0.4 μ s or 0.8 μ s which implies an absence of any cathode secondaries at this anode voltage. As stated above, the γ parameter remained zero using A-CH₄(50%) and A-CH₄(10%) at charge gains of 1.29×10^6 (anode voltage at 2.60 kV) and 6.29×10^4 (anode voltage at 1.75 kV), respectively. A-CO₂(20%), therefore, would have been very suitable for electron counting experiments since a higher signal-to-noise ratio would have been possible without the onset of cathode secondaries. Unfortunately, this mixture showed an extremely small mean electron lifetime as discussed in section 2.5 making it very unsuitable for this work.

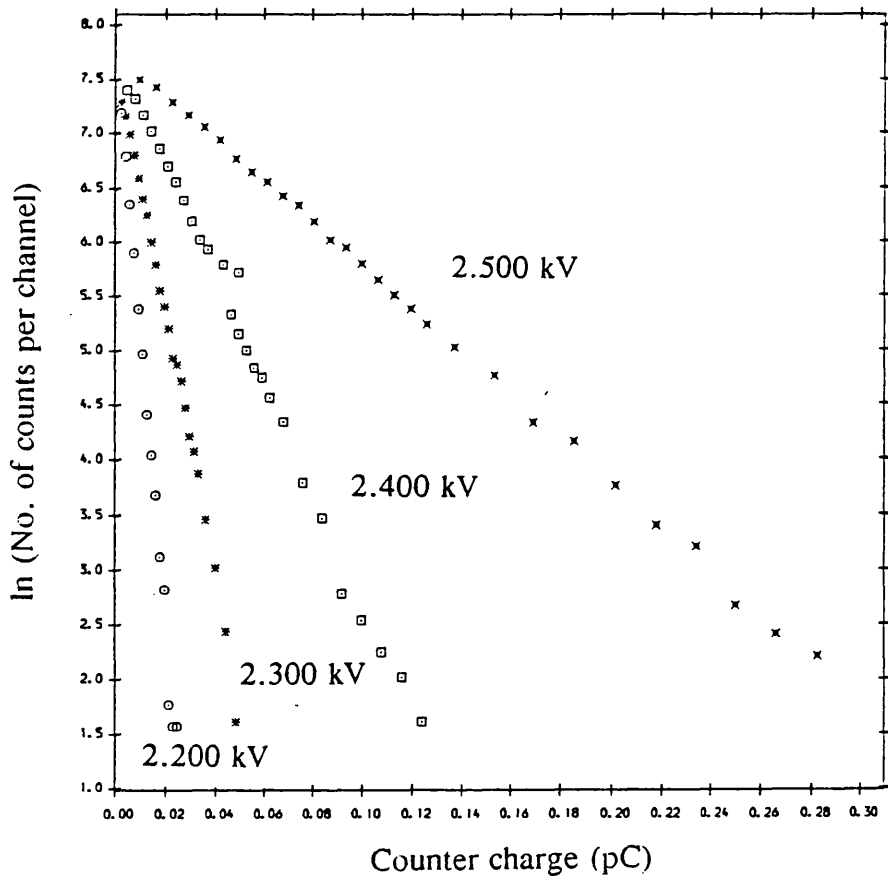


Figure 2.32a : Single electron differential pulse height spectra using A-CH₄(50%)-N₂(2.5 %) at a number of different anode voltages.

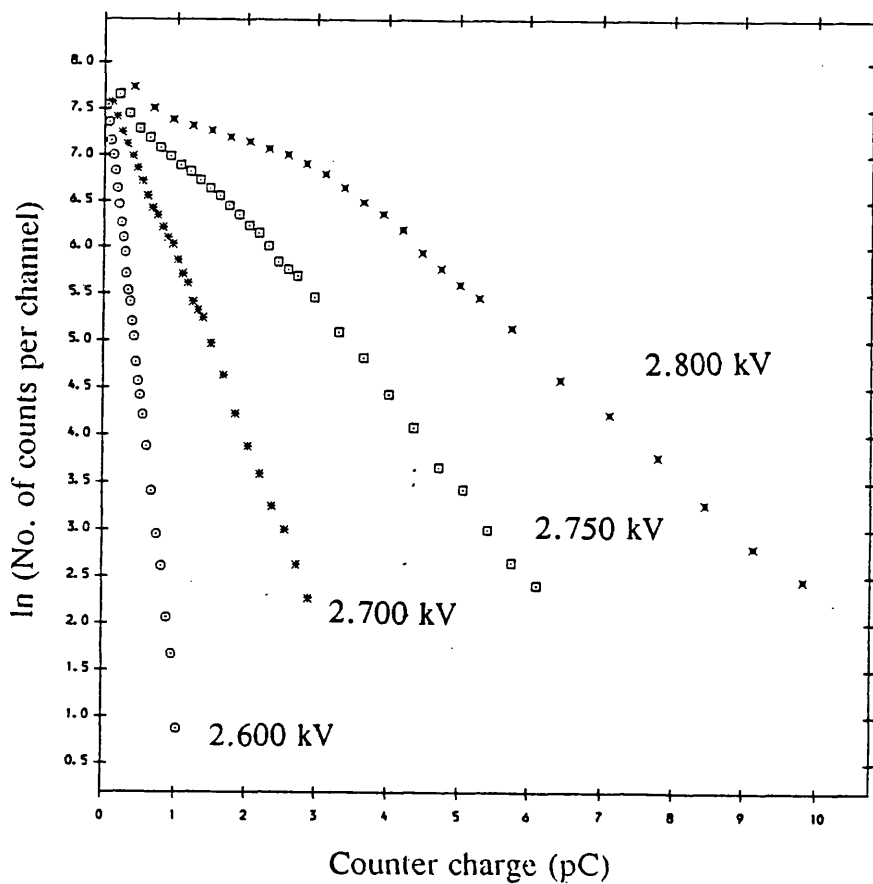


Figure 2.32b : Single electron differential pulse height spectra using A-CH₄(50%)-N₂(2.5%) at a number of different anode voltages.

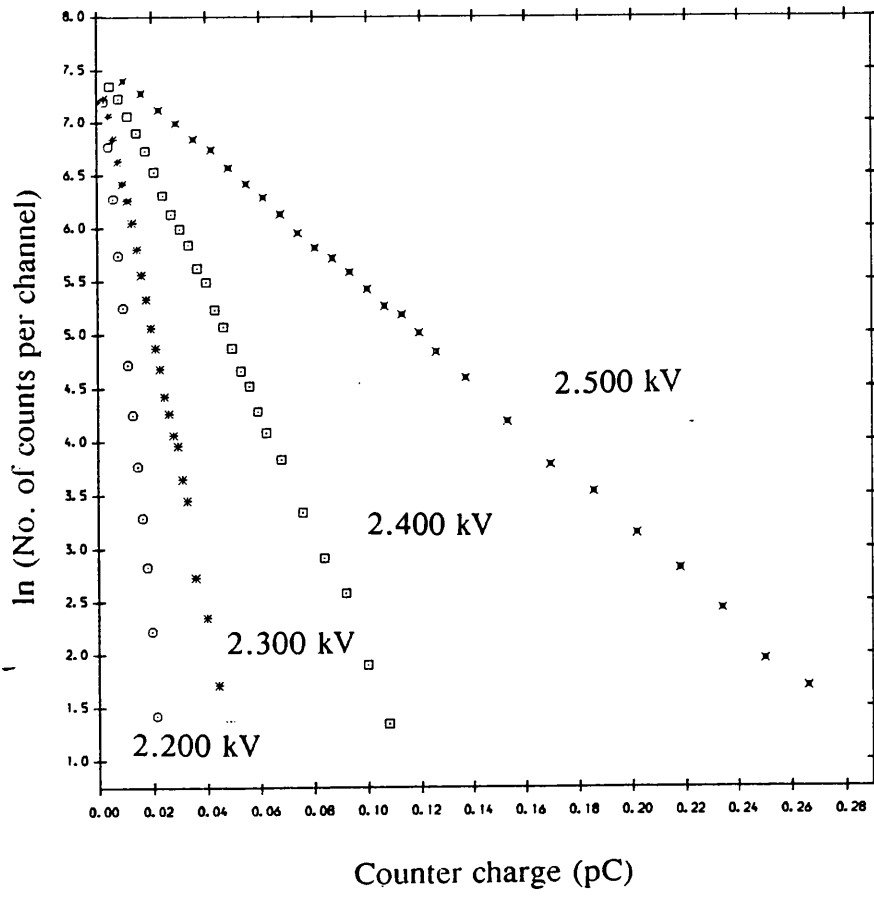


Figure 2.32c : Single electron differential pulse height spectra using $A-CH_4(50\%)-N_2(5.0\%)$ at a number of different anode voltages.

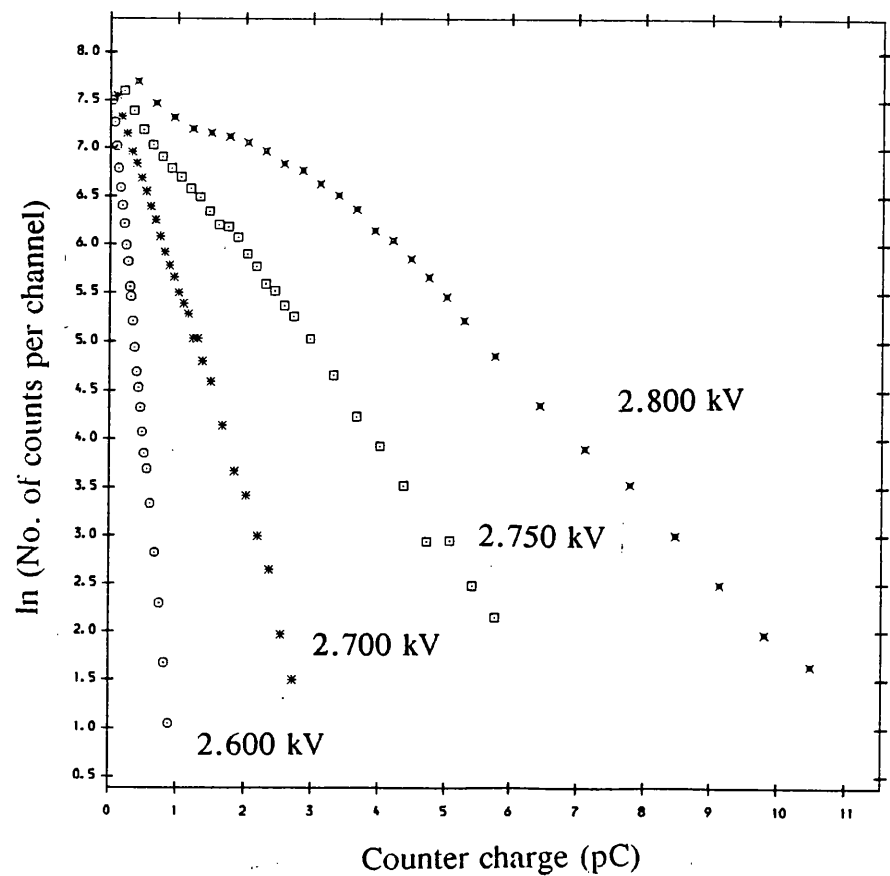


Figure 2.32d : Single electron differential pulse height spectra using $A-CH_4(50\%)-N_2(5.0\%)$ at a number of different anode voltages.

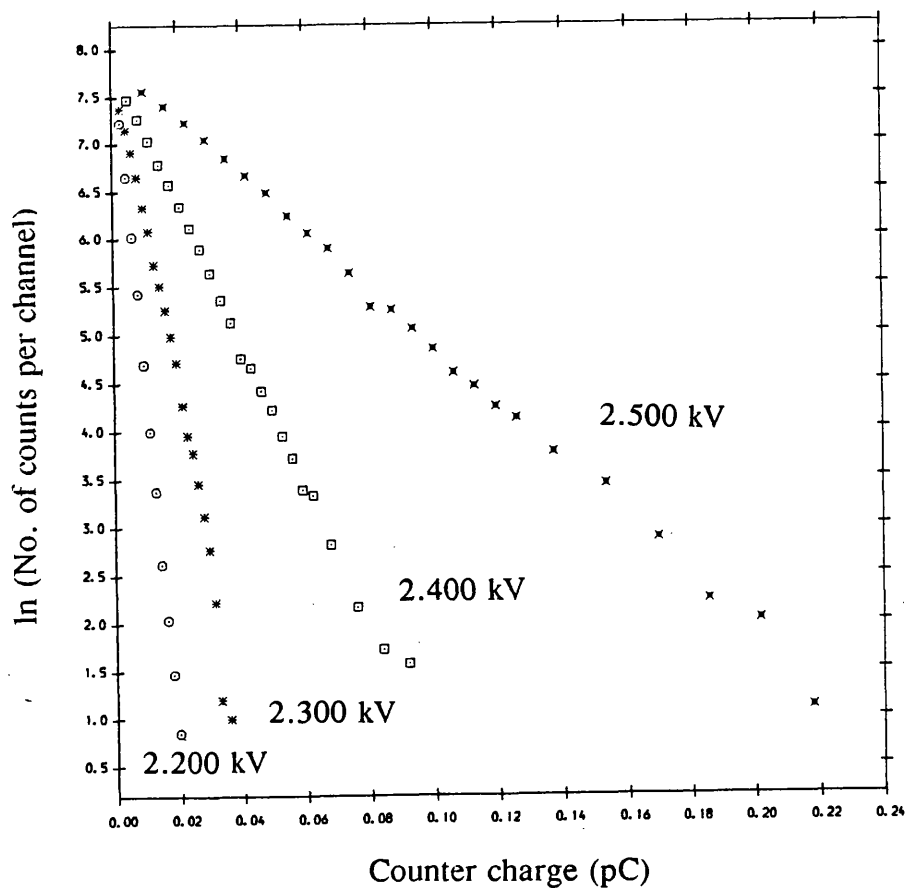


Figure 2.32e : Single electron differential pulse height spectra using A-CH₄(50%)-N₂(10.0%) at a number of different anode voltages.

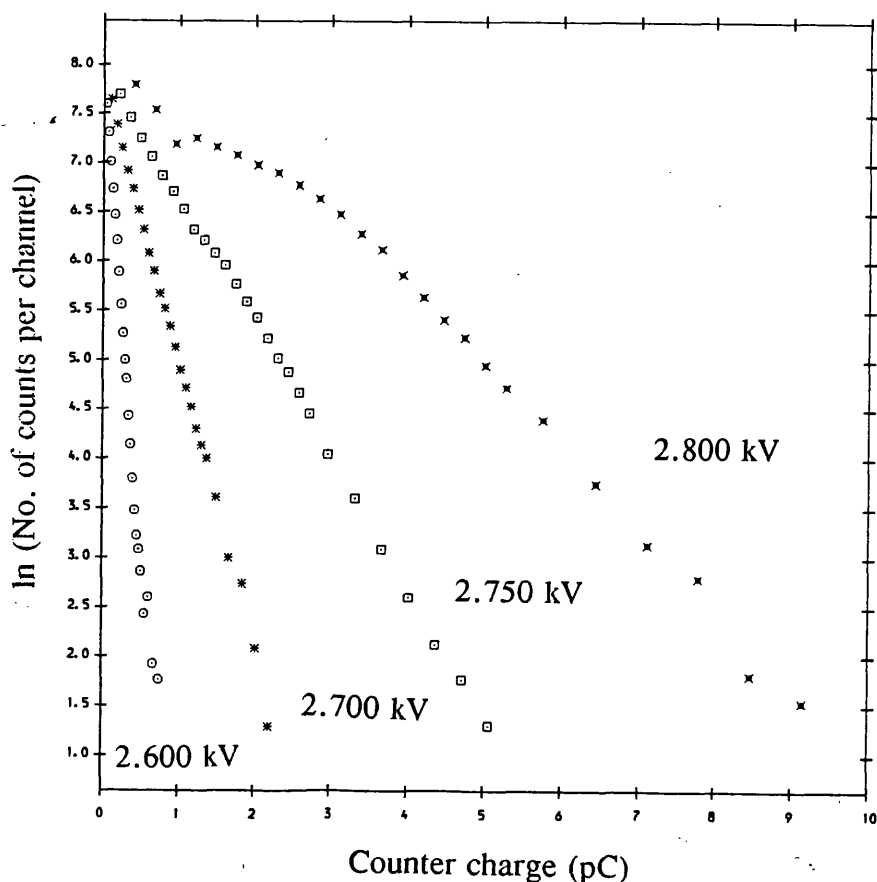


Figure 2.32f : Single electron differential pulse height spectra using A-CH₄(50%)-N₂(10.0%) at a number of different anode voltages.

Anode Voltage (kV)	n_{av} for A-CH ₄ (50%) -N ₂ (2.5%)	n_{av} for A-CH ₄ (50%) -N ₂ (5.0%)	n_{av} for A-CH ₄ (50%) -N ₂ (10%)
2.20	2.31×10^4	2.06×10^4	1.60×10^4
2.30	5.20×10^4	4.72×10^4	3.29×10^4
2.40	1.23×10^5	1.08×10^5	8.67×10^4
2.50	3.14×10^5	2.78×10^5	2.07×10^5
2.60	9.50×10^5	8.31×10^5	6.86×10^5
2.70	3.32×10^6	2.92×10^6	2.16×10^6
2.75	7.12×10^6	6.48×10^6	4.76×10^6
2.80	1.10×10^7	1.02×10^7	8.70×10^6

Table 2.5 : A comparison of the average charge gains between A-CH₄(50%)-N₂(2.5%), A-CH₄(50%)-N₂(5.0%) and A-CH₄(50%)-N₂(10.0%) using differential pulse height analysis.

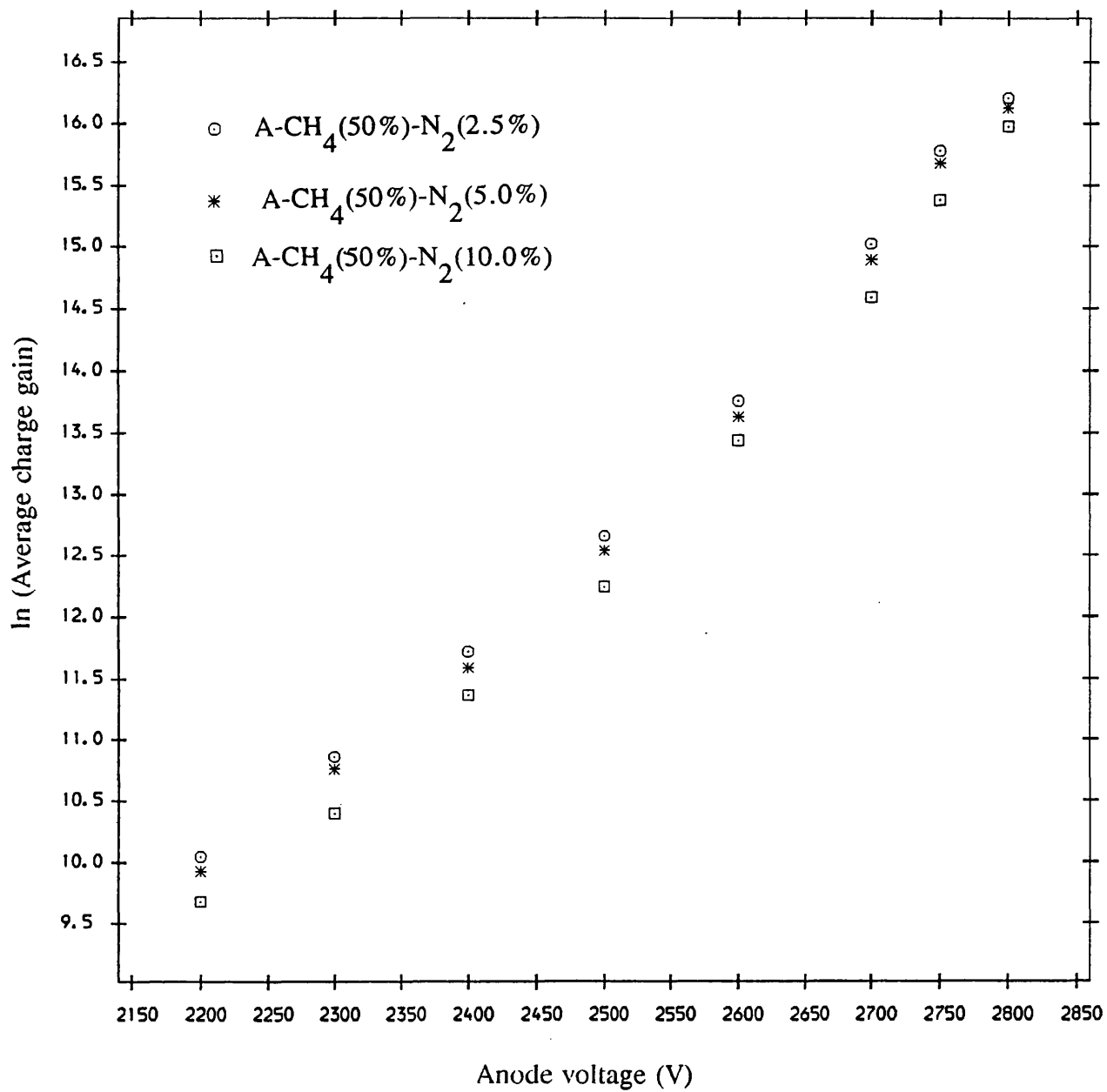


Figure 2.33 : The variation of the average charge gain with anode voltage for A-CH₄(50%)-N₂(2.5% to 10.0%). These curves were obtained using UV.

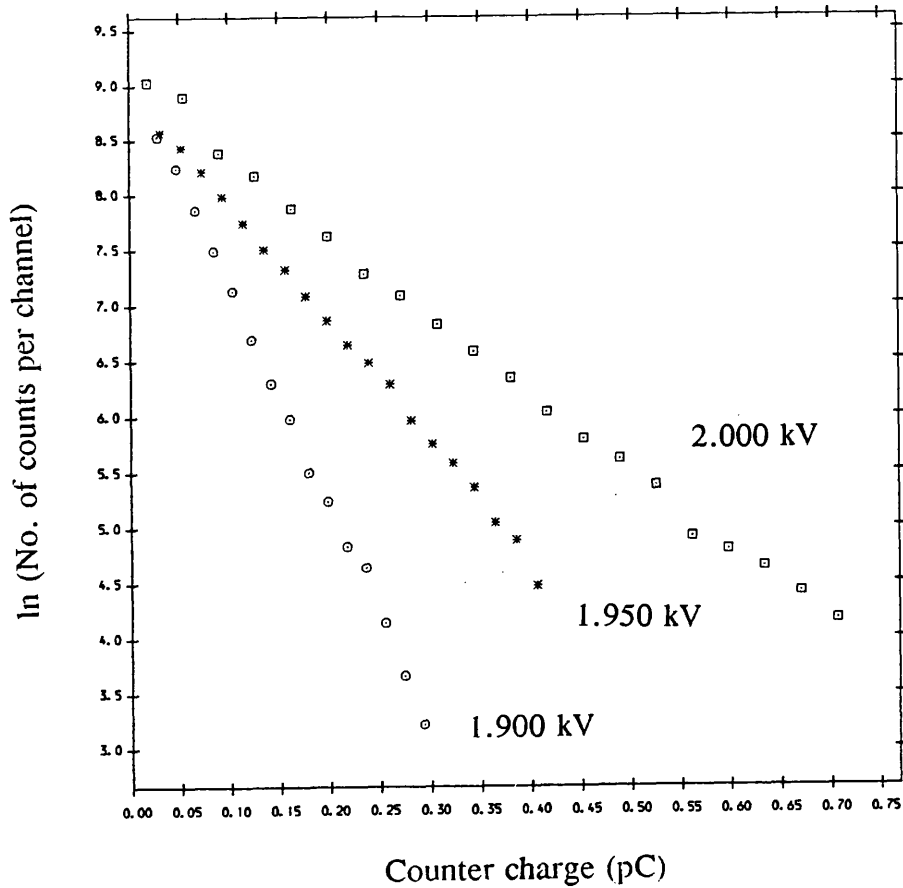


Figure 2.34a : Single electron differential pulse height spectra using A-CO₂ (20%) at a number of different anode voltages.

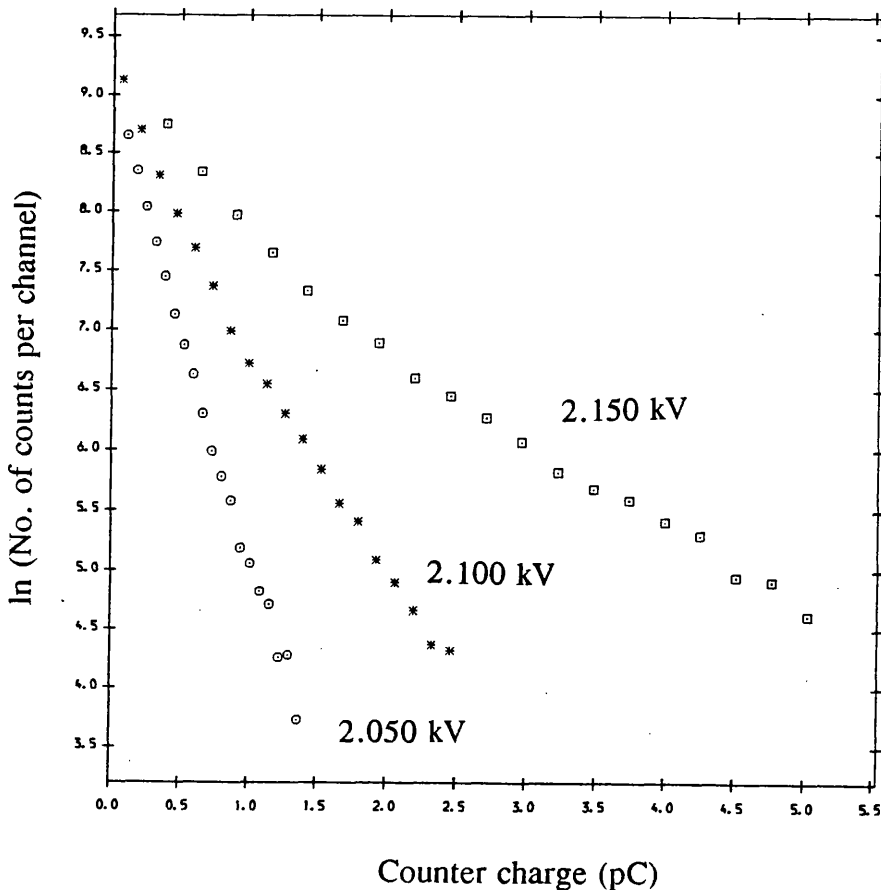


Figure 2.34b : Single electron differential pulse height spectra using A-CO₂ (20%) at a number of different anode voltages.

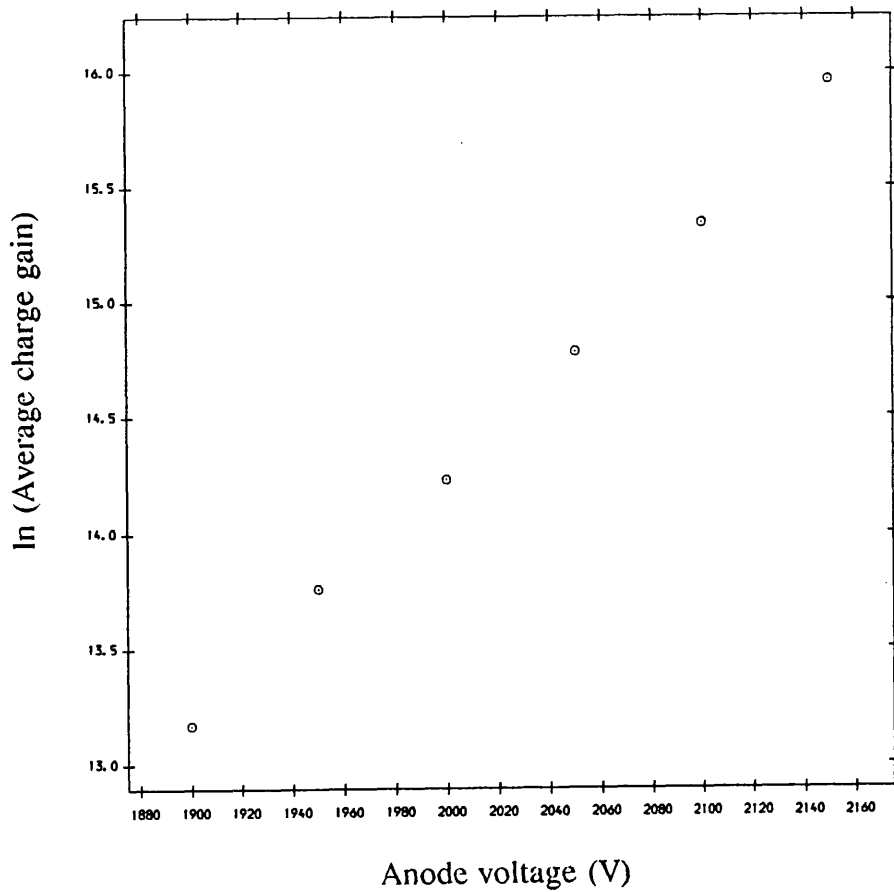


Figure 2.35 : The variation of the average charge gain with anode voltage using A-CO₂(20%). This curve was obtained using UV.

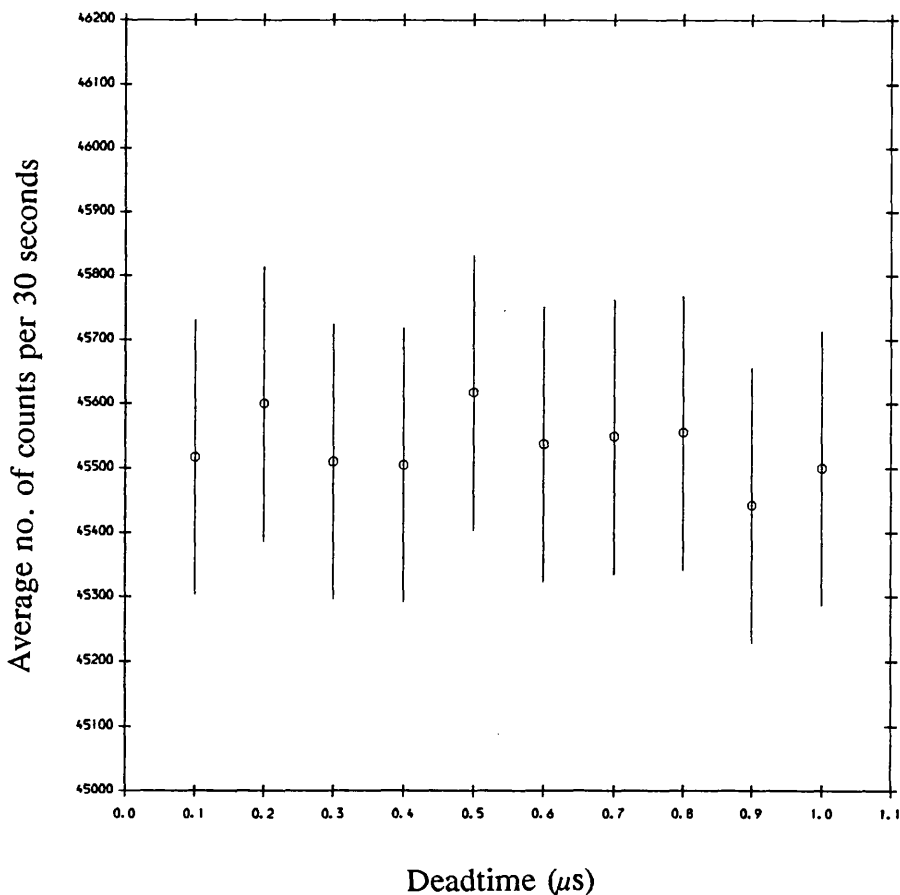


Figure 2.36 : Variation of the count rate at the discriminator output with deadtime using A-CO₂(20%) when the anode voltage was set at 2.05 kV.

Anode Voltage (kV)	Average charge gain in A-CO ₂ (20%) by differential spectra
1.900	5.24 x10 ⁵
1.950	9.42 x10 ⁵
2.000	1.52 x10 ⁶
2.050	2.61 x10 ⁶
2.100	4.61 x10 ⁶
2.150	8.53 x10 ⁶

Table 2.6 : Average charge gains for A-CO₂(20%) using differential pulse height analysis.

Anode voltage (kV)	q _n (no. of electrons)	n _{av}	f _d	S _d
1.700	5.40 x10 ⁴	3.13 x10 ⁴	0.178	4.62
1.725	-	4.05 x10 ⁴	0.264	2.79
1.750	-	4.90 x10 ⁴	0.332	2.01

Table 2.7 : The parameters f_d and S_d for A-CH₄(10%) for a number of different anode voltages.

Anode voltage (kV)	q_n (no. of electrons)	n_{av}	f_d	S_d
2.40	3.75×10^4	1.95×10^5	0.825	0.212
2.45		2.98×10^5	0.882	0.134
2.50	-	4.94×10^5	0.927	0.079
2.55	-	8.02×10^5	0.954	0.048
2.60	7.50×10^4	1.29×10^6	0.944	0.059

Table 2.8 : The parameters f_d and S_d for A-CH₄(50%) for a number of different anode voltages.

2.7 Conclusions

The experimental determinations of the maximum electron noise, q_n , associated with each electron counting electronics have been carried out. The maximum charge gains before the onset of secondary avalanching have also been measured using A-CH₄(10%) and A-CH₄(50%). It is therefore possible to calculate the parameters f_d and S_d (see eqns. 1.23 and 1.24). For example, f_d and S_d using A-CH₄(10%) at 1.75 kV were calculated as follows :

The average charge gain at 1.75 kV using A-CH₄(10%) equals 4.90×10^4 (see table 2.2) and the maximum noise level equals 5.40×10^4 electrons (see table 2.1). Substituting the average charge gain and the maximum noise level values into equation 1.24 gives f_d as 0.332. Substituting f_d into equation 1.23 gives the corresponding S_d which equals 2.01 at 1.75 kV.

Tables 2.7-2.8 show the variation of f_d and S_d for a number of different anode voltages using A-CH₄(10%) and A-CH₄(50%). It is clear from these tables that f_d increases with an increasing charge gain. Ideally f_d should be unity for direct electron counting experiments. A-CH₄(50%) is therefore, more suitable for electron counting since its associated f_d is much higher than that achieved using A-CH₄(10%).

Chapter 3

Determination of electron losses due to capture.

3.1 Introduction

A practical counter must utilise counter gas mixtures with adequately low impurity levels to minimize any electron loss which may occur between the time of their creation as single electrons or primary clusters, their passage through the drift region under the influence of a very weak drift field and their subsequent collection at the anode wire. An accurate knowledge of electron transport coefficients for low energy, non-ionizing electrons forms an essential part of the present work. The three mechanisms of electron loss encountered during the present work have already been described in section 1.11. This chapter is concerned with the experimental determination of the parameters f_a and S_a (see eqns. 1.21 and 1.22). Measurements were made of the electron mobility μ , the characteristic electron energy D_1/μ and the mean electron lifetime against capture τ_a for a number of different counter gas mixtures. The experimental determination of these parameters not only assists towards the evaluation of electron counting efficiency but may also prove useful in providing transport data for calculating electron cross sections for elastic scattering for the various counter gas mixtures used. There is a very limited data available in the literature to date for the gas mixtures used in the present work, particularly for very low E_d/p values. The experimental determination of μ and D_1/μ is described in section 3.2 and of τ_a in section 3.7.

The counter gas mixtures examined were : A-CH₄ (10%), A-CH₄ (50%), A-CH₄ (50%)-N₂ (2.5% to 10%) and A-CO₂ (20%). Time of flight (TOF) experiments were used to determine the parameters μ and D_1/μ . The experimental results were compared with calculations (Mathieson et al. (1979); Mathieson, private communication (1989)).

3.2 Basic theory for μ and D_1/μ measurements

The study of the principles of diffusion of matter has a long history (Townsend (1947) and Huxley and Crompton (1974)). In this section the basic theory of electron transport in gases with and without a drift field will be considered.

In the absence of an applied drift field electrons diffuse in all directions. Let n be the electron density, t be the time and x, y, z be the space coordinates. The rate of electron transfer in a given direction, say x , may be written as :

$$J = -D \frac{dn(x,t)}{dx} \quad 3.1$$

where J is the rate of transfer of electrons per unit area (i.e. electron flux) and D is the transverse diffusion coefficient. The negative sign on the right hand side of equation 3.1 indicates that the electron flow is in the direction of decreasing electron density. From the law of conservation of matter, the change in electron flux with time must be the same as the local decrease of electron flux. This statement may be written as :

$$\frac{dn(x,t)}{dt} = -\frac{dJ(x,t)}{dx} \quad 3.2$$

If we substitute equation 3.1 into equation 3.2 then the following equation is obtained :

$$\frac{dn(x,t)}{dt} = \frac{d}{dx} \left[D \frac{dn(x,t)}{dx} \right] \quad 3.3$$

Equation 3.3 may be rewritten in the following form :

$$\frac{dn(x,t)}{dt} = D \frac{d^2 n(x,t)}{dx^2} \quad 3.4$$

Huxley and Crompton (1974) have shown that the root mean square size of an electron cloud in the x , y and z directions after time t can be written as follows :

$$\sigma_x = \sigma_y = \sigma_z = (2Dt)^{1/2} \quad 3.5$$

In the present work, a drift field was applied to transport electrons from the drift chamber to the proportional chamber. In the presence of a drift field the diffusion motion of electrons was superimposed by drift motion. The drifting electrons experience the sum of the drift field E_d and the leakage field E_o due to the anode potential. Electron diffusion described by equation 3.5 is said to be isotropic i.e. the rate of electron diffusion is the same in x , y and z directions. Electron transport, however, in the presence of a strong drift field ($E_d > 200$ V/cm) has been found to be anisotropic using the counter gases argon, hydrogen, helium and nitrogen (Wagner et al. (1967) and Parker and Lowke (1969)). It was found that the diffusion coefficient D_1 (longitudinal diffusion coefficient) in the direction of electron motion (i.e. z direction) was less than the transverse diffusion coefficient D . For example, when using hydrogen, helium

and nitrogen, D_1 was found to be approximately a factor of 2 lower than D and when using argon D_1 was approximately a factor of 7 lower than D . Siegmund et al. (1983) found similar results using A-CH₄ (5% to 20%) and A-CH₄(5%)-CO₂ (1.25% to 25%). For example, when using A-CH₄(10%), $D_1/D \approx 1$ at weak drift fields ($E_d < 30$ V/cm), at moderately high drift fields ($E_d > 50$ V/cm) $D_1/D \approx 2$ but at very strong drift fields ($E_d > 200$ V/cm) $D_1/D < 1$. Fraser et al. (1986a, 1986b and 1987) have carried out a comprehensive study using Monte Carlo simulation to determine D_1/D for argon, methane, neon, carbon dioxide, xenon and ethane counter gas mixtures. These calculations were consistent with the observed values of D_1/D including those of Siegmund et al. (1983) and Skelding (1984).

The transport coefficients can be expressed in terms of the electron energy distribution. For a uniform drift field, the electron velocity and transverse diffusion coefficient are given by following equations (Parker and Lowke (1969), Huxley and Crompton (1974)) :

$$w = -8\pi e/3m^2 E_d/N \int \epsilon dF(\epsilon)/q(\epsilon) d\epsilon \quad 3.6$$

$$D = -8\pi/3m^2 N \int \epsilon F(\epsilon) d\epsilon/q(\epsilon) \quad 3.7$$

where e is the electron charge, E_d is the drift field, ϵ is the electron energy, m is the electron mass, N is the number of gas molecules per unit volume, q the elastic cross section for electron-atom/molecule collisions and $F(\epsilon)$ is the electron energy distribution function which can be expressed as follows :

$$F(\epsilon) = C(\epsilon)^{1/2} \exp[\int -3\lambda(\epsilon)\epsilon d\epsilon / (eE_d\lambda_e(\epsilon))^2 + 3\lambda(\epsilon)\epsilon kT] \quad 3.8$$

where C is a normalization constant, ϵ is the electron energy, E_d is the drift field, λ_e is electron mean free path during elastic collisions with atoms or molecules, k is Boltzmann's constant, T is the absolute temperature and $\lambda(\epsilon)$ is the mean fractional energy loss per collision. In the absence of a drift field the first term in the denominator on the right hand side of equation 3.8 vanishes so that only the diffusion term remains. Consequently, the electron energy distribution becomes Maxwellian. The mean fractional loss for those gases with no rotational or vibrational cross sections (such as argon), is given by the following equation :

$$\lambda(\epsilon) = 2m/M_e \quad 3.9$$

where m and M_e are electron mass and atomic mass of counter gas atoms, respectively.

Theoretical analysis (Lowke and Parker (1969)) has attributed the reduction of D_1 at higher drift fields due to an increase in collision frequency with energy. Thus, in the drift field direction the electron mobility of the leading edge of the electron swarm is reduced due to higher kinetic energy and collision frequency. Conversely, the electron mobility of the trailing edge is enhanced. At weak drift fields, the electron energy distribution remains Maxwellian thus D_1 equals D . At higher drift fields, in addition to electron density gradients due to diffusion the electron density gradient due to drift modifies the electron energy distribution. In order to derive an equation for D_1 similar to equation 3.7 for D , the effects of electron density gradients must be allowed for when calculating $F(\epsilon)$.

Equations 3.10-3.14 describe the behaviour of electrons under the influence of a drift field (Huxley and Crompton (1974)). Assuming the drift field was applied in the z direction, the root mean square radius of an electron cloud after undergoing diffusion and drift for a drift time t_d in x and y directions can be written as follows :

$$\sigma_x = \sigma_y = (2Dt_d)^{1/2} \quad 3.10$$

$$= [2(D/\mu)d/(E_d + E_o)]^{1/2} \quad 3.11$$

where D is the transverse diffusion coefficient, t_d is the average drift time, μ is the electron mobility, d is the drift distance, E_d is the drift field and E_o is the leakage field due to the anode potential.

Similarly, in the direction of the drift field (i.e. z direction) the root mean square radius of an electron cloud after a drift time t_d can be written as :

$$\sigma_z = [\{2(D_1/\mu)d/(E_d + E_o)\}^{1/2} + \{wt_d\}^2]^{1/2} \quad 3.12$$

where D_1 is the longitudinal diffusion coefficient and w is the electron drift velocity. The r.m.s width of the arrival time spectrum can be written as follows :

$$\tau = [\{2(D_1/\mu)d\}^{1/2}/\mu(E_d + E_o)^{3/2}] \quad 3.13$$

The electron drift velocity can be written as follows :

$$w = \mu(E_d + E_o) = d/t_d(1-\beta) \quad 3.14$$

where β is the ratio D_1/wd , which equals $(D_1/\mu)/(E_d + E_o)d$.

Equations 3.10 and 3.14 are used to determine electron mobility and electron characteristic energy. These equations are only accurate if the following assumptions are fulfilled :

- 1) There is no secondary ionization caused by drifting electrons.
- 2) There is no attachment of drifting electrons to electronegative impurities such as oxygen.
- 3) The initial electron distribution must be approximated by a delta function i.e. the half-width at time $t=0$ must be negligible when compared with the half-width at $t = t_d$.
- 4) The broadening of electron distribution due to fluctuations, caused by the TOF electronics, is negligible.
- 5) There must be random sampling of the electron distribution by the detection system i.e. each electron arriving at the detector must have an equal probability of being recorded. Non-random sampling occurs, for example, when electrons in the trailing edge of an electron cloud are not detected due to the deadtime of the detection system.

In practice, the above assumptions may not be fulfilled adequately during TOF experiments. For example, the effects of attachment, electronic fluctuations and initial finite width of electron cloud broaden the arrival time spectrum. The initial finite width of the primary swarm is caused by a finite UV pulse duration. For example, the pulse duration of the present xenon flash tube (EG & G type FX108AU) was quoted by the manufacturers as approximately $0.8 \mu s$. In the present work, this duration is negligible compared to the r.m.s. width of an electron cloud after it has drifted at low fields. For example, the r.m.s. width of an electron cloud in A-CH₄(10%) at 1.4 V/cm after 5 cm drift equals $14.3 \mu s$. Other experimental studies have used alternative methods to produce prompt photoelectrons in the drift chambers. For example, Anderhub et al. (1979) and Becker et al. (1983) have used a pulsed N₂-laser to produce 335 nm UV light of 0.5 ns pulse duration. The purchase of a N₂-laser is very costly. In view of this, Wong (1987) has used cosmic rays to produce prompt photoelectrons in a drift chamber.

The effect of non-random sampling is to narrow as well as to displace

the arrival time spectrum resulting in drift velocity values that are larger and D_1 values that are smaller than the actual values. This effect is known as Poisson distortion (Wagner et al. (1967)). The experimental requirement to reduce Poisson distortion is to ensure that no more than one electron arrives at the detector for every group released at the inner drift window. Let the initial electron distribution at the inner surface of drift window resulting from a UV flash be a Poisson distribution. It is then possible to correlate the fraction of two or more electron events with the ratio of the arrival time count rate to UV flash rate. A Poisson distribution, $P(n)$, can be described by the following equation :

$$P(n) = \frac{(n_{av})^n \exp(-n_{av})}{n!} \quad 3.15$$

where n_{av} is the mean value of the Poisson distribution. Table 3.1 shows the electron number distribution for $n_{av} = 0.2$ (i.e. 1 photoelectron per 5 UV flashes on the average). It can be seen that approximately, 1 in 10 recorded events correspond to 2 or more electrons. Table 3.1 also shows the electron distribution for $n_{av} = 0.1$ (i.e. 1 photoelectron per 10 UV flashes on the average). In this case, approximately, 1 in 20 recorded events correspond to 2 or more electrons. Table 3.1 shows the electron distribution for $n_{av} = 0.01$ (i.e. 1 photoelectron per 100 UV flashes on the average). For $n_{av} = 0.01$ approximately 1 in 100000 recorded events will correspond to 2 or more electrons. Therefore, the Poisson distortion was minimized by keeping the arrival time count rate/UV flash rate ratio as small as possible.

Figure 3.1 shows the Poisson distortion of the arrival time spectrum for a number of different values of n_c which range from 0 to 100 where n_c is the symbol used by Hurst and Parks (1966) to denote the mean value of the ratio of arrival time count rate to UV flash rate. It can be seen from this figure that when $n_c < 0.1$ then the effects of Poisson distortion on w and D_1 become negligible.

3.3 Experimental system

A Time of Flight (TOF) technique (Wagner et al. (1967)) was used to determine the electron mobility and the characteristic electron energy D_1/μ in a number of different counter gas mixtures. The characteristic electron energy can be described in terms of Boltzmann's constant k , absolute temperature T and the electronic charge e as follows :

$$D_1/\mu = (kT/e) \quad 3.16$$

n	P(n) when $n_{av}=0.2$	P(n) when $n_{av}=0.1$	P(n) when $n_{av}=0.01$
0	0.8187	0.9048	0.9901
1	0.1638	0.0905	0.0099
2	0.0160	0.0045	5.0×10^{-5}
3	0.0011	0.0002	1.7×10^{-7}

Table 3.1 : Poisson distribution for different number of photoelectrons per UV flash.

A xenon flash tube (EG & G type FX108AU) provided pulsed UV using a master pulse generator which produced positive 10 μ s. pulses of 10 V amplitude at 500 Hz. The flash tube specification provided by the manufacturer is as follows :

Operating voltage = 0.4-1.6 kV
Energy input per flash = 0.01 Joule
Maximum repetition rate = 0.5 kHz
Pulse duration = 0.8 μ s
Minimum trigger pulse = 2.5 V

Figure 3.2 shows the circuit used to trigger the flash tube. A photodiode (BPX 65) had been installed near the flash tube. Each UV flash triggered the photodiode to produce a negative pulse which was used as the start signal during the TOF experiments. Figure 3.3 shows the circuit used to operate the photodiode. The specification of the photodiode at 25 °C is as follows :

Reverse voltage = 50 V
Forward current = 10 mA
Junction temperature = 125 °C
Power dissipation = 250 mW

The photodiode output was fed into a pulse generator (Marconi instruments Ltd. TF 2010). The pulse generator provided the start signals with a suitable delay before they entered the time to amplitude convertor (TAC)(Ortec 437A). UV photons released electrons from the inner surface of the drift window which drifted towards the anode under the influence of drift field. The anode signals were processed by a charge sensitive preamplifier (Canberra 2001), a single integration and double differentiation shaping amplifier (bipolar mode) (NE 4636) with filter time constants adjusted to 0.45 μ s and by a cross-over detector (NE 4636). The cross-over detector produces a negative pulse coinciding with the zero voltage cross-over point of the bipolar input which is used as a stop signal for the TAC. The TAC output voltage was proportional to the time taken for the electrons released by UV at the drift window to reach the anode. Figure 3.4 shows the relationship between various signals involved in the TOF technique. The TAC output was fed into the MCA (Northern TN 1705). The MCA was calibrated for time using a TAC calibrator. The calibrator for the TAC provided an accurately known time interval. Start and a stop pulse from the

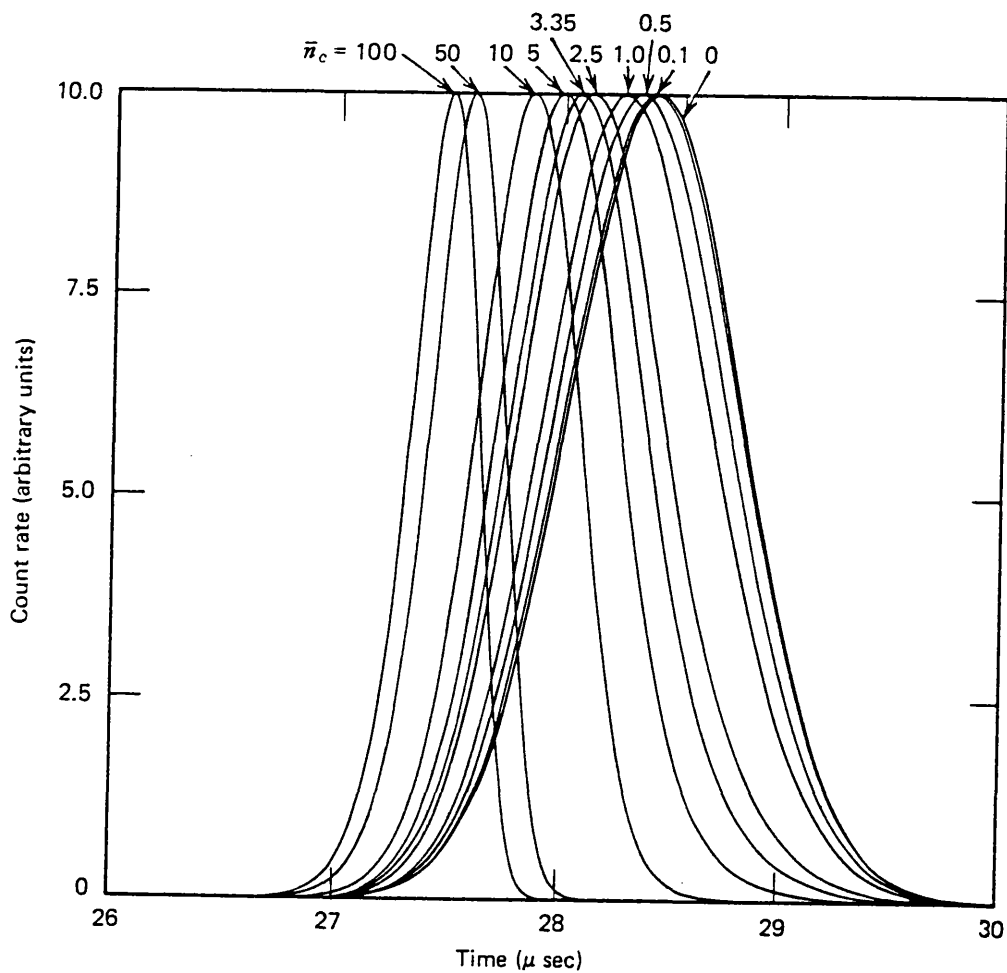


Figure 3.1 : Poisson distortion for a number of different values of n_c (Hurst and Parks (1966)).

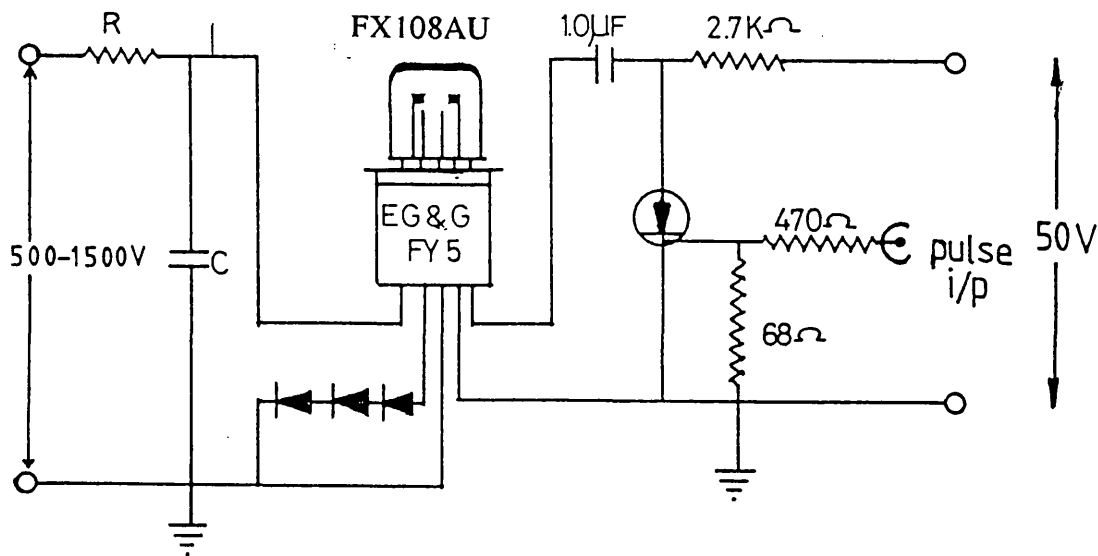


Figure 3.2 : The circuit for the UV flash-tube trigger.

calibrator could be varied from 0.5 μs to 10 μs . Start and stop pulses of known time separation from the calibrator were fed into the TAC. The corresponding channel number at the MCA was recorded. The MCA was, therefore calibrated in terms of number of channels per μs .

The present experimental system to determine the electron mobility and the characteristic electron energy differed in two aspects compared with the Skelding system (1984). For example, Skelding used a Geiger counter instead of a proportional counter. In the present work, the photodiode output was used as the basis of start pulses. Skelding, however, used a master pulse generator to trigger the UV flash tube and a cathode pulse generator. The delayed output of the cathode pulse generator provided the start pulses.

3.4 Experimental procedure

The experimental arrangement used to determine the electron mobility and the characteristic electron energy in various counter gas mixtures is shown in figure 3.5. The counter gas mixtures A-CH₄(10%), A-CH₄(50%), A-CH₄(50%)-N₂(2.5% to 10%) and A-CO₂(20%) gas mixtures were used. The anode voltages for each gas mixture were chosen to give a proportional response (see chapter 2). The anode voltage used for A-CH₄(10%) was 1.75 kV and for A-CH₄(50%), A-CH₄(50%)-N₂(2.5% to 10%) and A-CO₂(20%) was 2.50 kV. The drift distance, d , was measured accurately by a travelling microscope. The shaping amplifier gain was adjusted to a bipolar mode. The TAC gain was adjusted so that 80 μs corresponded to a 10 V output and the MCA was calibrated for time. For example, when the start and stop pulses of the TAC calibrator of 9.0 μs separation were fed into TAC then a sharp line was observed at the 68th channel on the MCA. The MCA gain was normally adjusted to 256 but an offset facility with up to 7 reference points was available to obtain arrival time spectra for large drift times.

The pulsed UV source irradiated the inner surface of the drift window and the arrival time spectrum for a given drift field was accumulated until adequate counting statistics were obtained. The total number of counts for each spectrum was obtained by integrating the number of counts per channel with respect to channel number for the relevant channel number range. An integrating facility was available in the MCA for this purpose. The count rate/UV flash rate was maintained at approximately 0.10 to ensure that no Poisson distortion took place. The drift field was varied, typically from 2 V/cm to 10 V/cm.

The net zero time offset due to the drift time in the proportional chamber and due to various electronics delays was determined by releasing

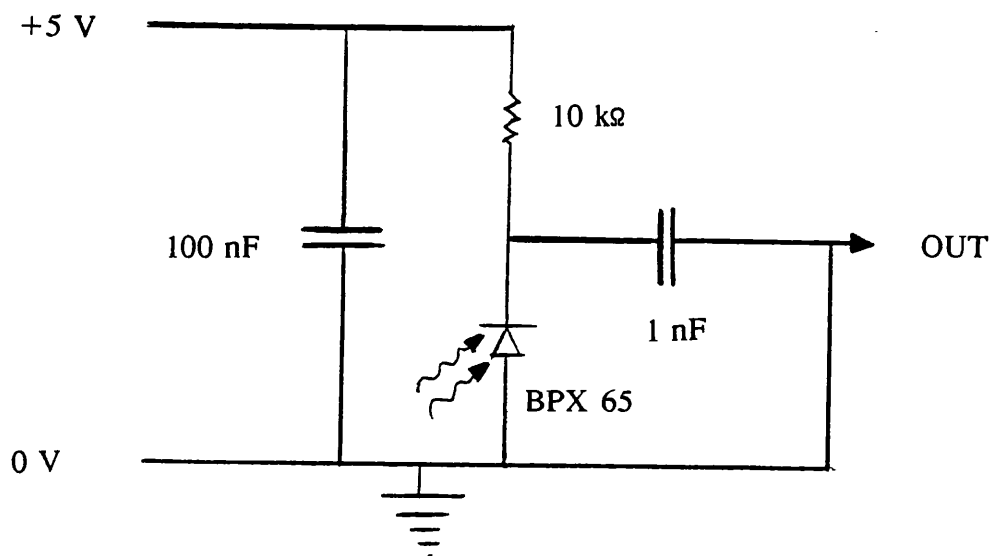


Figure 3.3 : The circuit for the photodiode operation.

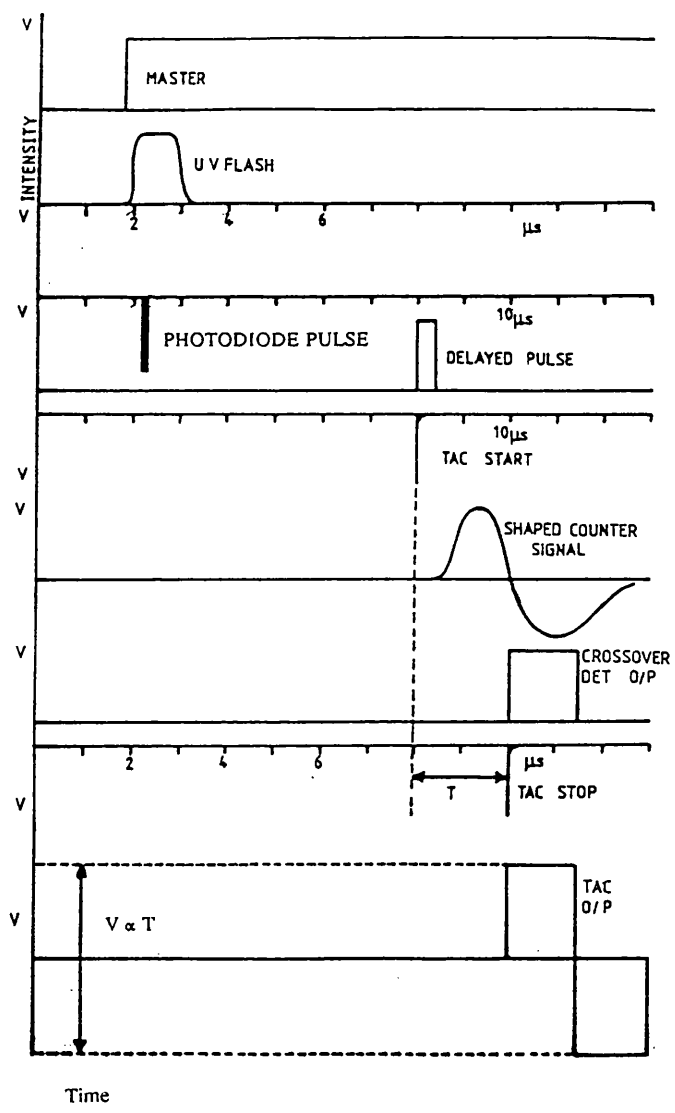


Figure 3.4 : The relationship between different signals involved during TOF experiments.

electrons from the inner surface of a stainless-steel transmission grid. This was achieved by using pulsed UV from the chamber base window to irradiate the grid and recording the arrival time spectrum (see figure 3.5). The peak channel was calibrated for time by TAC thus giving the net zero time offset.

3.5 Experimental μ and D_1/μ measurements : results and discussion

Figure 3.6 show typical arrival time spectra for A-CH₄ (50%) with 5.06 cm drift length, when the drift fields were 3.71 V/cm, 4.20 V/cm, 6.18 V/cm and 12.10 V/cm. It can be seen that the peak channel and the r.m.s. width of arrival time spectrum decrease with increasing drift fields. Each arrival time spectrum was verified as Gaussian distribution using equation 3.18. It is possible to infer electron mobility and characteristic electron energy using a number of these spectra. The peak channel of a distribution corresponds to the sum of the mean electron drift time and the net zero time offset for a given drift field. The electron drift velocity for a given drift field can be calculated from the knowledge of the time calibration of the arrival time spectrum and net zero time offset (see section 3.4). If the drift distance equals 5.06 cm then the mean drift velocity can be expressed by the following expression :

$$w = 5.06 / (t_d - t_z) \quad \text{cm}/\mu\text{s} \quad 3.17$$

where t_d is the drift time and t_z is the net zero time offset. Although the FWHM width of the distribution and hence the r.m.s. width can be estimated graphically, it is more accurate to calculate these quantities. Let n , be the channel number containing k counts. If n_o , is the channel number containing the maximum number of counts k_o then the number of counts is related to the channel number by the following equation :

$$k = k_o \exp[-(n - n_o)^2 / 2\tau^2] \quad 3.18$$

where τ is the r.m.s. width of the arrival time spectrum. The total number of counts, K , for a given distribution can be expressed by the following equation :

$$K = \int k dn \quad 3.19$$

$$= k_o (2\pi\tau^2)^{1/2} \int 1 / (2\pi\tau^2) \exp[-(n - n_o)^2 / 2\tau^2] dn \quad 3.20$$

$$= k_o (2\pi)^{1/2} \tau \quad 3.21$$

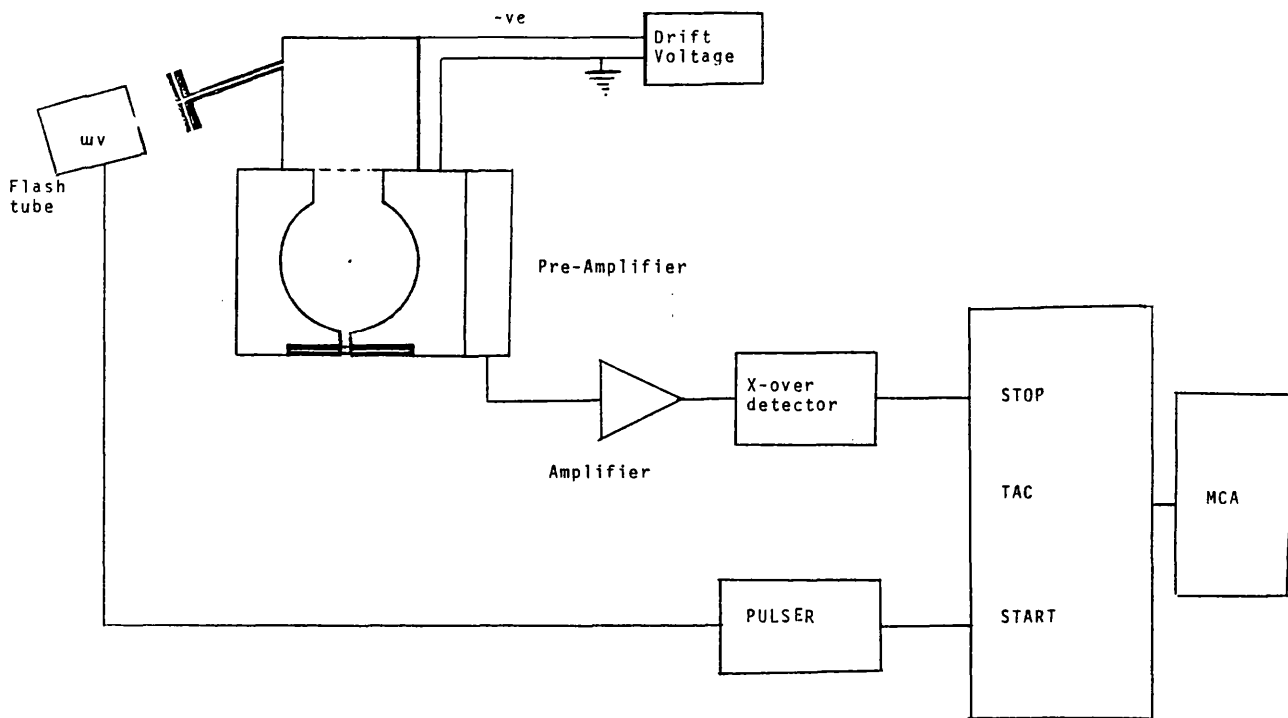


Figure 3.5 : Experimental arrangement to determine the electron mobility and the characteristic electron energy in a number of different counter gas mixtures.

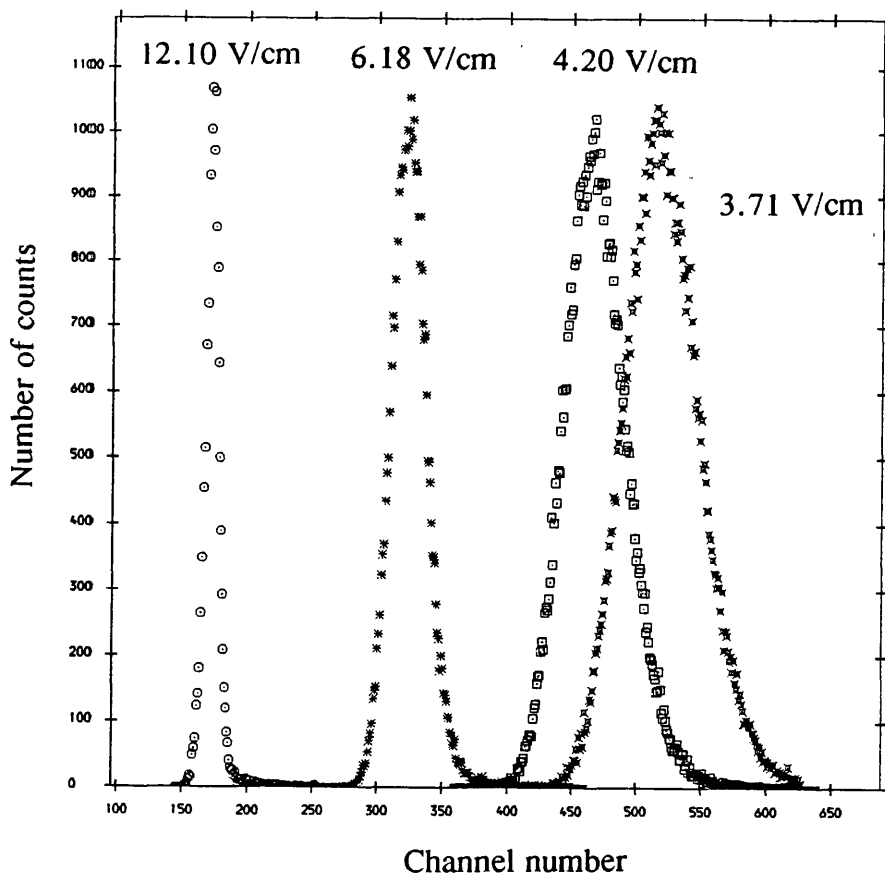


Figure 3.6 : The arrival time spectra at a number of different drift fields using A-CH₄(50%).

Therefore, τ can be expressed by the following equation :

$$\tau = [1/(2\pi)]^{1/2} [(K/k_0)] \quad 3.22$$

For example, the r.m.s. width of arrival time spectrum for A-CH₄(50%) at 3.71 V/cm was calculated as follows (see figure 3.6). In this case K equals to 71931 counts (area under the curve) and k₀ equals to 1030 counts. Using equation 3.37, τ then equals 27.9 channels. This represents an r.m.s. temporal width of the electron cloud of 3.7 μ s. This procedure is repeated for each arrival time spectrum obtained.

Figure 3.7 shows the variation of electron drift velocity with drift field in A-CH₄(10%). The intercept on the drift field axis represents the leakage field, E₀, from the anode. In case of A-CH₄(10%), where the anode voltage was 1.75 kV, the leakage field was 0.25 V/cm. In the case of A-CH₄(50%), A-CH₄(50%)-N₂ (2.5% to 10%) and A-CO₂(20%), where the anode voltage was 2.50 kV, the leakage field was 0.36 V/cm. These values must be added to the applied field in further data analysis. Figures 3.8 and 3.9 show the variation of electron drift velocity with the sum of applied drift field and leakage field for A-CH₄(10%), A-CH₄(50%), A-CH₄(50%) (2.5% N₂), A-CH₄(50%) (5% N₂), A-CH₄(50%) (10% N₂) and A-CO₂(20%). It was not possible to obtain experimental data for A-CO₂(20%) below approximately 40 V/cm. At lower drift fields (at large drift times) arrival time spectrum distortion occurred when using A-CO₂(20%) due to electron loss by capture.

The electron mobility, μ , is obtained from the slopes of the electron velocity versus drift field plots (see eqn. 3.14). These graphs show two interesting features. Firstly, it is evident that the electron mobility remains independent of the applied drift field for the present low drift fields. A saturation in electron velocity occurs at much higher drift fields leading to electron mobility becoming field dependent (Mathieson et al (1979); Fraser et al. (1986a and 1986b)). Secondly, electron mobility is reduced when the quench gas concentration is increased. For example, the electron mobility in A-CH₄(10%) was found to be $3.47 \times 10^{-2} \text{ cm}^2/\text{V}\mu\text{s}$, compared with $2.00 \times 10^{-2} \text{ cm}^2/\text{V}\mu\text{s}$ in A-CH₄(50%) for the present drift field range.

Figures 3.10-3.15 show the variation of the r.m.s. width of the electron cloud with $(E_d + E_0)^{-3/2}$ using the counter gas mixtures A-CH₄(10%), A-CH₄(50%), A-CH₄(50%)-(2.5%N₂), A-CH₄(50%)-(5%N₂), A-CH₄(50%)-(10%N₂) and A-CO₂(20%). The slopes of these plots equal $[\{2(D_1/\mu)\}^{1/2}/\mu]$ (see eqn. 3.13). The characteristic electron energy, D_1/μ , can

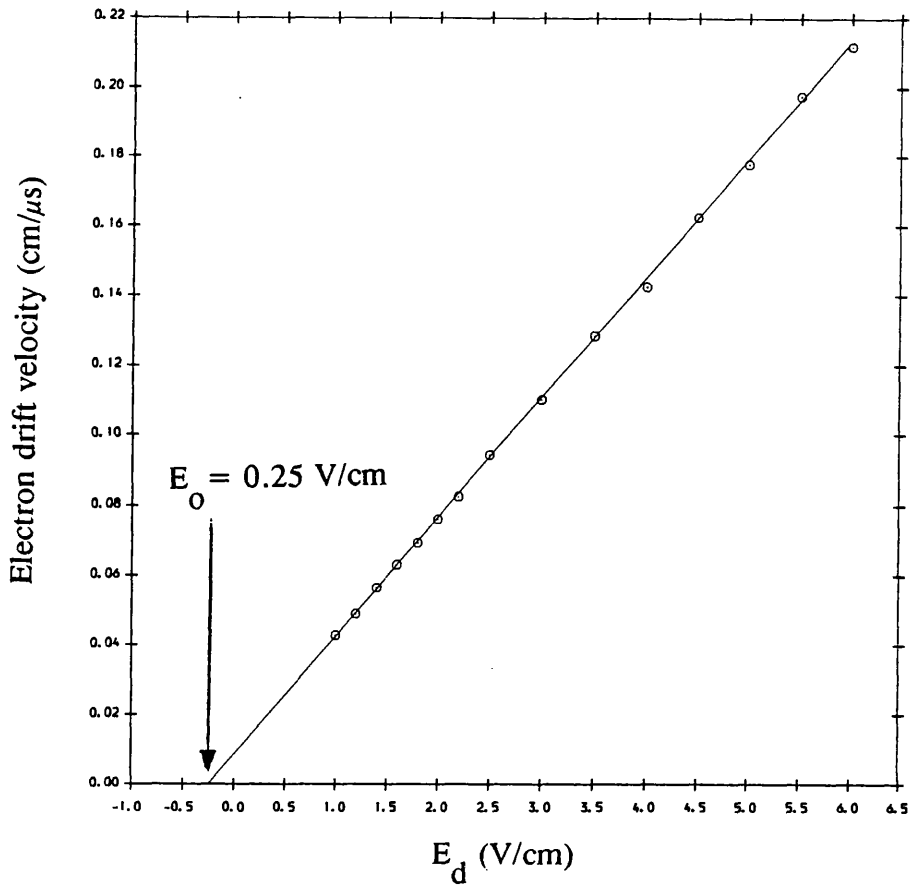


Figure 3.7 : The variation of electron drift velocity with applied field using A-CH₄ (10%).

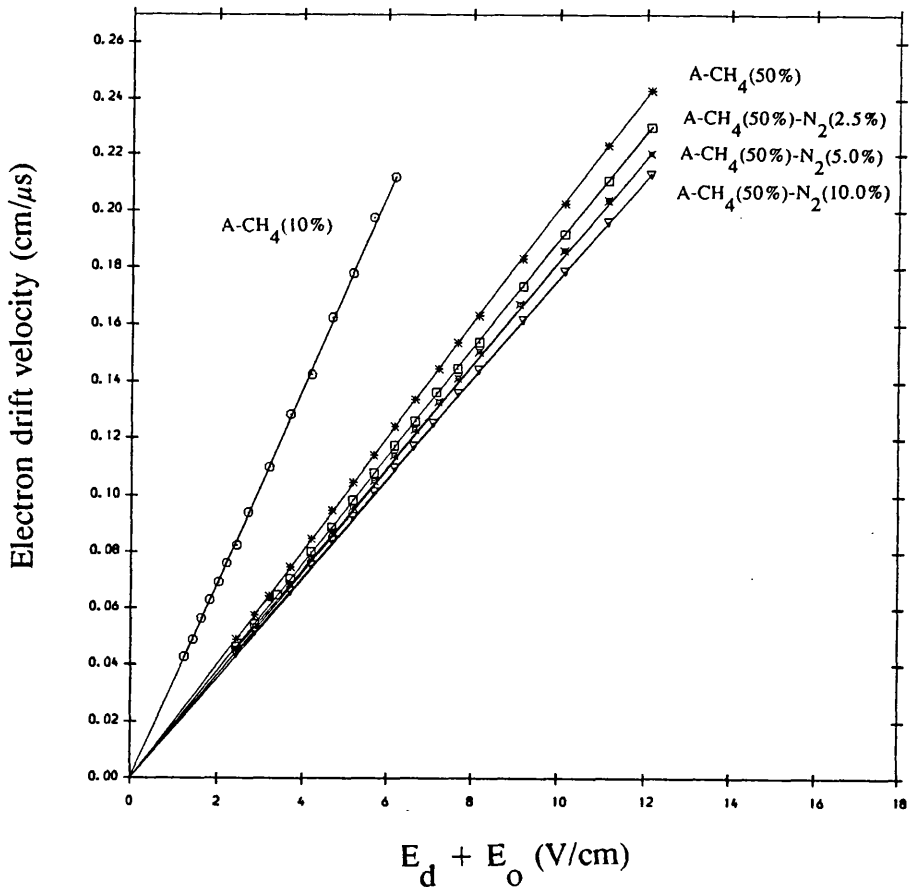


Figure 3.8 : The variation of electron drift velocity with the sum of applied drift field and leakage field using a different number of counter gas mixtures.

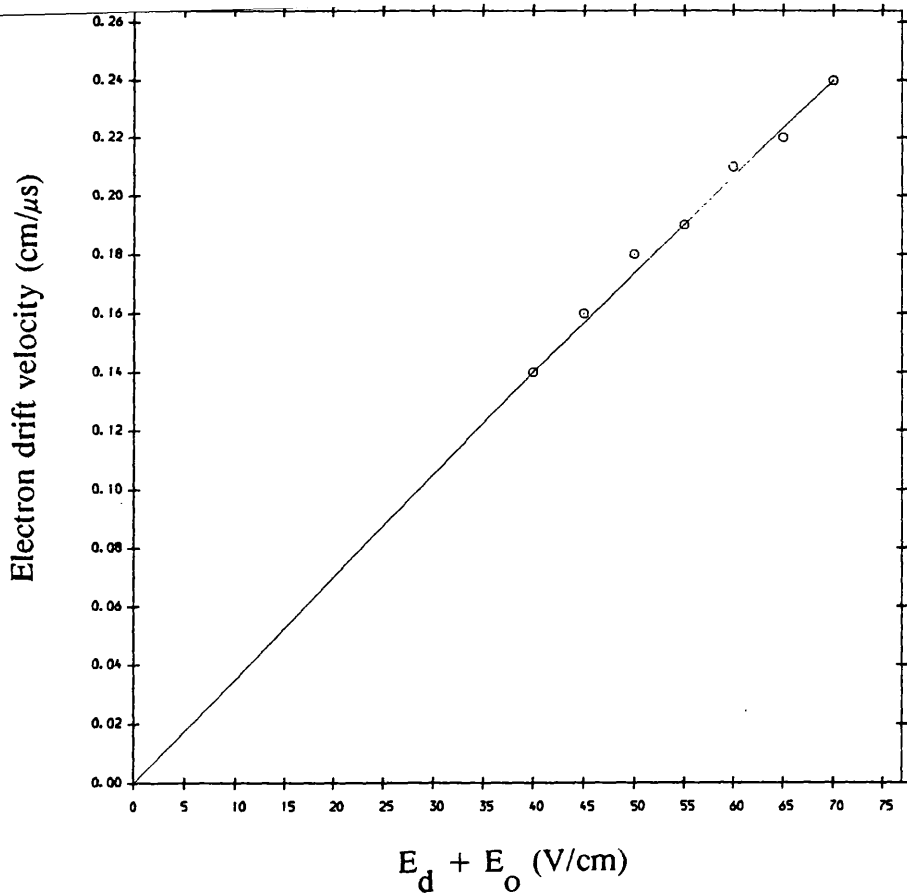


Figure 3.9 : The variation of electron drift velocity with the sum of applied drift field, E_d , and leakage field, E_o , using A-CO₂(20%).

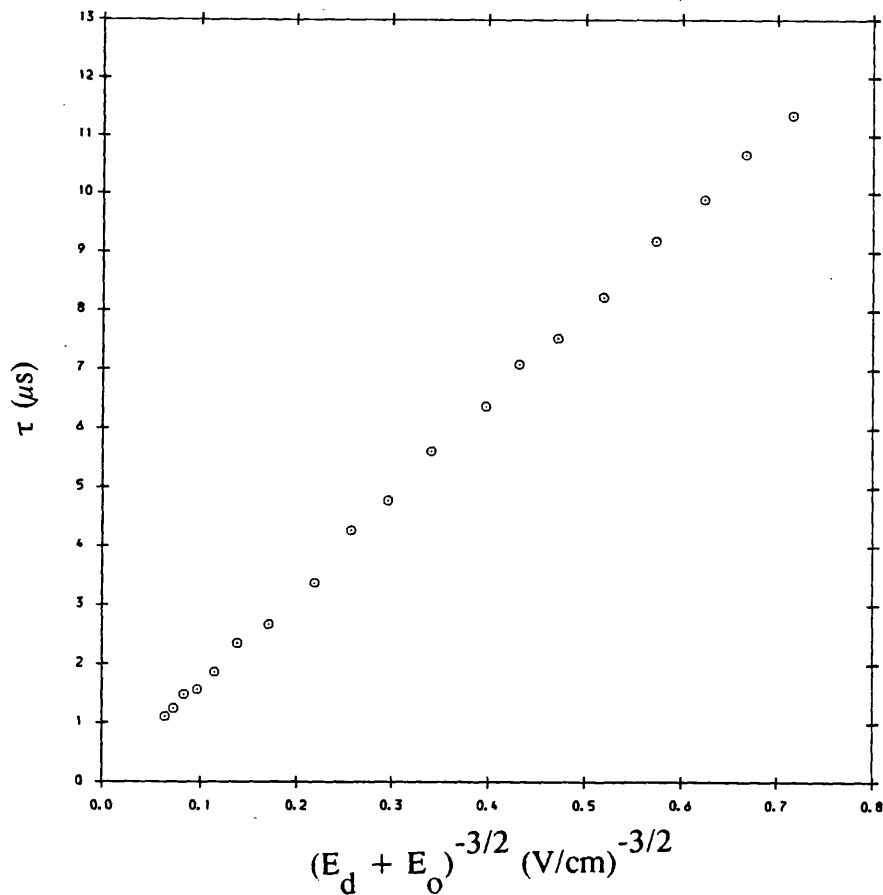


Figure 3.10 : The variation of the r.m.s. width of the arrival time spectrum with $(E_d + E_o)^{-3/2}$ using A-CH₄(10%).

therefore be written as follows :

$$D_1/\mu = (\mu \text{slope})^2 / 2d \quad 3.23$$

where μ has already been determined from electron velocity versus drift field plots. Table 3.2 shows the experimental and theoretical electron mobilities and characteristic energies for different counter gas mixtures. The theoretical calculations were performed by Mathieson (Private communication (1989)) using equations 3.12-3.14 with the assumption that no inelastic scattering occurred in argon, methane, nitrogen and carbon dioxide. The elastic cross sections for argon and methane were obtained from Mathieson et al. (1979) and Fraser et al. (1986a). The elastic cross sections for nitrogen were obtained from Huxley and Crompton (1974).

The experimental electron mobilities were measured with approximately $\pm 0.6\%$ accuracy and characteristic electron energy was measured with approximately $\pm 2.0\%$ accuracy. There is a good agreement between experimental electron mobilities and theoretical values. There is, however, a discrepancy between experimental and theoretical values of characteristic electron energy for all counter gas mixtures used. At low drift fields when the electron distribution is assumed to be Maxwellian, D_1/μ should approximately be at the thermal value of 25 meV. This view is supported by the independence of electron mobility of applied drift field. Figure 3.16 shows the calculated electron energy distribution $F(\epsilon)$ plotted versus ϵ for A-CH₄(10%)-(5%N₂) at a 5 V/cm drift field and at 760 Torr using equation 3.1. This calculation also assumes that no inelastic scattering occurred between electron and atoms or molecules. Figure 3.16 confirms that at the conditions specified above the mean electron energy remains at 25 meV (Mathieson, private communication (1989)). Despite these expectations, experimental D_1/μ values were found to be abnormally high. This led to a close examination of the fifth assumption in section 3.2 regarding random sampling by the detection system where all electrons in a given swarm should have equal probabilities of being detected. Although the correction factor β always remained less than 0.5% ($\beta = (D_1/\mu)/(E_d + E_o)d$), thus ensuring that no Poisson distortion occurred and justifying the calculation of drift velocity from $w = d/t_d$, two further mechanisms, in addition those already outlined in section 1.11, may operate to cause electron loss in the drifting swarms. If these new mechanisms were present in the apparatus, then broadening of the arrival time spectrum would occur leading to higher D_1/μ values.

Let us consider the first additional mechanism by which electron loss

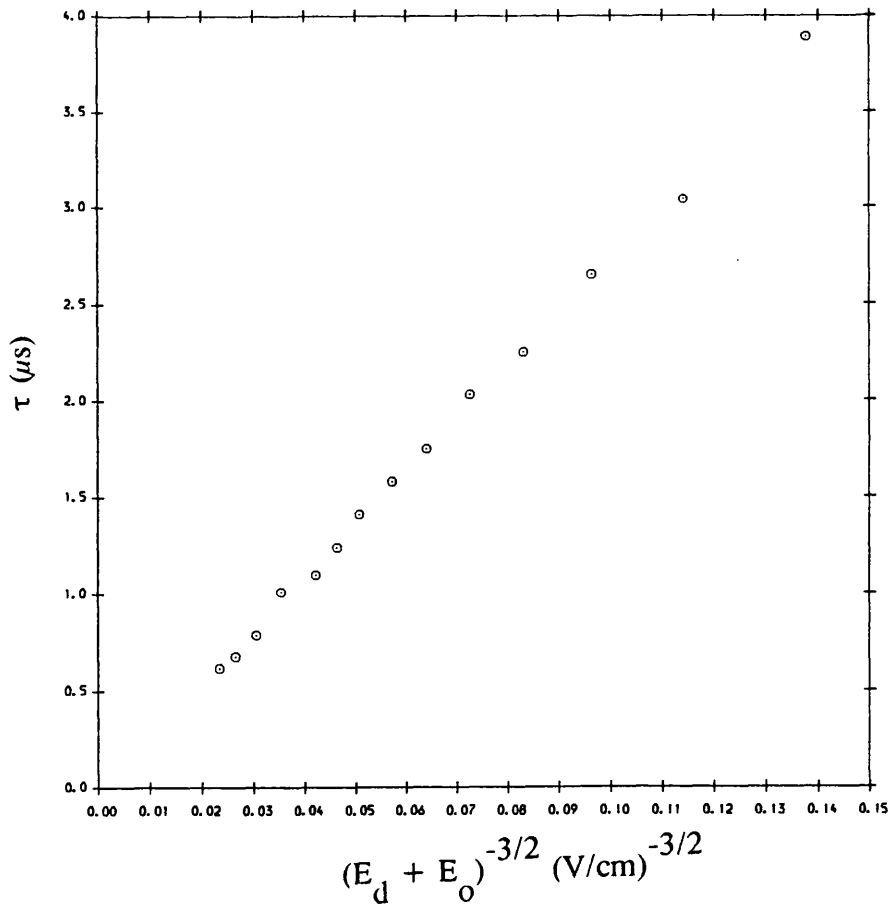


Figure 3.11 : The variation of the r.m.s. width of the arrival time spectrum with $(E_d + E_o)^{-3/2}$ using A-CH₄ (50%).

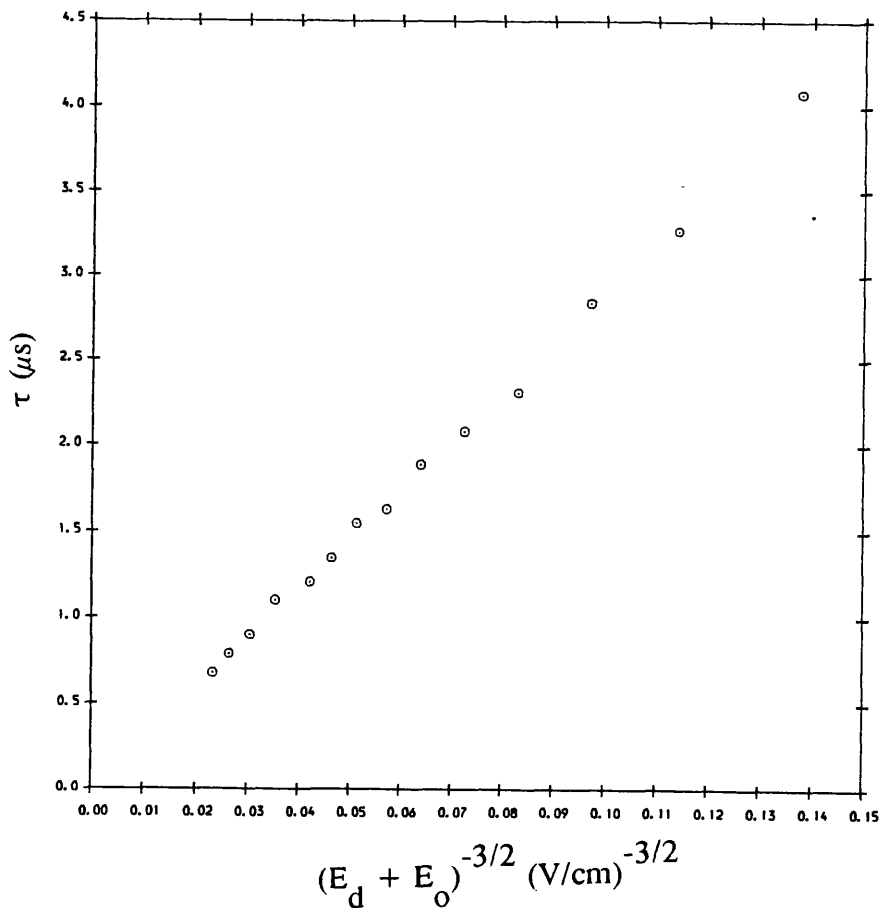


Figure 3.12 : The variation of the r.m.s. width of the arrival time spectrum with $(E_d + E_o)^{-3/2}$ using A-CH₄ (50%) - N₂ (2.5%).

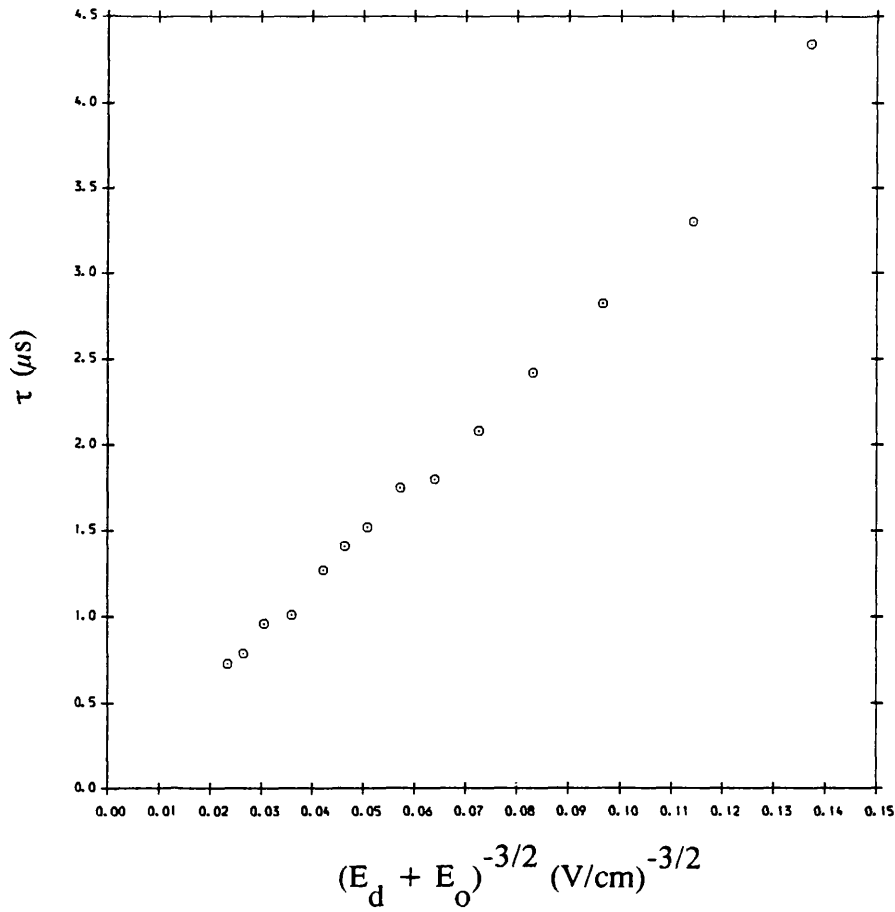


Figure 3.13 : The variation of the r.m.s. width of the arrival time spectrum with $(E_d + E_0)^{-3/2}$ using A-CH₄(50%)-N₂(5%).

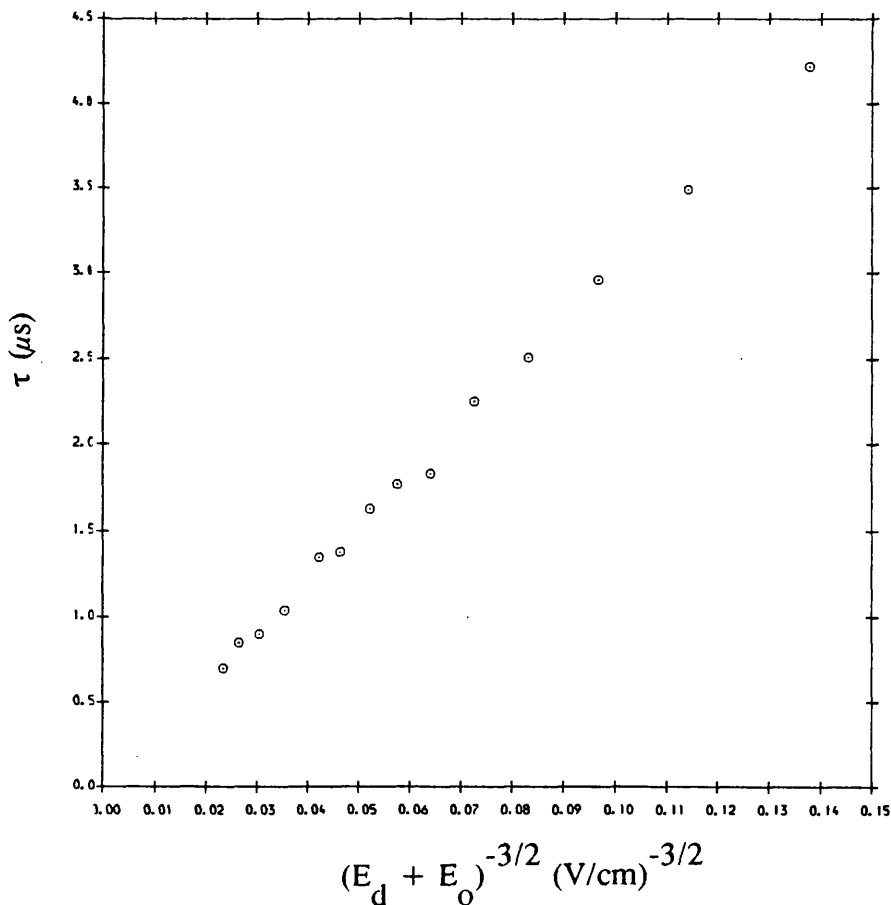


Figure 3.14 : The variation of the r.m.s. width of the arrival time spectrum with $(E_d + E_0)^{-3/2}$ using A-CH₄(50%)-N₂(10%).

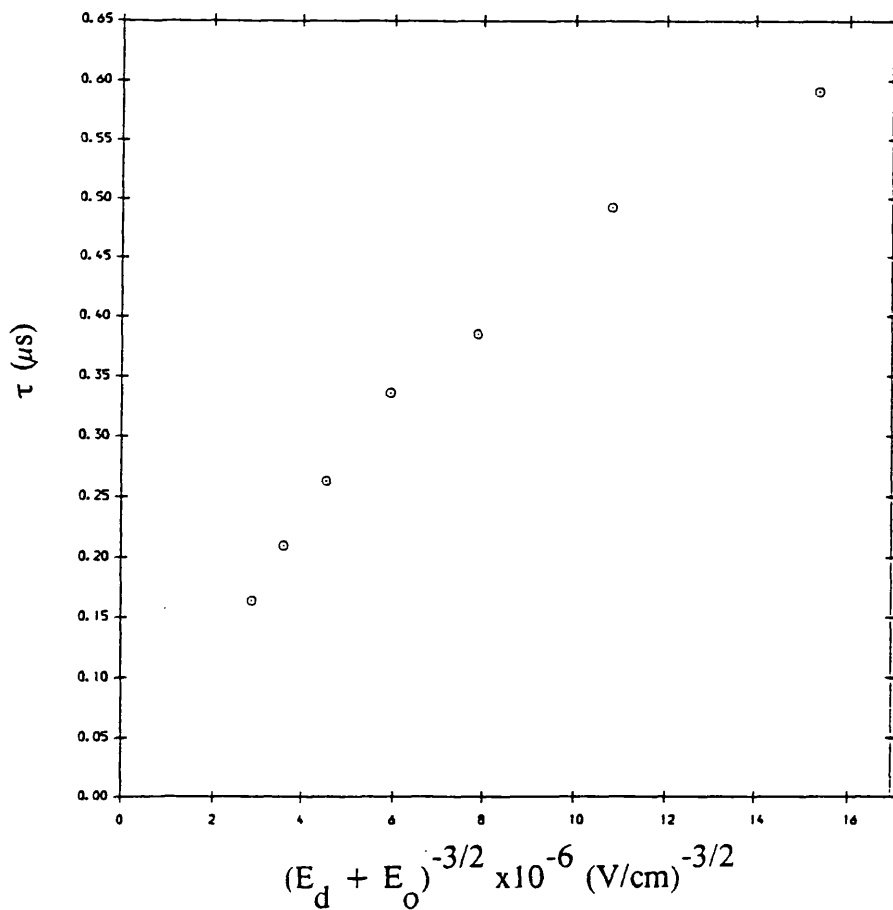


Figure 3.15 : The variation of the r.m.s. width of the arrival time spectrum with $(E_d + E_0)^{-3/2}$ using A-CO₂ (20%).

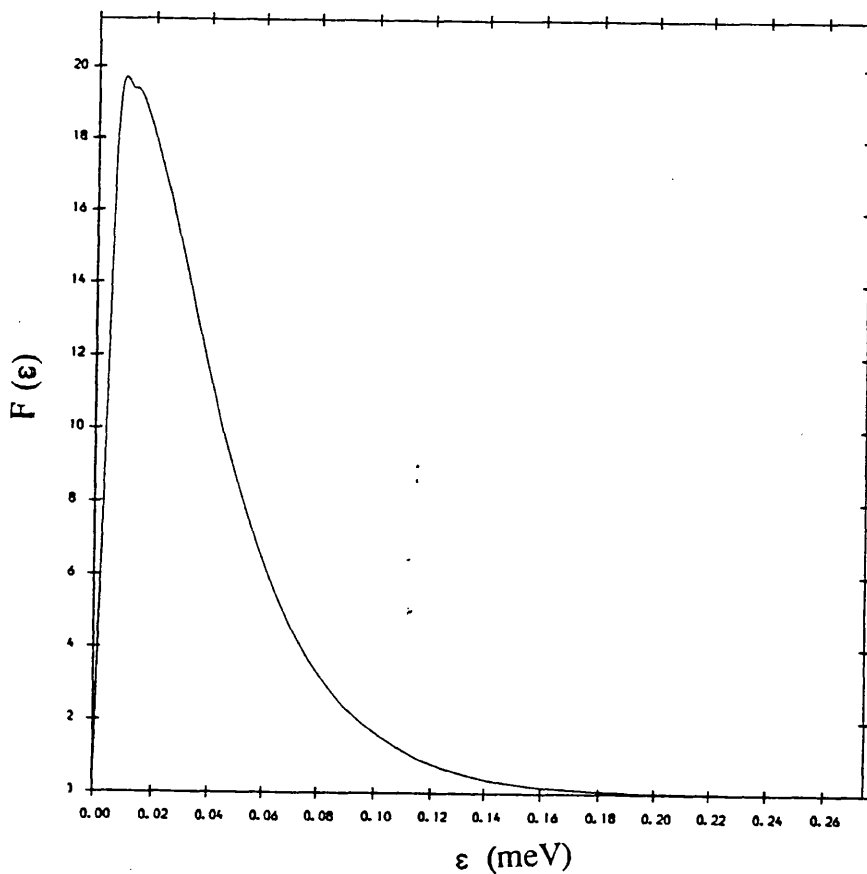


Figure 3.16 : The calculated electron energy distribution in A-CH₄(10%)-N₂(5%) at one atmosphere and a drift field of 5 V/cm (Mathieson, private communication (1989)).

Gas Mixture	Exptl. Electron Mobility x1000 (cm ² /Vμs)	Th. Electron Mobility x1000 (cm ² /Vμs)	Exptl. D ₁ /μ (meV)	Th. D ₁ /μ (meV)	Mean Electron Lifetime (ms)
A-CH ₄ (10%)	34.7 ±0.2	35.3	35.6 ±0.6	25.0	≥5.0
A-CH ₄ (50%)	20.0 ±0.2	21.0	36.4 ±0.6	25.0	≥5.0
A-CH ₄ (50%) (2.5%N ₂)	18.9 ±0.2	19.0	34.8 ±0.6	25.0	≥3.0
A-CH ₄ (50%) (5.0%N ₂)	18.5 ±0.2	18.5	34.3 ±0.6	25.0	≥3.0
A-CH ₄ (50%) (10%N ₂)	17.7 ±0.2	16.9	35.7 ±0.6	25.0	≥3.0
A-CO ₂ (20%)	3.50 ±0.2	3.21	35.0- 45.0	25.0	≤0.2

Table 3.2 : Summary of experimental and theoretical results : electron mobilities, characteristic electron energies and mean electron lifetimes for a number of different counter gas mixtures.

might occur. This involves electron loss due to electron absorption at the transmission grid. The experimental arrangement to investigate this type of loss mechanism is shown in figure 2.1. An A-CH₄ (10%) counter gas mixture was operated at 1.70 kV. Fe⁵⁵ X-rays (5.89 keV) irradiated the drift window and a pulse height spectrum was accumulated for a given drift field. This procedure was repeated over a drift field range of 2 V/cm to 80 V/cm. If there is no electron capture at the transmission grid then the position of peak pulse height should remain independent of the drift field. It was found that this behaviour was only valid for drift fields above approximately 10 V/cm. A sharp reduction in peak pulse height occurred below this value. However, this reduction was not a result of absorption at the transmission grid but was attributed to the diffusion of electron swarms which is described in section 3.7, below.

Bunemann et al. (1949) have developed a theoretical model to describe the transfer of electrons through a transmission grid. The electron transfer ratio T can be expressed in terms of transmission grid wire radius r, wire spacing l and R which is the ratio E_g/E_d where E_g is the leakage field at the transmission grid due to the anode potential and E_d is the drift field. When R is greater than unity, as in the present case, then the transfer ratio can be written as follows (Bunemann et al. (1949) :

$$T(R) = 1 - (A/\pi) \{ [(\rho B/A)^2 - 1]^{1/2} - \cos^{-1}(A/\rho B) \} \quad 3.24$$

where $A = R - 1$, $B = R + 1$ and $\rho = (2\pi r/l)$

The electron transfer ratio for the present apparatus was calculated from the knowledge of E_g , E_d and ρ using equation 3.24. The parameter ρ for the transmission grid equals 0.90. When the anode voltage equals 1.70 kV then the value of E_g equals 193 V/cm (see eqn. 1.4). The drift field range during the TOF experiments was approximately 1 V/cm to 15 V/cm (i.e. R values ranging between 12.9 and 193). The electron transfer ratio, for example, at a drift of 15 V/cm equals 0.962. It was concluded that no electron losses occurred due to absorption at the transmission grid.

The second additional mechanism by which electron loss may occur involves the electrons in the trailing edge of the swarm being lost at the transmission grid periphery. The dimension of the transmission grid, D/μ and μ for various gas mixtures are known. The spatial dimension of a given electron swarm at a given field can therefore be inferred from equation 3.11. For example, assuming the transmission grid radius equals 12.5 mm, the drift

distance d equals 5.06 cm, the sum of drift field and leakage field due to the anode potential ($E_d + E_g$) equals 5.0 V/cm and D/μ truly equals 25 meV, then the r.m.s. radius of the electron swarm on reaching the transmission grid is approximately 2.25 mm. Since the spatial distribution of electrons in the swarm is assumed to be Gaussian then it implies that 68.3%, 95.4%, 99.7% and 99.9% of the charge is found within $\pm 1\sigma$, $\pm 2\sigma$, $\pm 3\sigma$, $\pm 4\sigma$, respectively. It may therefore be concluded that no electron losses occurred at the transmission grid periphery provided the centroid of the drifting electron swarm was exactly central to the transmission grid aperture. In reality, this may not be the case since the present drift window radius equalled to 3.5 mm. Taking the worst case where primary electrons were formed at the periphery of the drift window, the centroid of the drifting electron swarm shifts from the centre of transmission grid aperture by 3.5 mm. Since the r.m.s. radius at a drift field of 5.0 V/cm equals 2.25 mm, no electron losses occur at the transmission grid periphery even for the worst case.

As a final attempt to explain the abnormal high D_1/μ values, boundary effects (Chamberlain (1987)) were examined. Field inhomogeneities occur at the side boundaries of the drift volume. These may cause some electrons to deviate from their linear motion towards the transmission mesh causing electron loss at the inner surface of the drift tube walls. The present work requires a highly uniform drift field. In order to minimize this effect the "difference method" was attempted. This involved an observation of the changes in swarm characteristics between two different drift lengths. Additional experiments for another drift length (7.23 cm) were carried out. The data were subtracted from the corresponding data for a drift length of 5.06 cm. Hence the effective drift length was 2.17 cm. However, similar high D_1/μ were consistently obtained. These results remain very puzzling and require a separate study. In particular, the effects of UV flash pulse width upon D_1/μ should be examined. In the present work, the broadening of the arrival time spectrum due to the finite pulse width, 0.8 μ s, of UV flash was ignored (see section 3.2). Wagner et al. (1967), however, calculated a correction factor (≤ 1) due to the finite pulse width of UV flash and multiplied it with the observed D_1/μ . This gave adequate values of D_1/μ for a number of different counter gas mixtures.

3.6 Mean electron lifetime measurements in counter gas mixtures

Mean electron lifetimes have been determined in A-CH₄(10%), A-CH₄(50%), A-CH₄(50%)-N₂ (2.5% to 10%) and A-CO₂(20%). The determination of electron lifetime is an accurate indication of the purity of the counter gas mixture being used. The electron capture rate can be correlated to

the concentration of impurity species and to the mean agitation energy, ϵ of the electrons. This has been done by defining the attachment rate coefficient $k(\epsilon)$, as follows (Walenta (1979)) :

$$\tau_a = 1/k(\epsilon)\alpha_1\alpha_2 \quad 3.25$$

where τ_a is the mean electron lifetime, α_1 and α_2 are the concentrations of the impurity species and the quencher concentration, respectively. Trace impurities such as water vapour, oxygen or dust particles introduced into the detector by gas leaks or otherwise, have very high electron capture cross sections which cause serious reduction in electron lifetime.

3.7 Theory of electron lifetime determination

Measurement of the mean electron lifetime for a particular counter gas mixture is more straightforward than, for example, the measurements of electron mobility or transverse and longitudinal diffusion coefficients. If N_o is the primary number of electrons produced near the inner surface of the drift tube window by X-rays, then the fraction of remaining electrons N/N_o , after electron capture during drift as a function of average drift time, t_d , is given by equation 1.22 (see figure 3.17). The experimental arrangement to determine the mean electron lifetime in a given counter gas mixture is shown in figure 3.18. Let n be the peak channel number for a drift time t_d and n_o be the peak channel number when t_d approaches zero (i.e. when N equals N_o). The remaining fraction of electrons with drift time can be expressed by the following equation :

$$N/N_o = n/n_o = \exp(-t_d/\tau_a) \quad 3.26$$

The electron drift velocity w can be expressed as follows :

$$w = (d-\lambda)/t_d = \mu(E_d + E_o) \quad 3.27$$

where d is the drift tube length, λ is the mean photon absorption depth for a given X-ray energy and the type of gas mixture used, μ is the electron mobility, E_d is the applied drift field, E_o is the leakage field at the transmission grid due to the anode voltage. Equation 3.27 can be rewritten as follows :

$$t_d = (d-\lambda)/\mu(E_d + E_o) \quad 3.28$$

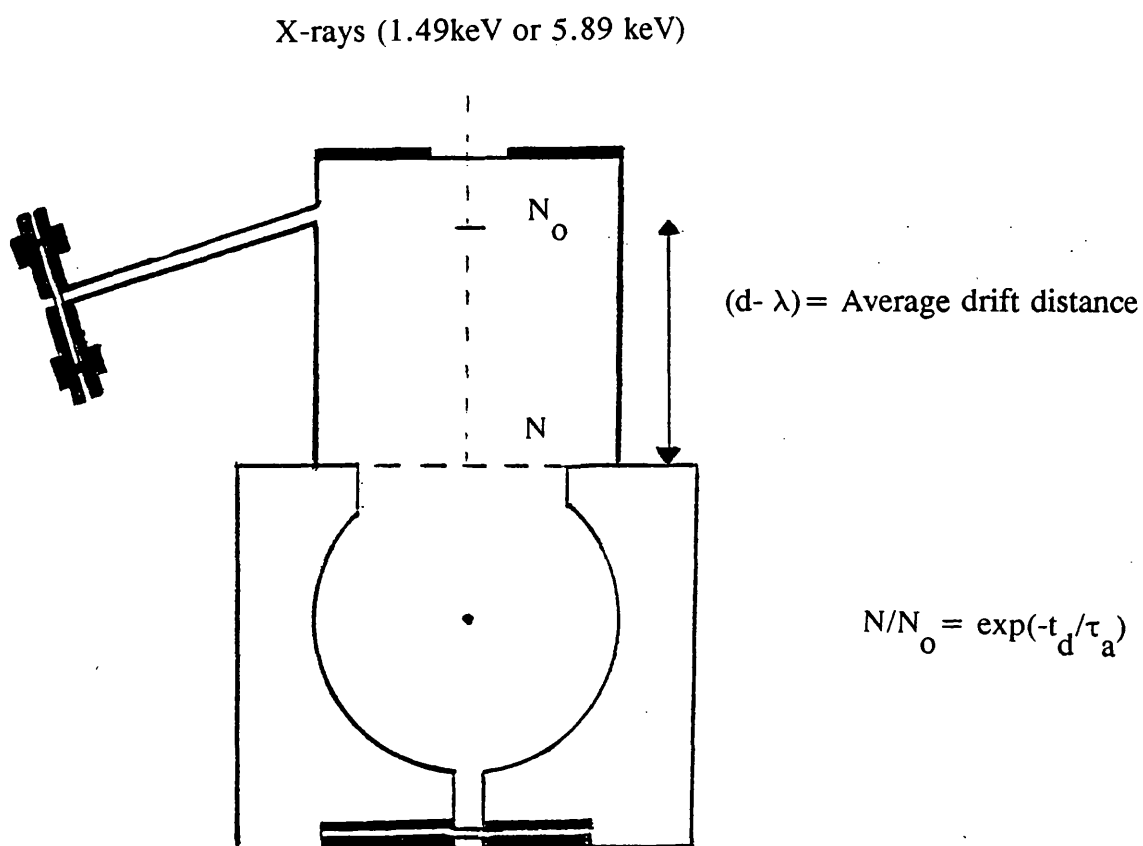


Figure 3.17 : A schematic diagram of the experimental chamber showing the principals involved in electron lifetime measurement.

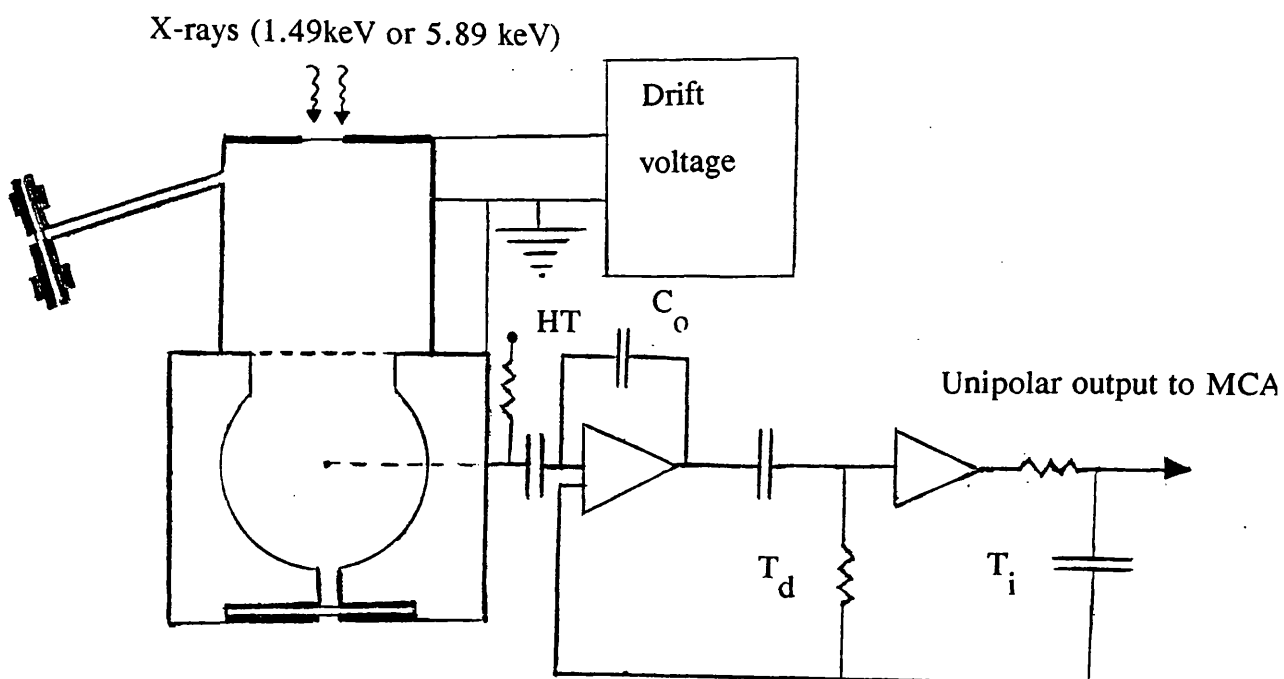


Figure 3.18 : Experimental arrangement to determine the mean electron lifetime in a number of different counter gas mixtures.

Substituting for t_d into 3.26 gives the following equation :

$$\ln(n/n_0) = -(d-\lambda)/[\mu\tau_a(E_d + E_0)] \quad 3.29$$

If $\ln(n/n_0)$ is plotted versus $1/(E_d + E_0)$, τ_a may be calculated from the slope of this graph. A zero slope, therefore, implies an infinite electron lifetime .

It was found, however, that such plots were non-linear and large pulse height reductions occurred at large drift times. It was concluded that the above simplistic calculations were incomplete since they ignored the effect of diffusion on pulse height. In reality, diffusion begins to dominate at the large drift times used in the present work leading to large pulse height reductions. At lower drift fields, the r.m.s. width of the electron swarms after diffusion is much greater than at higher drift fields. As a result, electron avalanching spreads along the anode wire causing an increase in risetime of the output pulse at the anode wire (Gott et al. (1969)). In the present case, the output pulses were shaped using a $0.45 \mu s$ filter time constant. The shaped pulses therefore had an amplitude which was less than an amplitude corresponding to an infinite filter time constant by an amount known as the "ballistic deficit". This pulse height reduction due to diffusion is much larger than that due to the electron capture. Therefore, the effect of diffusion on pulse height must be incorporated into the simple theory above as shown below (Mathieson, private communication (1988)) :

The current, $i(t)$ due to primary clusters at the anode wire is Gaussian in time, which can be written as :

$$i(t) \approx q/(2\pi)^{1/2} \tau^{-2} \exp(-t/2\tau^2) \quad 3.30$$

where q is the counter charge, t is the time from the start of the electron multiplication and τ is the r.m.s. width of the arrival time spectrum. The counter output waveform, $v(t)$ is given by the following expression :

$$v(t) = qC/C_0 \ln(1+t/t_0) \quad 3.31$$

where C is a geometric constant for a given proportional counter, C_0 is the associated chamber capacitance and t_0 is the chamber characteristic time. The parameter t_0 can be expressed by the following equation :

$$t_0 = (r_a)^2 / 4\mu_i VC \quad 3.32$$

where r_a is the anode radius, μ_i is the positive ion mobility and V is the anode voltage. The parameter C can be written in the following form :

$$C = 1/\ln(r_c/r_a)^2 \quad 3.33$$

where r_c is the mean cathode radius.

Firstly, the Gaussian current waveform of electron clusters is convolved with the known counter output waveform for single electrons as shown below :

$$v(t) = i(t) \circ C/C_o \ln(1+t/t_o) \quad 3.34$$

where \circ denotes convolution. Secondly, the resultant waveform from the above convolution operation is then convoluted, numerically, with the known impulse response, $h(t,T)$ of the amplifier (unipolar mode, $5 \mu s$ time constants), as shown below :

$$v_o(t) = v(t) \circ h(t,T) \quad 3.35$$

$$v_o(t) = i(t) \circ (C/C_o) \ln(1+t/t_o) \circ h(t,T) \quad 3.36$$

$$\text{where } h(t,T) = (1/T) \exp(-t/T)[1-t/T] \quad 3.37$$

The calculations of the pulse height reduction with $1/(E_d + E_o)$, allowing for diffusion effects and electron capture, have been performed using equation 3.36 (Mathieson, private communication (1988)). A number of different graphs showing $\ln(n/n_o)$ versus $1/(E_d + E_o)$ were plotted assuming a number of different electron lifetimes. These were then compared with the experimental pulse height reductions with $1/(E_d + E_o)$ (i.e. with increasing drift times).

3.8 Experimental procedure

The experimental configuration used to determine the mean electron lifetime in a number of different gas mixtures is shown in figure 3.18. The gas mixture under investigation was passed through the chamber for at least an hour prior to start of an experiment at approximately 100 cc/minute and this flow rate was maintained during the experiment. The anode voltage was maintained at 1.30 kV when using A-CH₄ (10%) and at 2.20 kV when using A-CH₄ (50%) or A-CH₄ (50%)-N₂ (2.5 to 10%). The shaping amplifier was adjusted to a unipolar mode (single integrating stage followed by a single differentiating stage) while

the filter time constants were adjusted to 5 μ s.

Al-K X-rays (1.49 keV) irradiated the drift window and the drift field was varied approximately between 2 V/cm and 12 V/cm. The corresponding pulse height spectra were recorded on a MCA. The peak channel for each drift field was noted. The count rates at the MCA were maintained at approximately 100 Hz.

The A-CH₄(50%) flow rate was reduced from 100 cc/minute to 50 cc/minute and the above procedure was repeated to investigate the effect of flow rate upon the mean electron lifetime. In another experiment A-CH₄(50%) was fed directly into the chamber without passing through the Oxy-trap to investigate the efficiency of the Oxy-trap.

The experimental arrangement shown in figure 3.18 was not suitable to determine the mean electron lifetime in A-CO₂(20%) since this gas mixture gave very poor X-ray pulse height spectra. The energy resolution at 5.89 keV using A-CO₂(20%) was found to be 27 %FWHM (see section 2.5). The mean electron lifetime in A-CO₂(20%) was, therefore estimated by measuring the charge directly from the anode wire. Figure 3.19 shows the experimental arrangement used to estimate the mean electron lifetime in A-CO₂(20%). Fe⁵⁵ X-rays (5.89 keV) irradiated the drift window. The drift field was varied between 2 V/cm to 10 V/cm. The output voltage across the 50 μ F capacitor was measured for each drift field used.

3.9 Experimental electron lifetime measurements : results and discussion

Figure 3.20 shows a logarithmic plot of fractional pulse height reduction with $1/(E_d + E_o)$ for A-CH₄(10%) when Al-K X-rays (1.49 keV) were used. Figure 3.20 also shows the theoretical fractional pulse height reductions with drift times (Mathieson, private communication (1988)). These calculations allow for pulse height reduction due to diffusion (see eqn. 3.36). The three solid lines represent theoretical pulse height reductions when the electron lifetime is ∞ , 1.0 ms and 0.5 ms. The calculation of theoretical pulse height reduction requires a knowledge of electron mobility μ , electron characteristic energy D_1/μ , filter time constant T, characteristic proportional chamber time t_o and a proportional chamber constant C, as described above.

The following data was used to calculate pulse height reductions : Electron mobility in A-CH₄(10%) was taken to be 3.47 cm²/V μ s, D_1/μ equal to 25 meV, C = 0.0724, t_o = 1.62 ns and T = 5 μ s. It is evident from figure 3.20 that the electron lifetimes are very long when the experimental pulse height reduction is compared with theoretical pulse height reduction. The theoretical

mean electron lifetime \propto effectively corresponds to a time duration of ≥ 5.0 ms. A lower limit of approximately 5.0 ms mean electron lifetime in A-CH₄(10%) can therefore be inferred.

The mean electron lifetime in A-CH₄(50%) was found to be as high as that for A-CH₄(10%) i.e. at least 5.0 ms. This is demonstrated by figure 3.21 where the experimental pulse height reductions with $1/(E_d + E_0)$ for A-CH₄(50%) are compared with the theoretical pulse height reductions. Two solid lines represent theoretical pulse height reductions when electron lifetime is \propto (5.0 ms) and 3.0 ms. For these calculations the electron mobility in A-CH₄(50%) was assumed to be $2.00 \times 10^{-2} \text{ cm}^2/\text{V } \mu\text{s}$, $D_1/\mu = 25 \text{ meV}$, $C = 0.0724$, $t_0 = 1.08 \text{ ns}$ and $T = 5 \mu\text{s}$.

A reduction in the mean electron lifetime was observed when the A-CH₄(50%) flow rate was reduced from approximately 100 cc/minute to 50 cc/minute. This is demonstrated by figure 3.22 which shows that at the lower gas flow rate the mean electron lifetime is approximately 3.0 ms. A reduction in the mean electron lifetime was also observed when A-CH₄(50%) was passed directly into the chamber without the use of Oxy-trap. In this case the mean electron lifetime was also found to be 3.0 ms (see figure 3.23).

The mean electron lifetimes in A-CH₄(50%)-N₂ counter gas mixtures were also reduced when compared to the values for A-CH₄(10%) or A-CH₄(50%). For instance, the mean electron lifetimes in A-CH₄(50%)-N₂(2.5% N₂, 5.0% N₂ and 10.0% N₂) were found to be 3.0 ms (see figures 3.24-3.26). The lower mean electron lifetimes in A-CH₄(50%)-N₂ counter gas mixtures were due to some trace impurities in the gas mixing system rather than due to impure nitrogen. This was demonstrated as follows : When the counter gas mixtures A-CH₄(10%) and A-CH₄(50%) were passed into the chamber without passing through the gas mixing system then high mean electron lifetimes (5.0 ms) were obtained (see figures 3.20 and 3.21). When the counter gas mixture A-CH₄(50%) was, however, passed through the gas mixing system it was found that the mean electron lifetime in A-CH₄(50%) was reduced from 5.0 ms to approximately 3.0 ms (see figure 3.27).

Figure 3.28 shows a plot of v/v_0 versus the sum of applied field and leakage field when the experimental arrangement shown in figure 3.19 was used to determine the mean electron lifetime in A-CO₂(20%). In this experiment, A-CO₂(20%) was passed into the chamber without going through the gas mixing system. The voltage across the 50 μF capacitor at lower drift field is denoted as v and v_0 is the voltage at highest drift field. The solid lines in figure 3.28 show theoretical variation of v/v_0 with drift field assuming a number of different

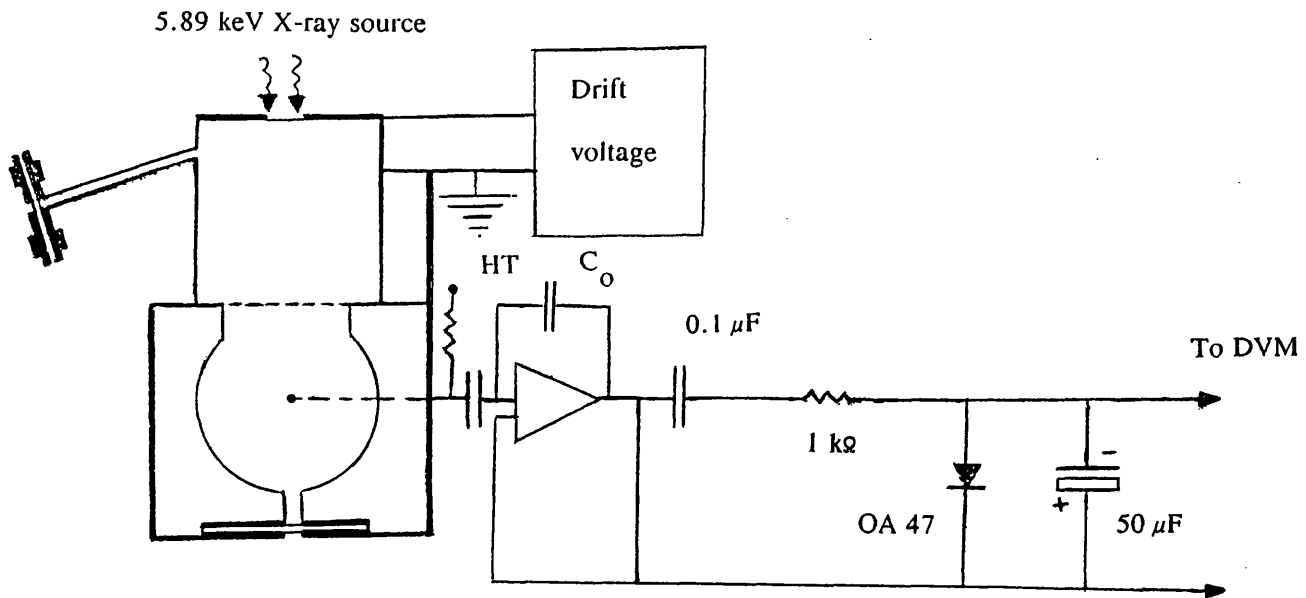


Figure 3.19 : Experimental arrangement to determine the mean electron lifetime in A-CO₂(20%).

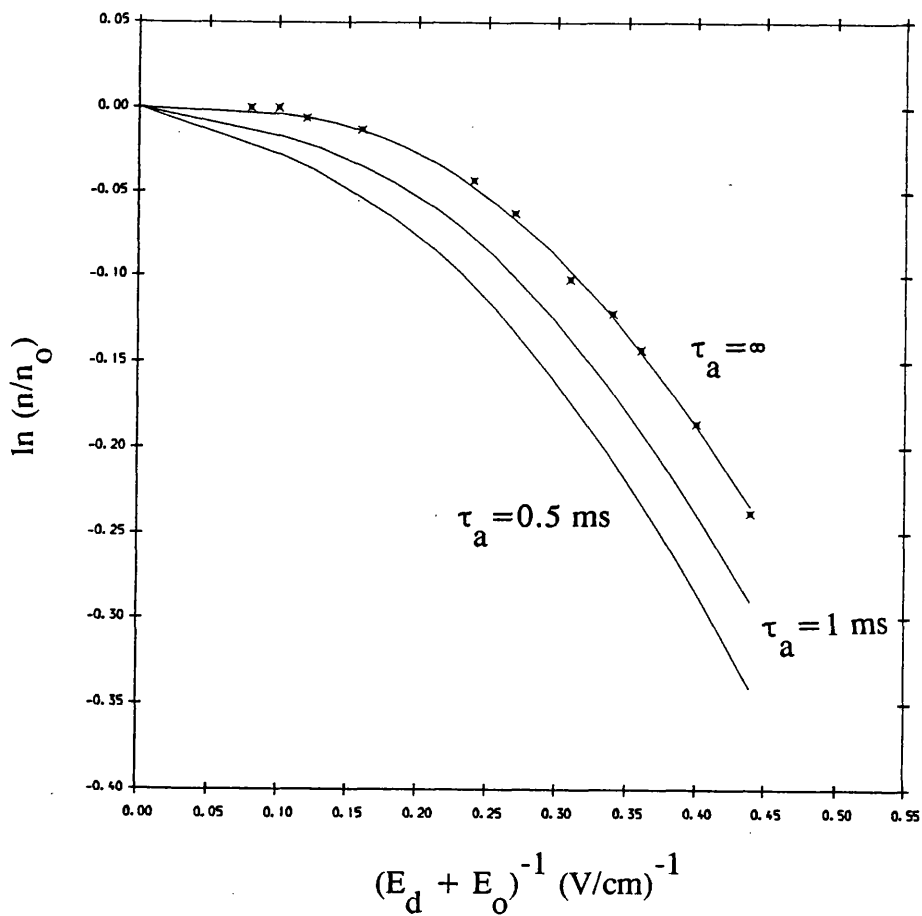


Figure 3.20 : Measurement of the mean electron lifetime in A-CH₄(10%). The solid lines indicate the calculated pulse height reductions allowing for the effects of electron capture and diffusion (Mathieson, private communication 1988).

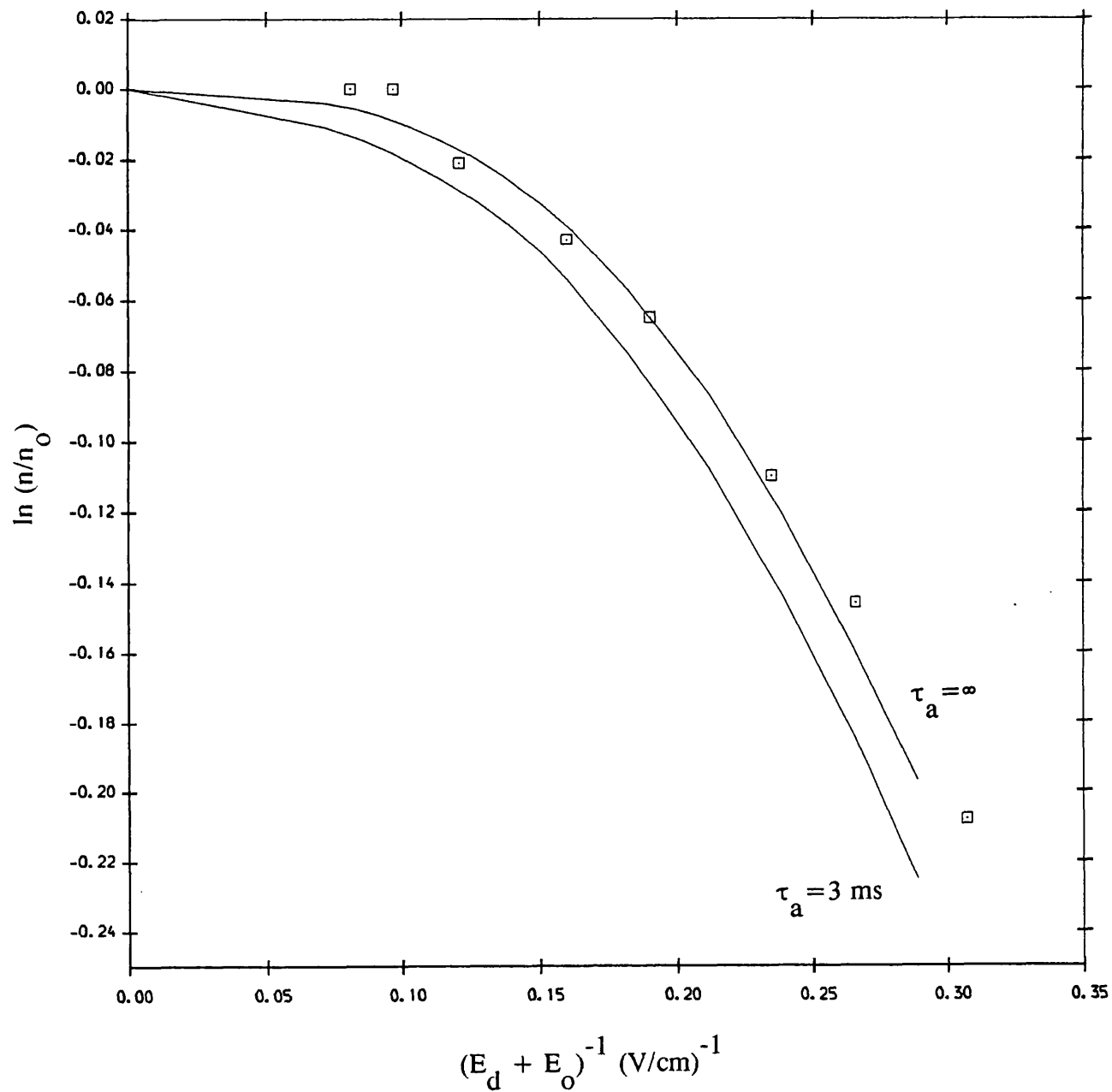


Figure 3.21 : Measurement of the mean electron lifetime in A-CH₄(50%). The solid lines indicate the calculated pulse height reductions allowing for the the effects of electron capture and diffusion (Mathieson, private communication (1988)).

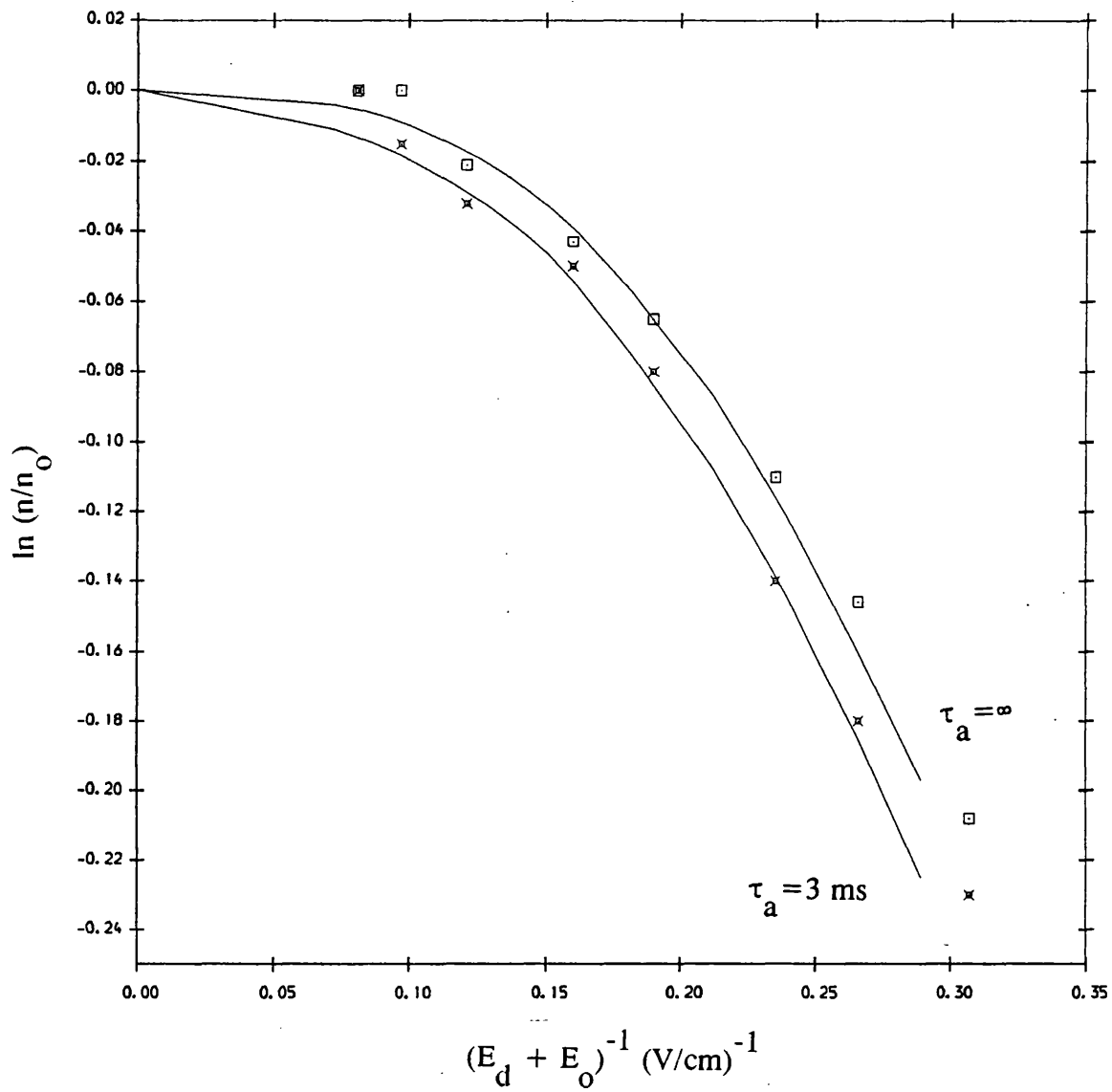


Figure 3.22 : The dependence of the mean electron lifetime upon the gas flow rate. The lower solid curve shows the pulse height behavior at a reduced A-CH₄ (50%) flow rate.

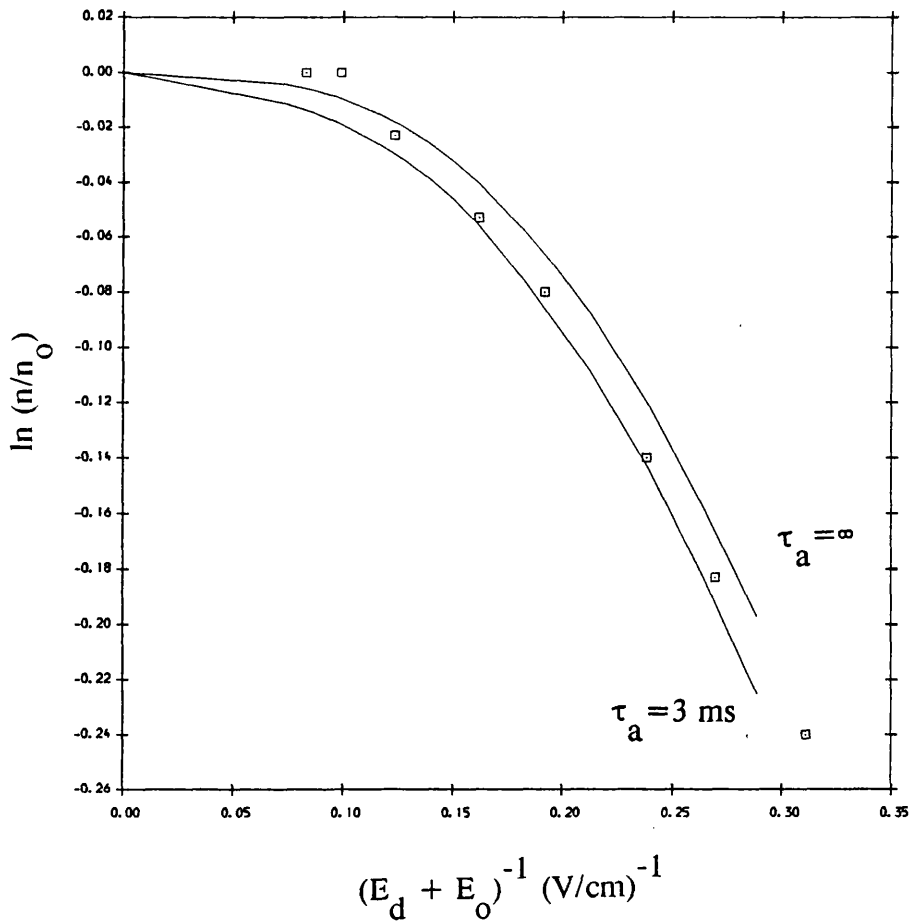


Figure 3.23 : A graph showing the reduction of the mean electron lifetime when the Oxy-trap was removed and A-CH₄(50%) fed directly into the experimental chamber.

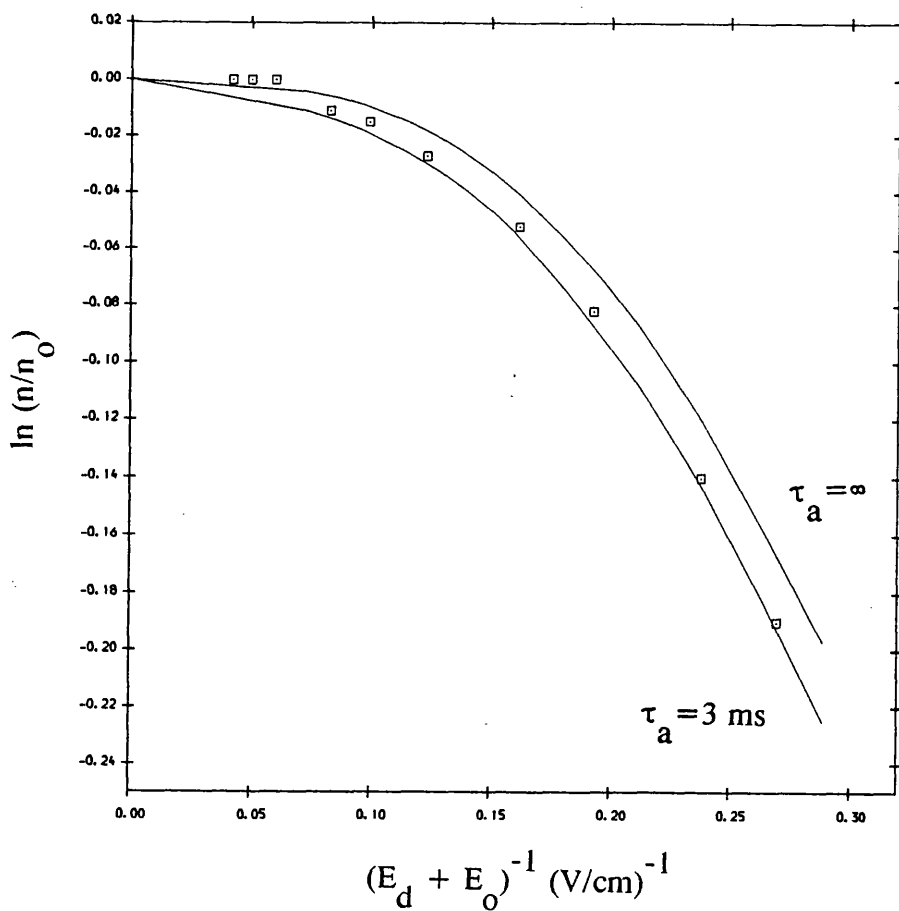


Figure 3.24 : Measurement of mean electron lifetime in A-CH₄(50%)-N₂(2.5%)

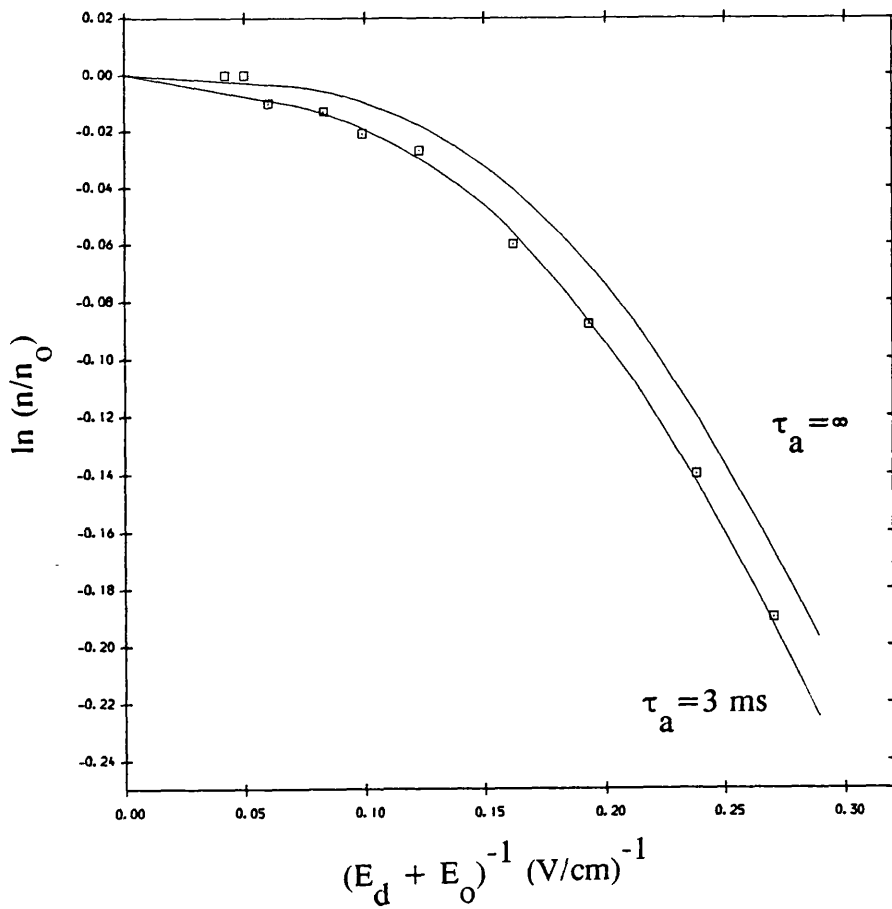


Figure 3.25 : Measurement of mean electron lifetime in A-CH₄(50%)-N₂(5.0%)

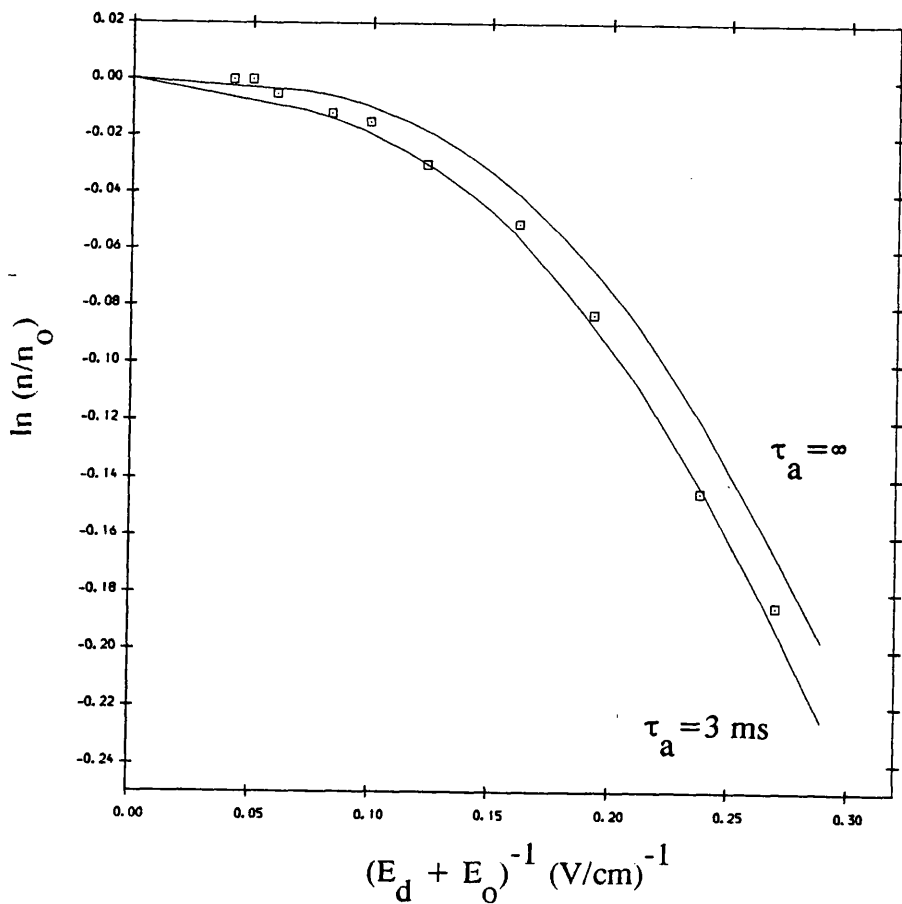


Figure 3.26 : Measurement of mean electron lifetime in A-CH₄(50%)-N₂(10.0%)

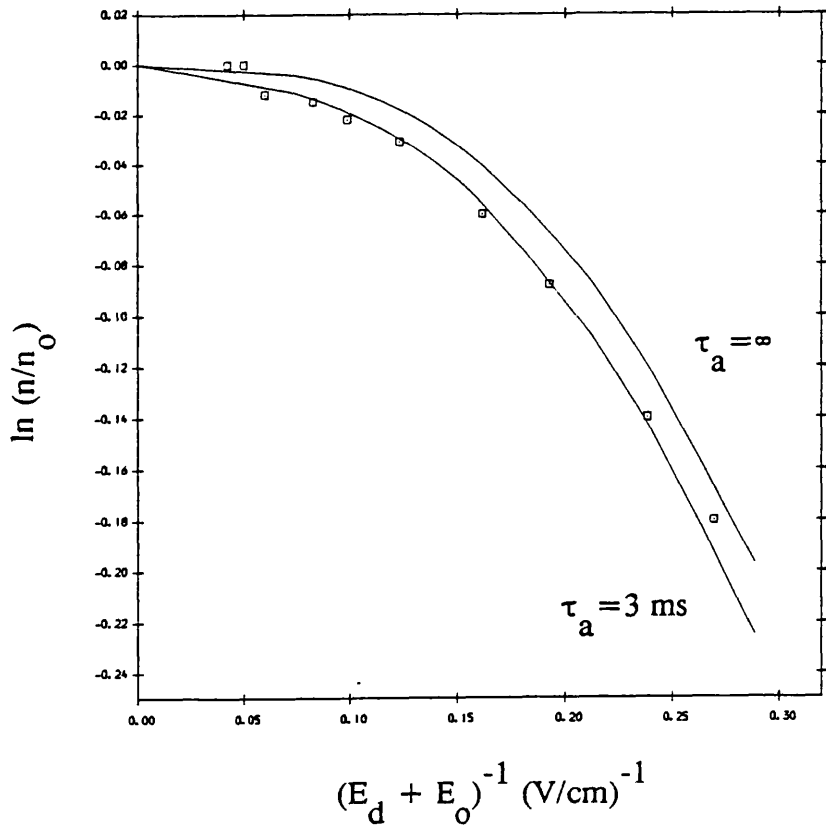


Figure 3.27 : A graph showing the reduction of the mean electron lifetime in A-CH₄ (50%) to 3 ms when it was passed through the gas mixing system before going into the detector via the Oxy-trap.

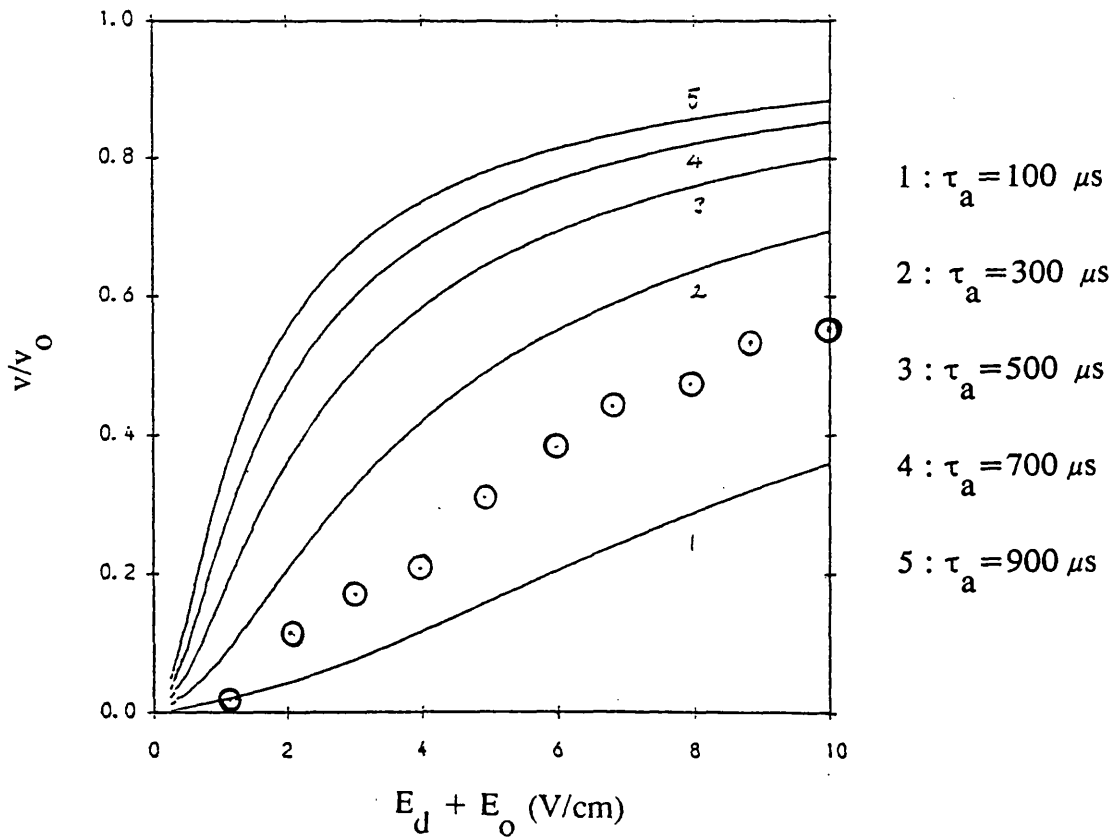


Figure 3.28 : Measurement of the mean electron lifetime in A-CO₂ (20%). The solid lines indicate the theoretical pulse height reductions for a number of different mean electron lifetimes.

electron lifetimes (Mathieson, private communication (1988)). These calculations have also allowed for the pulse height reduction due to diffusion. Five solid lines indicate the theoretical variation of v/v_0 with drift field assuming 100 μ s, 300 μ s, 500 μ s, 700 μ s and 900 μ s mean electron lifetimes. The mean electron lifetime using in A-CO₂(20%) using figure 3.28 was found to be approximately 200 μ s. This result was very puzzling and disappointing since this gas mixture had shown a proportional response at very large charge gains without the onset of cathode secondaries (see figures 2.35 and 2.36). A-CO₂(20%) also has a very low mobility (see table 3.2) and a relatively high X-ray absorption which makes it very suitable gas mixture in electron counting experiments. The low electron lifetime for A-CO₂(20%) is not consistent with the experience of other workers who have successfully used this gas mixture (Allison et al. (1974), Pack et al. (1966)). The experimental system (gas pipes, experimental chamber and Oxy-trap) was kept contamination free at all times. Despite these efforts A-CO₂(20%) consistently showed a low electron lifetime. From the knowledge of electron lifetime in A-CO₂(20%) contaminated with oxygen it was possible to infer the oxygen concentration as 11 parts per million by $2.2/\tau_a$ where τ_a is the mean electron lifetime in milliseconds (Harris et al. (1990)).

3.10 Conclusions

Experimental determinations of the electron mobility and the mean electron lifetime have successfully been carried out. The experimental determination of D_1/μ , however, remained unsatisfactory. At the low drift fields used during the present work, one would expect D_1/μ to be at 25 meV. The experimental results were contrary to this showing the characteristic electron energy to be approximately 35 meV (see table 3.2).

It is now, possible to calculate f_a and hence S_a (see eqns. 1.22 and 1.23) for a number of different drift fields. The mean electron lifetime against capture when using A-CH₄(10%) and A-CH₄(50%) was assumed to be 5.0 ms. Equation 3.7 was used to calculate the average drift time where the average drift distance was assumed to be the difference between the drift tube length (5.06 cm) and the mean free path of X-ray photons. The mean free path of X-ray photons in A-CH₄(10%) and A-CH₄(50%) at 1.49 keV was assumed to be approximately 0.55 cm and 0.96 cm, respectively (Zombeck (1982)). Tables 3.3 and 3.4 show the variation of f_a and S_a with drift field using A-CH₄(10%) and A-CH₄(50%), respectively. It is clear from these tables that f_a approaches unity with higher drift fields. In other words, at higher drift fields, a smaller number of electrons would be lost by capture.

The mean electron lifetime τ_a in A-CH₄(10%) and A-CH₄(50%) was found to be long (5.0 ms) compared with the average drift time (typically 100 μ s) for freshly activated Oxy-traps and a newly assembled experimental chamber. It was however discovered that a gradual reduction in τ_a occurred over the period of several months. This reduction was thought to arise partly from the saturation of Oxy-traps with oxygen and partly from the outgassing of neoprene O-rings.

It was found that A-CO₂(20%) was inadequate for any electron counting experiments due to its very short mean electron lifetime. A-CH₄(10%) and A-CH₄(50%), however, exhibited very long mean electron lifetimes which made them suitable for electron counting applications. A-CH₄(50%) however, appears to be more suitable for this purpose since it can sustain higher charge gains without the onset of cathode secondaries.

Drift Field (V/cm)	Average drift time (μ s)	f_a	S_a
1.25	104.0	0.979	21.5×10^{-3}
1.85	70.3	0.986	14.2×10^{-3}
2.25	57.8	0.989	11.1×10^{-3}
4.25	30.6	0.994	6.0×10^{-3}
6.25	20.8	0.996	4.0×10^{-3}
8.25	15.8	0.997	3.0×10^{-3}
10.26	12.7	0.998	2.0×10^{-3}

Table 3.3 : The parameters f_a and S_a for A-CH₄(10%) at a number of different drift fields.

Drift Field (V/cm)	Average drift time (μ s)	f_a	S_a
1.25	164.0	0.968	33.1×10^{-3}
1.75	117.1	0.977	23.5×10^{-3}
1.84	111.4	0.978	22.5×10^{-3}
2.25	91.1	0.982	18.3×10^{-3}
4.25	48.2	0.990	10.1×10^{-3}
5.25	39.1	0.992	8.1×10^{-3}
6.25	32.8	0.994	6.0×10^{-3}
7.29	28.1	0.994	6.0×10^{-3}
8.25	24.9	0.995	5.0×10^{-3}

Table 3.4 : The parameters f_a and S_a for A-CH₄(50%) at a number of different drift fields.

Chapter 4

Determination of electron counting losses due to the finite resolving time of the electron counting electronics.

4.1 Introduction

The design of any practical detector for counting single electrons must attempt to minimize the counting losses, otherwise unacceptable fluctuations will occur which will limit the ultimate X-ray energy resolution. This chapter is concerned with the experimental determinations of the parameters f_c and S_c (see eqns. 1.25-1.27). The electron counting loss at a given drift field is determined by the resolving time τ_r of the electron counting electronics, the r.m.s. width τ of the arrival time spectrum, and the average number of counts per event N , present in the burst counter. As pointed out in section 1.11, N is determined by the X-ray energy, by electron loss by capture and by electron loss due to the finite noise-to-signal ratio of the counting electronics. In other words, N equals the product of the original number of primary electrons N_o , the fraction of electrons remaining after electron capture f_a (see chapter 3) and the fraction of electrons remaining after loss below the discriminator threshold level f_d (see chapter 2). Although it was possible to calculate N from a knowledge of N_o , f_a and f_d , it was also possible to deduce N from the data obtained during the present chapter. In order to fully determine electron counting losses, only τ_r remains to be determined. This determination is carried out in the following sections.

4.2 Experimental procedure

Two different experimental methods were used to determine the resolving time of the fast electron counting electronics. The first experimental arrangement to determine the resolving time is shown in figure 4.1. The fast electron counting electronics no. 2 were used during the present experiment (see sections 2.3 and 2.4). The proportional counter was operated at 2.50 kV using A-CH₄(50%) at 1.49 keV. The charge signals were firstly processed by the fast electron counting electronics. The fast discriminator output was then fed into a burst counter which required a 6 V bias. The burst counter was built at Leicester University Electronic Workshop and consisted of an assembly of a number of different integrated circuits (see appendix B). The burst counter became operational when its D type flip-flops and monostables were activated by pulses arriving at its input. A binary counter then registered each pulse which had

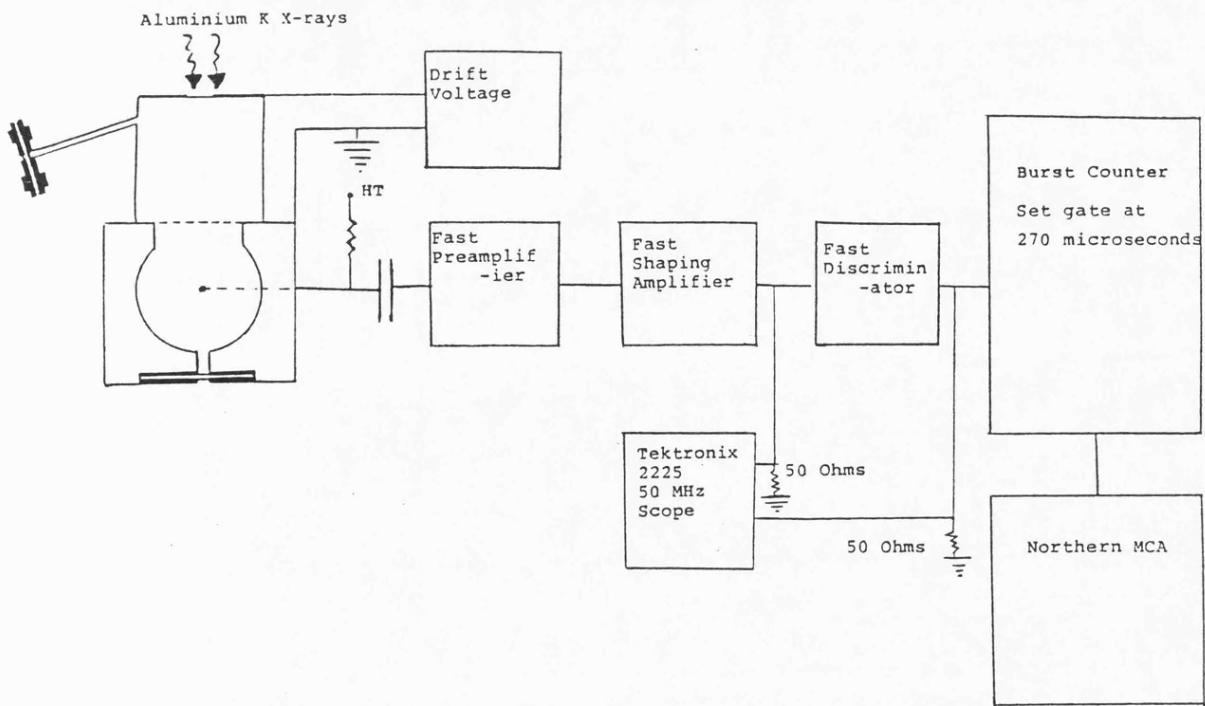


Figure 4.1 : Experimental arrangement to determine the resolving time of the fast electron counting electronics.

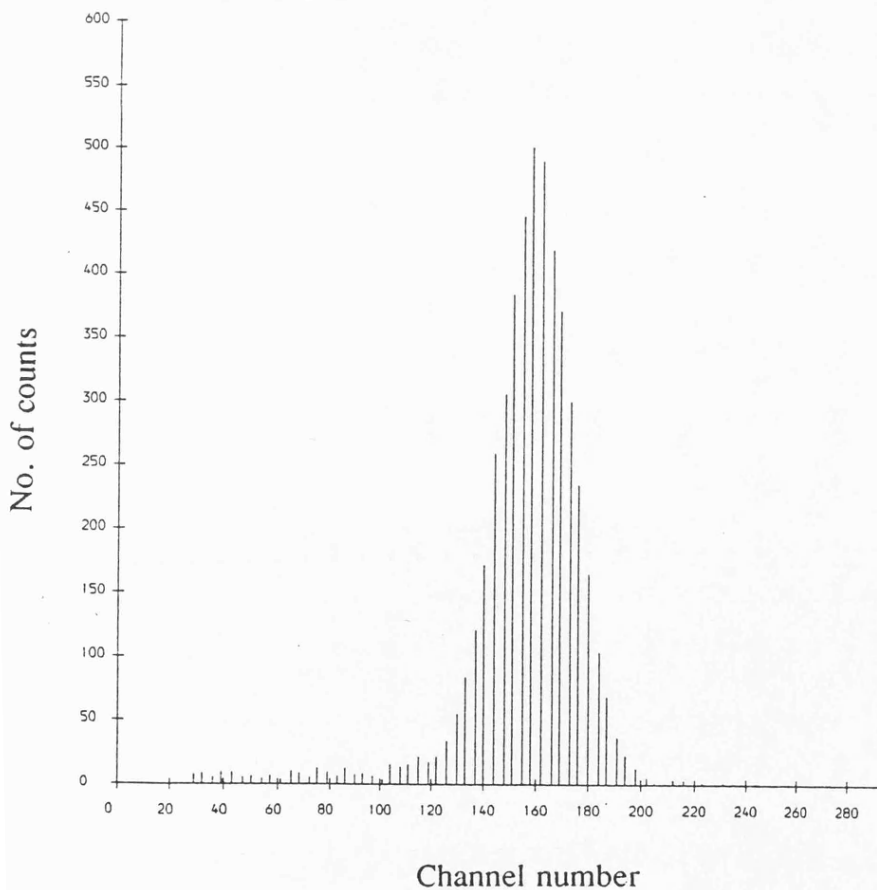


Figure 4.2 : An electron counting spectrum at the MCA using A-CH₄ (50%) when the drift field was set at 2.23 V/cm.

arrived at the burst counter input. The output of the binary counter was fed into a digital to analogue converter (DAC). The output of the DAC was then examined by an MCA. The burst counter therefore counted the number of electrons per X-ray event and converted the signals into an analogue output. The burst counter output was examined by a MCA. The discriminator threshold level was adjusted to lie just above the noise level of the fast electron counting electronics no. 2. The digital voltmeter (DVM) reading corresponding to this level was found to be 0.15 V. This value corresponds to the 3.75×10^4 counter electrons (see table 2.2). Al-K X-rays (1.49 keV) irradiated the drift window and burst counter spectra were recorded for a number of different drift fields on the MCA. The drift field range was varied from approximately 2 V/cm to 8 V/cm. This procedure was repeated with the discriminator threshold level raised to 0.50 V. This value corresponds to 1.29×10^5 counter electrons (see figure 2.26).

The second experimental arrangement to determine the resolving time is shown in figure 2.4. The pulse generator was set to a double pulse mode. The pulse generator output was fed into the test capacitor at the fast preamplifier input. The pulse heights were examined at the fast discriminator output by an oscilloscope. The separation between the twin pulses was reduced until the fast electron counting electronics failed to resolve these pulses. The time duration between the twin pulses just before the fast electron counting electronics failed to recognise the twin pulses corresponded to the resolving time of the electronics.

4.3 Experimental measurement of τ_r : results and discussion

Figure 4.2 shows the typical burst counter spectrum at 2.23 V/cm when the discriminator threshold level was set at 0.15 V. The channel number axis represents the number of counts per X-ray event at the burst counter output. It can be seen that each X-ray event is separated by discrete number of channels. The channel number axis was calibrated for the number of counts per X-ray event i.e. number of primary electrons were determined for each X-ray event. This required the knowledge of the average channel separation between the adjacent X-ray events as shown by MCA. The average number of counts per X-ray event for a given spectrum were found by the following expression :

$$N^* = n_c / \Delta n \quad 4.1$$

where N^* is the number of counts per X-ray event at the burst counter output, n_c is the average (centroid) channel number of the burst counter spectrum and Δn is the average channel separation of the burst counter spectrum. Equation 2.16

was used to calculate the average (centroid) channel number of the burst counter spectrum. For example, when the threshold discriminator level was at 0.15 V then the average channel number at 2.23 V/cm was found to be 160 channels and the average channel separation was found to be approximately 3.5 channels. The average number of counts per X-ray event at this field was therefore, approximately 46 electrons.

If N counts per X-ray event are present in the burst counter then N^* can be expressed as follows :

$$N^* = N_0 f_a f_d f_c = N f_c \quad 4.2$$

where N_0 is the original number of primary electrons, f_a is the fraction of electrons remaining after capture, f_d is the fraction of electrons above a given discriminator threshold level, f_c is the fraction of electrons which are actually counted by the burst counter (see eqn. 1.26). N is therefore the number of electrons remaining after electron loss by capture and electron loss below the discriminator threshold level. If we substitute for f_c into equation 4.2 then N^* can also be expressed as follows :

$$N^* = N - N^2 \tau_r^2 / 2\tau(\pi)^{1/2} \quad 4.3$$

where τ_r is the resolving time of the electron counting electronics and τ is the r.m.s. width of the arrival time spectrum. Tables 4.1 and 4.2 show the variation of N^* at the two different discriminator level settings used, with the drift field, r.m.s. width of the arrival time spectrum and the inverse r.m.s. width of the arrival time spectrum. The r.m.s. width of the arrival time spectrum, was calculated using equation 1.27. This required a knowledge of characteristic electron energy, the average drift distance and electron mobility. The characteristic electron energy was assumed to be 25 meV. The experimental values for electron mobility in A-CH₄(50%) were assumed to be $2.00 \times 10^{-2} \text{ cm}^2/\text{V}\mu\text{s}$ (see chapter 3). The average drift distance for the primary clusters was assumed to be 4.10 cm since the drift length equalled 5.06 cm and the mean free photon path in A-CH₄(50%) at 1.49 keV equalled 0.96 cm.

Figure 4.3 shows the variation of the average number of counts per X-ray event N^* at the burst counter output with the inverse r.m.s. width of the arrival time spectrum. The intercept on the N^* axis represents N and the slope of the line can be expressed as follows (see equation 4.3) :

Drift Field (V/cm)	τ (μs)	$1/\tau$ (μs) ⁻¹	Exptl. N* (no. of electrons)
2.23	6.80	0.15	46
2.72	5.05	0.20	45
3.21	3.93	0.25	44
4.21	2.62	0.38	42
5.19	1.92	0.52	39
6.19	1.47	0.68	37
7.20	1.17	0.85	34

Table 4.1 : Average number of counts per X-ray event at 1.49 keV for a number of different drift fields using A-CH₄(50%). The discriminator threshold level was set at 0.15 v.

Drift Field (V/cm)	r.m.s. width (μ s)	1/r.m.s width (μ s) ⁻¹	Exptl. N [*] (no. of electrons)
2.23	6.47	0.15	39
3.21	3.75	0.25	38
4.20	2.50	0.38	36
5.20	1.82	0.52	34
6.18	1.40	0.68	32
7.21	1.12	0.86	30

Table 4.2 : Average number of counts per X-ray event at 1.49 keV for a number of different drift fields using A-CH₄(50%). The discriminator threshold level was set at 0.50 V.

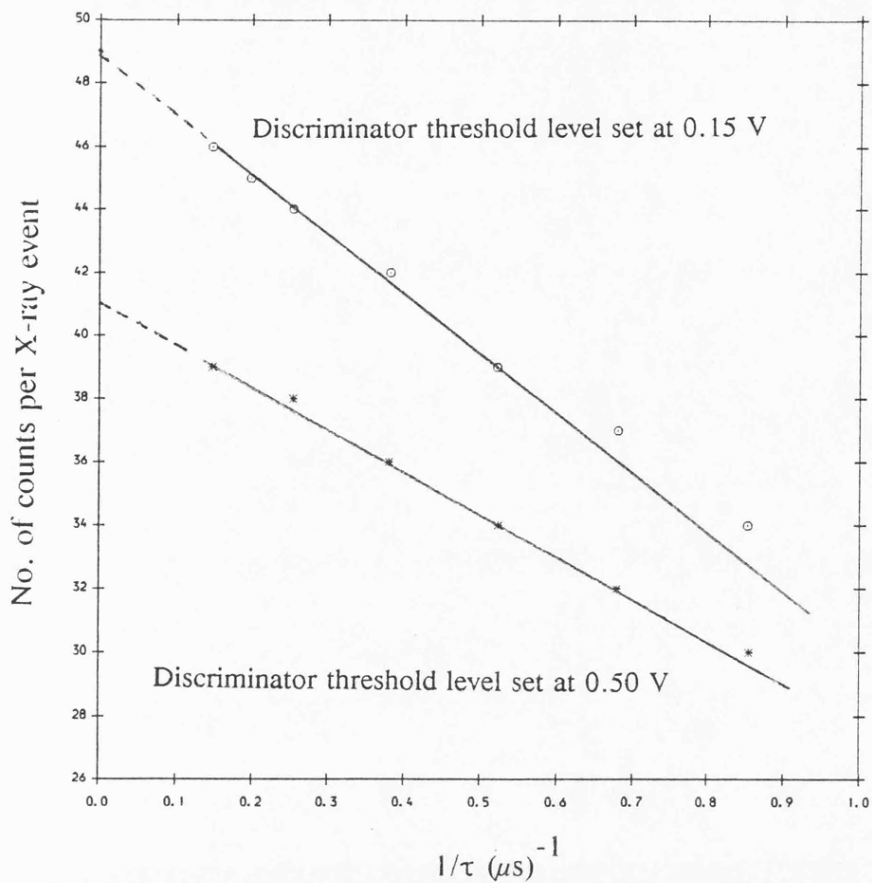


Figure 4.3 : The variation of the average number counts per X-ray event with the inverse r.m.s. width of the arrival time spectrum. A-CH₄ (50%) was used with 1.49 keV X-rays during this experiment.

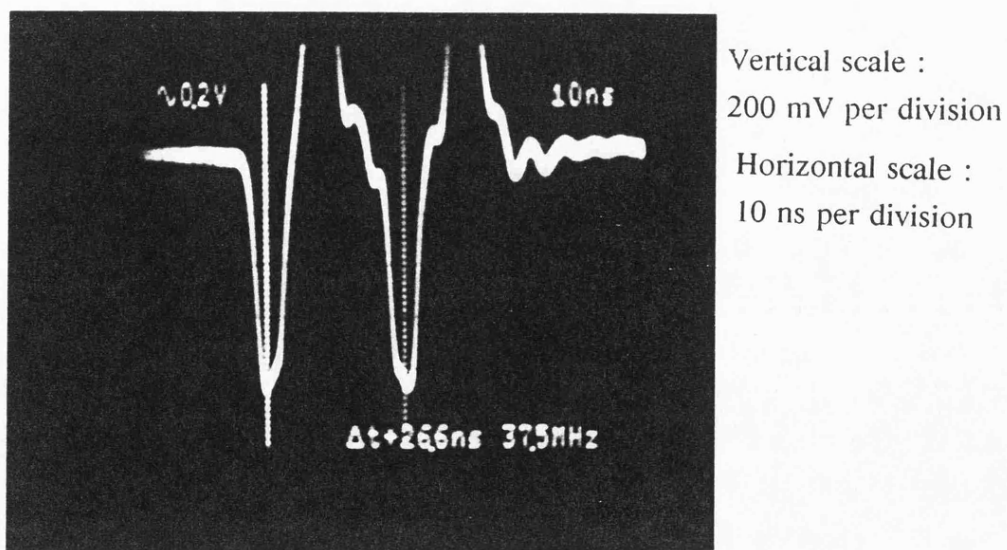


Figure 4.4 : An oscilloscope photograph demonstrating the minimum resolving time of the fast electron counting electronics (Photograph taken by the author).

Drift Field (V/cm)	f_c	S_c
2.23	0.944	0.059
2.72	0.925	0.081
3.21	0.904	0.106
4.21	0.855	0.170
5.19	0.803	0.245
6.19	0.742	0.348
7.20	0.676	0.479

Table 4.3 : The parameters f_c and S_c using A-CH₄(50%) when the fast discriminator threshold level was set at 0.15 V (N= 49 electrons).

Drift Field (V/cm)	f_c	S_c
2.23	0.951	0.052
3.21	0.916	0.092
4.20	0.873	0.146
5.20	0.826	0.211
6.18	0.774	0.292
7.21	0.717	0.395

Table 4.4 : The parameters f_c and S_c using A-CH₄(50%) when the fast discriminator threshold level was set at 0.50 V (N= 41 electrons).

$$\text{Slope} = N^2 \tau_r / 2(\pi)^{1/2} \quad 4.4$$

Using figure 4.3, the intercepts on the N^* axis were found to be 49 electrons and 41 electrons when the discriminator threshold level was at 0.15 V and 0.50 V, respectively. The slopes at 0.15 V and 0.50 V were found to be $17.8 \mu\text{s}^{-1}$ and $13.3 \mu\text{s}^{-1}$, respectively. The resolving time of the fast electron counting electronics was found by substituting these values into equation 4.4. The resolving time using data taken with 0.15 V and 0.50 V was 26.7 ns and 28.1 ns, respectively. Thus the average resolving time of the fast electron counting electronics was found to be 27.4 ns.

Figure 4.4 shows a resolving time of approximately 26.6 ns using experimental arrangement shown in figure 2.5. This result is in good agreement with the average resolving time estimated above.

4.4 Conclusions

All the variables relevant to the estimations of f_c and S_c have been determined. It is now, therefore, possible to calculate f_c and S_c at a number of different drift fields and discriminator threshold levels. Tables 4.3 and 4.4 show the variation of f_c and S_c with drift field at two different values of discriminator threshold levels. It can be seen from these tables that f_c decreases with a higher discriminator threshold level and higher drift fields. This is in contrast to the behavior of f_a which increases with higher drift fields (see tables 3.3 and 3.4). Ideally, both f_a and f_c should be unity during electron counting experiments. The parameter f_c reduces very sharply with increasing drift fields compared to the reduction of f_a with decreasing drift fields. The best electron counting efficiencies would therefore be obtained at lower drift fields (see chapter 5).

Chapter 5

Electron counting spectra.

5.1 Introduction

This chapter is concerned with the experimental determination of the X-ray energy resolution using the direct electron counting method. Electron counting spectra were taken at a number of different anode voltages at 1.49 keV and 5.89 keV using A-CH₄(10%) and A-CH₄(50%) counter gas mixtures. The essential parameters related to the X-ray energy resolution and the single electron counting efficiency have been determined in the previous chapters. These were f_a and S_a (see chapter 3), f_d and S_d (see chapter 2) and f_c and S_c (see chapter 4). The determination of these parameters allows the calculation of a theoretical X-ray energy resolution using the direct electron counting method. Hence a comparison between the theoretical and experimental X-ray energy resolutions was carried out. A comparison between the "best" experimental X-ray energy resolution achieved by the direct electron counting method and the conventional proportional counter method was also carried out.

5.2 Experimental procedure

The experimental arrangement to determine the X-ray energy resolution using the direct electron counting method is shown in figure 4.1. A-CH₄(10%) and A-CH₄(50%) were used during the present experiment. The upper charge gains prior to the onset of cathode secondaries have also been established for these counter gas mixtures in chapter 2. For example, no secondaries were present up to a charge gain 4.90×10^4 (anode voltage 1.75 kV) using A-CH₄(10%) and up to a charge gain of 1.29×10^6 (anode voltage 2.60 kV) using A-CH₄(50%). The fast electron counting electronics nos. 1, 2, 3 and 4 have already been described in chapter 2 (see sections 2.3 and 2.4). The electronic gain of the counting electronics decreased in the order no. 1, 2, 3 and 4. Thus electron counting electronics no. 1 had the highest electronic gain and no. 4 the lowest. The choice of a particular electron counting electronics depended upon the charge gain values. For example, electron counting in A-CH₄(10%) at 1.49 keV was carried out using a low charge gain of 4.90×10^4 . In this case electron counting electronics no. 1 were used. In contrast, electron counting electronics no. 3 were used for A-CH₄(50%) at 1.49 keV since a higher charge gain value of 1.29×10^6 was used for this counter gas mixture.

Electron counting spectra were taken at 1.49 keV with A-CH₄(10%) at a

number of different discriminator threshold levels using the fast electron counting electronics no. 1. The anode voltages used with A-CH₄(10%) were 1.725 kV and 1.75 kV. The primary electrons produced near the drift window travelled towards the anode wire in a low uniform drift field maintained at 1.83 V/cm. The charge signals at the anode wire were processed by the fast electron counting electronics and then by the burst counter.

Electron counting spectra at 1.49 keV were also taken using A-CH₄(50%). Electron counting electronics no. 3 were used to obtain electron counting spectra at a number of different discriminator threshold levels at 2.55 kV and 2.60 kV. The drift field in these cases was maintained at 1.22 V/cm.

Electron counting spectra using A-CH₄(50%) were also taken for a number of different drift fields while the discriminator threshold level was kept constant. This was done using the electron counting electronics no. 3 at an anode voltage of 2.60 kV. The discriminator threshold level was maintained just above the maximum counter noise level during this experiment.

Finally, the "best" electron counting spectrum at 5.89 keV using A-CH₄(50%) was also recorded. At the time of this experiment only electron counting electronics no. 1 and 2 were available. Electron counting electronics no. 2 were used. Although the maximum permissible charge gain for A-CH₄(50%) was 1.29×10^6 (anode voltage 2.60 kV), it was not possible to use a charge gain higher than 9.87×10^4 (anode voltage 2.37 kV) because of the saturation of the counting electronics. The anode voltage in this case was therefore maintained at 2.37 kV. An electron counting spectrum was taken with the drift field set to 1.63 V/cm.

The X-ray energy resolution at 5.89 keV using the direct electron counting method was also measured at Brookhaven National Laboratory, USA (Harris et al. (1990)). A MWPC with a drift region was used. The drift length was 39 mm deep and the upper cathode of the chamber consisted of an electroformed Ni grid with 360 μ m aperture. The chamber anode-cathode spacing was 4 mm with a 5 mm anode wire pitch. The counter gas mixture consisted of A-CO₂(20%). Fe⁵⁵ X-rays (5.89 keV) were incident obliquely at the drift region window to maximise the drift distance of primary electron clusters. Furthermore, a low drift field, 4.2 V/cm, was used to disperse the electron clusters adequately in time. These precautions were necessary to reduce the electron losses due to the finite resolving time of the electron counting electronics. In the present work, no electron counting was attempted using A-CO₂(20%) because of a low mean electron lifetime in this counter gas mixture (see section 3.9). The results from Brookhaven National Laboratory are,

however, included in this chapter to provide a comparison between the "best" X-ray energy resolution possible at 5.89 keV which was measured here using A-CH₄(50%).

5.3 X-ray energy resolution measurements : results and discussion

Figure 5.1 shows the electron counting spectra at 1.49 keV using A-CH₄(10%) operated at 1.725 kV and 1.750 kV. The number of counts per X-ray event at the burst counter output, N^* , for a given discriminator threshold level were calculated from the electron counting spectrum using equation 4.1. Each spectrum has been corrected for a small amount of electron loss due to a finite resolving time of the fast electron counting electronics (see appendix C). The fast electron counting electronics no. 1. were used to obtain electron counting spectra using A-CH₄(10%). The discriminator charge level shown in figure 5.1 was obtained from the charge calibration of these electronics carried out in chapter 2 (see figure 2.20). The intercept on the vertical axis of figure 5.1 corresponds to the original number of primary electrons, N_0 , produced in A-CH₄(10%) and the inverse slope of the lines equals the average charge gain in A-CH₄(10%) at the given anode voltages. Using figure 5.1, N_0 equals 52 electrons. The average energy dissipated to create a single electron-ion pair W therefore equals 28.7 eV. The average charge gains at 1.725 kV and 1.750 kV equal 3.81×10^4 and 4.71×10^4 , respectively. These charge gains are in good agreement with those obtained in chapter 2 using differential and integral pulse height spectra resulting from UV excitation (see table 2.2).

Figure 5.2 shows the variation of the relative %FWHM X-ray energy resolution at 1.49 keV in A-CH₄(10%) with the discriminator charge level. The X-ray energy resolution deteriorates with increasing discriminator threshold levels due to a reduction in signal-to-noise ratio i.e. a reduction in N^* . The solid line shown in figure 5.2 represents the variation of the theoretical %FWHM X-ray energy resolution at 1.49 keV with discriminator charge level. The theoretical %FWHM X-ray energy resolution was calculated from a knowledge of f_a , S_a , f_d , S_d , f_c , S_c and N_0 (original number of primaries). These parameters were substituted into equation 1.20 which was then by multiplied by a factor of 2.35 to yield the relative FWHM X-ray energy resolution. Table 5.1 shows the variation of these parameters and the variation of theoretical and experimental %FWHM X-ray energy resolution with increasing discriminator threshold level. The calculation of f_a required the knowledge of the average drift time, therefore the electron mobility, and the mean electron lifetime in A-CH₄(10%). The determination of these quantities was carried out in chapter 3

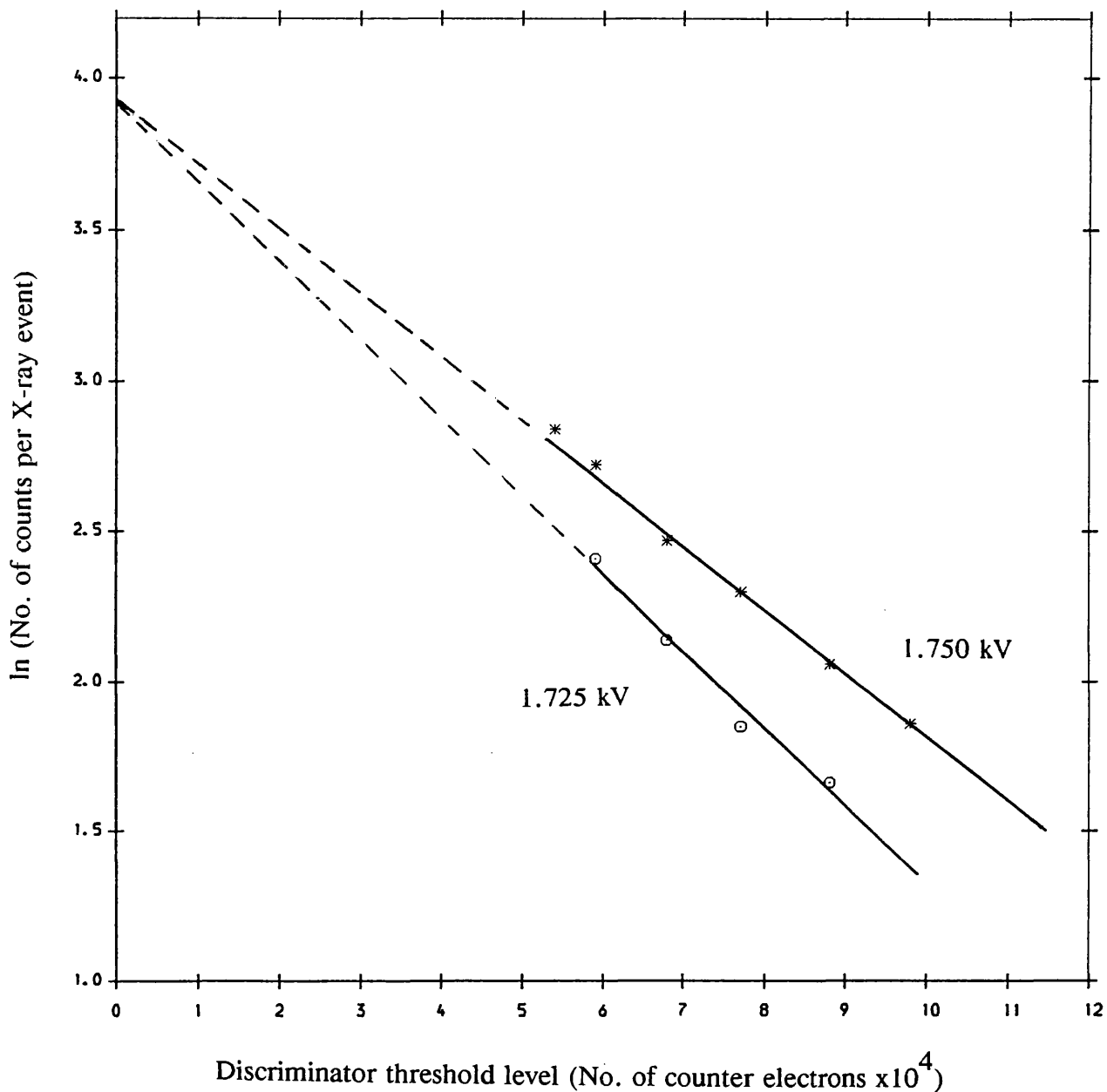


Figure 5.1 : "Single" electron spectra from 1.49 keV clouds using A-CH₄(10%) operated at 1.725 kV and 1.75 kV. A small correction has been made for counting losses. The abscissa represents the discriminator threshold level measured in electrons from the counter. The intercept on the vertical axis represents the original number of primary electrons created by 1.49 keV X-rays. Thus W equals 28.7 ± 0.6 eV for A-CH₄(10%).

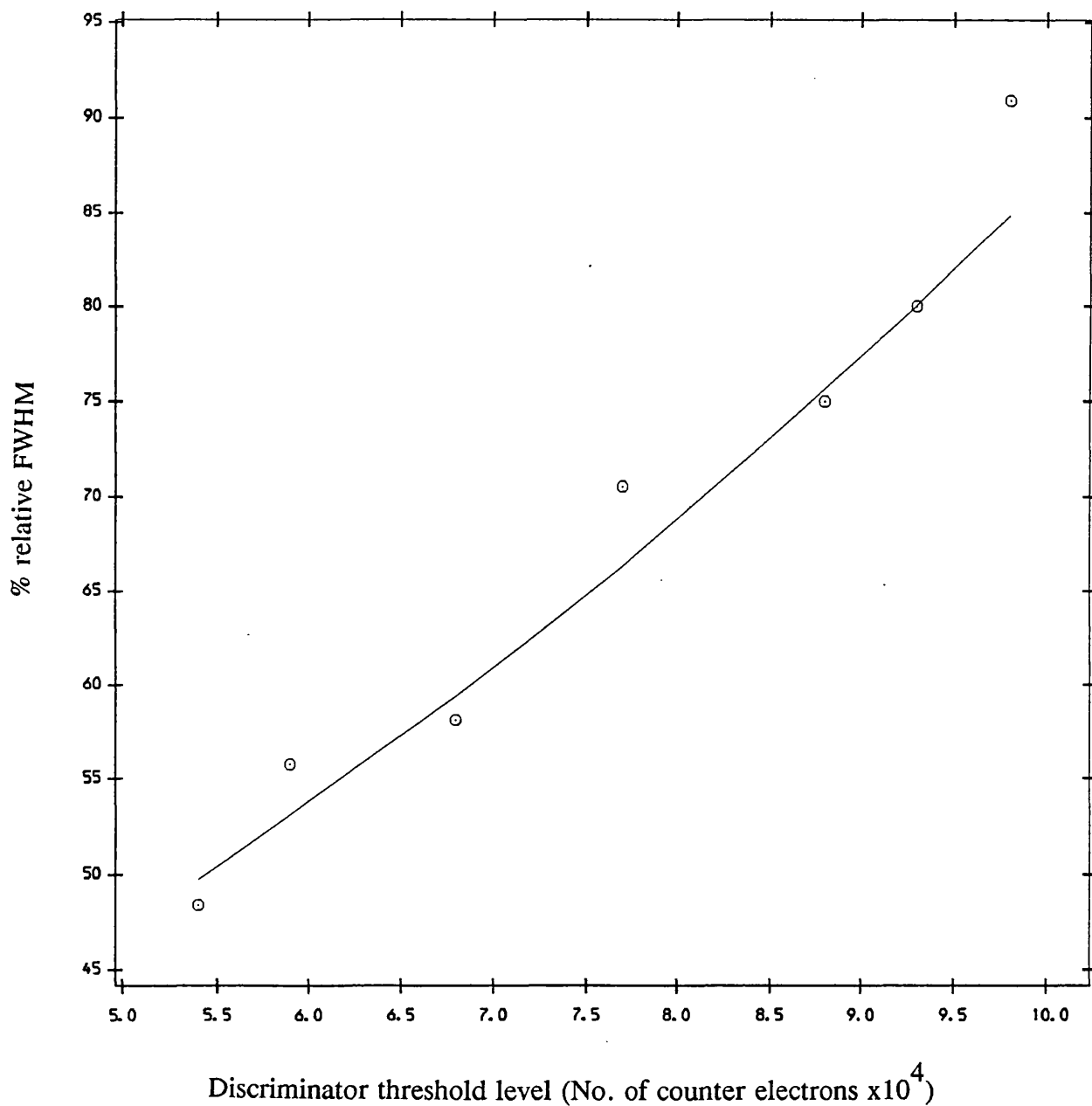


Figure 5.2 : X-ray energy resolution by the direct electron counting method. This figure shows the variation of %FWHM energy resolution at 1.49 keV with discriminator threshold level using A-CH₄(10%). The solid line indicates the theoretical %FWHM energy resolution (see table 5.1). The X-ray energy resolution is poor due to a low signal-to-noise ratio for A-CH₄(10%).

Disr. th. level (V)	Disr. charge (no. of counter electrons)	f_d	S_d/f_a	N	f_c	$S_c / f_a f_d$	Th. %FWHM X-ray rsln.	Exp. %FWHM X-ray rsln.
0.45	5.40×10^4	0.332	2.04	17.02	0.977	0.072	49.74	48.39
0.50	5.90×10^4	0.300	2.37	15.38	0.979	0.073	53.15	55.77
0.60	6.80×10^4	0.250	3.04	12.82	0.983	0.070	59.38	58.14
0.70	7.70×10^4	0.208	3.86	10.66	0.986	0.069	66.31	70.56
0.80	8.80×10^4	0.166	5.10	8.51	0.988	0.074	75.66	75.00
0.85	9.30×10^4	0.150	5.75	7.69	0.990	0.068	80.03	80.00
0.90	9.80×10^4	0.135	6.50	6.92	0.991	0.068	84.86	90.91

Table 5.1 : To show the variation of the theoretical and experimental X-ray energy resolution with discriminator threshold level using A-CH₄(10%). The drift field was set at 1.83 V/cm (i.e. $f_a=0.986$ and $S_a=0.014$, respectively).

(see table 3.2). Using equations 1.21 and 1.22 the parameters f_a and S_a at 1.83 V/cm equal 0.986 and 0.014, respectively. The calculation of f_d and S_d required the knowledge of the discriminator charge level and the average charge gain using A-CH₄(10%) operated at 1.75 kV. The average charge gain at 1.75 kV was assumed to be 4.90×10^4 (see table 2.1). The variation of f_d and S_d with discriminator charge level was calculated using equations 1.23 and 1.24 and is shown in table 5.1. The calculation of f_c and S_c required the knowledge of the resolving time τ_r of the electron counting electronics, the r.m.s. width τ of the arrival time spectrum at 1.83 V/cm and the number of counts per X-ray event N^* at the fast discriminator output. The resolving time of the fast electron counting electronics has been found to be 26.6 ns (see chapter 4). Using equation 1.27, the r.m.s. width of the arrival time spectrum at 1.83 V/cm was found to be 5.53 μ s. The parameters f_c and S_c were calculated using equations 1.25 and 1.26 and are also shown in table 5.1.

The "best" experimental X-ray energy resolution in A-CH₄(10%) at 1.49 keV using the direct electron counting method was found to be 48.4 %FWHM at 1.75 kV when the discriminator level was set to a minimum value i.e. at 54000 counter electrons. This value is in good agreement with the 49.7 %FWHM theoretical X-ray energy resolution at 1.49 keV (see table 5.1). Figure 5.3 shows the corresponding electron counting spectrum. The best X-ray energy resolution at 1.49 keV using the conventional proportional counter was found to be 28 %FWHM (see section 2.5).

It can be seen from table 5.1 that when the discriminator charge level was at 54000 counter electrons then $(1-f_a)$, $(1-f_d)$ and $(1-f_c)$ equalled 0.014, 0.668 and 0.023, respectively. Thus 1.4 % electron loss occurred by electron capture to the counter gas impurities, 66.8 % electron loss occurred below the discriminator threshold level of the electron counting electronics and 2.3 % electron loss occurred due to the finite resolving time of the electron counting electronics. The main limiting factor to the X-ray energy resolution using A-CH₄(10%) was therefore a low signal-to-noise ratio. This limitation was imposed by an "early" onset of cathode secondaries above the charge gain 4.90×10^4 .

Figure 5.4 shows the electron counting spectra at 1.49 keV using A-CH₄(50%) operated at 2.55 kV and 2.60 kV. The discriminator charge level shown in figure 5.4 was obtained from the calibration of the fast electron counting electronics which has already been carried out in chapter 2. For example, electron counting electronics no. 3 were used to obtain electron counting spectra at 2.55 kV and 2.60 kV. Figure 2.9 was therefore used to find

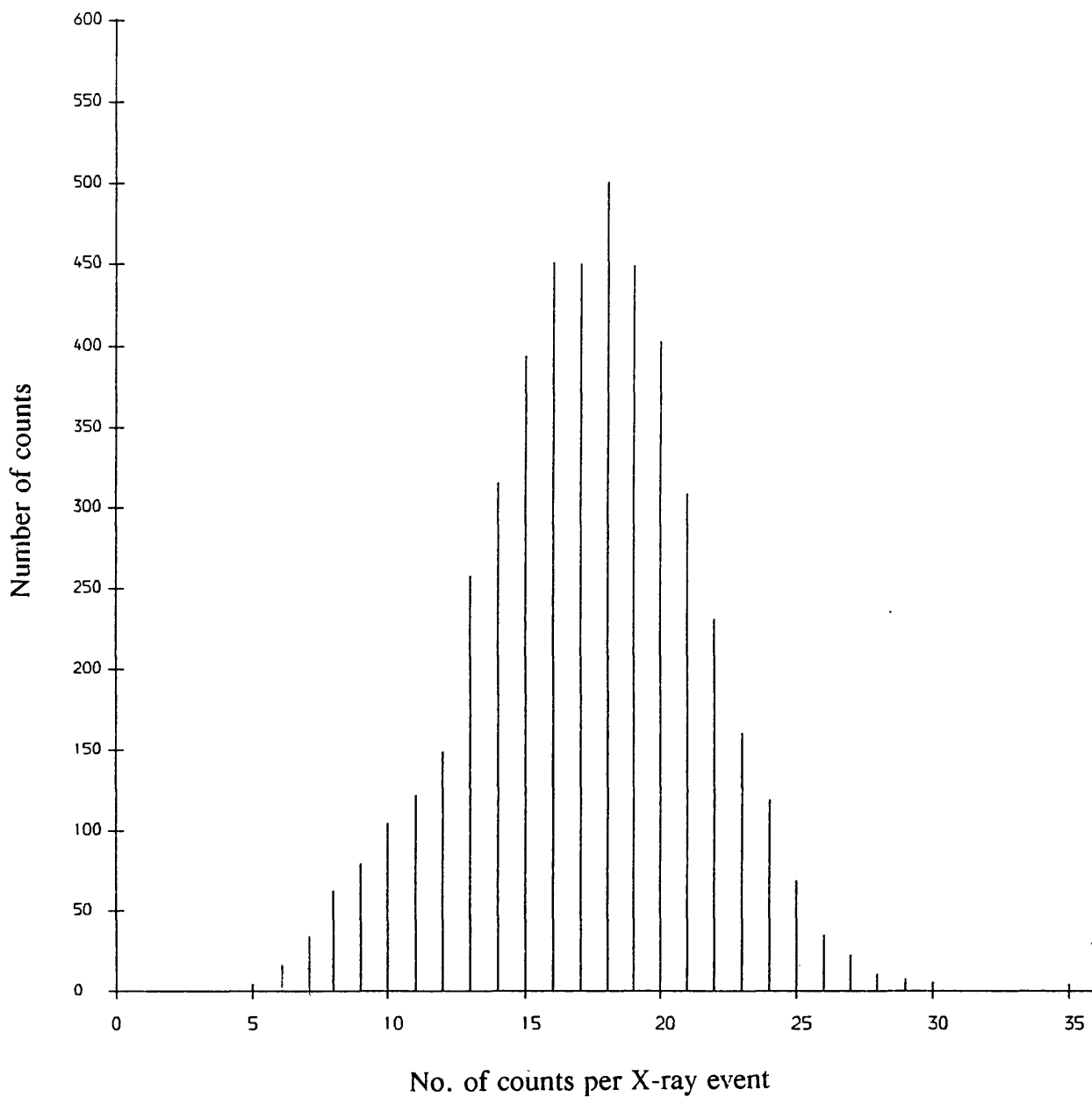


Figure 5.3 : The best electron counting spectrum from 1.49 keV using A-CH₄(10%). The X-ray energy resolution is 48.4 %FWHM. This compares to 28.0 %FWHM obtained from a charge spectrum using A-CH₄(10%) with the same counter.

the charge level corresponding to a given discriminator threshold level. A small amount of correction has also been applied to each electron counting spectrum to take into account the electron loss due to the finite resolving time of the electron counting electronics. The intercept on the vertical axis of figure 5.4 was found to be 52 electrons (original number of primaries in A-CH₄(50%)). The value of the parameter W in A-CH₄(50%) therefore equals 28.7 eV. The average charge gains calculated from the inverse slopes of these lines were 6.67×10^5 and 1.02×10^6 at 2.55 kV and 2.60 kV, respectively. These results are also in good agreement with those determined in chapter 2 using the differential and integral pulse height spectra resulting from UV excitation (see table 2.4).

Figure 5.5 shows the variation of the relative %FWHM X-ray energy resolution at 1.49 keV using A-CH₄(50%) with the discriminator charge level. The solid line shown in figure 5.5 indicates the theoretical %FWHM X-ray energy resolution at 1.49 keV using the direct electron counting method. The theoretical %FWHM X-ray energy resolution in A-CH₄(50%) at a number of different counter charge levels was calculated in a similar manner to that described for A-CH₄(10%) above. Table 5.2 shows the variation of f_a , S_a , f_d , S_d , f_c , S_c and theoretical and experimental X-ray energy resolution at a number of different discriminator threshold levels.

Figure 5.6 shows the variation with drift field of the relative %FWHM X-ray energy resolution at 1.49 keV using A-CH₄(50%) operated at 2.60 kV. The solid line in figure 5.6 indicates the variation of the theoretical X-ray energy resolution using A-CH₄(50%) with the sum of drift field and leakage field. Table 5.3 shows the variation of the theoretical and experimental X-ray energy resolution with the sum of drift and leakage field. Figure 5.6 and table 5.3 demonstrate that the useful drift range for the best X-ray energy resolution using the direct electron counting method is rather small, approximately 0.75 V/cm to 1.75 V/cm. At drift fields below 0.75 V/cm the drift times become comparable to the mean electron lifetime causing a large amount of electron loss due to electron capture. Furthermore, below a drift field of 0.75 V/cm the back-diffusion of primary electrons to the entrance window occurs due to a relatively small mean absorption X-ray depth, 0.96 cm at 1.49 keV. These two factors lead to a rapid deterioration of X-ray energy resolution below 0.75 V/cm. Figure 5.6 shows a large discrepancy between the theoretical and experimental curves below 0.75 V/cm. This has arisen because electron losses by back-diffusion were not allowed for when calculating theoretical X-ray energy resolutions. At drift fields above 1.75 V/cm electron losses due to the finite resolving time of the electron counting electronics become a dominant factor

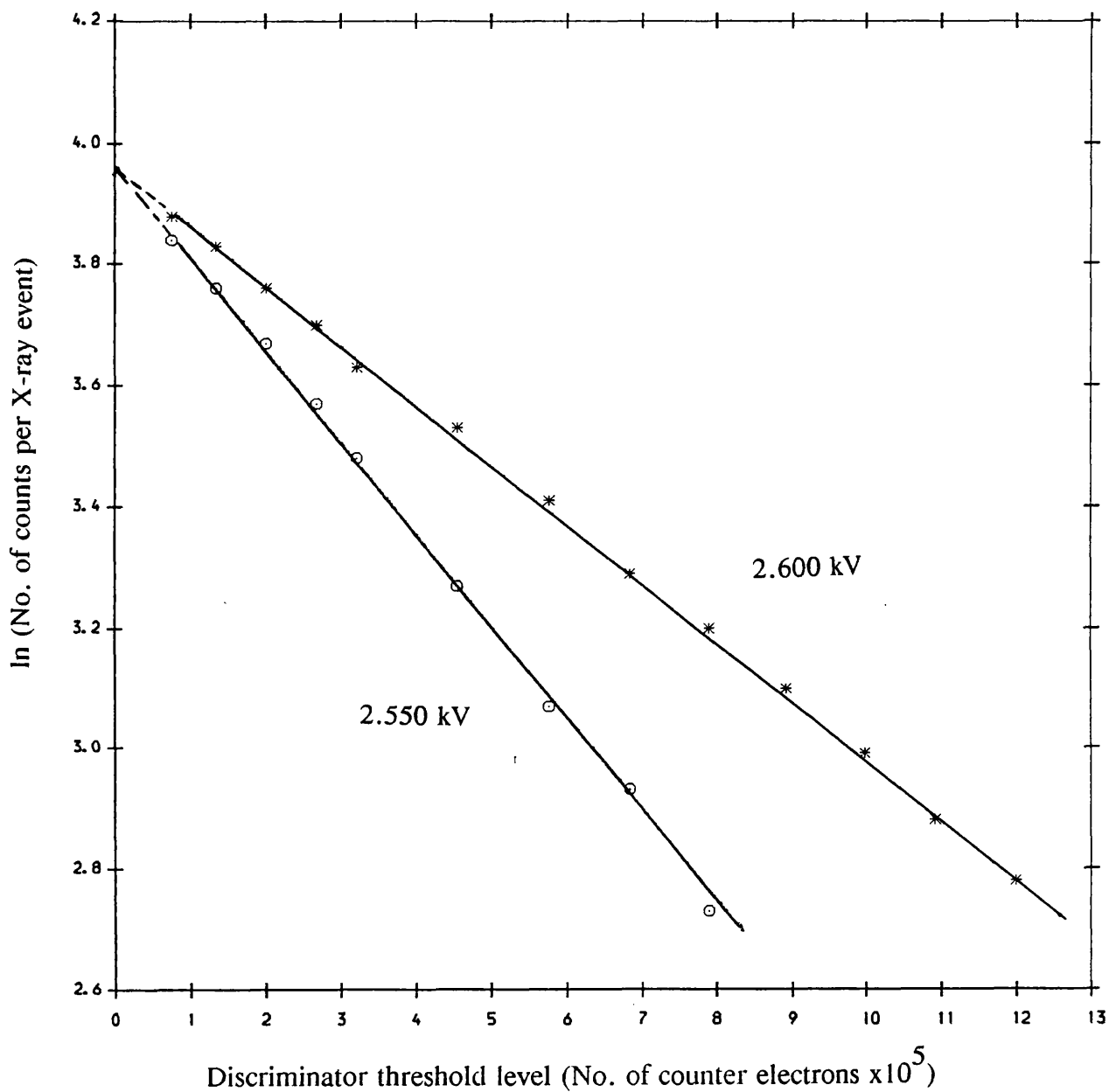


Figure 5.4 : "Single" electron spectra from 1.49 keV clouds using A-CH₄(50%) operated at 2.55 kV and 2.60 kV. A small correction has been made for counting losses. The abscissa represents the discriminator threshold level measured in electrons from the counter. The intercept on the vertical axis represents the original number of primary electrons created by 1.49 keV X-rays. Thus W equals 28.7 ± 0.6 eV for A-CH₄(50%).

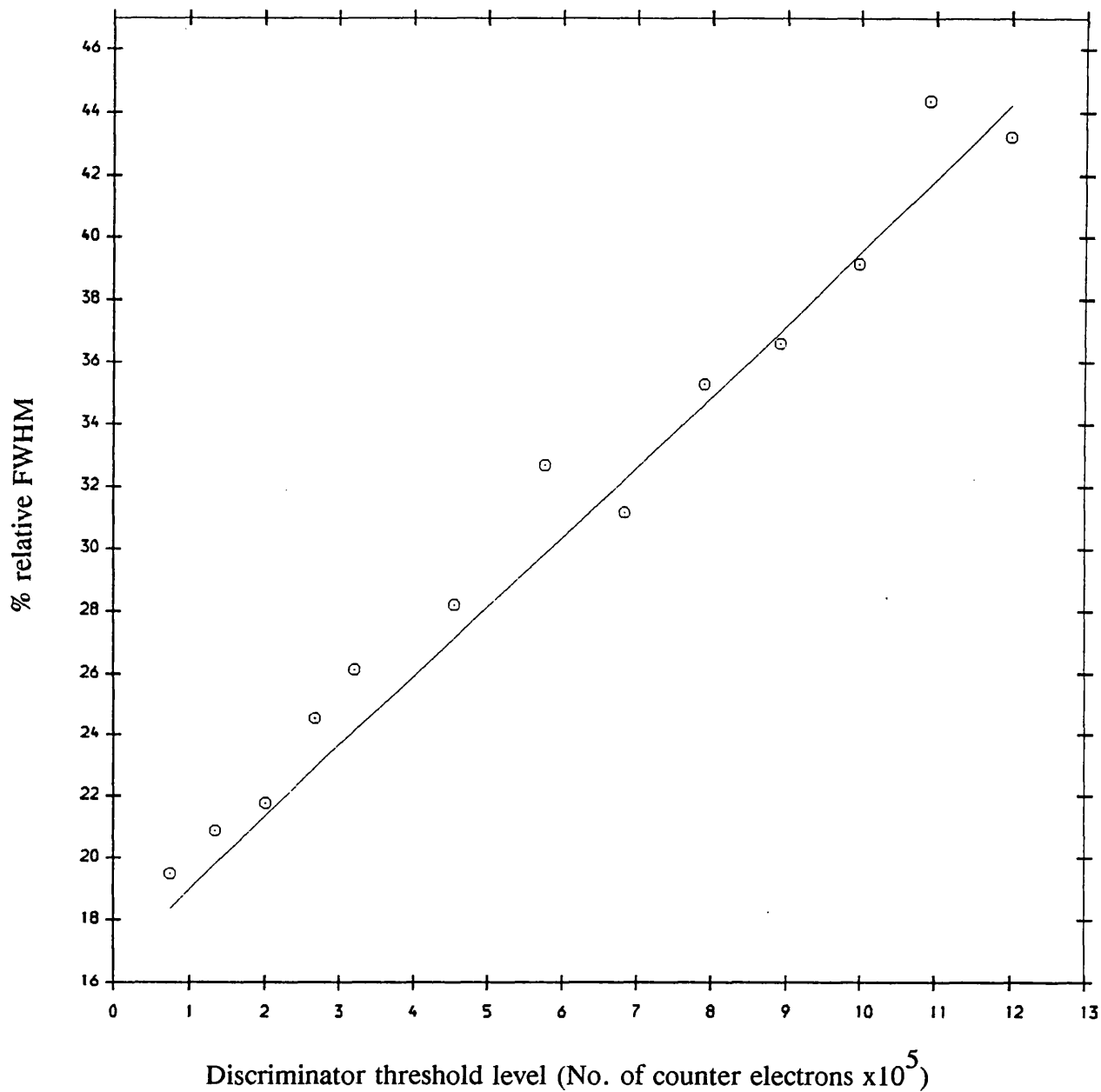


Figure 5.5 : X-ray energy resolution by the direct electron counting method. This figure shows the variation of %FWHM energy resolution at 1.49 keV with discriminator threshold level using A-CH₄(50%). The solid line indicates the theoretical %FWHM X-ray energy resolution (see table 5.2).

Disr. th. level (V)	Disr. charge (no. of counter electrons)	f_d	S_d/f_a	N	f_c	$S_c / f_a f_d$	Th. %FWHM X-ray rsln.	Exp. %FWHM X-ray rsln.
0.00	7.50×10^4	0.944	0.061	47.47	0.979	0.024	18.38	19.50
0.05	13.39×10^4	0.901	0.114	45.31	0.980	0.023	19.82	20.89
0.10	20.09×10^4	0.856	0.174	43.04	0.981	0.023	21.37	21.77
0.15	26.79×10^4	0.813	0.238	40.88	0.982	0.023	22.91	24.55
0.20	32.15×10^4	0.779	0.293	39.17	0.983	0.023	24.15	26.15
0.30	45.54×10^4	0.703	0.437	35.35	0.984	0.024	27.15	28.21
0.40	57.60×10^4	0.640	0.582	32.18	0.986	0.023	29.83	32.69
0.50	68.31×10^4	0.589	0.722	29.62	0.987	0.023	32.23	31.18
0.60	79.03×10^4	0.542	0.874	27.25	0.988	0.023	34.64	35.29
0.70	89.07×10^4	0.501	1.030	25.19	0.989	0.023	36.96	36.60
0.80	99.79×10^4	0.461	1.209	23.18	0.990	0.023	39.44	39.13
0.90	10.92×10^5	0.429	1.376	21.57	0.990	0.024	41.65	44.36
1.00	11.99×10^5	0.395	1.584	19.86	0.991	0.024	44.22	43.24

Table 5.2 : To show the variation of the theoretical and experimental X-ray energy resolution with discriminator threshold level using A-CH₄(50%). The drift field was set at 1.22 V/cm (i.e. $f_a=0.967$ and $S_a=0.033$, respectively).

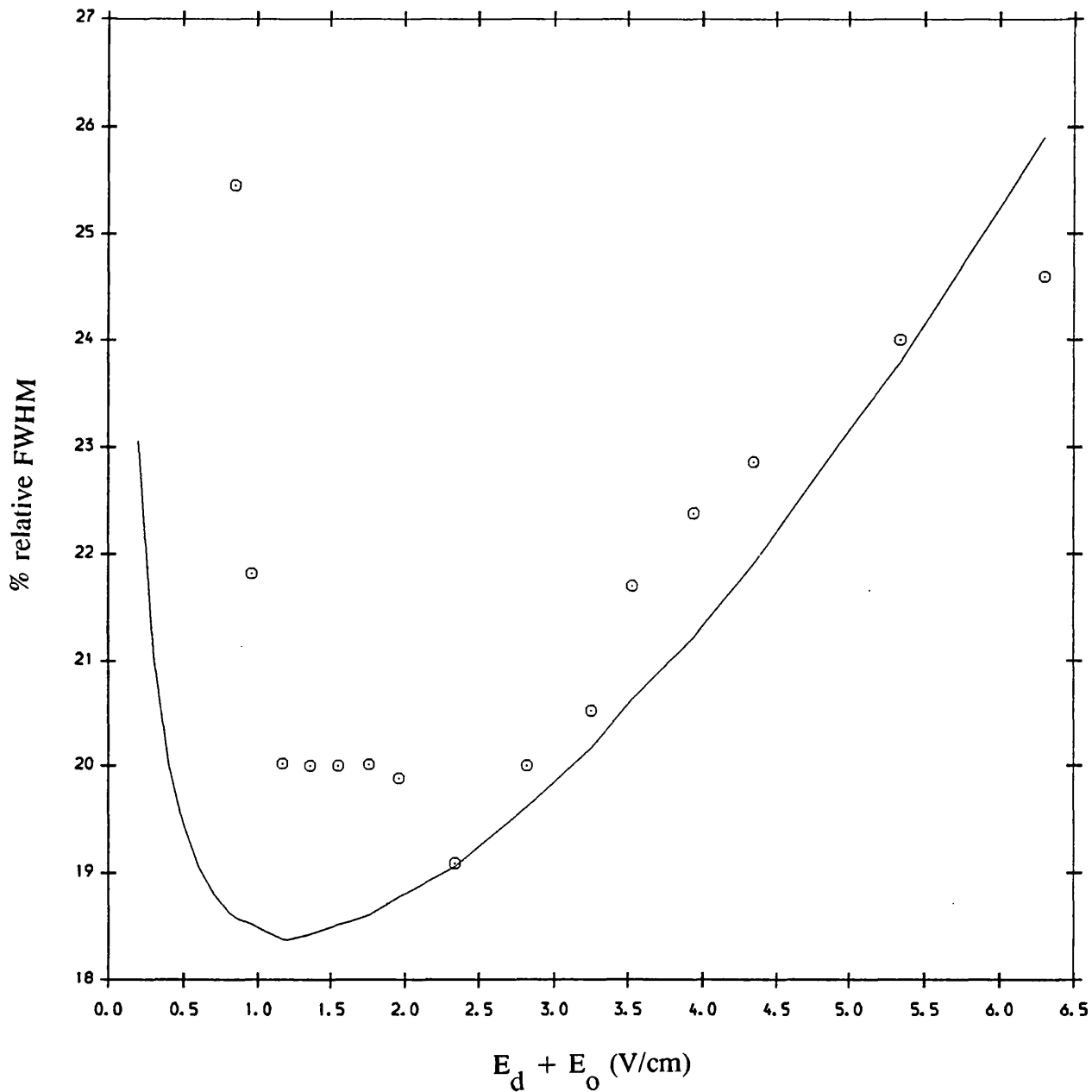


Figure 5.6 : X-ray energy resolution by the direct electron counting method. This figure shows the variation of %FWHM energy resolution at 1.49 keV with drift field using A-CH₄ (50%). The solid line indicates the theoretical %FWHM X-ray energy resolution (see table 5.3).

E_d	t_d	f_a	S_a	S_d/f_a	τ	N	f_c	S_c	Th.	Exp.
+	(μs)				(μs)			$/f_a f_d$	%FWHM	%FWHM
E_o									X-ray	X-ray
V/cm									rsln.	rsln.
0.20	1025	0.815	0.227	0.072	253.1	40.01	0.999	0.001	23.06	-
0.30	683.1	0.872	0.147	0.068	137.8	42.81	0.998	0.002	21.04	-
0.40	512.5	0.903	0.107	0.065	89.49	44.33	0.996	0.005	20.01	-
0.50	410.0	0.921	0.086	0.064	64.03	45.21	0.995	0.006	19.44	-
0.60	341.7	0.934	0.071	0.063	48.71	45.85	0.993	0.008	19.06	25.46
0.70	292.8	0.943	0.060	0.063	38.65	46.29	0.991	0.010	18.81	21.82
0.80	256.3	0.950	0.053	0.062	31.64	46.63	0.989	0.012	18.64	20.00
0.85	241.2	0.953	0.049	0.062	28.89	46.78	0.988	0.014	18.58	25.46
0.96	213.5	0.958	0.044	0.062	24.07	47.03	0.985	0.017	18.52	21.82
1.17	175.2	0.966	0.035	0.061	17.89	47.42	0.980	0.022	18.38	20.02
1.36	150.7	0.970	0.031	0.061	14.27	47.62	0.975	0.028	18.43	20.00
1.55	132.3	0.974	0.027	0.061	11.73	47.81	0.969	0.035	18.43	20.00
1.76	116.5	0.977	0.024	0.060	9.70	47.96	0.963	0.042	18.07	20.01
1.96	104.6	0.979	0.022	0.060	8.25	48.06	0.956	0.050	18.78	19.88
2.34	87.6	0.983	0.017	0.060	6.32	48.25	0.943	0.065	19.06	19.09

continued overleaf.....

E_d	t_d	f_a	S_a	S_d/f_a	τ	N	f_c	S_c	Th.	Exp.
+	(μs)				(μs)			$/f_a f_d$	%FWHM	%FWHM
E_o									X-ray	X-ray
V/cm									rsln.	rsln.
2.82	72.7	0.986	0.014	0.060	4.78	48.40	0.924	0.088	19.61	20.00
3.25	63.1	0.988	0.012	0.060	3.86	48.50	0.906	0.111	20.17	20.53
3.53	58.1	0.988	0.012	0.060	3.41	48.50	0.893	0.129	20.64	21.70
3.94	52.0	0.990	0.010	0.060	2.90	48.60	0.874	0.154	21.22	22.38
4.34	47.2	0.991	0.009	0.060	2.50	48.65	0.854	0.183	21.91	22.86
5.34	38.4	0.992	0.008	0.060	1.84	48.70	0.801	0.265	23.79	24.00
6.30	32.5	0.994	0.006	0.059	1.43	48.79	0.744	0.367	25.91	24.59

Table 5.3 : To show the variation of the theoretical and experimental X-ray energy resolution with the sum of drift field and leakage field using A-CH₄(50%). The discriminator threshold level was set at 75000 electrons and charge gain was maintained at 1.29×10^6 (i.e. $f_d=0.944$ and $S_d=0.059$, respectively).

leading to a deterioration in X-ray energy resolution.

The "best" experimental X-ray energy resolution in A-CH₄(50%) at 1.49 keV using the direct electron counting method was found to be 19.5 %FWHM at 2.60 kV when the discriminator charge level was set to its minimum value i.e. at 75000 counter electrons. This value is in good agreement with the 18.4 %FWHM theoretical X-ray energy resolution at 1.49 keV (see table 5.2). Table 5.2 indicates the different types of electron losses with the discriminator threshold level set to 75000 counter electrons. It can be seen from this table that $(1-f_a)$, $(1-f_d)$ and $(1-f_c)$ equal 0.033, 0.056 and 0.021, respectively. Thus 3.3 % electron loss occurs due to electron capture, 5.6 % electron loss occurs below the discriminator threshold level and 2.1 % electron loss occurs due to the finite resolving time of the electron counting electronics. Figure 5.7 shows the "best" electron counting spectrum at 1.49 keV using A-CH₄(50%) operated at 2.60 kV.

The "best" X-ray energy resolution in A-CH₄(50%) at 5.89 keV using the direct electron counting method was found to be 18.5 %FWHM (see figure 5.8). The maximum values of f_a , f_d and f_c were 0.981, 0.684 and 0.891, respectively i.e. $(1-f_a)$, $(1-f_d)$ and $(1-f_c)$ equal 0.019, 0.316 and 0.109, respectively. Thus, 1.9 % electron loss occurs due to electron capture, 31.6 % electron loss occurs below the discriminator threshold level and 10.9 % electron loss occurs due to the finite resolving time of the electron counting electronics. Taking these losses into account, the theoretical X-ray energy resolution becomes 15.3 %FWHM. The discrepancy between the observed and theoretical X-ray energy resolution may be attributed to electron losses at the transmission grid periphery (see section 3.5). The r.m.s. width of an electron swarm after drifting a distance $(d-\lambda)$, where d is the length of the drift tube and λ is the mean absorption depth of X-rays, equals 3.10 mm when the drift field equals 1.63 V/cm (see eqn. 3.11). Thus 99.9% of the charge is present within $\pm 4\sigma$. The transmission grid radius equals 12.5 mm thus no electron losses at the transmission grid periphery would occur provided that the X-rays incident on the drift window are well collimated. The radius of the present drift window equals 3.5 mm. Thus a few percent electron loss may have occurred due to the primary electron formation near the drift window periphery.

Electron counting spectrum at 5.89 keV showed a tail towards small amplitudes (see figure 5.8). This observation can be explained in terms of the residual number of counts per X-ray event remaining after loss by capture, losses below discriminator threshold level and counting loss. Although, the average electron loss is approximately 50 % i.e. average number of counts per X-ray events equals 100, some events will suffer a higher loss.

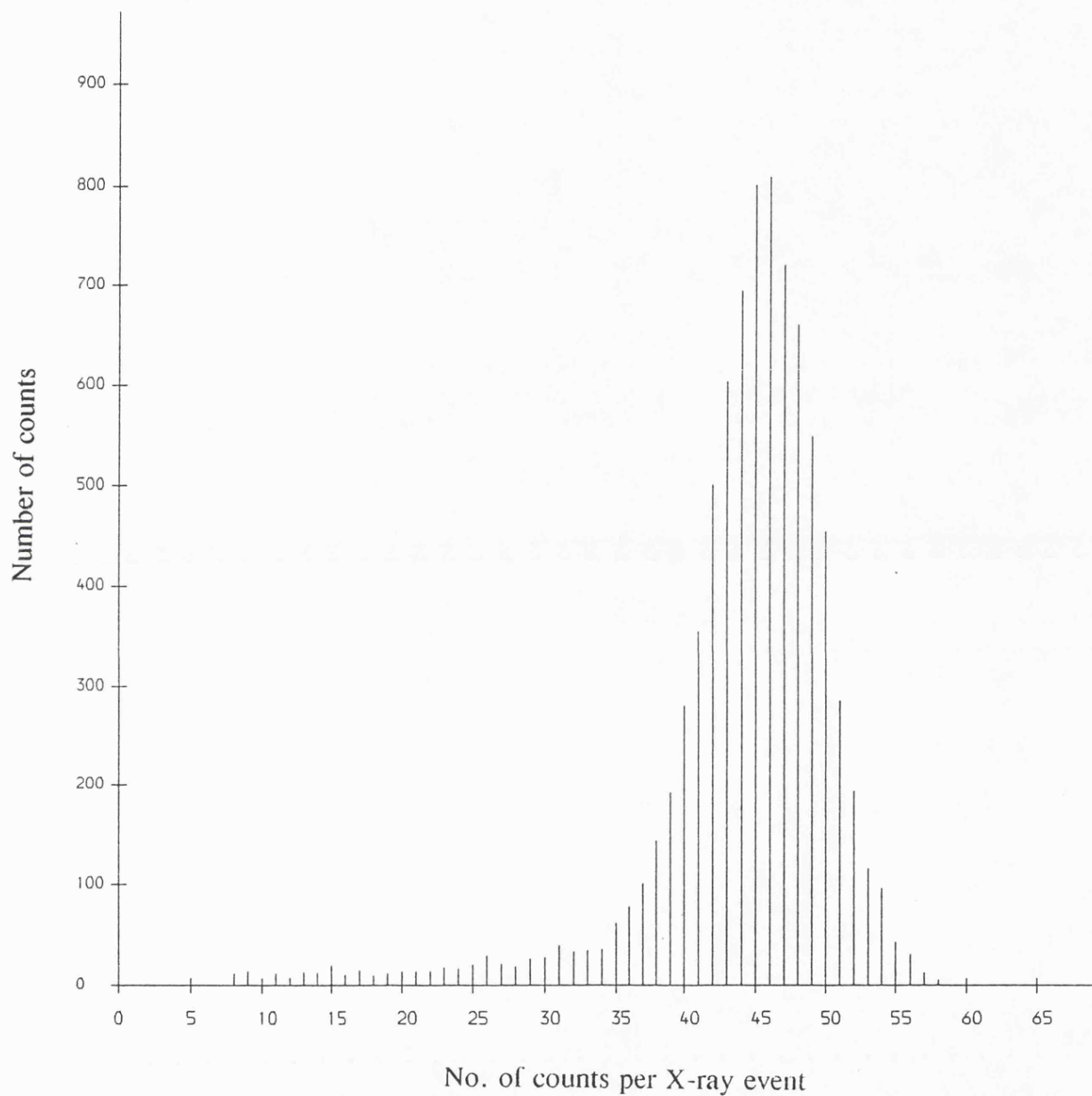


Figure 5.7 : The best electron-counting spectrum from 1.49 keV using A-CH₄ (50%). The X-ray energy resolution is 19.5 %FWHM. This compares to 28.0 %FWHM obtained from a charge spectrum using A-CH₄ (50%) with the same counter.

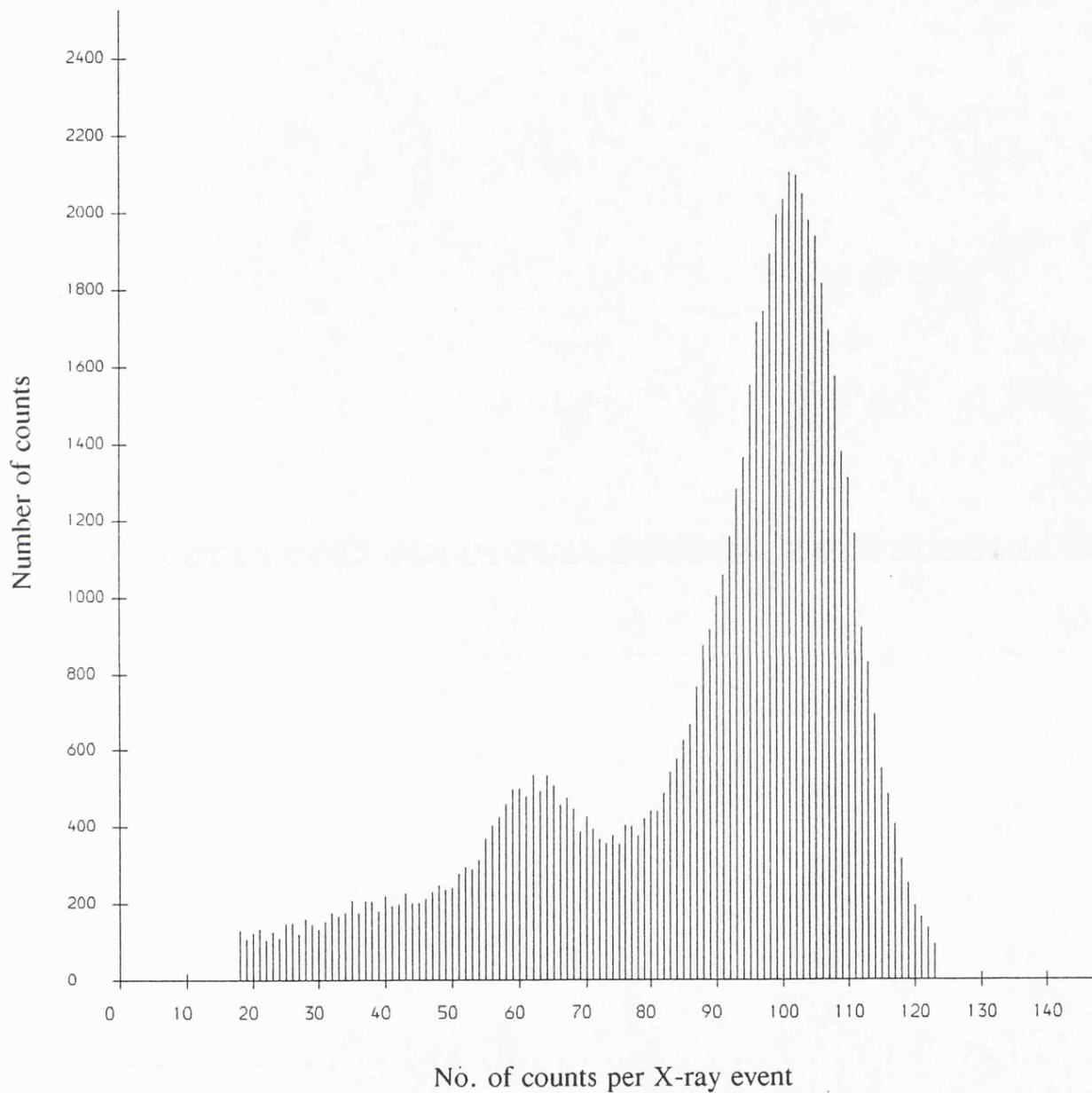


Figure 5.8 : The best electron counting spectrum from 5.98 keV using A-CH₄ (50%). The X-ray energy resolution is 18.5 %FWHM. This compares to 17.0 %FWHM obtained from a charge spectrum using A-CH₄ (50%) with the same counter.

Figure 5.8 shows the "best" electron counting spectrum at 5.89 keV using A-CH₄(50%) corresponding to an X-ray energy resolution of 18.5 %FWHM. This compares to the 19.0 %FWHM at 5.89 keV using A-CO₂(20%), achieved at the Brookhaven National Laboratory (Harris et al. (1990)). Although the theoretical X-ray energy resolution at 5.89 keV using the conventional proportional counter is 13 %FWHM, the "best" experimental value was found to be approximately 17 %FWHM (see section 2.5).

In the present investigations, the maximum values of parameters f_a , f_d and f_c using A-CO₂(20%) were found to be 0.04, 0.972 and 0.999, respectively. This implies that the theoretical X-ray energy resolution at 1.49 keV and 5.89 keV for A-CO₂(20%) equals approximately 163 %FWHM and 82 %FWHM, respectively. This very poor value is the direct result of the low mean electron lifetime in the present experiment.

5.4 Conclusions

Electron counting spectra at 1.49 keV in A-CH₄(10%) and A-CH₄(50%) using the direct electron counting method were successfully recorded. An electron counting spectrum at 5.89 keV using A-CH₄(50%) was also recorded. The theoretical X-ray energy resolution at 1.49 and 5.89 keV using the direct electron counting method is 14.6 %FWHM and 7.0 %FWHM, respectively, provided an 100 % electron counting efficiency is attained (i.e. f_a , f_d and f_c equal unity). It was found, however, that while using A-CH₄(10%) the maximum values of f_a , f_d and f_c were 0.986, 0.332 and 0.977, respectively. In other words, the main limiting factor to electron counting efficiency, and hence, the X-ray energy resolution, was a low signal-to-noise ratio. At the maximum charge gain, therefore at the maximum value of f_d , using A-CH₄(10%) without the presence of secondary processes, the X-ray energy resolution was found to be 48.4 %FWHM. This value is considerably higher than 28 %FWHM achieved by the conventional proportional counter at 1.49 keV (see section 2.5).

The maximum values of f_a , f_d and f_c using A-CH₄(50%) at 1.49 keV were found to be 0.967, 0.944 and 0.979, respectively. The X-ray energy resolution at the maximum f_a , f_d and f_c values was found to be 19.5 %FWHM. Thus an improvement in the X-ray energy resolution by approximately a factor of 1.44 has been achieved at 1.49 keV by the direct electron counting method over the conventional proportional counter method.

In the present work, the full potential of the direct electron counting was not realised at 5.89 keV. At the time of making measurements at 5.89 keV, lower gain electron counting electronics nos. 3 and 4 were not available.

Electron counting electronics no. 2 were used at 5.89 keV. Although, the maximum charge gain using A-CH₄(50%) was 1.29×10^6 (anode voltage 2.60 kV), it was only possible to use a charge gain of 9.87×10^4 (anode voltage 2.37 kV) due to the saturation of electron counting electronics no. 2. As a result, the electron counting efficiency at 5.89 keV using A-CH₄(50%) was found to be lower than that achieved at 1.49 keV. Furthermore, electron counting losses due to the finite resolving time of the electron counting electronics increase as the number of primary electrons increase (see eqn. 1.26). The number of primary electrons using A-CH₄(50%) at 5.89 keV equals 205 electrons compared to 52 electrons at 1.49 keV). Thus the value of $(1-f_c)$ at 5.89 keV was found to be higher than the corresponding value at 1.49 keV.

Chapter 6

Summary and discussion.

This chapter is concerned with a brief examination of the experimental objectives achieved in chapters 2-5.

It has been demonstrated using the direct electron counting method that a significant improvement in the X-ray energy resolution at 1.49 keV is possible over the conventional proportional counter method (see chapter 5). Ideally, the X-ray energy resolution using any electron counting method at a given X-ray energy should only be limited by the Fano factor F (see eqn. 1.2). In this case, for instance, the X-ray energy resolution at 1.49 keV should be 14.6 %FWHM. It has been established, however, during the course of the present studies that three different electron loss mechanisms operate during direct electron counting experiments. Each of these mechanisms contributes an additional statistical fluctuation towards the overall width of the electron counting spectrum leading to an increase in the ultimate X-ray energy resolution.

An experimental chamber consisting of a uniform-field drift tube and a coaxial proportional counter was constructed. The experimental determination of the X-ray energy resolution, by conventional charge signal measurements, at 1.49 keV and 5.89 keV was firstly carried out. These studies provided a "baseline" X-ray energy resolution. The best proportional counter X-ray energy resolutions at 1.49 keV and 5.89 keV, using A-CH₄ (10%) and A-CH₄ (50%), were found to be 28 %FWHM and 17 %FWHM, respectively. The best X-ray energy resolution at 5.89 keV using A-CO₂ (20%) was found to be 27 %FWHM (see section 2.5). Later work with A-CO₂ (20%) confirmed a high level oxygen concentration (11 ppm) which caused a large reduction in the mean electron lifetime (see section 3.9).

The main aim of the present project was to determine the maximum electron counting efficiency using a number of different counter gas mixtures. The experimental determination of the parameters relevant to the X-ray energy resolution using the direct electron counting method was carried out. The knowledge of these parameters assisted in the prediction of the X-ray energy resolution using the direct electron counting method (see eqn. 1.20). The knowledge of these parameters should also assist in the prediction of the X-ray energy resolution using light pulse systems.

Detailed experimental work was also carried out in chapter 2 to determine the maximum signal-to-noise ratio, and therefore the maximum f_d

value and the minimum S_d value, using the present electron counting system. Six different counter gas mixtures were used for this purpose. These were A-CH₄(10%), A-CH₄(50%), A-CH₄(50%)-N₂(2.5%), A-CH₄(50%)-N₂(5%), A-CH₄(50%)-N₂(10%) and A-CO₂(20%). Differential and integral pulse height spectra using UV excitation were taken over a wide range of charge gains. These studies showed that a useful departure from an exponential spectrum was not possible without the onset of cathode secondaries. It was shown that the secondary electrons produced by UV emission from an original genuine avalanche arrived at the anode wire after approximately 0.4 μ s delay. Clearly in the present short resolving time of the electron counting electronics, it was essential to carry out the electron counting experiments at a charge gain which was not accompanied by secondary processes. It was discovered that the examination of the single electron response alone was insufficient to verify the absence of the secondary processes. In order to ensure their absence, it was necessary to analyse the time structure of the signals from single electron excitations. The "true" proportional charge gain region was determined for A-CH₄(10%), A-CH₄(50%) and A-CO₂(20%). It was found that the average charge gains attained before the onset of the secondary processes in A-CH₄(10%), A-CH₄(50%) and A-CO₂(20%) were 4.29×10^4 , 1.29×10^6 and 2.61×10^6 , respectively. The associated maximum f_d value for A-CH₄(10%) using the fast electron counting electronics no. 1 (maximum noise level at 5.40×10^4 counter electrons) was equal to 0.332. This value implies that 66.8 % electron loss occurs below the discriminator threshold when using A-CH₄(10%). This large value makes A-CH₄(10%) an unsuitable counter gas mixture for any practical electron counting detector. The maximum f_d value for A-CH₄(50%) using the fast electron counting electronics no. 3 (maximum noise level at 75000 counter electrons) was equal to 0.944. A higher concentration of methane in argon, therefore, leads to a much enhanced f_d value. The maximum f_d value for A-CO₂(20%) using the fast electron counting electronics no. 3 was equal to 0.972.

It was also demonstrated in chapter 2 that the cathode secondaries were not responsible for the peaked single electron pulse height at very high charge gains. This was achieved by suppressing the charge signals due to the cathode secondaries and then examining the single electron response. It was found that the pulse height spectrum retained the peaked shape.

Determinations of f_a and S_a were carried out in chapter 3 using A-CH₄(10%), A-CH₄(50%), A-CH₄(50%)-N₂(2.5%), A-CH₄(50%)-N₂(5%), A-CH₄(50%)-N₂(10%) and A-CO₂(20%). This required measurement of

electron mobility and the mean electron lifetime against capture for a given counter gas mixture. A TOF technique was used to determine the electron mobility and D_1/μ in these counter gas mixtures at very low drift fields ($E_d/p < 0.02$ V/cm Torr). The experimental electron mobilities were found to be in good agreement with theoretical values (see table 3.2). At the low drift fields used, D_1/μ must equal 25 meV. The independence from the drift field of the electron mobility supports this simplified view. The experimental values of D_1/μ , however, were found to be much higher than expected (see table 3.2). Further research is needed to explain this anomaly. For example, the broadening of the arrival time spectrum due to the finite UV flash width should be examined. Measurement of the mean electron lifetime using A-CH₄(10%) and A-CH₄(50%) showed that it was so long that only a lower limit, 5.0 ms, can be quoted. For instance, the f_a parameter at 1.83 V/cm using A-CH₄(10%) equals 0.986 i.e. $(1-f_a)$ equals 0.014. This implies a 1.4 % electron loss by electron capture using A-CH₄(10%) at 1.83 V/cm. For the A-CH₄(50%)-N₂ mixtures the mean electron lifetime was found to be approximately 3.0 ms. It was shown that this reduction occurred due to some trace impurity in the gas mixing system rather than because of a property of nitrogen. The f_a parameter for A-CH₄(50%)-N₂ mixtures was, therefore smaller than A-CH₄(10%) and A-CH₄(50%). For example, f_a was found to be 0.959 at 1.83 V/cm when using A-CH₄(50%)-N₂. The mean electron lifetime using A-CO₂(20%) was found to be approximately 200 μ s. This result may imply, despite the use of freshly activated Oxy-traps, the persistence of some trace impurity in A-CO₂(20%). A high electron capture rate in A-CO₂(20%), however, may be attributed to the much lower electron mobility in A-CO₂(20%) compared with an A-CH₄ counter gas mixtures. Electrons drifting through A-CH₄ undergo many inelastic collisions with counter gas molecules and resume their motion in the direction of the applied field. In contrast, electrons drifting in A-CO₂(20%) undergo many elastic collisions with counter gas molecules. Consequently, electron motion in A-CO₂(20%) can be described as "zigzag" which enhances the probability of a collision with impurity molecules such as oxygen. The f_a parameter using A-CO₂(20%) was much reduced. For example, f_a at 1.83 V/cm equals 0.04 for the present A-CO₂(20%) counter gas mixture.

Although only a small amount of electron loss was associated with capture to impurities when using A-CH₄(10%) and A-CH₄(50%), it was discovered, however, that a gradual reduction in the mean electron lifetime occurred over the period of several months. This problem was thought to originate from a saturation of the Oxy-trap with oxygen and outgassing of the

neoprene O-rings. It is recommended, therefore, that these O-rings be replaced in any future modification of the experimental chamber. Hermetically sealed ceramic O-rings would show better performance than the present neoprene O-rings.

Determinations of f_c and S_c were carried out in chapter 4. This required the knowledge of the remaining number of counts per X-ray event after the electron loss by capture and the electron loss below the discriminator threshold level of the electron counting electronics, the resolving time of the electron counting electronics and the r.m.s. width of the arrival time spectrum. Only approximately 2 % electron loss was attributed to the finite resolving time of the present electron counting electronics.

Electron counting spectra at 1.49 keV and 5.89 keV were taken in chapter 5. The theoretical X-ray energy resolution at 1.49 keV and 5.89 keV is 14.6 %FWHM and 7.0 %FWHM, respectively provided the parameters f_a , f_d and f_c remain unity. The best X-ray energy resolution at 1.49 keV using A-CH₄(10%) was found to be only 48.4 %FWHM when compared with the 28 %FWHM using the conventional proportional counter. This counter gas mixture was unsuitable for a practical electron counting detector because it showed an "early" onset of secondary processes. The A-CH₄(50%)-N₂ counter gas mixtures were not used to obtain any electron counting spectrum due to the contaminated gas mixing system. Nevertheless, the data obtained on their single electron response and electron mobility will prove useful in any future investigation concerning the performance of light pulse systems. Contrary to the experience at Brookhaven National Laboratory with A-CO₂(20%), the results obtained during the present studies were very disappointing and puzzling. The very low electron mobility, $3.50 \times 10^{-3} \text{ cm}^2/\text{V}\mu\text{s}$, and the relatively high X-ray absorption makes A-CO₂(20%) a potentially attractive counter gas mixture for the electron counting experiments. A-CO₂(20%) achieved the highest f_d and therefore lowest $(1-f_d)$ values of any counter gas mixture used here. For example, f_d and $(1-f_d)$ were found to be 0.971 and 0.029, respectively. The parameter f_a for A-CO₂(20%) was, however, found to be much reduced. Hence, no electron counting spectrum was taken using A-CO₂(20%).

The best X-ray energy resolution at 5.89 keV using A-CH₄(50%) was found to be approximately 18.5 %FWHM (see figure 5.8). Clearly, electron counting losses increase with an increasing number of primary electrons (see eqn. 1.26). Increasing the drift length would increase the r.m.s. width of the arrival time spectrum thus increasing the parameter f_c (see eqn. 1.26). Furthermore, the parameter f_d may also be increased using the maximum

permissible charge gain of 1.29×10^6 for A-CH₄(50%). For example, using electron counting electronics no. 3, it would be possible to achieve a f_d value of 0.944 compared to the 0.684 achieved using electron counting electronics no. 2.

The best X-ray energy resolution at 1.49 keV for A-CH₄(50%) was found to be 19.5 %FWHM using the present electron counting method (see figure 5.7). This represents a factor 1.44 improvement in the X-ray energy resolution over that achieved using the conventional proportional counter. The corresponding values of the parameters f_a , f_d and f_c were 0.967, 0.944 and 0.979, respectively. The present studies may be pursued further, at the Space Sciences Laboratories, Berkeley, to improve the X-ray energy resolution at 1.49 and 5.89 keV. The resolving time τ_r of the fast electron counting electronics at Berkeley is approximately 1 ns compared to the 26.6 ns for the present electron counting electronics. Clearly, electron counting electronics with a shorter resolving time reduce electron counting losses (see eqn. 1.26). The parameter f_a increases with increasing drift fields whereas the opposite is true for the parameter f_c . In the present experiment, however, a weak drift field 1.22 V/cm was used to obtain the electron counting spectrum since f_c decreased very sharply with drift fields (see tables 4.3 and 4.4). As a result, 3.3 % electron loss occurred due to electron capture. The availability of faster electron counting electronics implies that electron counting spectrum may be obtained using higher drift fields. For example, if electron counting is carried out using A-CH₄(50%) operated at 2.60 kV (charge gain at 1.29×10^6) at a drift field of 5.0 V/cm then the parameters f_a , f_d and f_c would equal 0.992, 0.944 and 1.000, respectively. This corresponds to a theoretical X-ray energy resolution of 16.8 %FWHM using equation 1.20. The X-ray energy resolution would still be limited by 5.6 % electron losses below the discriminator threshold of the electron counting electronics. This type of loss may also be minimized by using another counter gas mixture such as A-C₂H₆ which may attain a charge gain higher than A-CH₄(50%) without the presence of cathode secondaries.

The useful X-ray energy range of the present detector is approximately 1.0-6.0 keV. The lower energy limit is determined by counter's window material, window thickness and the mean absorption depth of X-rays. The window material used in this work was mylar (100 μ m thick). In order to obtain a better quantum detection efficiency, a thinner window (1 μ m) may be used. Furthermore, the mean absorption depth of X-rays below 0.1 keV is of the order 1 mm. As a result, serious electron counting losses would occur due to the back-diffusion of primary electrons towards the entrance window. The upper X-ray energy limit is determined by the resolving time of electron counting

electronics as well as the mean absorption depth, λ , of X-rays. Argon based electron counting gas mixtures become transparent at higher X-ray energies. For instance, the mean absorption depth of X-ray at 6.0 and 10.0 keV equal 1.9 cm and 10.0 cm, respectively compared to the present drift length 5.1 cm. The present upper X-ray energy limit may be extended to 10 keV using a longer drift length, typically 20 cm, and by using faster counting electronics.

The present electron counting detector may find applications in laboratory based X-ray spectroscopy. For instance, a semiconductor research group at Brookhaven National Laboratories needs to assess the level of oxygen contamination in a predominately carbon matrix. A conventional proportional counter cannot resolve the emission lines of C-K (0.28 keV) and O-K (0.53 keV) X-rays. The present detector, however, should prove adequate for this purpose.

The present studies may also be extended to investigating X-ray energy resolution at sub-keV X-ray energies. During the present work, C-K (0.28 keV) or O-K X-rays (0.53 keV) were not available. Further work may also be carried out to determine electron mobilities and characteristic electron energies in a number of different counter gas mixtures using cosmic rays as the source of prompt signals (Wong (1987)). The present TOF method was limited to the determination of longitudinal diffusion coefficients compared to Wong's arrangement which can also be used to determine the transverse diffusion coefficients.

Appendix A

Correction factors for a number of different anode voltages at a 0.45 μ s shaping filter time constant.

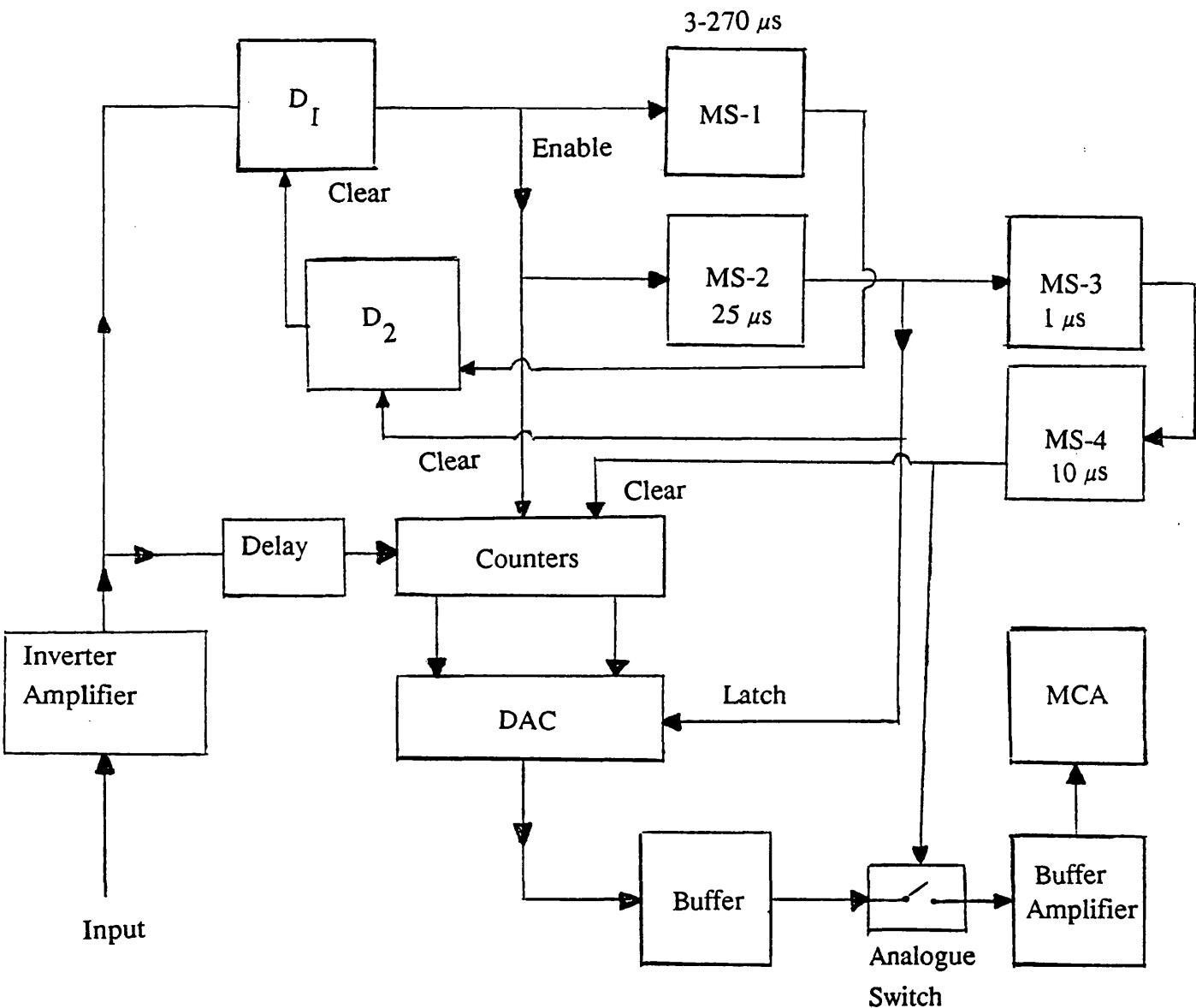
Anode Voltage (kV)	Correction factor (Unipolar)	Correction factor (Bipolar)
1.15	2.70	2.94
1.20	2.68	2.92
1.25	2.66	2.90
1.30	2.64	2.88
1.35	2.63	2.87
1.40	2.61	2.85
1.45	2.59	2.83
1.50	2.58	2.82
1.55	2.56	2.80
1.60	2.55	2.79
1.65	2.54	2.78
1.68	2.53	2.77
1.70	2.52	2.76
1.73	2.52	2.76

continued overleaf.....

Anode Voltage (kV)	Correction factor (Unipolar)	Correction factor (Bipolar)
1.75	2.51	2.75
1.78	2.51	2.75
1.80	2.50	2.74
1.83	2.49	2.73
1.85	2.49	2.73
1.88	2.49	2.73
1.91	2.47	2.71
1.95	2.46	2.70
2.00	2.46	2.70
2.20	2.42	2.66
2.30	2.40	2.64
2.40	2.39	2.63
2.50	2.37	2.61
2.60	2.36	2.60
2.70	2.34	2.58
2.75	2.33	2.57
2.80	2.33	2.57

Appendix B

Burst counter operation.



Block diagram showing the components of the burst counter.

Signal processing sequence :

- 1) First pulse from the discriminator clocks D_1 .
- 2) D_1 enables counters and triggers MS-1 which determines the gate time.
- 3) At the end of gate time, D_2 is clocked which clears D_1 and disables counters. Furthermore, MS-2 is also triggered.
- 4) MS-2 latches counters to DAC. MS-3 is also triggered which provides time for DAC.
- 5) MS-4 is triggered which clears the counters and closes the analogue switch.
- 6) The output of the burst counter is displayed on an MCA.

Appendix C

Correction to electron counting spectra due to the finite resolving time of the electron counting electronics.

The fraction of the number of counts per X-ray event lost, due to the finite resolving time, τ_r , of the electron counting electronics is given by $(1-f_c)$. The fraction of electrons, f_c , which are counted by the burst counter is expressed in terms the number of electrons remaining after capture and losses below the discriminator threshold level, resolving time of the electron counting electronics and the r.m.s. width of the arrival time spectrum (see equation 1.26). If N counts per X-ray event are counted by the burst counter, then the observed number of number of counts per X-ray event at the burst counter output, N^* , can be expressed as follows :

$$N^* = Nf_c \quad \text{B1}$$

Combining equations 1.26 and B1, the following expressions are obtained :

$$(N-N^*/N^*) = N^2 \tau_r / 2\tau N^* (\pi)^{1/2} \quad \text{B2}$$

$$= N \tau_r / 2\tau f_c (\pi)^{1/2} \quad \text{B3}$$

$$= N^* \tau_r / 2\tau (f_c)^2 (\pi)^{1/2} \quad \text{B4}$$

The fraction $(N-N^*/N^*)$ in above equations represents the number of counts per X-ray event which are lost due to the finite resolving time of the electron counting electronics. Now provided $(1-f_c) \ll 1$ (say ≤ 0.1), then equation A 5.4 simplifies to the following equation :

$$(N-N^*/N^*) \approx N^* \tau_r / 2\tau (\pi)^{1/2} \quad \text{B5}$$

Thus the correction $[N^* \tau_r / 2\tau (\pi)^{1/2}]$ must be applied to each point on the electron counting spectrum.

List of References.

- Agrawal P.C., Ramsey B.D. and Weisskopf M.C., Nuclear Instruments & Methods in Physics Research A277 (1989) 557.
- Aitken D.W. Beron B.L. Yenicay G. & Zulliger H.R., IEEE Transactions on Nuclear Science NS-14 (1967) 468.
- Alice M. Alves F. Policarpo A.P.J.L. & Salet M., IEEE Transactions On Nuclear Science NS-22 (1975) 109.
- Alkhazov G.D. Komar A.P. & Vorobev A.A., Nucl. Instr. & Meth. 48 (1967) 1.
- Alkhazov G.D., Nucl. Instr. & Meth. 75 (1969) 161.
- Alkhazov G.D., Nucl. Instr. & Meth. 89 (1970) 155.
- Allison W.W.M. Brooks C.B. Bunch J.N. Cobb J.H. Lloyed J.L. & Fleming R.W., Nucl. Instr. & Meth. 119 (1974) 499.
- Alves M.A.F. Policarpo A.J.P.L. & Dos Santos M.C.M. Nucl. Instr. & Meth., 111 (1973) 413.
- Anderhub H. Devereux M.J. & Seiler P.G., Nucl. Instr. & Meth. 166 (1979) 581.
- Anderson D.F. PhD. Thesis, University of Columbia, NY, (1978).
- Aoyama T., Nucl. Instr. & Meth. A234 (1985) 125.
- Bambynek W., Nucl. Instr. & Meth. 112 (1973) 103.
- Becker U. Capell M. Chen M. White M. Yee K. Fehlmann J. & Seiler P.G., Nucl. Instr. & Meth. 214 (1983) 525.
- Birks J.B., The Theory & Practice of Scintillation Counting (Macmillan, New York (1964)).
- Bleeker J.A.M. Huizenga H. den Boggende A.J.F. & Brinkman A.C., IEEE Transactions on Nuclear Science NS-27 (1980) 176.
- Boie R.A. Hrisoho A.T. & Rehak P., Nucl. Instr. & Meth. 192 (1982) 365.
- Borer K. et al., Nucl. Instr. & Meth. A253 (1987) 548.
- Borkowski C.J. & Kopp M.K., IEEE Transactions on Nuclear Science NS-19 (1972) 161.
- Bourene M. & Le Calve J., Jour. of. Chem. Phys. 58 (1973) 1452.
- Breskin A. Charpak G. Majeswski S. Melchart G. Patersen G. & Sauli F., Nucl. Instr. & Meth. 161 (1979) 19.
- Breskin A. & Chechik R., IEEE Transactions on Nuclear Science NS-32 (1984) 504.
- Breskin A. Chechik R. Dangendorf V. Majewski S. Malamud G. Pansky A. & Vartsky D., Nuclear Instruments & Methods in Physics Research A310 (1991) 57.

- Breskin A. Chechik R. Dangendorf V. Malamud G. Gordon A.S. Pansky A. & Vartsky D., *IEEE Transactions on Nuclear Science* 38 (1991) 158.
- Broyles C.D. Thomas D.A. & Haynes S.K., *Phys. Rev.* 89 (1953) 715.
- Bunemann O. Cranshaw T.E. & Harvey J.A., *Can. Jour. Res.* 27 (1949) 191.
- Byrne J., *Nucl. Instr. & Meth.* 74 (1969) 291.
- Byrne J. Shaikh F. & Kyles J., *Nucl. Instr. & Meth.* 79 (1970) 286.
- Campion P.J., *Instrumentation Journal of Applied Radiation & Isotopes* 19 (1968) 219.
- Charles M.W. & Cooke B.A., *Nucl. Instr. & Meth.* 61 (1968) 31.
- Chamberlain O., *New Directions in Physics* (Academic Press, Orlando (1987)).
- Charpak G. & Renard G.A., *Journal De Physics et Radium* 17 (1956) 585.
- Charpak G. Bouclier R. Bressani T. Favier J. & Zupancic C., *Nucl. Instr. & Meth.* 62 (1968) 262.
- Charpak G., *Nature* 270 (1977) 479.
- Charpak G. Sauli F. & Kahn R., *Nucl. Instr. & Meth.* 152 (1978) 185.
- Charpak G. Melchart G. Petersen G. & Sauli F., *Nucl. Instr. & Meth.* 167 (1979) 455.
- Charpak G. Dominik W. Santiard J.C. Sauli F. & Solomey N., *Nuclear Instruments & Methods in Physics Research A274* (1988) 275.
- Charpak G, Dominik W, Santiard J.C., Sauli F & Solomey N., *Nuclear Instruments & Methods in Physics Research A274* (1989) 275.
- Colli L & Facchini U , *Revised Scientific Instrumentation* (1952) 39.
- Cookson A.H. & Lewis T.J., *Brit. Jour.Appl.Phys.* 17 (1966) 1473.
- Crompton R.W. Elford M.T. & Gascoigne J., *Australian Journal of Physics* 18 (1965) 409.
- Curran S.C. Angus J. & Cockroft A.L., *Phil. Mag.* 40 (1949) 36.
- Curran S.C., *Proportional Counter Spectrometry* (Elsevier-North Holland, (1955)).
- Diethorn W., *A Methane Proportional Counter System for Natural Radiocarbon Measurements*, NYO-6628 (1956).
- Ellison J. Hall G. & Roe S. , *Nucl. Instr. & Meth. A* 260 (1987) 353.
- Fano U., *Phys. Rev.*, 72 (1947) 26.
- Ferbel T., ed 1982 *Proceedings of Fermilab Workshop on Silicon Detectors for High Energy Physics*, Batavia (1981).
- Fisher J. Hrisoho A.T. Radeka V. & Rehak P., *Nucl. Instr. & Meth. A238* (1985)

249.

Fischer J. Radeka V. & Smith G.C., Nucl. Instr. & Meth. A252 (1986) 239.

Fraser G.W. & Mathieson E., Nuclear Instruments & Methods in Physics Research A247 (1986a) 544.

Fraser G.W. & Mathieson E., Nuclear Instruments & Methods in Physics Research A247 (1986b) 566.

Fraser G.W. & Mathieson E., Nuclear Instruments & Methods in Physics Research A257 (1987) 339.

Fraser G.W., X-ray Detectors in Astronomy (Cambridge University Press, Cambridge (1989)).

Frommhold Z., Z. Physik 150 (1958) 172.

Furry W.H., Phys. Rev. 52 (1937) 569.

Gatti E. & Rehak P., Nucl. Instr. & Meth. 225 (1984) 608.

Gedanken A. Jortner J. Raz B. & Szoke A., Journal of Chemical Physics 57 (1972) 3456.

Genz H., Nucl. Instr. & Meth. 112 (1973) 83.

Giacconi R. Gursky H. Paolini F.R. & Rossi B., Phys. Rev. Lett. 9 (1962) 439.

Gilvin P.J. Mathieson E. Smith G.C., IEEE Transactions on Nuclear Science NS-28 (1981) 835.

Gold R. & Bennett E.F., Phys. Rev. 147 (1966) 201.

Gott R. Charles M.W., Nucl. Instr. & Meth. 72 (1969) 155.

Grun A.E.V. Schopper E. Z., Naturforsch 9a (1954) 134.

Gwin R. & Murray R.B., I.R.E. Transactions on Nuclear Science NS-9 (1962) 28.

Harris T.J. Mathieson E. Mir J.A. & Smith G.C., Nucl. Instr. & Meth. A299 (1990) 195.

Heath R.L. Hofstadter R. & Hughes, Nucl. Instr. & Meth. 162 (1979) 431.

Hempel G. Hopkins F. & Schatz G., Nucl. Instr. & Meth. 131 (1975) 445.

Hendricks R.W., Rev. Sci. Instr. 40, No.9 (1969) 1216.

Hough J. & Drever R.W.P., Nucl. Instr. & Meth. 103 (1972) 365.

Hurst G.S. & Parks J.E., Jour. Chem. Phys. 45 (1966) 1.

Huxley L.G.H. & Crompton R.W., The Diffusion & Drift of Electrons in Gases (Wiley, New York (1974)).

Inoue H. Koyama K. Matsuoka M. Tanaka Y. & Tsunemi H., Nucl. Instr. & Meth.

157 (1978) 295.

Jahoda K. McCammon D., Nuclear Instruments & Methods in Physics Research A272 (1988) 800.

Janesick J.R. & Blouke M.M., Sky & Telescope 74 (1987) 238.

Kaizer W.C. Baker S.I. Makay A.J. & Sherman I.S., I.R.E. Transactions on Nuclear Science NS-9 (1962) 22.

Kaufmann R.G.K. Hadley W.B. & Hersh H.N., IEEE Transactions on Nuclear Science NS-17 (1970) 82.

Kiser R.W., Appl. Sci. Res. 8 (1960) 183.

Klucklow R., Z. Physik 148 (1957) 564.

Knoll G.F., Radiation Detection & Measurement (Wiley, New York (1979)).

Kowalski T.Z., Nuclear Instruments & Methods in Physics Research A244 (1986) 533.

Kowalski T.Z., Smith A. & Peacock Nuclear Instruments & Methods in Physics Research A279 (1989) 567.

Lauer E.J., Journal of Applied Physics 23 (1952) 301.

Legler W., Z. Physik 140 (1955) 221.

Manzo G. Peacock A. Andresen R.D. & Taylor B.G., Nucl. Instr. & Meth. 174 (1980) 301.

Mathieson E. & Charles M.W, Nucl. Instr. & Meth. 72 (1969) 155.

Mathieson E. & Hakeem N., Nucl. Instr. & Meth. 159 (1979) 489.

McCann M.F. & Smith K.M., Nucl. Instr. & Meth. 65 (1968) 173.

McKenzie J.M., Nucl. Instr. & Meth. 162 (1979) 49.

Murray R.B., IEEE Transactions on Nuclear Science NS-22 (1975) 54.

Nawrocki P.J. & Papa. R., Atmospheric Processes (Prentice-Hall (1962)).

Nicholson P.W., Nuclear Electronics (John Wiley & Sons, London (1974)).

Pack J.L. & Phelps A.V., Journal Of Chemical Physics 45 (1966) 4316.

Parker J.H. & Lowke J.J., Phys. Rev. 181 (1969) 290.

Policarpo A.P.J.L. Alves M.A.F. & Conde C.A.N., Nucl. Instr. & Meth. 55 (1967) 105.

Policarpo A.J.P.L. Alves M.A.F. Dos Santos M.C.M. & Carvalho M.J.T., Nucl. Instr. & Meth. 102 (1972) 337.

Policarpo A.J.P.L., Space Science Instrumentation 3 (1977) 77.

- Piuz F., Nucl. Instr. & Meth. 205 (1983) 425.
- Ramsey B.D. & Agrawal P.C., Nuclear Instruments & Methods in Physics Research A278 (1989) 576.
- Rancoita P.G. & Seidman A., Riv. Nuovo Cimento 5 7 (1982).
- Raether H., Electron Avalanches and Breakdown in Gases (Butterworth, London (1964)).
- Rawlings K.J., Nucl. Instr. & Meth. A253 (1986) 85.
- Reid P.B. Ku H.M. Long K.S. Novick R. & Pisarski R.L., IEEE Transactions on Nuclear Science NS-26 (1979) 46.
- Rice-Evans P., Spark, Streamer, Proportional & Drift Chambers (The Richelieu Press, London (1974)).
- Romero L. & Campos J., Int. Jour. appl. Radiat. Iso. 31 (1980) 194.
- Rossi B.B. & Staub H.H., "Ionization Chambers and Counters" (McGraw Hill (1949)).
- Rutherford E. & Geiger H., Proceedings Of Royal Society A 81 (1908) 141.
- Sanford P.W. Mason I.M. Dimmock K. & Ives J.C., IEEE Transactions on Nuclear Science NS-26 (1979) 169.
- Saudinos J., Topical Seminar on Interactions of elementary Particles on Nuclei, Trieste (1970) 313.
- Schlumbohm H. Z. Physik 182 (1965) 306.
- Sephton J.P. Turner M.J.L. & Leake J.W. Nuclear Instruments & Methods in Physics Research 219 (1984) 534.
- Siegmund O.H.W., PhD. Thesis (University of London, (1981)).
- Siegmund O.H.W. Culhane J.L. Mason I.M. & Sanford P.W., Nature 295 (1982) 678.
- Siegmund O.H.W. Clothier S. Culhane J.L. & Mason I.M., IEEE Transactions On Nuclear Science NS-30 (1983) 350.
- Sipila H., Nucl. Instr. & Meth. 133 (1976) 251.
- Siplila H., IEEE Transactions on Nuclear Science NS-26 (1979) 181.
- Skelding R, PhD. Thesis, (University of Leicester, (1984)).
- Slapa M. Huth G.C. Seibt W. Scheiber M.M. & Randtke P.T., IEEE Transactions on Nuclear Science NS-23 (1976) 102.
- Smith G.C. Fischer J. & Radeka V., IEEE Transactions on Nuclear Science NS-31 (1984) 111.
- Smith G.C. Fischer J. & Radeka V., IEEE Transactions on Nuclear Science NS-32 (1985) 521.

- Stefanini A., *Miniaturisation of High-Energy Physics Detectors* (Ettore Majorana International Sciences series New York (1983)).
- Stelzer H., *Nucl. Instr. & Meth.* 133 (1976) 409.
- Stevens A.L.N. & Pingault F., *Philips Res. Report* 30 (1975) 277.
- Strickler T.D. & Arakawa E.T., *Journal of Chemical Physics* 41 (1964) 1783.
- Stumpel J.W. Sanford P.W. & Goddard H.F., *Journal of Physical Electronics* 6 (1973) 397.
- Sumner T.J. Rochester G.K. & Hall G., *Nucl. Instr. & Meth.* A273 (1988) 701.
- Suzuki M. & Kubota S., *Nucl. Inst. & Meth.* 164 (1979) 197.
- Swierkowski S.P. Armantrout G.A. & Wichner R., *IEEE Transactions on Nuclear Science* NS-21 (1974) 302.
- Snyder H.S., *Phys. Rev.* 72 (1947) 181.
- Teresa H.V.T.Dias, Filomena P. Santos, & Conde C.A.N., *Nuclear Instruments & Methods in Physics Research* A310 (1991) 137.
- Townsend J.S., *Phil. Mag.* (1901) 198.
- Townsend J.S., *Electrons in Gases* (Hutchinson London (1947)).
- Wagner E.B., Davies F.J. & Hurst G.S. *Journal Of Chemical Physics* 47 (1967) 3138.
- Walenta A.H. Heintze H. & Schurlein B., *Nucl. Instr. & Meth.* 92 (1971) 373.
- Walenta A.H., *IEEE Transactions on Nuclear Science* NS-26 (1979) 73.
- Wijsman R.A., *Phys. Rev.* 75 (1949) 833.
- Wilkinson P.G. & Johnston H.L., *Journal of Chemical Physics* 18 (1949) 190.
- Williams A. & Sara. R.I., *Int. Jour. Appl. Radiat. and Iso.* 13 (1962) 229.
- Wolff R.S., *Nucl. Inst. & Meth.* 115 (1974) 461.
- Wong L.K.C., PhD. Thesis (University of Carleton, Ottawa, Ontario, Canada (1987)).
- Zastawny J., *Jour. Sci. Instr.* 43 (1966) 179.
- Zombeck M.V., *Handbook of Space Astronomy & Astrophysics* (Cambridge University Press, Cambridge (1982)).

Studies of basic parameters of electron-counting detection

T.J. Harris, E. Mathieson and J.A. Mir *

Physics Department, Leicester University, Leicester LE1 7RH, England

G.C. Smith

*Brookhaven National Laboratory **, Upton, New York 11973, USA*

Measurements have been made of certain parameters relevant to the operation of electron-counting detectors. An experimental chamber consisting of a uniform-field drift tube and a coaxial proportional counter has been employed to obtain data, at very low drift fields ($E/p < 0.02$ V/cm Torr), on electron mobility and lifetimes in a range of gas mixtures. These mixtures included argon, methane, nitrogen and carbon dioxide. Measurements of single-electron spectra showed that, unexpectedly for the standard gas mixtures employed, useful departure from an exponential spectrum was not possible without the production of cathode secondaries. Although the present studies employed only the counter electrical signal the information obtained should be directly relevant to the operation of practical light-pulse systems. Examples of electron-counting spectra for soft X-rays are shown.

1. Introduction

Energy resolution in the conventional charge detection of ionising events with a gas proportional counter depends upon fluctuations in the number of primary electrons and in the gas amplification. Under proportional conditions, the relative rms resolution may be expressed as

$$\sigma_E/E = [(F + B)/N_0]^{1/2}, \quad (1)$$

where N_0 is the average number of primary electrons per event, F is the Fano factor (~ 0.2) and B is the gain fluctuation factor (~ 0.5). A detailed discussion of the above expression, and references to the basic studies in this area, may be found in ref. [1].

It is clear that significant improvement can be achieved by eliminating the second source of fluctuations. This has been successfully achieved in two ways. In the gas scintillation proportional counter [2] the average number of primary electrons is determined by observing the light emitted as these electrons drift in a non-ionising field. This important technique is now well established, with best resolutions at about one-half that of conventional detectors. The second method [3,4] counts the primary electrons directly, by observing the light pulses emitted as these electrons avalanche individually in a parallel-plate chamber. The necessary sep-

aration in time between avalanches is achieved by allowing the primary cloud to diffuse in a low-field drift region preceding the avalanche chamber. This technique cannot yet be regarded as well established but, nevertheless, excellent resolution has been reported [3], 34% relative FWHM for 0.28 keV X-rays.

In this electron-counting method the light emission processes have received detailed study [4]. The purpose of this paper is to report some studies on the other loss, fluctuation processes. By employing very long drift times, the relevant information could be obtained using the counter electrical signals directly, rather than the light signals. This represents a considerable simplification, but it must be emphasised that the main apparatus described here does not represent a practical detector. It is considered nevertheless that the data reported will be of direct use in the understanding and design of such detectors.

2. Theory

In an electron-counting system the relative energy resolution may be written as

$$\sigma_E/E = [(F + S_a + S_d/f_a + S_c/f_a f_d)/N_0]^{1/2}. \quad (2)$$

It has been assumed that there are only three significant loss processes operating.

i) Electron capture. $S_a = (1 - f_a)/f_a$ where $f_a = \exp(-t_d/\tau_a)$. Here t_d is the average time of drift of the primary electrons before the avalanche region and τ_a is

* J.A.M. acknowledges support from the Science and Engineering Research Council, UK.

** Research supported in part by the US Dept. of Energy; Contract no. DE-AC02-76CH00016.

the mean lifetime against capture. In a practical detector this loss should be very small.

ii) Loss below discriminator threshold. $S_d = (1 - f_d)/f_d$. Here f_d is the fraction of signals accepted above a discriminator threshold. This fraction clearly depends critically upon the system noise and the single-electron spectrum shape.

iii) Counting losses. $S_c = (1 - f_c)/f_c$. Here f_c is the fraction of signals from the discriminator that are counted. It may be shown that, approximately,

$$f_c = 1 - N\tau_r/2\tau\sqrt{\pi}, \quad (3)$$

where τ_r is the resolving time of the system, N is the average number of counts from the detector per event ($= f_d f_a N_0$) and τ is the rms spread in arrival time of the counts. This arrival time spread may be estimated from the expression

$$\tau^2 = 2Dt_d/w^2, \quad (4)$$

where D is the longitudinal diffusion coefficient and w is the drift velocity.

3. Apparatus

3.1. Experimental chamber

The essential features of the main apparatus employed in these studies are shown in fig. 1. Electrons

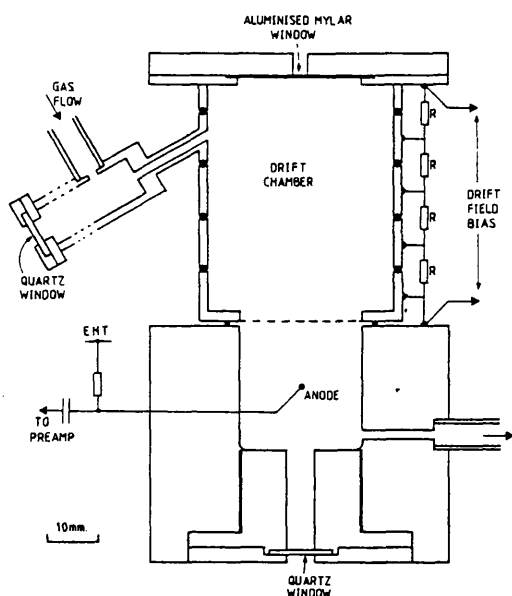


Fig. 1. Schematic diagram of experimental chamber. The chamber material was stainless steel. Essential features and dimensions are described in the text.

from a uniform-field drift chamber, depth 51 mm or 72 mm, passed through a coarse stainless-steel mesh, aperture 2.5 mm, and entered a conventional single-wire counter, mean radius 12.7 mm with anode wire diameter 25 μm . The drift chamber is of the type described and analysed by Crompton et al. [5] and consists in the present case of stainless-steel cylinders, internal diameter 37.5 mm and height 5 mm or 10 mm, separated and insulated by thin neoprene O-rings.

Soft X-rays entered the drift region through an aluminised mylar end window. Alternatively, photoelectrons could be ejected from the inner surface of this window by pulsed UV entering from a quartz side window. Radiation could also enter the counter directly from a window in the counter base.

A gas mixing system allowed the use of various mixtures of argon, methane, carbon dioxide and nitrogen. An oxygen trap was installed in the gas line immediately preceding the chamber itself.

3.2. Electronics

Although the chamber has been designed to be assembled later with a fast photomultiplier, the present studies employed only the electrical signals. These were usually processed by a fast amplifier system, designed at BNL [6]. With delay line clipping of 6 ns the rms noise of this system was about 2000 electrons, allowing a minimum discriminator threshold of about 7000 electrons (step pulse). Knowing the amplifier impulse response and the counter pulse shape, numerical convolution shows that this threshold represents about 75 000 counter electrons.

The fast amplifier was followed by a "burst" counter which counted the number of pulses per event and also converted this number to an analogue signal. The overall resolving time of the system could be estimated by means of expression (3) above. Thus suppose the burst counter output is $f_c N = N'$, say. Then

$$N' = N - N^2\tau_r/2\tau\sqrt{\pi}.$$

From measurements of N' and τ a value of τ_r can be derived. For the present system $\tau_r \approx 35$ ns. This of course represents too large a value for a practical detector with a high rate capability. It is doubtful whether this value could be reduced by much more than a factor of 2 even with the best currently available electronic methods. It is determined essentially by the counter pulse shape and the need to maintain the highest possible signal-to-noise ratio. Nevertheless there may be some special applications in which rate capability could be sacrificed for simplicity.

4. Electron mobility and lifetime

Very low field values have to be employed in the drift region of an electron-counting detector in order to allow sufficient time separation between avalanches. At these low field values one would expect the characteristic energy eD/μ (D is the longitudinal diffusion coefficient and μ is the mobility) to have approximately the thermal value, 0.025 eV, for any gas mixture. However, there is very little information available about mobility. The present apparatus allowed mobility to be measured directly by the time-of-flight method. Some lower limits could also be placed on electron lifetimes.

4.1. Mobility

Pulsed UV from a xenon flash tube (EG&G type FX108AU) ejected electrons from the inner surface of the drift tube window (see fig. 1). For these experiments the counter signal was processed by a low-noise, 2 μ s bipolar amplifier and cross-over detector, the time interval between UV pulse and cross-over being measured by a TAC. An arrival time spectrum could thus be accumulated by a pulse height analyser. The net zero time offset, due to the drift time in the counter itself and due to the various electronic delays, could be determined by ejecting photoelectrons from the inner surface of the stainless-steel mesh by pulsed UV entering the counter base window. By plotting the reciprocal of the drift time, t_d , against the drift field, the mobility could be determined from the slope, μ/d , where d is

Table 1
Electron mobility

Gas mixture	μ (expt.) $\times 10^3$ [cm ² /V μ s]	μ (th.) $\times 10^3$ [cm ² /V μ s]
A/10% CH ₄ (P10)	34.7 \pm 0.2	35.3
A/50% CH ₄ (P50)	20.0 \pm 0.2	21.0
P50/5% N ₂	18.5 \pm 0.2	18.5
P50/10% N ₂	17.7 \pm 0.2	16.9
A/20% CO ₂	3.50 \pm 0.02	3.21

the drift depth. The leakage field, E_0 , from the anode appears as a small intercept on the field axis. For example, $E_0 = 0.25$ V/cm for an anode voltage of 1.75 kV. Examples of drift velocity, w , plotted as a function of field are shown in fig. 2.

It is interesting to note that, even for the present very low drift field values, the correction factor $\beta = (D/\mu)/(E + E_0)d$ (see ref. [7], p. 324) remains always very small compared with unity ($\leq 0.5\%$). Thus calculation of drift velocity, from $w = d/t_d$, where t_d is the most probable arrival time, is adequately justified. "Poisson distortion" [9] of the arrival time spectrum was avoided by ensuring that the counter count rate was at least a factor of 10 less than the UV pulser rate.

Table 1 gives experimental values of low-field mobility for a range of gas mixtures. Also shown are some theoretical values calculated on the highly simplifying assumption that the drifting electron energy distribution remains Maxwellian, and at room temperature [7,8].

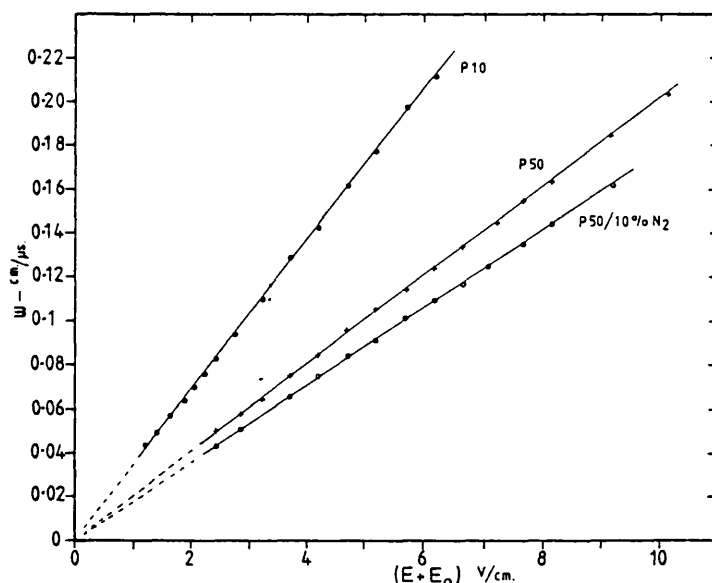


Fig. 2. Electron drift velocity plotted against field. The slope yields mobility.

Under this assumption necessarily D/μ must equal 25 mV. The independence from the electric field of the mobility supports this simplified view. For these calculations the elastic cross-section data for argon, methane and carbon dioxide were as employed in ref. [8]; data for nitrogen are given in ref. [7], p. 631. Space does not permit further discussion here but a more detailed study of this topic is being prepared as a separate report by one of us (E.M.). Clearly a reasonable estimate can be made of electron mobility in a gas mixture from a knowledge of the elastic cross sections of the component gases.

4.2. Electron lifetime

Normally this should not be a critical parameter in an electron-counting system but the present apparatus gave opportunity to obtain some very approximate limits. In principle this measurement is very simple; if the average drift time is t_d then the fraction of primary electrons arriving is $\exp(-t_d/\tau_a)$, where τ_a is the mean lifetime against capture. However, pulse height from the system also falls with t_d because of diffusion of the primary cloud. This latter is generally a much larger effect and therefore must be carefully taken into account. Space forbids a complete description here but, briefly, the procedure is as follows. The Gaussian current waveform of the arriving electron cloud is convoluted with the known counter output waveform (for a single electron). The resultant waveform is then convoluted, numerically, with the known impulse response of the amplifier (unipolar, 5 μ s time constants). The fall in pulse height due to diffusion can thus be allowed for. Remarkably, for the argon/methane gas mixtures, the lifetime was so long that only a lower limit, about 5 ms, can be quoted. For the nitrogen mixtures a finite lifetime, approximately 3 ms, could just be measured. However, it is very possible that this value reflects the presence of some trace impurity in the gas mixing system rather than a property of the nitrogen.

Experience with carbon dioxide mixtures was both puzzling and disappointing. The very low mobility, and relatively high absorption, makes this a potentially attractive gas to use in the present application. However, the present measurements revealed an extremely short lifetime, approximately 100 μ s, in argon/20% carbon dioxide mixture. This anomalous result does not accord with the experience of other workers (e.g. refs. [10,11]), nor indeed with experience at BNL (G.C.S.). Despite the greatest care to avoid contamination, and the use of freshly activated oxygen traps, it was not possible to employ carbon dioxide mixtures in the system at Leicester. As a matter of interest it may be noted, finally, that the electron lifetime in carbon dioxide contaminated with oxygen should be given, in ms, approximately, by

$2.2/x$ where x is the oxygen content in parts per million.

5. Single-electron spectra

A knowledge of the single-electron spectrum is essential in order to estimate the fluctuation due to loss below a discriminator threshold. With the present main apparatus, and counting gas mixtures, the single-electron spectrum at low and moderate gas gains was found to be, as expected (e.g. refs. [1,12,13]), very closely exponential in form. Fig. 3 shows two examples of integral spectra in A/50% CH₄ using the "single" electrons from 1.49 keV X-ray events. A small correction has been applied to take into account counting losses, but not for electron attachment. The intercept on the count axis of fig. 3 yields the average number of primary electrons per event, and hence $w = 1.49 \times 10^3 / 52.0 = 28.7 \pm 0.6$ eV, for P50.

Clearly for high-efficiency single-electron counting the gas gain must be large compared with the discriminator threshold. At high gains the single-electron spectrum indeed became more favourably shaped, the differential spectrum showing a peaked form [1,12]. Unfortunately, and unexpectedly, however, for the present gas mixtures, this form was inevitably accompanied by cathode secondaries. These secondaries were not of course the cause of the peaked spectrum. This is demonstrated by the integral spectra from UV excitation shown in fig. 4 where, for the lower curve, the effect of secondaries has been suppressed by increasing the system dead time to several microseconds. In the present sys-

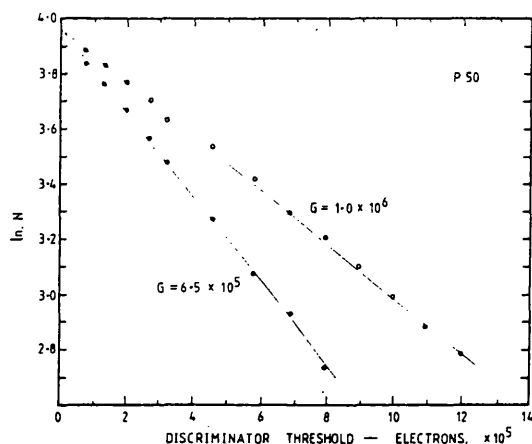


Fig. 3. Single-electron integral spectra from 1.49 keV electron clouds. A small correction has been made for counting losses. The abscissa represents the discriminator threshold measured in electrons from the counter. The intercept on the vertical axis represents $w = 28.7 \pm 0.6$ eV, for P50.

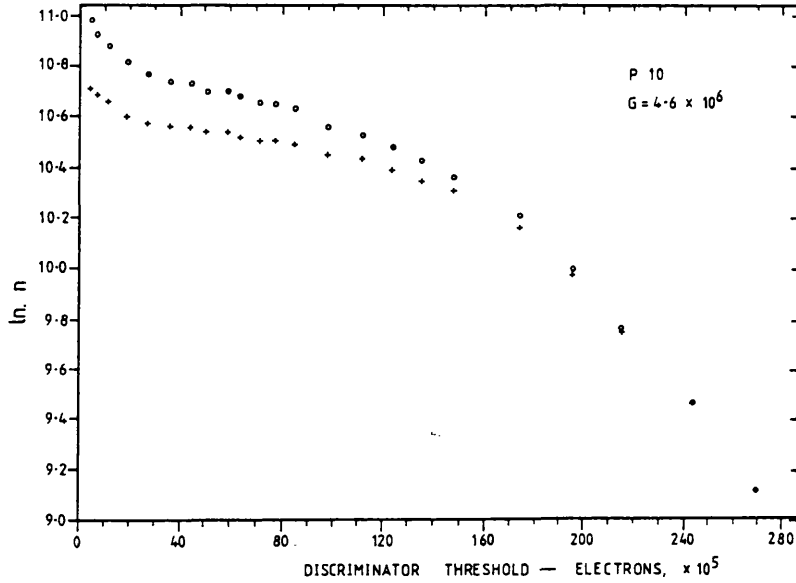


Fig. 4. Single-electron integral spectra from UV excitation, at very high gas gain, in P10. For the lower curve the system dead time was increased from 35 ns to 10 μ s. The abscissa represents the discriminator threshold measured in electrons from the counter.

tem the time delay of the secondaries was rather sharply defined at about 0.4 μ s. The spectra remained essentially independent of dead time provided it exceeded this value.

Clearly in a short resolving time system operating conditions must ensure that secondaries cannot be produced. Thus for the present studies, in which the counter electrical signal was employed, the gas gain was

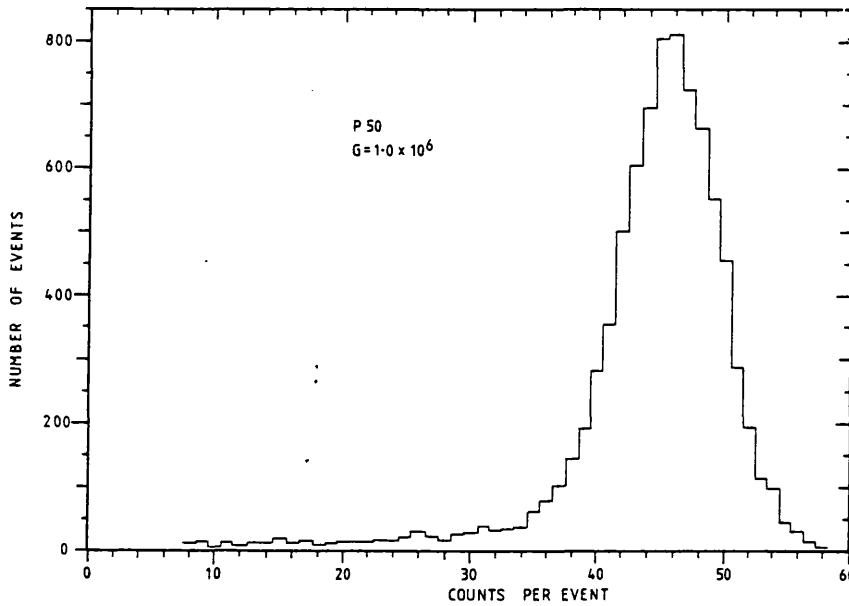


Fig. 5. Electron-counting spectrum from 1.49 keV X-rays, in P50 gas mixture. The relative FWHM is 19.5%. A charge spectrum for the same counter yielded 31%.

limited to that for which the single-electron spectrum remained essentially exponential in form. The maximum counting efficiency, f_d , that can be achieved under these conditions (see section 2.2) is then approximately given by $\exp(-q_d/G)$, where q_d is the discriminator threshold, in counter electrons, and G is the gas gain. This efficiency may be rather low for a practical system, which in any case would have to employ the counter light signal. However, this study emphasises the importance of an examination, in a light-pulse system equally, of the time structure of the signals resulting from single-electron excitation.

6. Electron-counting spectra

Although the experimental chamber was not designed to be a practical electron-counting detector, it is interesting nevertheless to produce count spectra from the counter electrical signals. An example of such a spectrum, for 1.49 keV X-rays in P50, is shown in fig. 5. The relative FWHM is 19.5%, the counting efficiency, mainly determined by the discriminator threshold value, being about 90%. The counter gas gain was approximately 1.0×10^6 . The drift field for this spectrum was 1.23 V/cm, this being near the lowest useable value. Values below about 1.0 V/cm resulted in rapid deterioration in resolution due mainly, it is thought, to back-diffusion to the entrance window.

Fig. 6 shows an electron-counting spectrum for 5.9 keV X-rays taken with an essentially practical detector, a normal MWPC with drift region, but nevertheless employing the chamber electrical signals. The drift region was 39 mm deep, the upper cathode of the chamber consisting of an electroformed Ni grid, 360 μm aperture. The ^{55}Fe radiation was incident obliquely at the drift region window in order to maximise the drift distance of the primary electron clouds. A very low drift

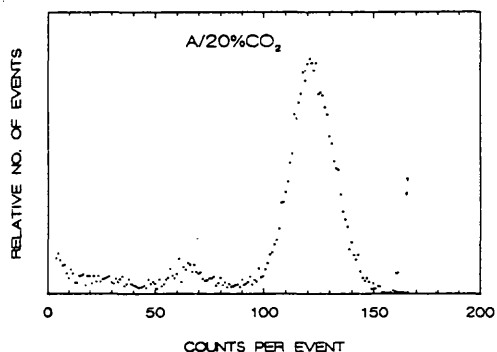


Fig. 6. Electron-counting spectrum for ^{55}Fe X-rays, in A/20% CO_2 gas mixture. This spectrum was taken with a conventional MWPC (see text, section 6). The mean number of counts in the photopeak is about 122.

field value, 4.2 V/cm, was employed in order to disperse the electron cloud adequately in time. The chamber anode/cathode spacing was 4 mm with anode wire pitch 5 mm and the gas was A/20% CO_2 . In fig. 6 the most probable number of counts in the photopeak is about 122, and the relative FWHM is approximately 19%, similar, as it happens, to that expected from conventional charge detection. This part of the present work was carried out at Brookhaven National Laboratory, USA.

7. Discussion

Elementary formulae, and data on electron mobility, have been given which should assist in the prediction of electron-counting detector performance. Furthermore, qualitative value has been placed on a knowledge, in any electron-counting detector, of its single-electron response. It has been demonstrated that the time structure of signals from single electron excitation must be analysed to ensure the total absence of secondaries. An examination of spectrum shape alone is insufficient.

Examples of electron counting spectra, although taken with the "slow" electrical signals from the anode, demonstrate clearly the potential performance of this method for detection of very low energy X-rays (≤ 1.5 keV). There may indeed be some special applications involving very slow count rates in which electrical signals alone would suffice.

References

- [1] G.F. Knoll, Radiation Detection and Measurement, chap. 6 (Wiley, New York, 1979).
- [2] A.J.P.L. Policarpo, Space Sci. Instr. 3 (1977) 77.
- [3] O.H.W. Siegmund, S. Clothier, J.L. Culhane and I.M. Mason. IEEE Trans. Nucl. Sci. NS-30 (1983) 350.
- [4] O.H.W. Siegmund, Ph.D. Thesis, Univ. of London (1981).
- [5] R.W. Crompton, M.T. Elford and J. Gascoigne, Aust. J. Phys. 18 (1965) 409.
- [6] J. Fischer, A.T. Hrisoho, V. Radeka and P. Rehak, Nucl. Instr. and Meth. A238 (1985) 249.
- [7] L.G.H. Huxley and R.W. Crompton, The Diffusion and Drift of Electrons in Gases (Wiley, New York, 1974).
- [8] E. Mathieson and N. El Hakeem, Nucl. Instr. and Meth. 159 (1979) 489.
- [9] E.B. Wagner, F.J. Davies and G.S. Hurst, J. Chem. Phys. 47 (1967) 3138.
- [10] W.W.M. Allison, C.B. Brooks, J.N. Bunch, J.H. Cobb, J.L. Lloyd and R.W. Fleming, Nucl. Instr. and Meth. 119 (1974) 499.
- [11] J.L. Pack and A.V. Phelps, J. Chem. Phys. 45 (1966) 4316.
- [12] H. Raether, Electron Avalanches and Breakdown in Gases (Butterworth, London, 1964).
- [13] F. Puiz, Nucl. Instr. and Meth. 205 (1983) 425.